Title
Interface Engineering of Voltage-Controlled Embedded Magnetic Random Access Memory

Author
Li, Xiang

Publication Date
2018

UNIVERSITY OF CALIFORNIA

Los Angeles

Interface Engineering of Voltage-Controlled Embedded Magnetic Random Access Memory

A dissertation submitted in partial satisfaction of the
requirements for the degree Doctor of Philosophy
in Electrical and Computer Engineering

by

Xiang Li

2018

ABSTRACT OF THE DISSERTATION

Interface Engineering of Voltage-Controlled Embedded Magnetic Random Access Memory

by

Xiang Li
Doctor of Philosophy in Electrical and Computer Engineering
University of California, Los Angeles, 2018
Professor Kang Lung Wang, Chair

Magnetic memory that utilizes spin to store information has become one of the most promising candidates for next-generation non-volatile memory. Electric-field-assisted writing of magnetic tunnel junctions (MTJs) that exploits the voltage-controlled magnetic anisotropy (VCMA) effect offers great potential for high density and low power memory applications. This emerging Magnetoelectric Random Access Memory (MeRAM) based on the VCMA effect has been investigated due to its lower switching current, compared with traditional current-controlled devices utilizing spin transfer torque (STT) or spin-orbit torque (SOT) for magnetization switching. It is of great promise to integrate MeRAM into the advanced CMOS back-end-of-line (BEOL) processes for on-chip embedded applications, and enable non-volatile electronic systems with low static power dissipation and instant-on operation capability. To achieve the full potential of MeRAM, it is critical to design magnetic materials with high voltage-induced writing efficiency, i.e. VCMA coefficient, to allow for low write energy, low write error rate, and high density MeRAM at advanced nodes.

In this dissertation, we will first discuss the advantage of MeRAM over other memory technologies with a focus on array-level memory performance, system-level 3D integration, and scaling at advanced nodes. Then, we will introduce the physics of the VCMA effect, map out the VCMA coefficients requirements and other challenges when MeRAM is scaled down, and discuss the electrical measurement techniques used in later chapters to characterize the VCMA effect. Next, we will discuss three experimental approaches taken to enhance the VCMA coefficient. First, a high dielectric-constant hybrid tunnel barrier is used to increase the VCMA coefficient. Then, by carefully controlling the Mg insertion thickness at the CoFeB/MgO interface, the Fe/O interfacial oxidation condition can be precisely controlled to identify the optimal oxidation condition for large VCMA coefficient. Last, different heavy metal based seed/Mo materials are explored to achieve stable VCMA coefficient, TMR, and perpendicular magnetic anisotropy (PMA) when annealed at temperatures exceeding 400°C, making MeRAM compatible with embedded applications. In addition, we have carefully studied the correlation between atomic elemental distribution and the magnetic properties of these stacks via high resolution transmission electron microscopy (TEM). The insight obtained will provide a critical guidance to future development of both spin-transfer torque and voltage-controlled magnetic memory.

The dissertation of Xiang Li is approved.

Oscar M. Stafsudd

Robert N. Candler

Gregory P. Carman

Kang Lung Wang, Committee Chair

University of California, Los Angeles

2018

To my family, my love, and my career

On the Road

Table of Contents

Chapter 3 Voltage-Controlled Magnetic Anisotropy: Fabrication and Characterization .. 64

List of Figures

List of Tables

ACKNOWLEDGEMENTS

First of all, I would like to thank Prof. Kang L. Wang for taking me into the DRL group. His grand vision on the whole electronics industry as well as rigorous inquiries into every experimental work through the fundamental point of view truly taught me how to make impact on the world by asking simple questions. Setting high goals and standards to achieve excellence is also one of his most admirable traits. In addition to research, I also have the privilege to learn first-hand from him the technology commercialization process. Joining Inston is definitely the best choice I have made in my Ph.D. life. All the challenges encountered have opened a new venue for me and enabled me to see how technology really interacts with the world. During this process, I also came to realize that technology commercialization is the true passion of my life.

The passion, perseverance, insight, and hard work he demonstrated will always be a high standard I strive for in my future life. I would also like to thank for the care, guidance, and shared wisdom my wife and I obtained from Prof. Wang and Mrs. Wang during our daily encounters. In particular, what I learnt most from Prof. Wang and Mrs. Wang is their optimistic attitude towards even the most difficult task as well as being able to manage many tasks and responsibilities at the same time with ease.

Secondly, I would like to thank Prof. Pedram Khalili Amiri, for his guidance through the major portion of my experimental work shown in this dissertation. His vision for magnetic memory attracted me into working on this project, and he always gave a practical engineering perspective that linked my experimental work with the real world engineering requirements.

Thirdly, I would like to thank Dr. Guoqiang Yu for supporting and guiding me through the early stages of my research career. I am forever grateful for his numerous advices on how to think about a direction for research and present the data in a compelling way. More importantly, his humble nature and collaborative spirit show to me how cross-disciplinary collaboration can bring out the best scientific work that could not have happened otherwise.

I want to also thank people in the spintronics group for helping me out along the way: Qi Hu, his technical expertise and professionalism will be indispensable for my future career; Juan Alzate, his hospitality and enthusiasm opened the door of spintronics to me; Kin Wong, his brilliant humor and professionalism make him the most accountable in our group and I must thank him for fabricating those lot of devices. Also, I would like to thank Cecile Grezes, Hochul Lee, Xue Qing Cai, Albert Lee, Aryan Navabi, Armin Razavi, Yuxiang Liu, Hao Wu, Pramey Upadhyaya, Wenyuan Li and all others for all your support! Also I would like to thank the visiting scholars who have helped me tremendously in my research years: Di Wu, Lezhi Wang, Farbod Ebrahimi, Yangqi Huang, Minghua Li, Min Zeng, Mustafa Akyol, Haili Ma, etc..

Being at DRL is actually only part of my experience of my Ph.D. career. I also had close interaction with fellow Ph.D. students from other departments and schools within TANMS: Diana Chien, Kevin Fitzell, Stephen Sasaki, Shauna Robbennolt, Jeff Kurish, Qianchang Wang, Andres Chavez, Sohee Kwon, Vu Ong, Malcom Jackson, to name a few. Also, I would like to thank TANMS faculties for their great advice on my research: Profs. Greg Carman, Jane Chang, Nick Kioussis, and Sarah Tolbert. These wide range of interdisciplinary research at the TANMS center also honed my communications and leadership skills. I would also like to thank my financial funding sources from TANMS, CEGN, WIN, NSF SBIR, IARPA, and Inston.

I would sincerely like to thank Prof. Oscar Stafsudd, Prof. Robert Candler, and Prof. Gregory Carman for taking the time and effort to go through my dissertation and providing valuable advices and comments. Finally, the emotional and financial support from my wife, family and friends is indispensable for me to go through the whole process of graduate career.

VITA

Education

2013-2016	M.S. in Electrical Engineering University of California, Los Angeles, California, United States
2009-2013	B.S. in Physics Peking University, Beijing, China

Employment history

2013-2018	Graduate Student Researcher Department of Electrical Engineering University of California, Los Angeles, California, United States
2017-2018	Ph.D. Device Engineer Intern (Part-time) Inston Inc., Los Angeles, California, United States
2016-2017	Ph.D. Technology Fellow (Part-time) Technology Development Group (Office of Intellectual Property) University of California, Los Angeles, California, United States
2015	Ph.D. Reader Test Intern Reader Test Group, Read Head Operations Seagate Technology, Bloomington, Minnesota, United States

Publication

1) **X. Li**, K. Fitzell, D. Wu, C. T. Karaba, A. Buditama, G. Yu, K. L. Wong, N. Altieri, C. Grezes, N. Kioussis, S. Tolbert, Z. Zhang, J. P. Chang, P. K. Amiri, and K. L. Wang, "Enhancement of voltage-controlled magnetic anisotropy through precise control of Mg insertion thickness at CoFeB/MgO interface," *Applied Physics Letters,* vol. 110, p. 052401, 2017.

2) D. Chien*, **X. Li***, K. Wong, M. A. Zurbuchen, S. Robbennolt, G. Yu, S. Tolbert, N. Kioussis, P. Khalili Amiri, K. L. Wang, and J. P. Chang, "Enhanced voltage-controlled magnetic anisotropy in magnetic tunnel junctions with an MgO/PZT/MgO tunnel barrier," *Applied Physics Letters,* vol. 108, p. 112402, 2016.

3) **X. Li**, G. Yu, H. Wu, P. V. Ong, K. Wong, Q. Hu, F. Ebrahimi, P. Upadhyaya, M. Akyol, N. Kioussis, X. Han, P. Khalili Amiri, and K. L. Wang, "Thermally stable voltage-controlled

perpendicular magnetic anisotropy in Mo/CoFeB/MgO structures," *Applied Physics Letters,* vol. 107, p. 142403, 2015.

4) L. Wang, W. Kang, F. Ebrahimi, **X. Li**, Y. Huang, C. Zhao, K. L. Wang, and W. Zhao, "Voltage-Controlled Magnetic Tunnel Junctions for Processing-In-Memory Implementation," *IEEE Electron Device Letters,* vol. PP, pp. 1-1, 2018.

5) Y. Huang, **X. Li**, L. Wang, G. Yu, K. L. Wang, and W. Zhao, "Interface control of domain wall depinning field," *AIP Advances,* vol. 8, p. 056314, 2018.

6) H. Almasi, C. L. Sun, **X. Li**, T. Newhouse-Illige, C. Bi, K. C. Price, S. Nahar, C. Grezes, Q. Hu, P. K. Amiri, K. L. Wang, P. M. Voyles, and W. G. Wang, "Perpendicular magnetic tunnel junction with W seed and capping layers," *Journal of Applied Physics,* vol. 121, p. 153902, 2017.

7) C. Grezes, H. Lee, A. Lee, S. Wang, F. Ebrahimi, **X. Li**, K. Wong, J. A. Katine, B. Ocker, J. Langer, P. Gupta, P. K. Amiri, and K. L. Wang, "Write Error Rate and Read Disturbance in Electric-Field-Controlled Magnetic Random-Access Memory," *IEEE Magnetics Letters,* vol. 8, pp. 1-5, 2017.

8) G. Q. Yu, P. Upadhyaya, Q. M. Shao, H. Wu, G. Yin, **X. Li**, C. L. He, W. J. Jiang, X. F. Han, P. K. Amiri, and K. L. Wang, "Room-Temperature Skyrmion Shift Device for Memory Application," *Nano Letters,* vol. 17, pp. 261-268, Jan 2017.

9) X. Ma, G. Yu, **X. Li**, T. Wang, D. Wu, K. S. Olsson, Z. Chu, K. An, J. Q. Xiao, K. L. Wang, and X. Li, "Interfacial control of Dzyaloshinskii-Moriya interaction in heavy metal/ferromagnetic metal thin film heterostructures," *Physical Review B,* vol. 94, p. 180408, 11/28/ 2016.

10) G. Yu, P. Upadhyaya, **X. Li**, W. Li, S. K. Kim, Y. Fan, K. L. Wong, Y. Tserkovnyak, P. K. Amiri, and K. L. Wang, "Room-Temperature Creation and Spin–Orbit Torque Manipulation of Skyrmions in Thin Films with Engineered Asymmetry," *Nano Letters,* vol. 16, pp. 1981-1988, 2016/03/09 2016.

11) M. Montazeri, P. Upadhyaya, M. C. Onbasli, G. Yu, K. L. Wong, M. Lang, Y. Fan, **X. Li**, P. Khalili Amiri, R. N. Schwartz, C. A. Ross, and K. L. Wang, "Magneto-optical investigation of spin-orbit torques in metallic and insulating magnetic heterostructures," *Nat Commun,* vol. 6, p. 8958, Dec 08 2015.

12) P. Khalili Amiri, J. G. Alzate, X. Q. Cai, F. Ebrahimi, Q. Hu, K. Wong, C. Grezes, H. Lee, G. Yu, **X. Li**, M. Akyol, Q. Shao, J. A. Katine, J. Langer, B. Ocker, and K. L. Wang, "Electric-Field-Controlled Magnetoelectric RAM: Progress, Challenges, and Scaling," *Magnetics, IEEE Transactions on,* vol. 51, pp. 1-7, 2015.

Chapter 1 Introduction

1.1 Memory Hierarchy, Memory Wall, and Intelligent Internet-of-Things (IIoT)

In the present memory market, there exist a wide range of memory technologies each occupying different application spaces based on their different performance attributes, as shown in Figure 1-1. By putting faster, while smaller density and more costly memory closer to the processor, the whole computing system can fully utilize the high speed of the fastest memory and low cost of the cheapest memory. This hierarchy of different memory technologies is also called the memory hierarchy.

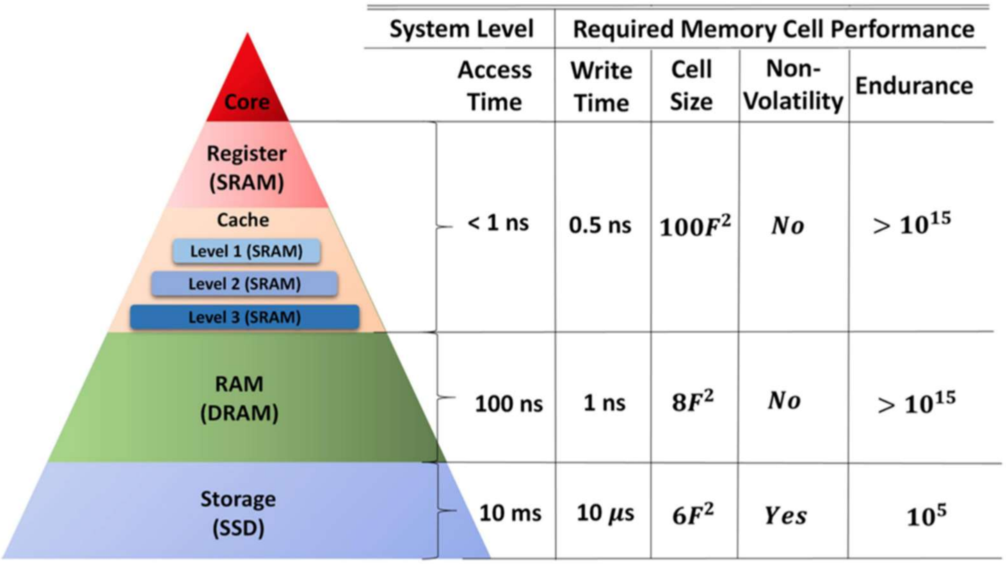

System Level	Required Memory Cell Performance			
Access Time	Write Time	Cell Size	Non-Volatility	Endurance
< 1 ns	0.5 ns	$100F^2$	*No*	$> 10^{15}$
100 ns	1 ns	$8F^2$	*No*	$> 10^{15}$
10 ms	10 μs	$6F^2$	*Yes*	10^5

Figure 1-1 Memory hierarchy in a conventional computer architecture with required system-level and device-level memory performance.[1]

Typically, static random access memory (SRAM) serves as CPU register and cache (L1-L3), (in some applications eDRAM might also be used as L2/L3 or an additional L4 cache), dynamic random access memory (DRAM) as the main working memory, flash as portable and integrated storage for consumer electronics, and magnetic hard disk as high-density storage used in data centers. At one end of this spectrum, SRAM possesses the fastest access speed and lowest dynamic power consumption (write energy per bit), however, consumes high static leakage power as well as data refreshing power due to its volatile nature. While at the other end of the spectrum, flash and hard disk drive demonstrate non-volatility and thus can retain data when powered off, but they show much lower access speed and larger energy consumption for read and write operations. Apart from power-delay considerations, cost and capacity are equally important factors in considering the memory hierarchy. As SRAM and DRAM are rather expensive to manufacture and usually offered in a rather low density, they normally are utilized as on-chip cache or working memory. On the other hand, the flash drive and hard disk drive can achieve low cost as well as high density thus becoming premium for long-term data storage.

The past few decades have witnessed the immense growth of electronic devices ranging from desktop and laptop to handheld and wearable. This is mainly driven by the ever-increasing logic computation capabilities which result in doubling of computer chip transistor density every 18 months. However, the memory performance has not kept up the pace with the logic processing unit, thus creating the processor-memory gap, memory wall, or memory bottleneck, both in terms of memory bandwidth, as well as memory access latency, as shown in Figure 1-2. The main cause of this memory wall is that no technology can fulfill the requirements for high speed, bandwidth, and energy efficiency at the same time. However, very few new technologies have emerged other than the existing SRAM, DRAM, NAND, and hard disk drives. The system level performance gaps between cache, main memory, and storage restrained by the limitations of these technologies thus inhibit the overall performance of the memory subsystem from catching up with other electronic subsystems.

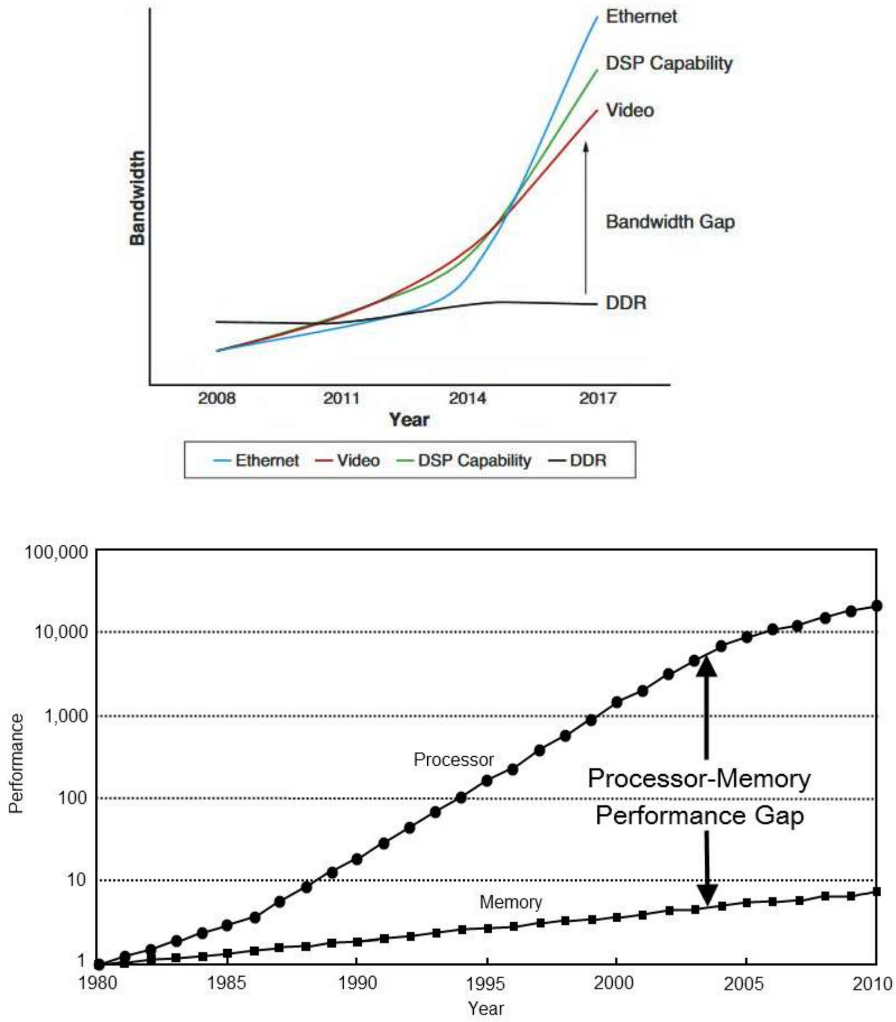

Figure 1-2 (Top) Bandwidth requirements of DRAM memory compared against those of ethernet, digital signal processing (DSP) capability, and video over the past decade, showing an enlarging bandwidth gap between what DRAM can supply and what applications demand.[2] (Bottom) Performance improvement of processor memory requests (for a single processor or core) compared with that of the speed of a DRAM access, from 1980 to 2010.[3]

It is also worth noting that not only the digital computation capabilities increase much faster than memory, the video and Ethernet bandwidths also outpace that of memory significantly as shown in Figure 1-2. This indicates if video and Ethernet has reached their full bandwidth of data generation and transmission, in order to store and process these data, more storage memory and cache memory need to be supplied to compensate the low bandwidth. On top of this, the total volume of video, Ethernet and many other sensory data generated through the Internet of Things (IoT) applications will keep growing. Hence, memory with fast speed, higher bandwidth, and low power consumption will continue to be a scarce commodity in the next few decades.

In addition to the growth of Big Data, the shift from PC and laptop to mobile devices enabled by advanced wireless communications also created a new divide of electronic systems of cloud and edge. More and more data processing needs are fulfilled in the cloud where a huge amount of data are being stored and processed in a centralized manner. While on the edge of these cloud data centers, mobile devices and laptops will download and upload information via fast speed internet, thus alleviate the computation and memory burden of the edge devices. This division of labor between cloud and edge effectively enables the edge devices to integrate more varieties of functionalities and digitalized almost every aspect of our daily lives.

Recently, a new trend of intelligent electronic devices and systems are quickly emerging as shown in Figure 1-3. Machine learning, artificial intelligence, and big data processing have opened up a new wealth of applications for computers to do pattern recognition utilizing the enormous amount of data generated around the globe every second. Though the machine learning training and inferencing of data has started with cloud level GPUs and CPUs clusters, more and more inferencing tasks are required to be executed real time on edge devices such as smartphones, drones, autonomous vehicles, security cameras, robots, etc., to ensure smooth, safe, and autonomous user experience. These applications inherently need a large number of fitting parameters to learn the patterns embedded in the data. Thus, memory is again needed to store the learning data, the machine learning model parameters, and supply these data to computation units in a fast and power-efficient way. While the energy efficiency requirement is especially critical for edge devices with limited battery lifetime.

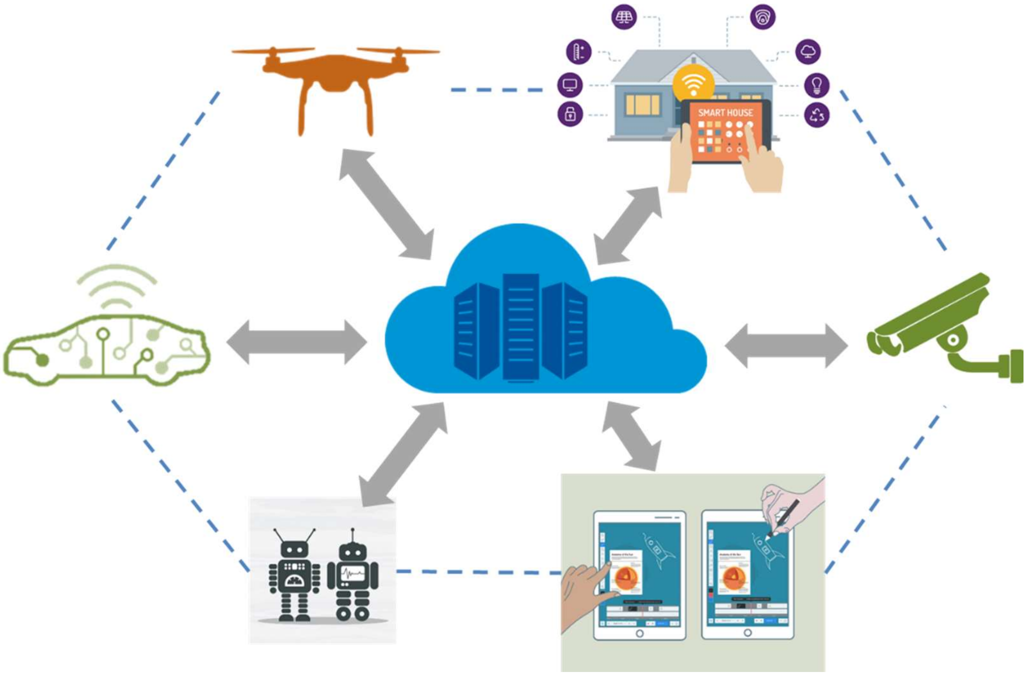

Figure 1-3 Cloud and edge devices divide for future Intelligent Internet-of-Things (IIoT) era. While all data training for machine learning applications will be executed on the cloud, the inferencing of sensory data from the edge devices will be completed on the edge devices.

In order to supply memory with high speed, bandwidth, and energy efficiency for this IIoT era, the whole memory hierarchy needs to be drastically improved with more innovative technologies to fulfill the performance gap between cache and main memory, as well as between main memory and storage. One method to close the gap between cache and main memory is to implement a fast on-chip cache. However, as the SRAM and eDRAM cell size keep skyrocketing with smaller nodes, the density becomes limited and SRAM/eDRAM must occupy more silicon real estate for larger capacity, see Figure 1-6. Nowadays, SRAM caches take up around 50% of the total chip area in system-on-chips (SoCs),[4] while consuming 25-50% of the processor power for personal mobile devices. Hence, it is critical for the whole electronics industry to search for SRAM/eDRAM alternatives.

1.2 Magnetoelectric Random Access Memory (MeRAM) Opportunities

To resolve this memory wall issue, various approaches have been explored, including further scaling down of existing technologies, various emerging non-volatile memory (NVM) technologies, and 3D stacking and packaging innovations over existing technologies to improve the memory bandwidth. In this dissertation, we will focus mainly on one newly emerging variation of Magnetoresistive Random Access Memory (MRAM), i.e. Magnetoelectric RAM (MeRAM) utilizing voltage-controlled magnetic anisotropy (VCMA) effect. We will explore MeRAM's opportunities in replacing SRAM, eDRAM, and eFlash as an embedded memory solution.

1.2.1 MeRAM Compared with Existing, Prototypical and Emerging Memory Technologies

Before we discuss the main focus of this dissertation which is MeRAM as an embedded solution, let us first make a comparison between emerging NVMs and existing DRAM/NAND Flash technologies for standalone applications based on the most recent published data. Note that all data for MeRAM are simulated array-level projections based on device-level data.[1, 5] The NVMs discussed include spin transfer torque magnetic random access memory (STT-MRAM), phase change random access memory (PCRAM), resistive random access memory (ReRAM), and magnetoelectric random access memory (MeRAM). As seen in Table 1-1, MeRAM which is the focus of this thesis is indeed promising to realize the stringent requirement for DRAM replacement comparing to the other emerging competing technologies. MeRAM provides similar density and cost efficiency as DRAM, and it offers 2x density and cost efficiency compared to direct competitor technology spin-transfer torque memory (STT-MRAM). In terms of energy consumption, MeRAM as a non-volatile memory can drastically reduce the standby refresh power consumption of DRAM, while its dynamic read/write energy consumption is 10-100x smaller than all other competitors including DRAM. Finally, speed wise, MeRAM is the fastest among all technologies. In addition, as DRAM applications require endurance of around 10^{15}, PCRAM, ReRAM and NAND Flash all fall short and cannot compete. Their low speed and high-density attributes are best suited for the emerging storage class memory (SCM) technologies residing between DRAM and NAND Flash. All data in Table 1-1 are taken from references [6][7][8][9-12].

Table 1-1. Comparison of existing, prototypical, and emerging **standalone** memory technologies, highlighting STT-MRAM (using current-induced switching) and MeRAM (using electric-field-controlled switching). For each technology, data are averaged values based on several most advanced technology nodes of that technology. [6][13][14][9-12]

	Existing	Prototypical	Emerging	Existing	Prototypical	Emerging
Technology	**NAND Flash**	**PCRAM**	**ReRAM**	**DRAM**	**STT-MRAM**	**MeRAM ****
Endurance (Cycles)	10^5	10^8	10^{12}	10^{16}	10^{15}	10^{15}
Read Time (ns)	10,000	100	100	20	1 - 5	1 - 5
Write/Erase Time (ns)	100,000 /1ms	100	500 /100µs	10	10 - 50	1 - 5
Cell Size (area in F2)	4	4	4	6	9 - 50	4 - 30
Bit Density (Gb/cm2)	200	10	20	10	0.5 - 4	1 - 10
Read Energy/Bit (fJ)*	1,000,000	1,000	1,000	1,000	10 - 20	1 - 5
Write Energy/Bit (fJ)*	1,000,000	10,000	1,000 /10^6	100	100 - 200	1 - 10
Nonvolatile	Yes	Yes	Yes	No	Yes	Yes
Standby Power	None	None	None	Refresh	None	None

**Energy only refers to single cell, without considering the bit lines and peripheral circuits*

*** All data for MeRAM are simulated array-level projections based on device-level data*

To realize the stringent density requirement for DRAM applications, the cell size of MeRAM needs to be smaller or at least equal to $8F^2$. Using a diode instead of a transistor as the selector device can achieve the cell size of around $4F^2$.[5] While by using DRAM-like specialized manufacturing process, the cell size of around $8F^2$ was demonstrated.[15, 16] But with standard CMOS process, due to the transistor spacing requirement, around 1/6 of the standard 6T-SRAM cell size is more realistic. We will also discuss the difficulties for MeRAM to replace DRAM in Section 1.2.2 when considering the scaling trends of both MeRAM and DRAM. All data in Table 1-2 are taken from references [6][17][18][9-12, 19].

Table 1-2. Comparison of existing, prototypical, and emerging **embedded** memory technologies, highlighting STT-MRAM and MeRAM. For each technology, data are averaged values based on several most advanced technology nodes of that technology. [6][20][21][9-12, 19]

	Existing	**Emerging**	**Existing**	**Prototypical**	**Emerging**	**Existing**
Technology	**eFlash**	**eReRAM**	**eDRAM**	**STT-MRAM**	**MeRAM ****	**SRAM**
Endurance (Cycles)	10^5	10^5	10^{15}	10^{15}	10^{15}	10^{15}
Read Time (ns)	10	3 - 10	1 - 2	1 - 5	1 - 5	1
Write/Erase Time (ns)	25μs/2ms	500 /100μs	1 - 2	10 - 50	1 - 5	1
Cell Size (area in F2)	40 - 100	15 - 30	40 - 100	40 - 50	20 - 30	>150
Bit Density (Gb/cm2)	0.5	0.1	0.5 - 2	0.5 - 2	1 - 4	0.1 - 0.5
Read Energy/Bit (fJ)*	1,000,000	1,000	100	10 - 20	1 - 5	1 - 5
Write Energy/Bit (fJ)*	1,000,000	1,000 /10^6	1,000	100 - 200	1 - 10	1
Nonvolatile	Yes	Yes	No	Yes	Yes	No
Standby Power	None	None	Refresh	None	None	Leakage

**Energy only refers to single cell, without considering the bit lines and peripheral circuits*

*** All data for MeRAM are simulated array-level projections based on device-level data*

Next, we will return to our main focus and examine the performance attributes of different existing and emerging embedded memories based on the most recent published data, which imposes less stringent density requirement compared to the standalone counterparts. Note that all data for MeRAM are simulated array-level projections based on device-level data.[22, 23] As illustrated in Table 1-2, existing embedded solutions mainly include eFlash, eDRAM, and SRAM. These three technologies are all based on CMOS transistors/capacitors, thus can be embedded into a CPU chip. They possess drastically different application space due to different performance attributes. Embedded Flash with pretty fast read speed and low standby power due to non-volatility is widely used in low-power micro-controller units (MCUs) for automobile, industrial, smart card, Internet-of-Things (IoT), and other consumer applications. Note that the low endurance and write speed provided by eFlash actually suffices the application requirements because these MCUs are mostly being read instead of write, thus write speed and write endurance is not as critical. While embedded SRAM and DRAM with much higher endurance and write speed are mostly employed as an on-chip cache memory for mobile, personal, and high-performance computing. The lower density and higher performance SRAM will act as L1 and L2 cache, while the higher density and lower performance eDRAM will act as L3 and/or L4 cache.

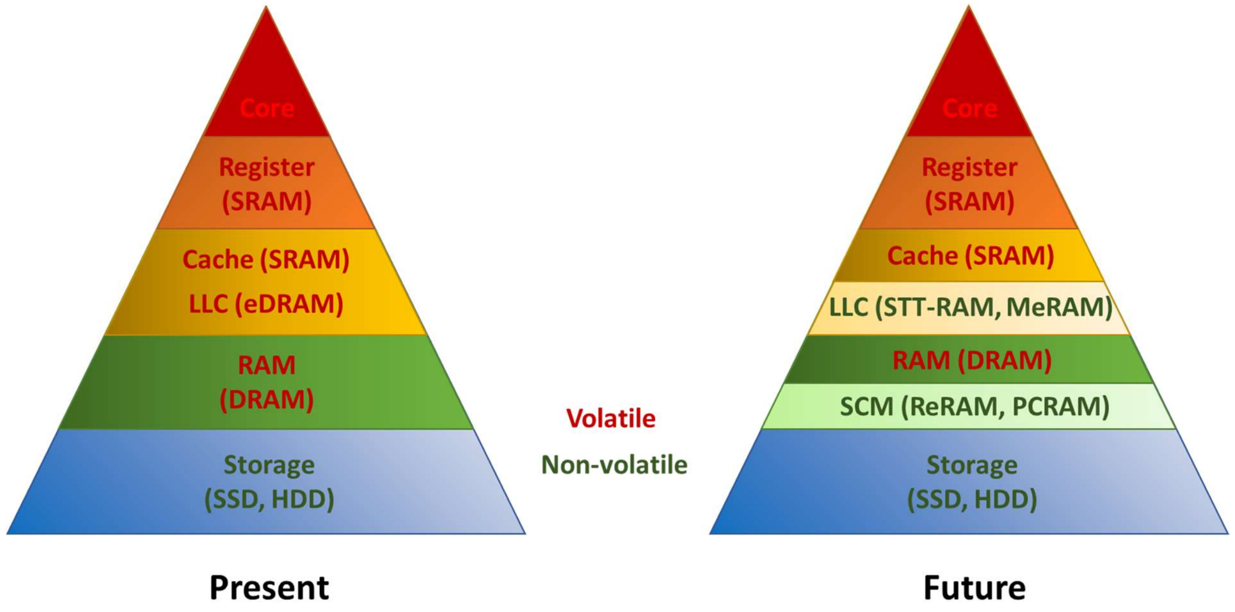

Figure 1-4 Present and future memory hierarchy in a conventional computer architecture. Different colors are used to code volatile and non-volatile memory technologies.

If we look at emerging NVMs including eReRAM, STT-MRAM, and MeRAM, MeRAM possesses the best performance potential compared against SRAM and eDRAM for cache applications.[1, 24] The main advantage for MeRAM is almost zero standby power enabled by its non-volatility. This will significantly reduce the power consumption for data-intensive applications in the next Intelligent Internet-of-Things (IIoT) era. In addition, MeRAM also has much higher density compared with SRAM in advanced nodes and about 2x density improvement over eDRAM, while possessing similar speed performance. Its high endurance can satisfy the requirements for replacing both eFlash and SRAM/eDRAM. A potential future memory hierarchy considering MeRAM, STT-RAM, PCRAM, and ReRAM is shown in Figure 1-4.

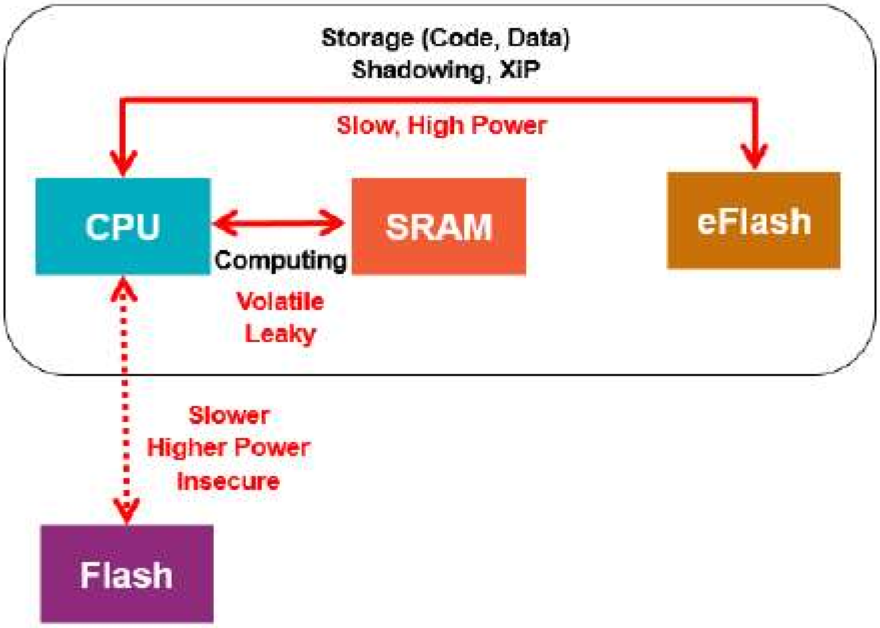

Figure 1-5 Memory and computation configuration for MCU and IoT applications. The data transfer between eFlash/Flash and CPU suffers from high power consumption and slow speed, while SRAM provides data in a very fast manner to CPU but suffers from severe leakage and is non-volatile.[25]

This flexibility of MeRAM will also drastically reduce the power consumption in present IoT and micro-controller (MCU) applications where both non-volatile memory (NVM) such as embedded Flash, external Flash, and SRAM are used. As shown in Figure 1-5, a unified memory subsystem where only MeRAM is used will thus eliminate the high power, low speed, and volatile data transfer between NVM and SRAM.[25] However, for eFlash replacement, eReRAM is a strong competitor due to its rather fast read time, high density and low cost in terms of initial capital investment. Here the initial capital investment for ReRAM is traditional CMOS processing tools, while for MRAM (including both STT-MRAM and MeRAM) new deposition and etching tools need to be developed as the magnetic materials involved in MRAM are not compatible with traditional CMOS processes.

1.2.2 Scaling Trends of Existing, Prototypical and Emerging Memory Technologies

To make a fair comparison between different technologies and analyze which technology has the most potential to be adopted in future, it is important to consider the trend of scaling. A summary of all published memory prototypes data has been summarized in Figure 1-6, and the projected bit cell size of MeRAM has been indicated by the yellow shaded region. To outperform an existing technology, it is critical to demonstrate smaller or at least equal bit cell size. As the bit cell sizes of SRAM and eDRAM are increasing rapidly at nodes smaller than 28nm, and eFlash has faced high power consumption and high lithography cost beyond 28nm,[26] the biggest opportunity for MeRAM is to replace SRAM/eDRAM, and eFlash. In addition to the higher density advantage, SRAM continues to consume high static leakage power which consists of up to half of the processor power consumption for personal mobile devices, while eDRAM consumes significant refreshing energy. By adopting on-chip MeRAM which is non-volatile, a large portion of processor power can thus be reduced. On the other hand, compared with existing embedded flash, MeRAM need fewer masks during processing, thus reducing the cost possibly.[25] Embedded flash also needs high gate voltage thus charge pumps which results in additional overhead, and embedded DRAM requires extremely high aspect-ratio capacitor to keep the cell capacitance.

A more detailed comparison in terms of technology scaling is as follows. In our projections, we consider two extreme cases for the technology scaling of MeRAM. At the upper end of the yellow region indicated in Figure 1-6, the MeRAM cell size is around 1/6 of the standard 6T-SRAM cell size if a 1MTJ-1Transistor cell is used. While the lower end of the region refers to using DRAM-like specialized manufacturing process with a cell size of around $8F^2$.[15, 16] In addition, the limitations of MeRAM intrinsic material parameters are also taken into account in determining the smallest node MeRAM can scale to. In particular, for SRAM/eDRAM replacement (cell size is around 1/6 of the standard 6T-SRAM cell size) with data retention of 1 day, MeRAM can scale to 3.5nm node. For SRAM replacement, MeRAM can demonstrate 6x density improvement over SRAM at same technology node. For eDRAM replacement, the advantage is not so much on the density but the better scalability in that MeRAM can scale beyond the current eDRAM node of 14nm to potentially around 5nm. Using the same cell size, for embedded flash replacement with data retention of 10 years, MeRAM can scale to 5nm node. But eFlash is facing challenges scaling below 28nm. On the other hand, if MeRAM adopts $8F^2$ cell size for DRAM replacement with data retention of 256ms, then MeRAM can scale to 14nm node. This is rather close to what has already been demonstrated for DRAM at 22nm. In view of the above scaling trends across SRAM[27-34], eDRAM[35-40], eFlash[41-48], DRAM[49], eReRAM[19, 50-53], STT-MRAM[15, 16, 54-64], and MeRAM, MeRAM has the most potential to replace eFlash in the short term, and replace eDRAM and SRAM subsequently. While for DRAM replacement, it requires materials development to extend MeRAM's scaling limits, specialized manufacturing tool and process development to achieve the $8F^2$ cell size, and thus more distant. The more detailed scaling analysis and materials parameters used in the calculations will be discussed in Section 2.4.

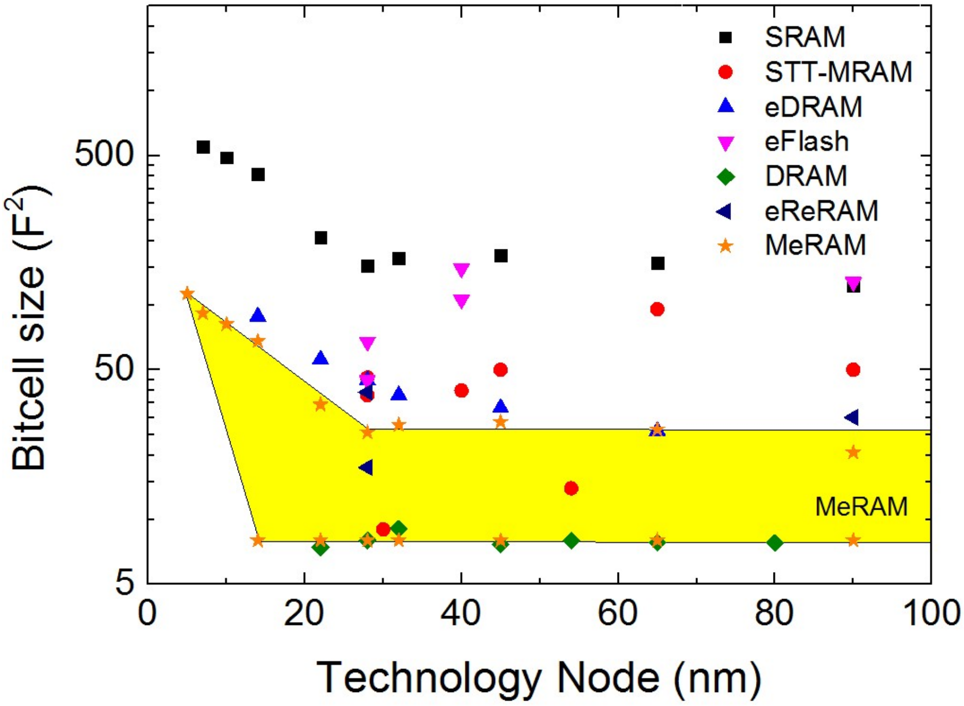

Figure 1-6 Scaling trends of various existing, prototypical and emerging memory technologies, including SRAM, STT-MRAM, eDRAM, eFlash, DRAM, and eReRAM. Standalone Flash is not included due to its recent trend of 3D stacking. The bit cell size for different technologies is evaluated using the unit of F^2, where F is the CMOS transistor technology node. The yellow shaded region indicates the projected bit cell size of MeRAM.

1.2.3 MeRAM Comparison against STT-MRAM

It is important to discuss the direct competing technology of MeRAM, i.e. STT-MRAM. Both of them are MRAM devices controlled by electrical means. As shown in the above Table 1-1 and Table 1-2, MeRAM and STT-MRAM are also very close in terms of performance. However, we can see that MeRAM will provide relatively higher writing speed, lower switching energy per bit, and higher density (smaller cell size). The fundamental cause for the higher MeRAM performance is due to its unique writing mechanism, i.e. voltage-assisted writing using voltage-controlled magnetic anisotropy (VCMA) effect. This effect is a voltage- or electric-field-induced effect, thus drastically different from current-induced switching of MTJs via spin-transfer torque

(STT) effect. Similar to the distinction between bipolar junction transistors (BJTs) and metal-oxide-semiconductor field effect transistors (MOSFETs), the use of electric-field or voltage to induce conduction of logic device or memory writing will consume very low dynamic energy but some unavoidable leakage energy. While if the current is used, a large amount of dynamic energy will be lost as Ohmic heating. We will touch upon the physics difference of STT and VCMA in a more detailed way in Section 1.3.2.

In addition, it is important to discuss the read operation of MeRAM compared with STT-MRAM. As MeRAM uses the voltage-driven VCMA effect rather than the current-driven STT for switching, the fundamental materials stack distinction of MeRAM is its relatively thick MgO barrier. As the barrier thickness increases, the tunneling current will decrease drastically [65] thus the MgO barrier will exhibit more capacitive behavior rather than resistor behavior. The high resistance of MeRAM memory cell will result in a larger RC delay. However, there are other factors to remedy MeRAM's read speed due to its high resistance including the higher read margin and impact of parasitic wire resistance, which will be discussed more in details in Section 2.6.

1.2.4 3D MeRAM Compared with 3D Stacking of Existing Technologies

In recent years, improvement of IC performance through scaling has saturated due to multiple constraints including increased leakage current and power consumption. Moreover, at the architecture level, the bandwidth of the system bus between the working memory (e.g., DRAM) and the processor cannot meet the demands of recent applications.

As a result, the semiconductor industry has begun to incorporate new system architectures for further performance improvement. For example, high bandwidth memory (HBM) and hybrid memory cube (HMC) techniques shorten the physical distance between working memories and processors and increase the number of channels by putting them together using through-silicon vias (TSV), as shown in Figure 1-7. Although this approach can achieve hundreds of GB/s bandwidth in stacked 8GB DRAMs, the latency of signal transmissions via the interposer (requiring 50 ~200 cycles), remains much longer than that of on-chip data transfer (only requiring 4~60 cycles), as shown in Figure 1-7.[1]

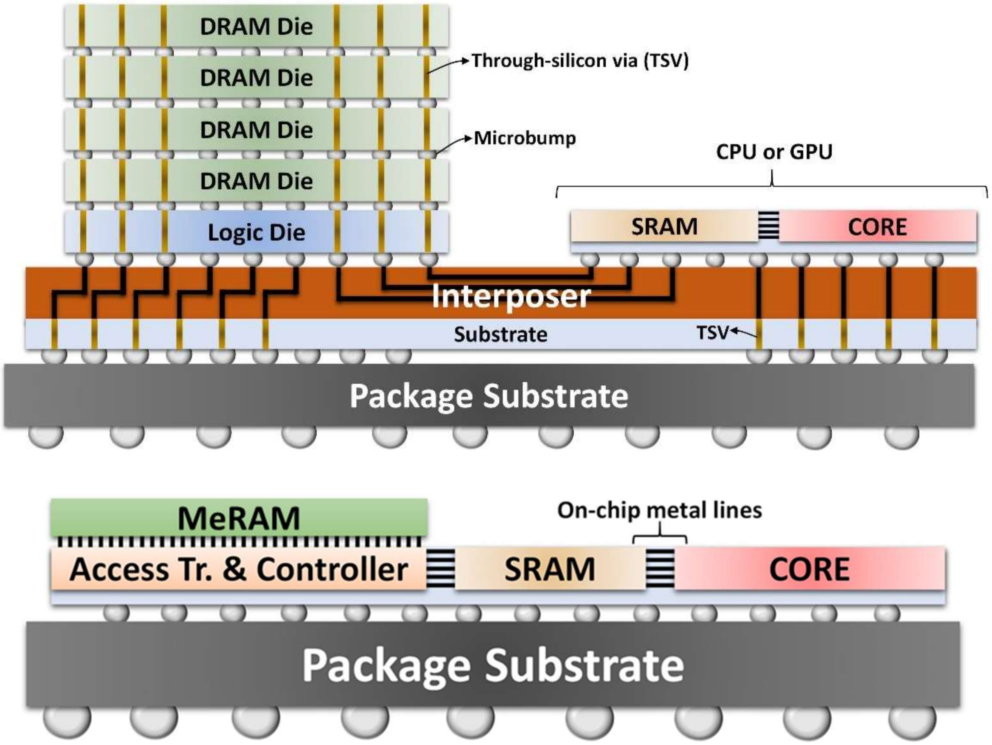

Figure 1-7 (Top) State of the art computing system architecture where the TSV connected main memory (Hybrid Memory Cube) and the processor are connected via the interposer (High Bandwidth Memory) in a packaged chip. (Bottom) An emerging system architecture with on-chip embedded MeRAM, which has the potential to improve the bandwidth and reduce the data transfer energy further.

However, for high-speed on-chip data transfer, the major bottleneck is the limited capacity of the processor's on-chip cache memory (usually a few tens of MB L3 cache) due to the large area overhead of SRAM. When the processor does not find needed data in the cache, it needs to fetch it from the slow main memory, or even storage at a large distance away from CPU and thus spend orders of magnitude large in energy and latency. Hence, at the architecture level, integrating high-density non-volatile Magnetoelectric RAM (MeRAM) device into the processor as on-chip embedded non-volatile memory has the potential to significantly improve throughput and energy efficiency over the abovementioned HBM/HMC solution while reducing chip area and cost. The improvement comes as a result of the following:

1) On-chip data transfers are faster by one order of magnitude and more energy-efficient by a factor of 100, compared to off-chip data transfers with large capacitive loads of IO pads and off-chip wire connections. HBM alleviates this situation, however, is still significantly slower and more energy consuming than on-chip embedded memories.
2) It is physically more feasible to expand the number of channels between different memory layers by using on-chip metal lines in the embedded memory compared to off-chip wires, thus achieving a higher throughput.
3) Non-volatility can reduce the total system power consumption via zero standby power. While for HBM, a constant refresh of data requires a large amount of energy.

Furthermore, the HBM/HMC approach can also be applied to MeRAM. Multiple MeRAM dies can be integrated with on-chip MeRAM via TSVs for further density and throughput enhancements, as shown in Figure 1-8.

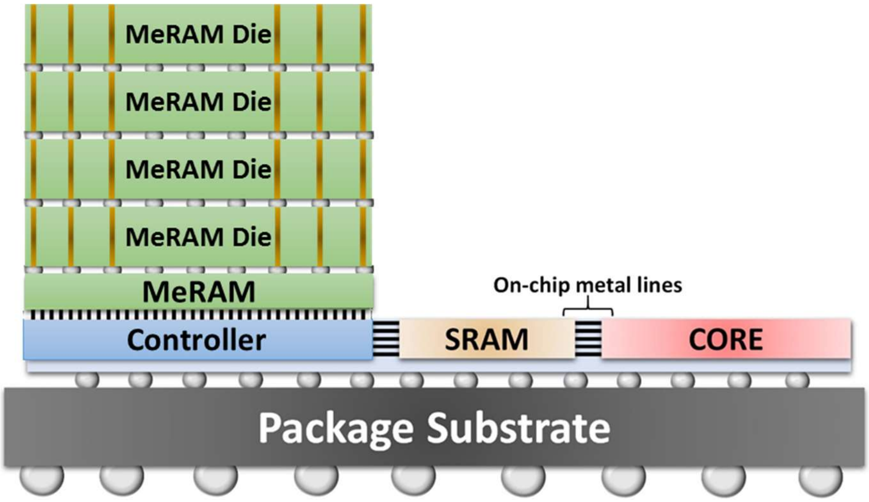

Figure 1-8 An additional system architecture with on-chip main memory consists of MeRAM dies connected via TSV, which has the potential to improve the bandwidth and reduce the data transfer energy further.

1.2.5 MeRAM Enabled Emerging System Architectures

As DRAM and SRAM face challenging scaling issues, the emergence of these different new memory technologies presents not only great opportunities for new memory hierarchies but also new system architecture that integrates memory and computation more cohesively as shown in Figure 1-9. The new system architectures include in-memory computing and neuromorphic computing for example. By embedding the Arithmetic Logic Unit (ALU) into the memory, the traditional von Neumann architecture will be drastically transformed with much-improved processing speed and bandwidth. The data will be located in direct connection to the ALU instead of separated from the ALU by multiple levels of cache. This can be achieved by using back-end-of-line memory technologies such as eMeRAM, eSTT-RAM and eReRAM, which sits on top of the front-end ALU CMOS circuitry. The use of eMeRAM, eSTT-RAM and eReRAM which are non-volatile can also enable non-volatile computing with minimal power consumption. These energy savings will also open up great potential for the system-level computation speed to exceed the current frequency bottleneck. Another emerging architecture built on top of the in-memory computing framework is neuromorphic computing. It uses semiconductor devices to mimic the behavior of synapses and neurons in a human brain which can achieve pattern recognition tasks just like the human brain. The majority of computation needed for this neural network architecture include multiplication, addition, and non-linear functions. By using non-volatile memory such as eSTT-RAM and eReRAM with inherent nonlinearity, the neuromorphic computation can be achieved while the data is also very close to the computation unit.

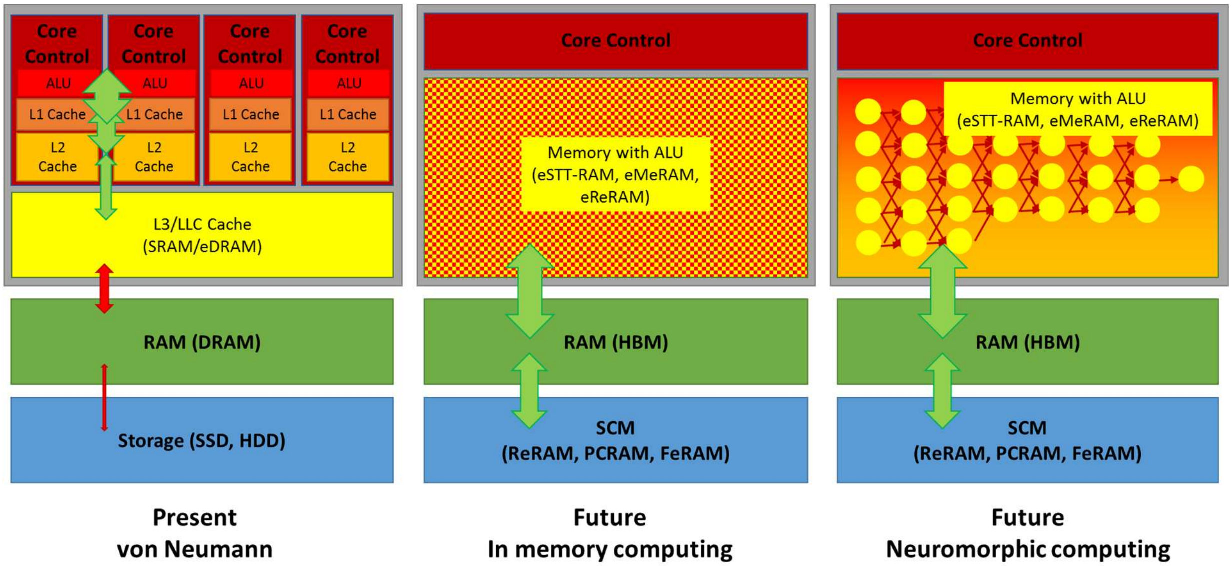

Figure 1-9 Computation systems architecture at present and in future

1.3 Overview of Magnetoresistive Random Access Memory (MRAM)

The field of Magnetoresistive Random Access Memory (MRAM) is an old one with continuous innovations in the past few decades driven by discoveries of new physics phenomena and novel materials as shown in Figure 1-10. The origin of this field is the magnetic sensor and hard disk drive read head industries where various methods of readout of magnetic signals were discovered and used, ranging from the simple inductive current generated in a wire by variation of external magnetic field via Faraday's law to various magnetoresistance (MR) effects up to 600% at room temperature. Then different methods to write magnetic signals into a magnetic storage layer were utilized and discovered ranging from the simple Oersted field generated from a wire carrying current, to spin transfer torque and various other mechanisms to electrically control magnetization. Combining these write mechanisms, a sensor or read head is thus transformed into a memory device or so-called MRAM. We will first discuss the different readout mechanisms for magnetic sensors, read heads, and MRAM, and then write mechanisms of MRAM.

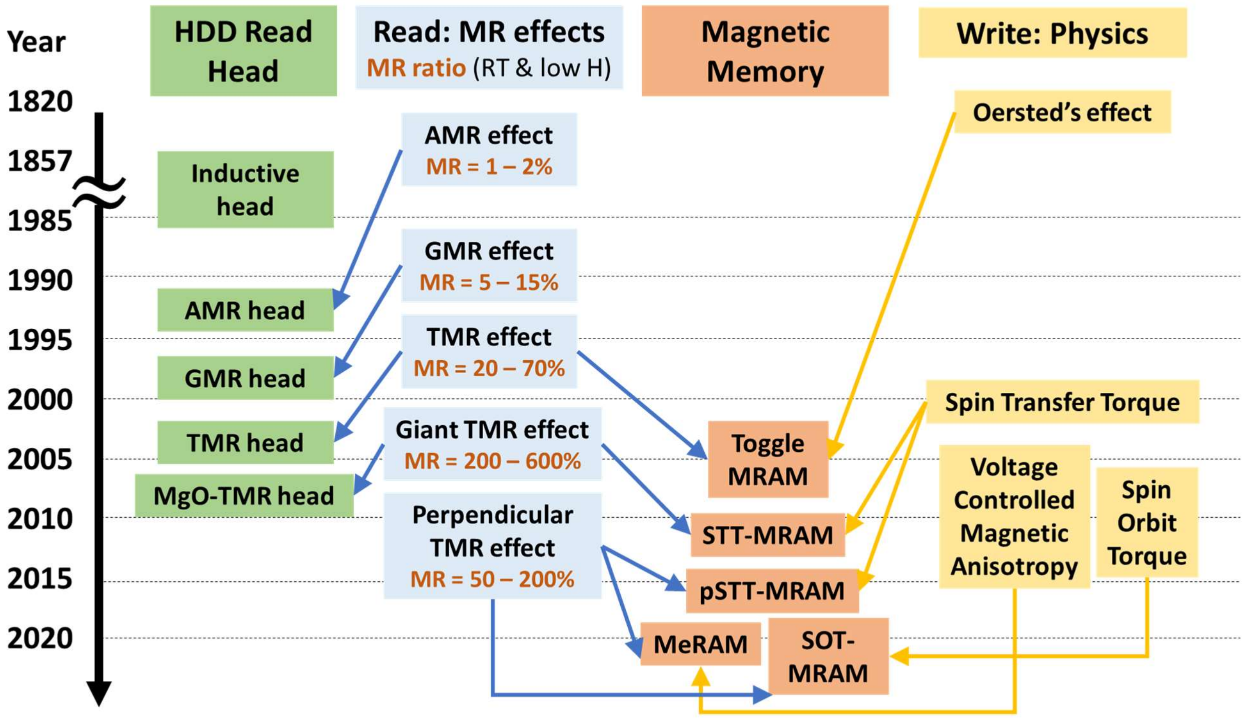

Figure 1-10 Historical evolution of the field of magnetism to read and write magnetic signals, and related industrial applications including hard disk drive read head and magnetic memory. Arrows indicate which application utilized which physics discovery in the field of magnetism. Picture revised from [66].

1.3.1 Evolution of Magnetic Signal Readout Mechanisms

To read out the magnetic signal is to link magnetism with electricity. The first link between these two is discovered by Faraday, who found that any change in the magnetic field a coil of wire experiences will induce a voltage in the coil. Hence, by carefully calibrating the voltage generated as a function of a sinusoidal change of external magnetic field, the magnetic signal can be converted into an electrical voltage. This method can be very accurate as nowadays the widely used magnetometer vibrating sample magnetometer (VSM) and superconducting quantum interference device (SQUID) still utilize this fundamental effect. However, the requirement of carefully controlling the external magnetic signal change is not realistic in a lot of applications where the magnetic signal needs to be measured real time.

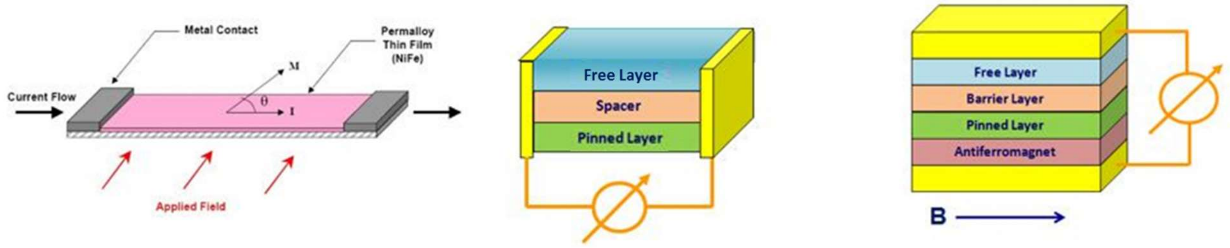

Anisotropic Magnetoresistance (AMR) head 1991-

Giant Magnetoresistance (GMR) head 1997-

Tunneling Magnetoresistance (TMR) head 2006-

Figure 1-11 Evolution of magnetic hard disk drive read head categorized by sensing mechanisms, the year number indicates the year each version of read head starts shipping by Hitachi.[67][68]

Before talking about various magnetoresistance (MR) effects used in hard disk drive heads, we need to introduce the normal magnetoresistance which is small and isotropic, i.e. does not depend on the direction of magnetic field with respect to the sample direction. For normal MR, the resistance of a metal will increase with the external field. The cause is the Lorentz force generated by the applied field will deflect the conduction electrons and thus reduces the mean free path. However, as this MR effect is isotropic, it can hardly be used to detect magnetic field with varying orientation.

Anisotropic Magnetoresistance (AMR)

In 1857, W. Thomson discovered that the electrical resistivity of ferromagnetic materials such as Ni and Fe changes depending on the relative angle between the sense current direction and the local magnetization, as shown in Figure 1-11.[69] The MR value change between the high resistance state (sense current parallel to magnetization) and low resistance state (sense current perpendicular to magnetization) $\Delta\rho$ divided by the low resistance state resistivity ρ is defined as the MR value $\Delta\rho/\rho$. As this effect is anisotropic with respect to the relative angle between the magnetization and the current, this effect is also coined as anisotropic magnetoresistance (AMR).

The origin of AMR is the anisotropic mixing of spin-up and spin-down conduction bands induced by spin-orbit interaction in ferromagnetic materials[70] and the AMR value is around 3-5% in bulk NiFe and CoFe alloys at room temperature. AMR has been a breakthrough and the use of AMR films in magnetic recording head led to doubling of the rate of increase of storage density per year from 30%/year to 60%/year from 1992 to 1998.[71]

Giant Magnetoresistance (GMR)

In 1988, another breakthrough came out that is the giant magnetoresistance (GMR) effect[72, 73] which later developments show as large as 15% MR. First, large MR values were discovered in antiferromagnetically coupled Fe/Cr multilayers where antiferromagnetically coupled multilayers at low external magnetic fields will give rise to high resistance, and parallel ordering of multilayers at large external magnetic field will give rise to low resistance. Later, spin-valve structures where the two ferromagnetic layers are separated by nonmagnetic metallic layers/spacer such as Cu were designed to uncouple the different ferromagnetic layers as compared with Fe/Cr multilayers, as shown in Figure 1-11.[74] In this way, the coercive field of each layer can be independently tuned and fewer layers are needed for the readout too. In particular, as shown in Figure 1-11, one ferromagnetic layer will be tuned to possess a larger coercivity by changing its thickness or material composition. This layer will be referred as the reference layer or pinned layer. While the other ferromagnetic layer will be tuned to possess a smaller coercivity compared with the reference layer, such that it is called the free layer. When an external field smaller than the reference layer coercivity is applied, only the orientation of the free layer will change, which will directly correlate with the strength of the external field.

The widely accepted theory to explain the origin of GMR is spin scattering asymmetry of conduction spin-up and spin-down electrons in ferromagnetic layers with different magnetization orientations. Note here that the nonmagnetic metallic layers used in spin-valve structures will not affect the transport of electrons as the mean free path of electrons and spin diffusion (flip) length is much larger than the thickness of various layers. In 1997, the first hard disk drive using GMR spin-valve based read head was produced by IBM. Then the increase of areal density of hard disk drive jumped again from 60%/year to 100%/year from 1998 to 2002. [75]

Tunneling Magnetoresistance (TMR)

After GMR, another innovation of tunneling magnetoresistance (TMR) continued to propel the increase of MR values. By replacing the nonmagnetic layers in the GMR spin-valve structures with an oxide layer such as $SrTiO_3$ or Al_2O_3, a TMR junction or so-called magnetic tunnel junction (MTJ) is formed, as illustrated in Figure 1-11. Compared with GMR whose physical origin is spin-dependent scattering, TMR is spin-dependent tunneling effect. In this case, the density of states (DOS) for spin-up and spin-down electrons at the Fermi level and tunneling probabilities are two important physical properties involved in determining the TMR ratio.

As discovered and theorized by Julliere in 1975, [76] the TMR value can be expressed by the following equation (also derived in detail in Appendix 1):

$$TMR = \frac{R_{AP}-R_P}{R_P} = \frac{2P_1P_2}{1-P_1P_2} \qquad \text{Equation 1-1}$$

In this equation, $R_{AP}(R_P)$ refers to the two magnetic layers sandwiching the oxide tunnel barrier are in anti-parallel (parallel) configuration, the polarization of the each ferromagnetic layer at the Fermi level P is defined as a function of the spin-split DOS at the Fermi level for majority and minority spin electrons N_M, N_m:

$$P = \frac{N_M-N_m}{N_M+N_m} \qquad \text{Equation 1-2}$$

Here, the DOS value describes the split of DOS for spin-up and spin-down electrons in magnetic 3d metals. As shown in Figure 1-12, the DOS will split into two halves and the majority band will shift down in terms of energy level with respect to the minority band, which can adequately describe the transport properties of ferromagnetic metals. To obtain Equation 1-1, Julliere assumed that the majority (minority) spin current tunneling through the two ferromagnetic electrodes are directly proportional to the product of the majority (minority) spin band density states at two electrodes, as written at the bottom of Figure 1-12. While the total current is proportional to the sum of these two spin currents. Note here the tunneling probabilities are implicitly assumed to be the same for the majority and minority spins. Otherwise, the respective tunneling probabilities need to be included in Equation 1-1. We will see in the following discussion that this assumption is invalid for MgO-based MTJs.

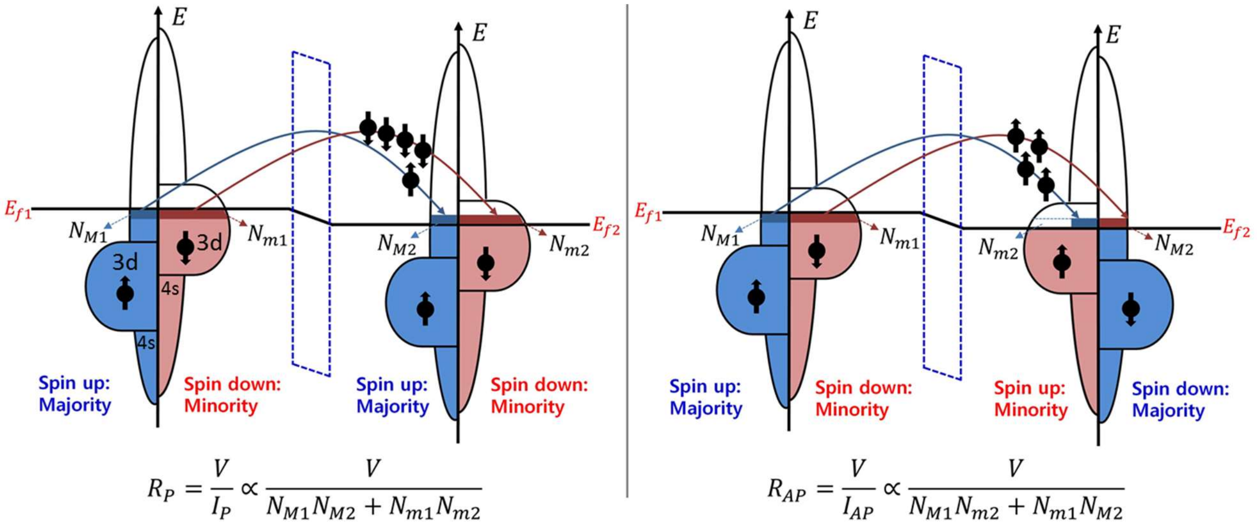

Figure 1-12 Schematic of the density of states at Fermi level for the majority and minority spin bands in two ferromagnetic layers sandwiching the tunnel barrier. (Left) When the two ferromagnetic layers are in parallel orientations, (Right) when the two ferromagnetic layers are in antiparallel orientations.[77]

When Julliere discovered the TMR value in Fe/Ge/Co junctions, the TMR ratio is 14% at 4.2K and did not generate much interest. In 1995, two groups demonstrated around 20% TMR values in Al_2O_3-based junctions[78] which initiated a new wave of active research that ultimately improves the TMR values of Al_2O_3-based MTJs to around 70%[79]. Considering that for spin polarization measured experimentally ($0 < P < 0.6$), the highest TMR ratio given by the Julliere model is around 100%, the maximum ratio of around 70% already approaches the theoretical limit for 3d transition metals.

In 2004, new materials innovation of MgO-based MTJs again revealed higher TMR ratios of over 200%.[80] This high ratio went beyond Julliere's model and a coherent tunneling in epitaxial MgO barrier theory is proposed to explain the high TMR value.[81] In this coherent tunneling model, the significance of the tunnel probabilities for different spin currents is emphasized in that the Bloch states in the ferromagnetic electrodes with different symmetries decay at different rates within the epitaxial MgO tunnel barrier. As seen in Figure 1-13, the tunneling probabilities do depend on the symmetry of the Bloch states. As the Bloch states compositions from different oriented ferromagnetic layers are different (minority spin current does not have Δ_1 Bloch states and majority spin current does not have Δ_2 Bloch states), the average tunneling probability considering the distribution of Bloch states will be different for the majority and minority spin currents. By including this difference in tunneling probabilities, the TMR values can be significantly increased and indeed theory showed up to 1000% TMR could be achieved. It is worth noting that the high TMR values predicted are not limited to the Fe/MgO/Fe junction, as long as the ferromagnetic layers are in bcc structures and the tunnel barrier is highly crystalline, the spin-dependent tunneling of Δ_1 Bloch states should be present.[66] However, experimentally only the CoFeB/MgO/CoFeB system yielded high TMR values up to 600%.[82] We will explain the reasons at in Section 3.1.2.

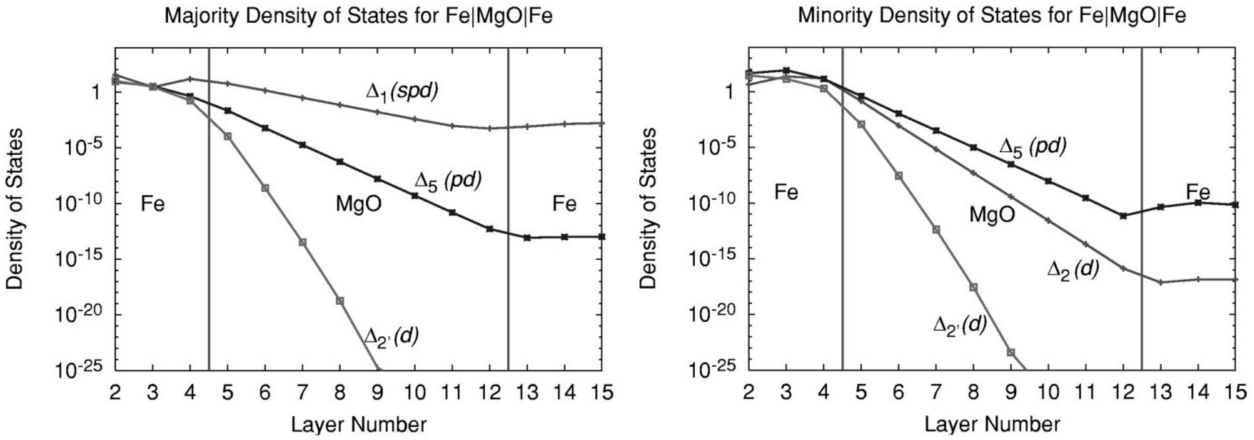

Figure 1-13 Tunneling DOS for Fe(100)/8Mg/Fe(100) junction at hot spots in k-space, (Left) majority state of one ferromagnetic electrode to majority state of another ferromagnetic electrode, (Right) minority state of one ferromagnetic electrode to minority state of another ferromagnetic electrode. Each curve is labeled by the symmetry of the incident Bloch state in the left Fe electrode.[81]

Though ab initio calculations are insightful, a simple theoretical TMR model is desired to consider the tunneling process and the effect of discontinuous change of the electric potential at the electrode/barrier interface. Slonczewski in 1989 studied exactly this. [83] By considering the tunneling electronic wave functions for both spin up and spin down electrons in a simple tunneling barrier problem, the electron transmissivity can be obtained. Then, the conductance can be deduced as the following equation (derived in detail in Appendix 2):

$$G = G_0(1 + p_F^2 cos\theta) \qquad \text{Equation 1-3}$$

where G_0 is the mean surface conductance, p_F is the effective polarization of the ferromagnetic layer, and θ is the angle between the reference layer and the free layer.

Before we discuss the write mechanisms of MRAM, we need to mention a recent new materials development that solved a major issue for the STT-MRAM industry, i.e. scaling. As illustrated in Figure 1-11, all the free layer and reference layers have magnetization orientations in the plane of the MTJ device. However, this configuration limits the density of the MTJs and impose a large switching current. In this section we mainly discuss the read aspects of the MTJs hence will leave the switching current argument to Section 1.3.2. For an in-plane magnetized MTJ device, the preference of in-plane orientation or so-called in-plane magnetic anisotropy is usually provided by the shape anisotropy of the MTJ free layer. If one patterns the MTJ device to be of an elliptical shape in the plane on the scale of tens or hundreds of nanometers while the free layer has nanometers thickness, then according to demagnetization effect, the magnetization of the free layer will prefer to lie along the major axis of the ellipse in the plane. As the shape of the MTJ device needs to be elliptical, the density of the MTJs is limited as compared with circular MTJs with perpendicular anisotropy. In 2010, H. Ohno's group demonstrated perpendicular MTJ devices with over 120% TMR at room temperature by reducing the thickness of the CoFeB free layer.[84] This method of using the interfacial perpendicular magnetic anisotropy of CoFeB/MgO structures has excited a new wave of research on perpendicular MTJs. Researchers have later improved the TMR ratio of perpendicular MTJs to around 200%.[63] Another major advantage of perpendicular MTJs is the lower switching current, which will be discussed in Section 1.3.2.

1.3.2 Evolution of Magnetic Signal Write Mechanisms

The above-mentioned various MR effects can convert a magnetic signal to electric signal which is effectively the core function of a magnetic sensor or magnetometer. To build a magnetic memory device, write operation or electrical control of magnetization is required. One way to categorize the evolution of MRAM is by its writing mechanisms as illustrated in Figure 1-14.

The first MRAM product uses the Oersted magnetic field generated by a current carrying wire to write the magnetic tunnel junction free layer. Because the Oersted field will distribute in the entire free space, the energy efficiency of this writing mechanism is very low, let alone the energy lost due to Ohmic heating of the write wire.

Spin Transfer Torque (STT) Effect

In 1996, Slonczewski [85] and Berger [86] both theoretically predicted that if a current is flowing perpendicular to the plane of a metallic multilayer, a spin transfer torque can be generated that will reorient the magnetization of one of the magnetic layers. Around 1998, experimental observations of current-induced resistance change were done in magnetic multilayer devices.[87, 88] Later around 1999, spin torque induced magnetization switching in lithographically defined samples were also demonstrated.[89, 90] Compared with the current-induced magnetic fields from a write wire, the spin transfer torque (STT) induced switching requires much lower switching current, thus more energy efficient and subsequently higher memory densities.

As the name spin transfer torque indicates, this effect essentially arises from the transfer of spin angular momentum between conduction electrons and local magnetization. When conduction electrons flow through a magnetized reference layer (RL) as shown in Figure 1-14, the majority of the electrons will be spin polarized to possess the same orientation as the reference layer. This is due to the spin angular momentum transfer from the RL to the conduction electrons. Then, when these spin-polarized electrons tunnel through the tunnel barrier and reach the free layer (FL), due to spin momentum conservation the spin angular momentum will be transferred from the conduction electrons to the free layer magnetization. This angular momentum transfer will produce an effective torque on the free layer and switch its orientation from being antiparallel to the RL direction to being parallel to the RL.

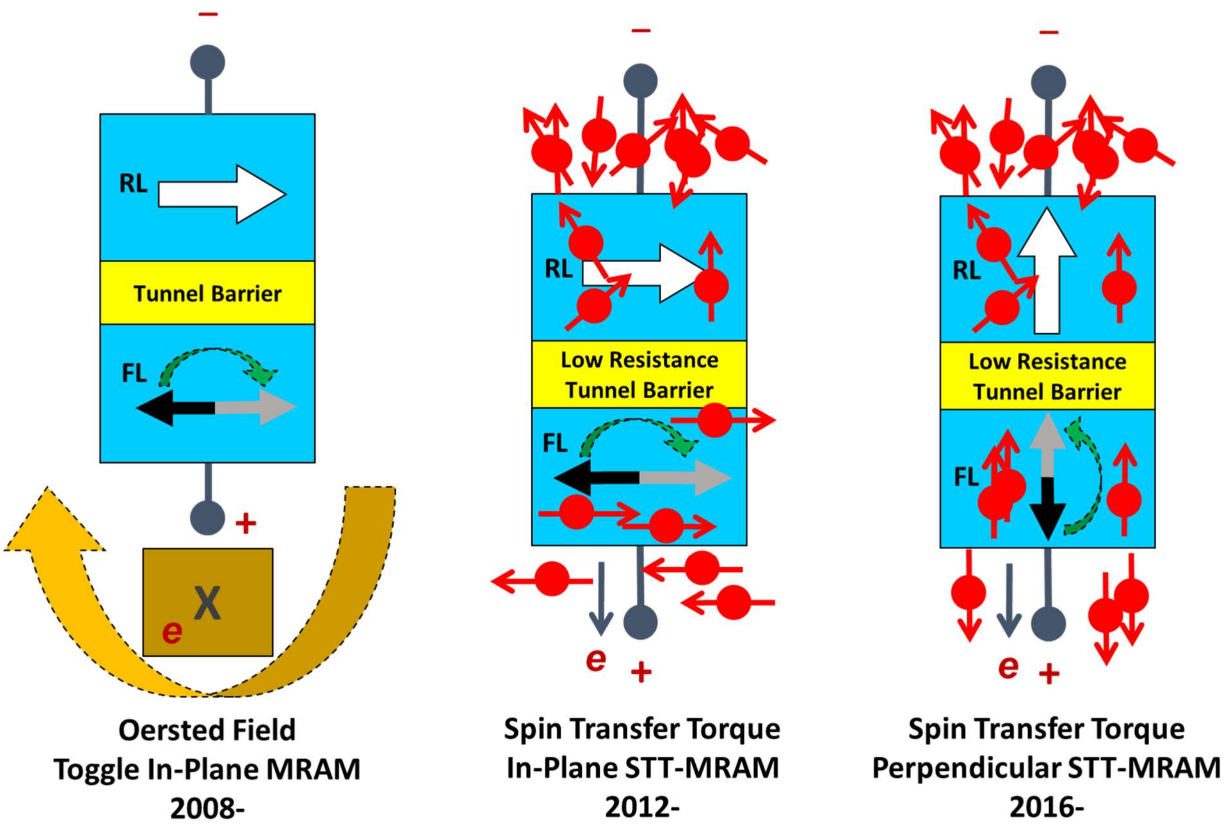

Figure 1-14 Evolution of MRAM products categorized by writing mechanisms, the year number indicates the year each version of MRAM starts shipping by the leading MRAM manufacturer Everspin Technologies.[91]

On the other hand, if one wants to switch the free layer from being parallel to the RL direction to being antiparallel to the RL, an opposite direction of electron flow will be utilized. In this case, the conduction electrons will be flowing from the free layer to the reference layer. Similar to the case above, the conduction electrons will be partially polarized to the orientation of the free layer. These spin-polarized electrons will not exert a torque to the reference layer because they have the same spin orientation. But not all conduction electrons are polarized to the free layer direction. A minority of the conduction electrons have the opposite orientation to the free layer. When these electrons reach the reference layer which has large magnetic anisotropy, due to spin momentum conservation, the reference layer will experience a torque to flip its own magnetization but will hardly change its orientation due to its large magnetic anisotropy, while the conduction electrons will then be reflected back. These reflected spin-polarized electrons having opposite orientation to the free layer will exert a torque on the free layer and change the free layer orientation to being antiparallel to the reference layer.

Hence, the switching between free layer parallel to the reference layer (P), and free layer antiparallel to the reference layer (AP) is asymmetric. The switching from AP to P depends on the polarized conduction electrons filtered by the majority spins of the reference layer, while from P to AP depends on the polarized conduction electrons filtered by the minority spins of the free layer. Hence, the switching current from AP to P is smaller than that from P to AP.

As mentioned in Section 1.3.1, the advent of perpendicular MTJs gives rise to a new wave of STT-MRAM research. The major driving force behind this not only includes the higher density provided by a circular perpendicular bit, but also the lower switching current. For an in-plane MTJ, the critical switching current to thermal stability figure is given by (derived in detail in Appendix 3):

$$\frac{I_{c0}}{\Delta} = \left(\frac{4e\alpha kT}{\hbar\eta}\right)\left(1 + \frac{H_d}{2H_k}\right) \qquad \text{Equation 1-4}$$

where α is the free layer damping factor, η is the spin-transfer efficiency, $H_d = 4\pi M_s$ is the out-of-plane demagnetization field, and H_k is the in-plane shape-induced anisotropy field. Effectively, the switching of an in-plane MTJ needs to overcome both the in-plane shape anisotropy field as well as the out-of-plane demagnetization field.

By introducing a perpendicular MTJ, the critical switching current to thermal stability figure is instead (derived in detail in Appendix 3):

$$\frac{I_{c0}}{\Delta} = \frac{4e\alpha k}{\hbar\eta}$$ Equation 1-5

Hence, the switching of a perpendicular MTJ just need to overcome the out-of-plane anisotropy which equals the out-of-plane interfacial perpendicular magnetic anisotropy (PMA) field subtracting the out-of-plane demagnetization field. Then, the MTJ switching current density is reduced. However, the only parameter here that can be tuned to further decrease the perpendicular STT-MRAM switching current is the damping constant. As shown in recent works, the best Δ/I_{c0} values obtained is around $2\mu A^{-1}$ at small MTJ diameters below 30nm. As a large CMOS transistor is required to drive the switching current, the density of STT-MRAM is limited by its high Δ/I_{c0} value, thus rather high damping constant. Though this figure of merit increases from around $1\mu A^{-1}$ in 50nm MTJs to $2\mu A^{-1}$ below 20nm, it remains unclear how STT-MRAM can further decrease the damping constant and switching power to achieve higher density.[92, 93]

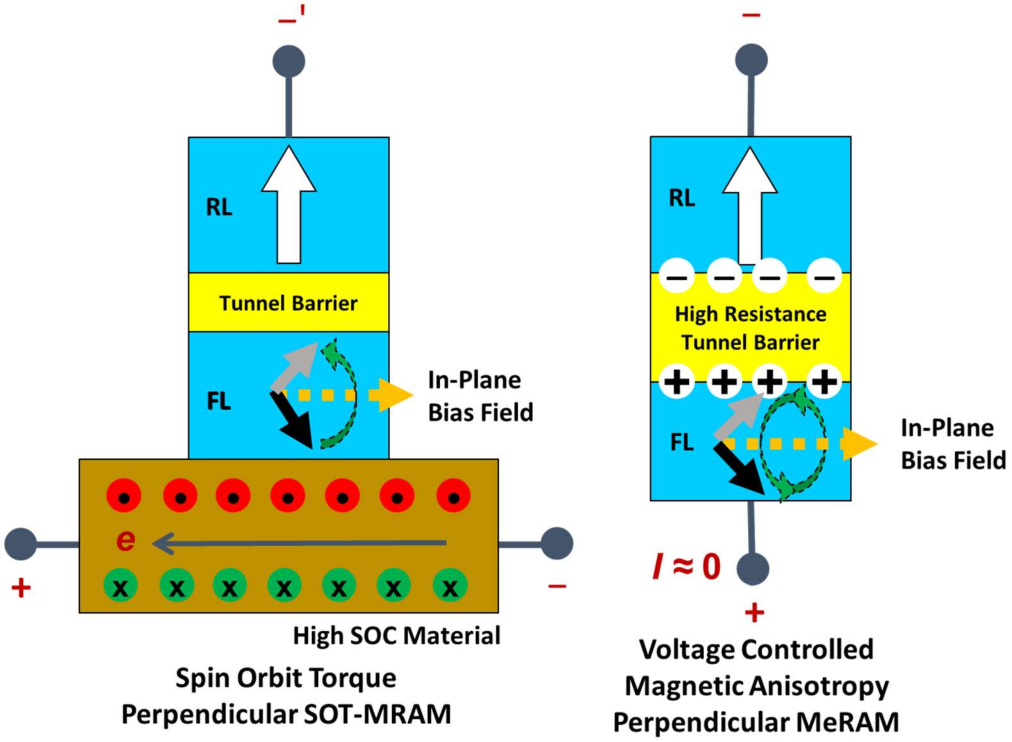

Figure 1-15 Emerging MRAM prototypes via new writing mechanisms.

To further decrease the power consumption and increase the density of MRAM, two new emerging types of MRAM are being intensively researched in recent years, as shown in Figure 1-15.

Spin Orbit Torque (SOT) Effect

Recently, a new way of using spin-polarized current to manipulate the local magnetization has been discovered coined as spin orbit torque. As shown in Figure 1-15, when a current flows through a metallic layer with large spin-orbit coupling (SOC) such as Ta, W, or Pt, a spin current will be generated perpendicular to the current direction and flow towards the magnetic free layer on top of the metallic layer. This spin polarized current originates from possibly a combination of Rashba effect [94, 95] and spin Hall effect [96, 97]. Aided by a longitudinal in-plane bias field, SOT can achieve deterministic switching depending on the direction of the SOT current as well as the direction of the bias magnetic field.

The major advantage of this SOT switching is the faster speed down to below 1ns.[98] SOT switching also has potentially higher current efficiency. The ratio of the switching current due to spin Hall (I_{SH}) to that of the STT effect (I_{STT}) can be approximated by [6] (derived in detail in Appendix 3):

$$\frac{I_{SH}}{I_{STT}} \cong \frac{\eta}{\theta_{SH}} \frac{A_{Ta}}{A_{MTJ}} \qquad \text{Equation 1-6}$$

where A_{Ta} and A_{MTJ} are the cross-sectional area of the underlying metal layer, and the MTJ device. Thus the switching current via spin Hall effect can be further reduced compared with the STT by reducing the heavy metal thickness and finding materials with large spin hall angle θ_{SH}. In addition, the read and write path will be separated which can enhance the read margin for the SOT-MRAM arrays. However, both the use of three-terminals to enable SOT switching as well as the high resistance ultrathin underlying metal layer limit the density of the memory array.

Voltage Controlled Magnetic Anisotropy (VCMA) Effect

The above mentioned writing mechanisms all utilize current-controlled means such as the spin transfer torque (STT) or spin-orbit torque (SOT)[95, 96] effects to write information into magnetic bits. However, the use of currents results in a memory cell size (i.e. bit density) limitation due to the large size of the required access transistors, [5, 99] and large dynamic switching energy due to Ohmic power dissipation. Another promising method to reduce the power consumption of STT-MRAM, which is also the main focus of this dissertation, is to use voltage instead of current to switch the magnetic free layer. In recent years, writing of information using the electric field in perpendicular magnetic tunnel junctions (MTJs) [100-103] is being investigated intensively, with the goal of realizing energy-efficient and high-density Magnetoelectric Random Access Memory (MeRAM) devices.[6, 23, 104]

Essentially, instead of using spin-polarized current, the charge accumulation and depletion at the tunnel barrier surface will modulate the magnetic anisotropy which can drastically reduce the energy barrier for free layer reversal. The electric-field effect, or the voltage-controlled magnetic anisotropy (VCMA) effect, is utilized to temporarily lower the interfacial perpendicular magnetic anisotropy (PMA) of the free layer during the writing operation, thus reducing the writing energy required to overcome the energy barrier between the two stable magnetization states, as shown in Figure 1-16.[6, 104] In order to enhance the effect of VCMA and suppress the effect of STT, a thicker MgO barrier is usually used, resulting in a much smaller write and read current, thus lower power consumption.

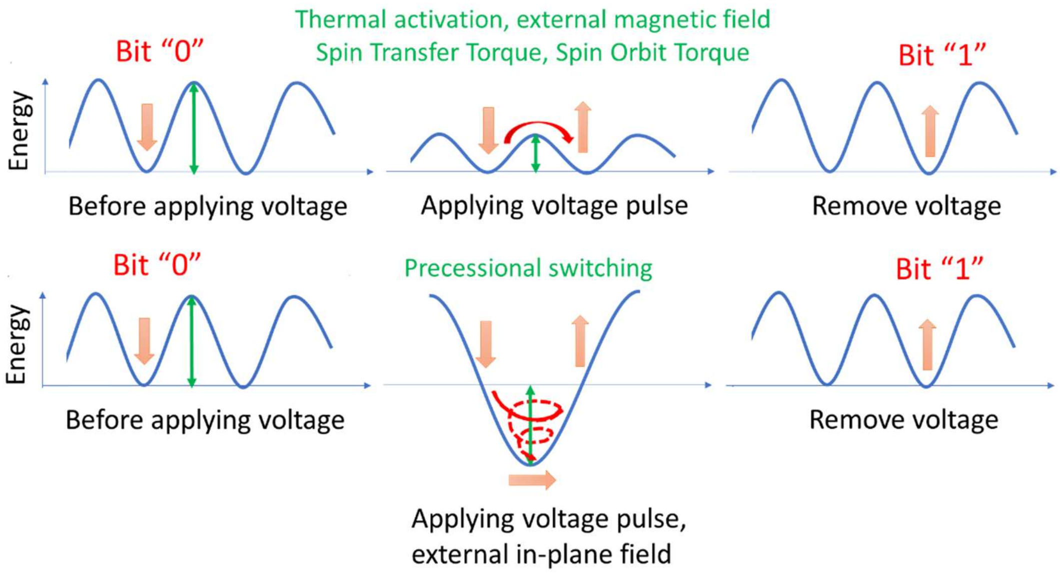

Figure 1-16 Schematic showing the process of magnetization switching using voltage-controlled magnetic anisotropy effect. (Top) External forces such as magnetic field, thermal activation, spin-transfer torque, or spin-orbit torques are required to switch the magnetization during the voltage pulse period. (Bottom) If the applied voltage is large enough to eliminate the energy barrier, then under an in-plane external field, precessional switching can happen.

There are several different ways of utilizing this VCMA effect to switch the free layer as shown in Figure 1-16. Because the VCMA effect temporarily lowers the energy barrier, any other switching mechanisms can be combined with the VCMA effect to reduce the energy consumption of that switching mechanism, for example external magnetic field generated from a write wire, spin transfer torque [105], or spin orbit torques. Thermal activation can also help achieve the switching when the energy barrier is sufficiently low. If the energy barrier is fully eliminated by the VCMA effect and there is an in-plane bias field built into the MTJ stack, the free layer will start precessional motion and oscillate between up and down directions until damping forces the free layer magnetization to align to the in-plane bias layer orientation. This precessional switching is also the physics behind MeRAM which is the main subject of this dissertation.

Chapter 2 Voltage-Controlled Magnetic Anisotropy: Physics and Devices Operation

2.1 Magnetization Energy Landscape at Equilibrium

As illustrated in Figure 1-16, an energy barrier must exist between different free layer magnetization orientations such that each state will be stable against thermal fluctuations. By changing the local energy minima of the free layer magnetization, the free layer orientation at equilibrium can be changed. For example, when VCMA effect is employed and the energy barrier between two perpendicular states is non-zero, the employment of external field opposite to the direction of the magnetization effectively changes the energy landscape and drives the magnetization into the same orientation as the external field. Here, we will detail the major different energy components that contribute to the total free layer energy in a real magnetic memory device. This will be enable the static analysis of the free layer magnetization under various external magnetic fields, and anisotropy fields. This is also the foundation for magnetization dynamics analysis of the free layer under non-equilibrium conditions such as STT and SOT current, as well as VCMA voltage pulses.

Magnetostatic Energy and Demagnetization

The first energy component is magnetostatic energy which will exist as long as there is magnetic moments in a magnetic material. A brief explanation is illustrated in Figure 2-1. For any uniform magnetization in a magnetic domain, there will be effective magnetic static poles accumulated at the end of the magnetization, which will act as the north and south poles for the magnetization. The magnetic charges will generate magnetic flux both inside and outside of the magnetization layer. The magnetic flux outside might act upon another magnetic material and generate some magnetostatic energy in the other magnetic material. While for the magnetic flux inside the material, it lies in the opposite direction with respect to the magnetization direction and thus will destabilize the magnetization. Therefore the magnetostatic energy generated by the material itself is named as demagnetization energy. To evaluate the magnitude of the demagnetization energy per volume of magnetization, the following equation can be used

$$E_{demag} = -\frac{\mu_0}{2V}\int_V M \cdot H_{mag}(r')d^3r' \qquad \text{Equation 2-1}$$

where $H_{mag}(r')$ is the magnetostatic interaction field from the magnetic static poles on the surface of the magnetization volume. M is the magnetization value. Therefore, $H_{mag}(r')$ is

$$H_{mag}(r') = -\sum_j \int_{S_j} \hat{n}' \cdot \frac{M(r_j)(r-r')}{|r-r'|^3} d^2r^2 \qquad \text{Equation 2-2}$$

where $\hat{n}'$ is the surface normal vector.

From the equation above, we can find that for a specific magnetization, the demagnetization energy depends on the strength of the demagnetization field, which is determined by the distance between each magnetic static poles and each magnetic moment in the magnetization. As illustrated in Figure 2-1 (a), if an MTJ free layer, which has much larger in-plane dimensions than the perpendicular thickness, has an in-plane magnetization, the distance between magnetic static poles and the magnetic moment is much larger (order of tens or hundreds of nanometers) than the case when the free layer has a perpendicular magnetization. The demagnetization energy of the perpendicular magnetization will act against the magnetization itself in a much stronger manner. If expressed in energy values, the demagnetization energy of a perpendicular magnetization will be larger than that of an in-plane magnetization for an MTJ free layer. Thus the in-plane magnetization will be preferred which possesses a lower energy level. Similarly, if the in-plane cross-section of the MTJ free layer has an elliptical shape as shown in Figure 2-1 (b), the magnetization oriented along the major axis of the ellipse will be preferred.

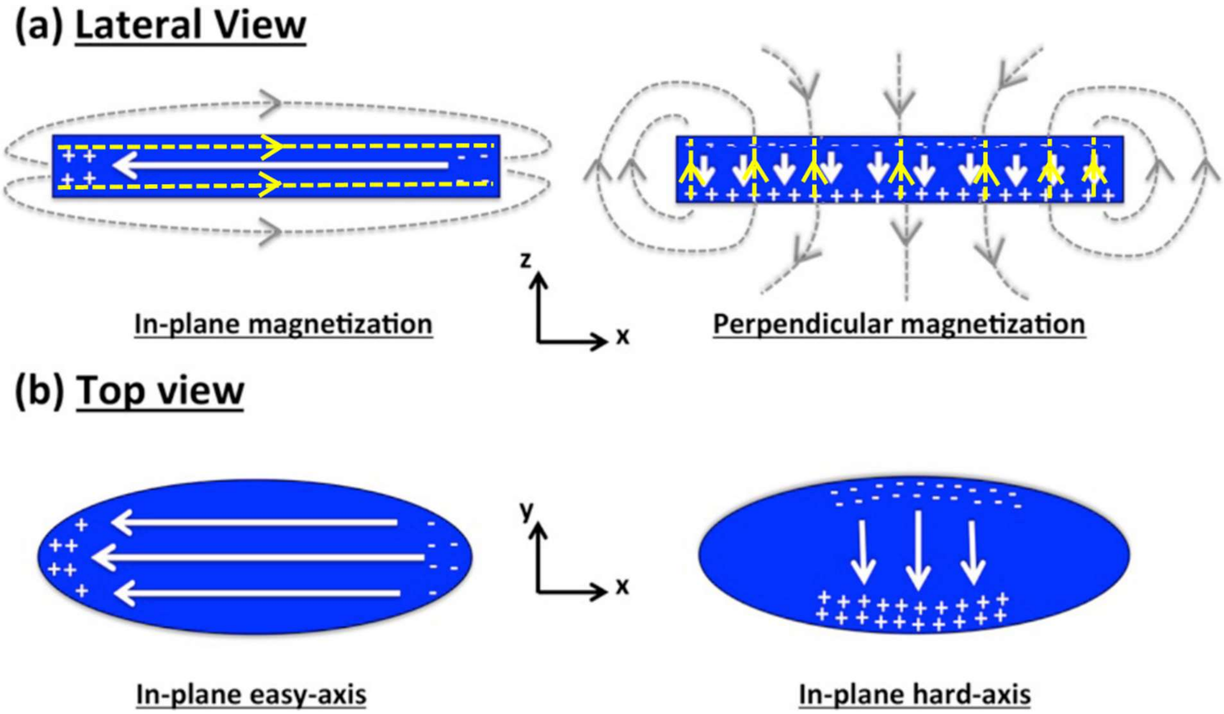

Figure 2-1 (a) Lateral view of a nanometer thick free layer showing the stray fields for in-plane magnetization and perpendicular (out-of-plane) magnetization. The in-plane configuration is preferred to minimize the demagnetization energy. The white arrows refer to the magnetization orientation while the yellow arrows refer to the magnetic field generated by the magnetostatic poles at the edge of the magnetization. (b) Top view of an elliptical free layer showing the stray fields for the magnetization along the major axis of the ellipse and along the minor axis of the ellipse. The major axis configuration is preferred to minimize the demagnetization energy.

Phenomenologically, the demagnetization energy will be expressed as the following:

$$E_{demag} = \frac{1}{2}\mu_0 M_s^2 (N_x m_x^2 + N_y m_y^2 + N_z m_z^2) \quad \text{Equation 2-3}$$

where M_s is the saturation magnetization, $N_{x,y,z}$ is the demagnetization factor in x, y, z directions with $N_X + N_y + N_z = 1$, and $m_{x,y,z}$ is the unit magnetization vector in x, y, z directions. The detailed calculation of the demagnetization factors can be found in reference [106].

Magnetocrystalline Magnetic Anisotropy Energy

As can be seen in the above section, the shape of a magnetic material will result in a favored orientation for the magnetization. However, if the shape of the magnetic material is spherical i.e. identical on every direction in space, sometimes the magnetic materials also have preferred magnetization orientation. In general, this type of preference of the magnetization to lie in a particular direction is called magnetic anisotropy. Among the many origins for magnetic anisotropy, we will focus on the magnetocrystalline anisotropy and interfacial magnetic anisotropy.

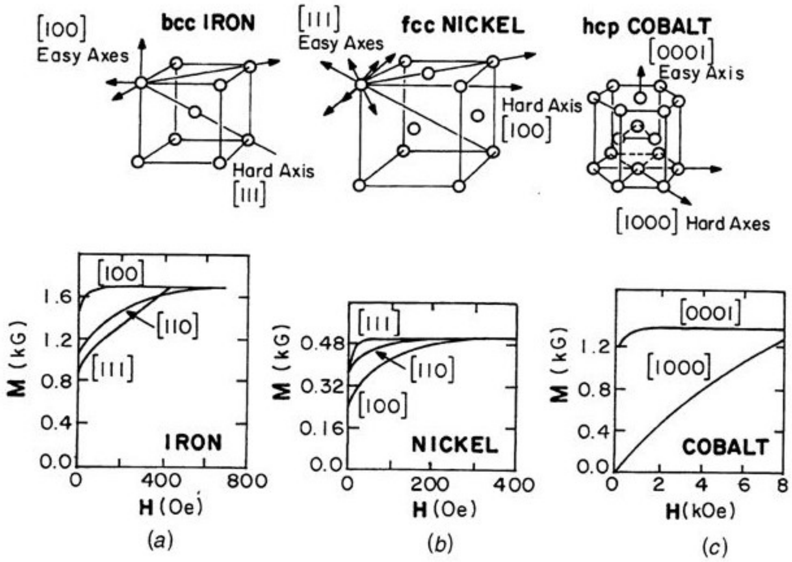

Figure 2-2 (Top) Crystal structure showing easy and hard magnetization directions for Fe (a), Ni (b), and Co (c). (Bottom) Respective magnetization curves under external magnetic field along different orientations.

A good example is the three ferromagnetic materials Fe, Ni, and Co as shown in Figure 2-2. As the bulk crystals have their crystal structures where atoms are aligned in periodic lattices, either bcc, fcc, or hcp. Therefore, the different directions in space are distinguished and the magnetization usually is preferred to align at some particular crystallographic directions than the others. For example for bcc Fe, the easy axis that the magnetization prefers to align to is the [100] orientation, while the hard axis that magnetization is least likely to align to is the [111] direction.

Phenomenologically, a uniaxial magnetocrystalline anisotropy energy density as exhibited by Cobalt could be described in the following equation.

$$K_u = K_{u0} + K_{u1} \sin^2 \theta + K_{u2} \sin^4 \theta + \cdots \qquad \text{Equation 2-4}$$

where K_{u0} is a spherical energy term without any anisotropy preference, K_{u1}, K_{u2} are the first and second order anisotropy coefficients, and θ is the angle of the magnetization with respect to the easy axis, i.e. [0001] of the Cobalt crystal. Usually the inclusion up to K_{u2} is enough to describe the anisotropy energy of many materials.

Interfacial Magnetic Anisotropy Energy

Another origin of the magnetic anisotropy is the interfacial magnetic anisotropy. When a bulk crystal is reduced to a thin film, the periodic crystal structure is destroyed along the film normal direction. Hence, there is a possibility that the interface of the magnetic thin film will give rise to some magnetic anisotropy. Take CoFe/MgO for instance, as indicated by *ab initio* calculations, the interfacial perpendicular magnetic anisotropy in K_i stems from the hybridization of Fe *3d* orbitals and O *2p* orbitals at the CoFe/MgO interface.[107, 108] In particular, the energy-and k-resolved analysis is conducted on the distribution of orbital characters of the minority-spin band of Fe at the CoFe/MgO interface.[109] The results show that a significant contribution to PMA originates from the spin-orbit coupling between occupied $d_{x^2-y^2}$ and unoccupied d_{xy} states. A detailed discussion of the physics will be covered in Section 2.3.1.

For an interfacial magnetic anisotropy, the energy density per volume of the magnetic material will depend on the thickness of the material t as the following equation. For a uniaxial interfacial magnetic anisotropy as exhibited by the CoFe/MgO interface, the magnetic anisotropy energy could be written as:

$$K_i = K_{i1}\, sin^2\,\theta\,/t + K_{i2}\, sin^4\,\theta\,/t + \cdots \qquad \text{Equation 2-5}$$

where K_{i1}, K_{i2} are the first and second order interfacial anisotropy coefficients, and θ is the angle of the magnetization with respect to the easy axis, i.e. direction perpendicular to the CoFe/MgO interface plane. Usually the inclusion up to K_{i2} is enough to describe the anisotropy energy of CoFe/MgO heterostructure. Note that when t is decreasing to at or below the thickness of the dead layer, the ferromagnetic portion of the thin film is not continuous and the above equation fails.

Zeeman Energy

Discovered by Pieter Zeeman, the energy spectral lines of a material vapor will split into several components in the presence of an external magnetic field and the energy splitting magnitude is proportional to the external magnetic field strength. Similarly the energy also will be changed for a magnetic material under an external magnetic field, which can be expressed as:

$$E_{Zeeman} = -\mu_0 \vec{M} \cdot \overrightarrow{H_{ext}} \qquad \text{Equation 2-6}$$

where $\vec{M}$ is the magnetization vector, and $\overrightarrow{H_{ext}}$ is the external magnetic field.

From the equation, we can see that when the magnetization aligns to the external field direction, the total energy will be lower than any other orientations, which is consistent with the physics picture.

Other Energy Components

Different from all the energy terms discussed before, exchange coupling arises when two different magnetic materials are in intimate contact with each other or separated by a layer which is thin enough (with thickness less than a few nm) that still allows spin momentum in the two materials to interact with each other. The electrons spin with different spin orientations will exhibit different exchange energy upon interaction, thus favoring certain alignment of the spins near the surface. It usually arises when a ferromagnetic material is in direct contact with an antiferromagnetic material, or when two ferromagnetic materials are separated by a spacer material thin enough which will allow the free conduction electrons spin in the two layers to interact.

An additional energy term which is also relevant for this dissertation is the magnetoelastic energy. By applying a stress to a crystallized material, the atoms location will be distorted such that the crystalline magnetic anisotropy along the stress orientation will be different than other directions, thus adding an additional energy term.

To account for finite temperature effects, the thermal excitation energy needs to be considered also especially when the magnetization dynamics is of interest. In equilibrium, the thermal energy will induce a small perturbation to the magnetization with energy of $k_B T$ above the equilibrium energy level.

2.2 Magnetization Dynamics and Equation of Motion

After discussing the static energy components, we will look at the dynamic process of the magnetization motion. When a magnetization is away from equilibrium, it will precess around the local effective field orientation with some precessional energy. In reality, dissipation of this energy will drive the magnetization to orient towards the local effective field direction at the end as shown in Figure 2-3. The energy dissipation rate is described using a phenomenological damping factor. There are two widely used forms to describe this motion, i.e. Landau-Lifshitz equation and Landau-Lifshitz-Gilbert equation.

$$\frac{dM}{dt} = -\gamma_0' M \times H_{eff} - \frac{\lambda}{M_s} M \times (M \times H_{eff}) \text{ (Landau-Lifshitz)}$$

$$\frac{dM}{dt} = -\gamma_0 M \times H_{eff} + \frac{\alpha}{M_s} M \times \frac{dM}{dt} \text{ (Gilbert)} \qquad \text{Equation 2-7}$$

where γ_0 is the electron gyromagnetic ratio, λ is the Landau-Lifshitz damping parameter, α is the Gilbert damping parameter of the magnetic material, and H_{eff} is the effective magnetic field experienced by the magnetization as described by its static energy landscape, as discussed in Section 2.1. These two forms of equation of motion are equivalent with the substitutions $\gamma_0' = \gamma_0/(1+\alpha^2)$ and $\lambda = \gamma_0 \alpha/(1+\alpha^2)$. A more detailed derivation of the equivalence of these two forms is presented in Appendix 4.

It is also important to understand the frequency of the precessional motion, which is characterized by the Larmor frequency ω. This can be directly calculated from the Landau-Lifshitz equation precession term:

$$\omega = \gamma_0' B_{eff} = \frac{\gamma_0}{1+\alpha^2} \mu_0 H_{eff} \qquad \text{Equation 2-8}$$

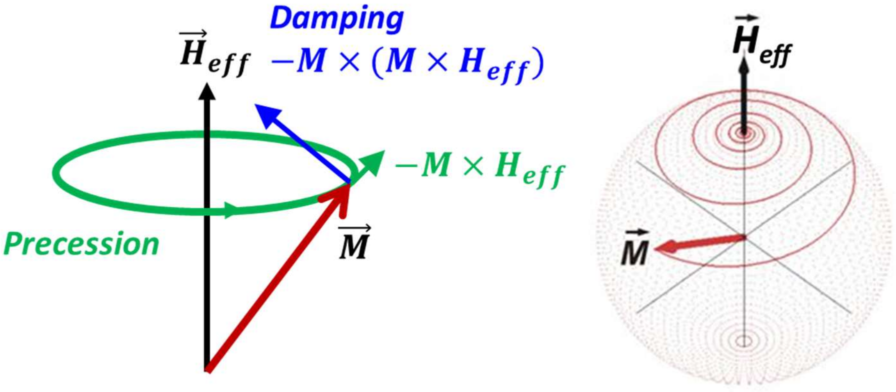

Figure 2-3 (Left) Precession and damping torques of a magnetization M in a local effect field H_{eff}. (Right) Example magnetization motion curve of magnetization under constant H_{eff}.

2.3 Voltage-Controlled Magnetic Anisotropy Physics

2.3.1 Spin-Orbit Coupling and Magnetic Anisotropy

At the base of ferromagnetism lies the concept of spin-orbit interaction. Effectively all the magnetism can be traced back to this fundamental special relativistic physics concept. A classic illustration of the phenomenon of spin–orbit interaction is the following: in the rest frame of the atom nucleus, there is no magnetic field acting on the electron. However in the rest frame of the electron, the nucleus rotation effectively acts as a current loop which will generate a magnetic field that the electron will experience. On the other hand, the electron itself possesses spin angular momentum. Thus the interaction between the magnetic field and the local electron magnetic moment gives rise to a coupling energy which will favor certain orientation of the electron spins. Hence, through the spin-orbit coupling (SOC) effect, the collective spins or magnetism is coupled to the electron orbital motion around a nucleus, which effectively originates from the spatial crystal structure of the materials. In this manner, the existence of magnetocrystalline anisotropy, the magnetoelastic effects, as well as the voltage-controlled magnetic anisotropy effects can all be understood in a simple manner.

As given in the relativistic theory, the SOC perturbed Hamiltonian of an electron spin is given by

$$H = H_0 + H_{SOC} = H_0 + \vartheta(r)\sigma \cdot L \qquad \text{Equation 2-9}$$

where σ and L are the spin and orbital angular momentum operator, H_0 is the crystalline part without any SOC, and the SOC amplitude $\vartheta(r)$ is given by the following with a detailed derivation in Appendix 5.

$$\vartheta(r) = -\frac{e\hbar^2}{2m_e^2c^2r}\frac{dV(r)}{dr} \qquad \text{Equation 2-10}$$

Note that the atomic number of the atom Z is embedded in the electric potential V experienced by the electron. Hence, the SOC magnitude is proportional to the element atomic number as shown in Appendix 5. The lowest perturbation to the SOC term is in second order:

$$E_{SOC} = -\vartheta^2 \sum_{o,u} \frac{|\langle o|\sigma \cdot L|u\rangle|^2}{\delta\epsilon_{uo}} \qquad \text{Equation 2-11}$$

where o represents an occupied state and u represents an unoccupied state, and $\delta\epsilon_{uo} = \epsilon_u - \epsilon_o$ refers to the energy difference between any two occupied and unoccupied states.

As the magnetic anisotropy is defined as the energy difference between the easy axis and hard axis, based on the above equation, we can write out the following equation for magnetic anisotropy determined by the orbital angular momentum operators L_x and L_z between occupied and unoccupied d-states and the energy difference between these states. Considering that the majority spin states of Fe are well below the Fermi energy level as shown in Figure 1-12, the energy difference between occupied majority spin states and unoccupied spin states are large, which shows up as the denominator in Equation 2-11. Therefore, the SOC energies for these pairs of spin states will be negligible. Similarly, if the energy difference between unoccupied majority spin states and occupied minority spins is large, the corresponding SOC energies will also be negligible. Therefore, only the minority spins contribution to the magnetic anisotropy is considered [109]:

$$E_{ani} = E_{SOC}(z) - E_{SOC}(x) = \vartheta^2 \sum_{o,u} \frac{|\langle o^m | L_z | u^m \rangle|^2 - |\langle o^m | L_x | u^m \rangle|^2}{\epsilon_u^m - \epsilon_o^m} \quad \text{Equation 2-12}$$

where the superscript m all denotes the minority spin states.

An energy- and k-resolved distribution of the Fe minority bands are shown in Figure 2-4, where the occupied $d_{x^2-y^2}$ states and unoccupied d_{xy} states generate a large magnetic anisotropy by coupling through L_z operator. [109]

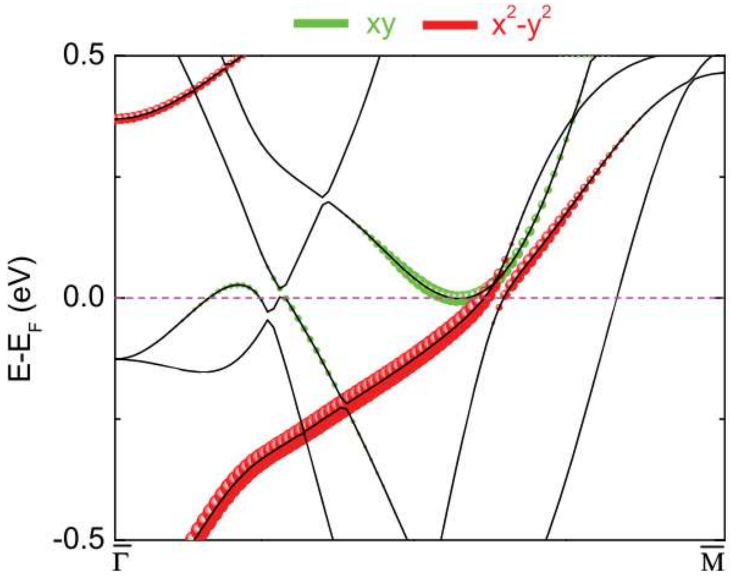

Figure 2-4 Energy- and k-resolved distribution of orbital characters of minority spin bands for Fe atom occupied $d_{x^2-y^2}$ states and unoccupied d_{xy} states. The Fe atom is located near MgO with zero lattice strain. [109]

2.3.2 Voltage-Controlled Magnetic Anisotropy

From Equation 2-12 there are possibly two mechanisms to induce the voltage control of magnetic anisotropy effects: 1) charge screening or band filling effect, as described in the numerators via the modulation of the electron states wave function;[110-112] 2) the changes in the energy separation of the spin-orbit coupled pairs of occupied and unoccupied states, as described in the denominator.[113-115]

First, we will illustrate an example where the charge screening at the Fe/MgO interface modulates the magnetic anisotropy.[110] As shown in Figure 2-5 (a), when an electric field is applied at the Fe/MgO interface, the electric field will be screened by free charges in Fe. Due to the ferromagnetism of Fe this screening effect is spin-dependent which can be seen in the modulation of orbital moment anisotropy as well as magnetic anisotropy. A more detailed understanding is illustrated by the electron density redistribution between different d-orbitals. From the Figure 2-5 (b), we see a reduced occupation of $d_{xz(yz)}$ orbitals, and enhanced occupation of d_{xy} orbitals. This will result in a decrease in the matrix element $\langle d_{xz}|L_z|d_{yz}\rangle$, thus a decrease in the perpendicular orbit magnetic moment. While for the L_x coupled elements $\langle d_{xz}|L_x|d_{xy}\rangle$ and $\langle d_{yz}|L_x|d_{xy}\rangle$, the decrease of occupancy in $d_{xz(yz)}$ orbitals and increase of occupancy in d_{xy} orbitals are canceled out. Therefore in total, the magnetic anisotropy decreases with the electric field.

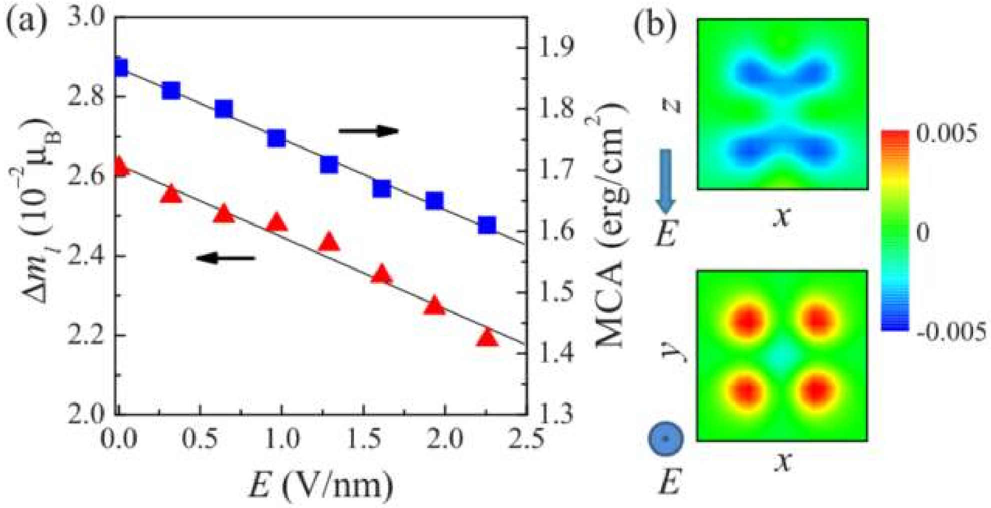

Figure 2-5 (a) Magnetic anisotropy energy (MCA) and orbital moment anisotropy (Δm_l) of the Fe/MgO interface as a function of electric field in MgO. (b) Electric-field induced charge density change (in units of $e/\text{Å}^3$) at the interfacial Fe atom for $E = 1.0\,V/nm$ in the x-z (010) plane (top) and x-y (001) plane (bottom). The electric field is applied along the z direction. [110]

Next, a detailed example of the effect of the change of energy separation is illustrated below.[116] The magnetic anisotropy change in Ta/FeCo/MgO structures under different external electric field has been calculated. A detailed breakdown of the modulation of the occupied and unoccupied energy bands near the Fermi level along the symmetry directions is shown in Figure

2-6. If we look at the peaks identified by number 1 and 2 in the vicinity of $\bar{\Gamma}$ point as shown in Figure 2-6 (b) (c), under both directions of electric field, the unoccupied Fe $d_{x^2-y^2}$ bands exhibit a downward energy shift, while the occupied Fe d_{xy} states remain un-shifted or shifts up (as illustrated in the green circles). The coupling of these states via L_z and the decrease of the denominator results in an increase of magnetic anisotropy as shown in Figure 2-6 (a). Similarly, we can explain the peak 3 under negative electric field by considering the significant downward shift of the Ta unoccupied $d_{x^2-y^2}$ states coupled via L_z (as illustrated in the red circle).

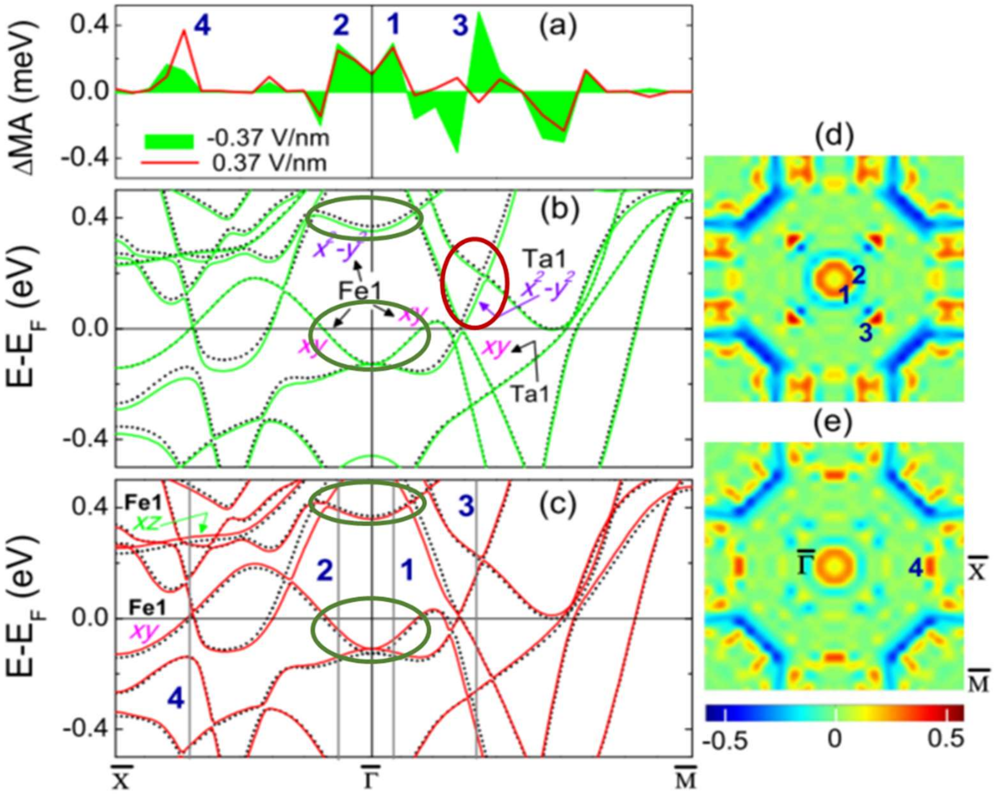

Figure 2-6 (a) Electric-field-induced change of magnetic anisotropy along symmetry directions in Ta/FeCo/MgO structures with FeCo under 0% strain with respect to zero electric field case. (b) and (c) are superposition of zero-field minority-spin band structures (dotted curves), under -0.37V/nm (green solid curves), and under +0.37V/nm electric fields (red solid curves). The Fe and Ta states dominant in the

VCMA effects are illustrated. (d) and (e) are the electric-field-induced change of magnetic anisotropy plotted in the 2D Brillouin zone under -0.37V/nm and +0.37V/nm respectively. [116]

For peak 4 under positive electric field, the upward shift of the unoccupied Fe d_{xz} will increase the energy difference in the denominator, while the upward shift of the occupied Fe d_{xy} bands will render some of the d_{xy} bands partially unoccupied, which effectively changes the numerator too. As d_{xz} and d_{xy} are coupled via L_x, the above mentioned modulation in both the energy spacing and the electron occupancy lead to a decreased contribution for the in-plane energy and an enhanced perpendicular magnetic anisotropy.

As indicated above, the modulation of bands will also result in a change of the electron occupancy thus a modulation of the matrix elements appearing in the numerator in Equation 2-12. This has the same consequence as the charge screening theory. Hence though the two mechanisms, i.e. charge screening and band separation energy change both can lead to the VCMA effect, both effects could be explained by the modulation of the electronic band structure under electric field.

Of course, all these *ab initio* theoretical calculations assume perfect Fe (FeCo) and MgO crystals with a perfect interface. However, in reality, there ultimately exist various types of defects in the crystals and at the interface. Especially for the sputter-deposited samples, the materials usually consist of polycrystalline crystallites exhibiting different crystal orientations as well as amorphous regions with no clear crystal structures. Hence, care needs to be taken when comparing between the *ab initio* calculations and experimental results.

2.3.3 Voltage Control of Interfacial Magnetization

Apart from the effects mentioned above, the charge screening from Fe conduction electrons at the CoFe/MgO interface will also induce an interfacial magnetization.[110] As shown in Figure

2-7, only the spin density at the interfacial Fe atoms is modulated significantly. From the calculations, it is shown that the interface magnetoelectric coefficient α_s as defined in $\mu_0 \Delta M = \alpha_s E$ is larger than that for the Fe/vacuum interface by a factor of 3.8. This could be explained by a rigid band model that all the screening charge will be localized within the first atomic monolayer, and the charge polarized according to the density of states at the Fermi level will be seen as the induced interface magnetization. Therefore, the surface magnetoelectric coefficient is given by $\alpha_s = \frac{\epsilon \mu_B P}{ec^2}$, where P is the spin polarization of the interface density of states at the Fermi energy level. It can thus be derived that the induced magnetization change is proportional to the dielectric constant ϵ of the insulator layer.

$$\Delta M = \frac{\epsilon \mu_B P}{\mu_0 e c^2} E \qquad \text{Equation 2-13}$$

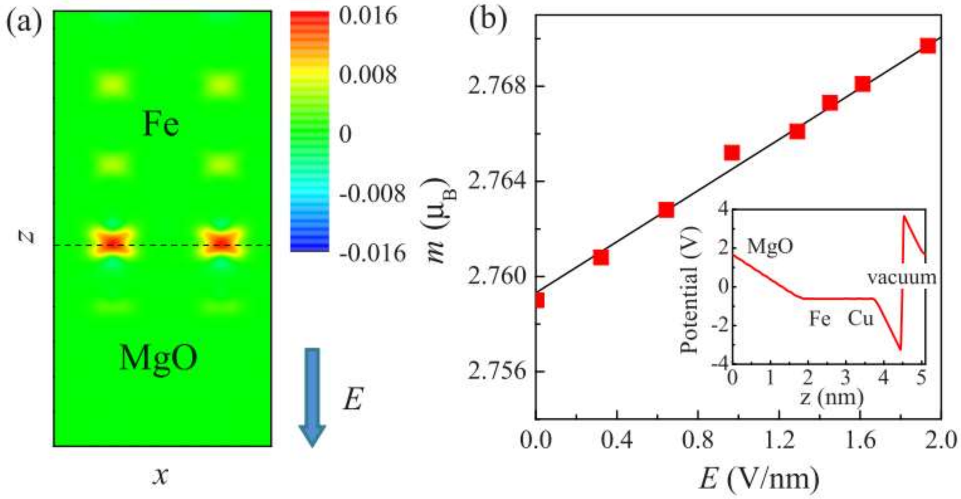

Figure 2-7 (a) Electric-field-induced spin density change with respect to zero electric-field, in units of $e/\text{Å}^3$, projected to the *x-z* or (010) plane at the Fe/MgO interface with an electric field E=1.0V/nm in MgO. (b) Magnetic moment of Fe at the Fe/MgO interface dependence on the electric field in MgO. The inset shows the calculated electrostatic potential across the MgO/Fe/Cu layers under an electric field E=4.0V/nm. [110]

2.3.4 Strain Modulation of Magnetic Anisotropy and Voltage-Controlled Magnetic Anisotropy

Another important consideration in the above theoretical frameworks is the strain effect in the multilayers. Because there is a wide distribution of crystal lattice constants among CoFe, MgO and various heavy metals, assuming a zero strain on CoFe while all the other layers will be strained to have the same lattice constant as CoFe is unrealistic in reality. In addition, during any post-annealing process of the MTJ stacks, the strain at various interfaces will tend to relax, [82] contributing to the change of various magnetic properties at different annealing temperatures. Hence, it is very important to consider the effect of strain on both the magnetic anisotropy and the VCMA effect.

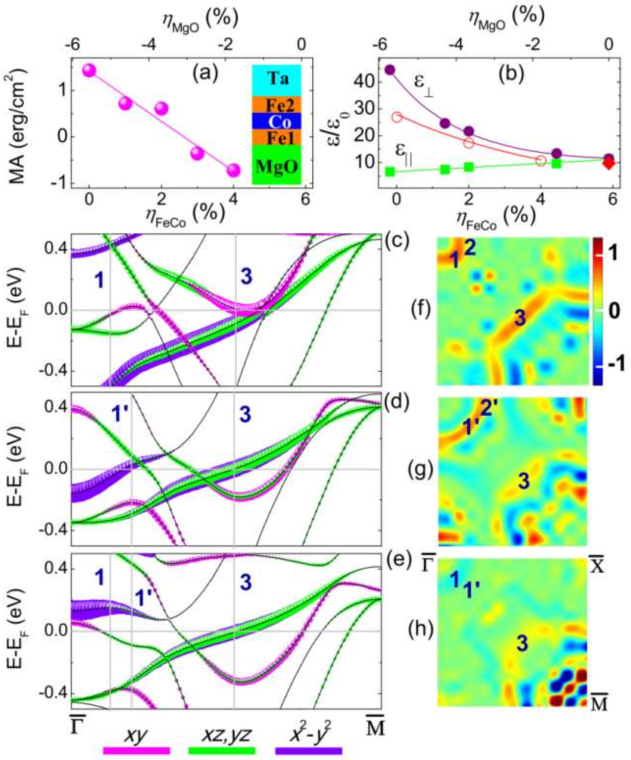

Figure 2-8 (a) Magnetic anisotropy under zero external electric field dependence on strain in FeCo/MgO in a Ta/FeCo/MgO structure. (b) Dielectric constant of MgO dependence on strain in FeCo/MgO in a

Ta/FeCo/MgO structure, with the bulk MgO's in-plane component $\epsilon_{\parallel}$ in solid squares, and out-of-plane component $\epsilon_{\perp}$ in solid circles, and $\epsilon_{\perp}$ of thin films in open circles. (c)-(e) Energy- and k- resolved distributions of the orbital character of minority-spin bands along $\overline{\Gamma M}$ for the interfacial Fe1 atom d states under strain $\eta_{FeCo} = 0\%$, 2%, and 4%, respectively. (f)-(h) Magnetic anisotropy in two dimensional Brillouin zone for $\eta_{FeCo} = 0\%$, 2%, and 4%, respectively. [115]

First, by *ab initio* calculations, the modulation of magnetic anisotropy by strain can be modeled by the change of spacing between atoms. The calculation results fit pretty well to existing experimental data on thin film magnetoelastic coefficients.[115] A physics understanding behind this is illustrated in Figure 2-8 (c)-(h), the shift of bands with different spin and symmetry character will result in a rearrangement of occupied and unoccupied bands and thus change of both the numerator matrix elements and the denominator energy separations in Equation 2-12. This argument can also be used to explain the strain effect on VCMA because under different strain conditions, the modified energy band structures will behave differently under electric field compared with zero strain conditions.

On the other hand, the strain will also induce a change on the MgO dielectric constant as illustrated in Figure 2-8 (b) where an expanding stress on MgO will lower the MgO dielectric constant. One way to understand the effect of the MgO dielectric constant on the VCMA coefficient is as follows. First the VCMA coefficient is defined as:

$$\xi = \Delta K_i / \Delta E \qquad \text{Equation 2-14}$$

Next, based on Section 2.3.2, the modulation of energy bands will induce both screened charges at the CoFe/MgO interface, as well as the band energy separation modulation. Hence, it is possible to correlate the VCMA coefficient with the interface charge density σ_q, which could be expressed as $\sigma_q = \epsilon_0 \epsilon_{eff} V/d = \epsilon_0 \epsilon_{eff} E$, where ϵ_0 was the permittivity of free space, and ϵ_{eff} was the effective dielectric constant of the tunnel barrier.[110, 117] Further, at rather small electric fields, the change of magnetic anisotropy with respect to the electric field can be approximated as a linear dependence. Therefore, from this linear dependence $\Delta K_i = k\Delta\sigma_q$, we can deduce the linear dependence of VCMA coefficient on the tunnel barrier dielectric constant

$$\xi = \frac{\Delta K_i}{\Delta E} = \frac{k\Delta\sigma_q}{\Delta E} = k\epsilon_0\epsilon_{eff} \qquad \text{Equation 2-15}$$

where k is a linear coefficient that describes the interfacial PMA change per charge density change at the ferromagnetic/insulator interface. The value of k can be determined by running *ab initio* calculations to see the evolution of complex band structures under external electric fields. Hence, with a larger tunnel barrier dielectric constant, the VCMA coefficient could be increased. This is similar in spirit as the interfacial magnetization dependence on electric field as expressed in Equation 2-13.

2.4 MeRAM Scaling Trends

For MeRAM to successfully capture a portion of the memory markets in the future, it is critical to evaluate MeRAM in terms of scaling. Below, we first illustrate the scaling requirement for MeRAM at various MTJ diameters. Then we estimate the critical MeRAM device parameters as required to replace various existing standalone and embedded technologies, including SRAM, eDRAM, eFlash, and DRAM at different technology nodes.

First, we consider the critical MeRAM materials parameters for different circular MTJ diameter. The following two equations are the most important:

$$\Delta = \frac{E_b}{kT} = \frac{\left(K_i - \mu_0(N_z - N_x)M_s^2 t/2 + K_b\right)A}{kT} \qquad \text{Equation 2-16}$$

$$E_b = \xi \frac{V_C}{d} A \qquad \text{Equation 2-17}$$

Where Δ refers to the thermal stability of the MTJ, E_b is the energy barrier between two stable states of a memory cell, i.e. P and AP configurations of the free layer and reference layer, K_i is the interfacial perpendicular magnetic anisotropy, K_b is the bulk magnetocrystalline magnetic anisotropy, $N_{x,y,z}$ is the demagnetization factor along x, y, z directions, M_S is the saturation magnetization of the free layer, t is the thickness of the free layer, A is the area of the free layer, ξ is the voltage controlled magnetic anisotropy coefficient, d is the thickness of the MgO barrier, V_C is the critical voltage needed to decrease the energy barrier to zero, k is the Boltzmann constant, T is the temperature of the MTJ. The reason why N_y is not included is that for a circular MTJ pillar, N_x and N_y are the same. Hence, the demagnetization energies of magnetization aligning along *x* and *y* directions are the same. The magnetic anisotropy from demagnetization energy thus can be expressed as the subtraction of demagnetization energy between *z* and *x (y)* direction.

Specifically, Equation 2-16 describes the magnetic anisotropy in the case of a perpendicular MTJ consisting of two parts, the interfacial PMA K_i and the in plane shape anisotropy originated from the demagnetization, as discussed in Section 2.1. Usually for a 1-2 nm CoFeB free layer deposited by sputtering, the thickness is much smaller than the MTJ diameter. In this case, $N_z \cong 1$ while $N_{x,y} \cong 0$, and the bulk magnetic anisotropy is negligible as the sputtered films are poly-crystalline in nature. [84] When the device scales down to smaller and smaller sizes with decreasing A, in order to keep the same thermal stability Δ, one way is to keep the t relatively small such that the shape anisotropy is small, and simultaneously increase the K_i value.

Recently, another innovative solution has been demonstrated to solve this scaling issue when the size of the MTJ diameter is below 20nm.[93] In this proposal, the free layer thickness t

can be increased to be larger than the MTJ diameter, such that the demagnetization factors $N_z - N_{x,y}$ will become negative. In this dissertation, as we will show in the following, the MTJ diameter are mostly still above 20nm diameter for SRAM, eDRAM, and eFlash replacement applications. Hence we will mainly focus on the case where t is set to be around 1nm and increasing K_i value is required. From calculation as shown in Figure 2-9, we can see K_i values remain rather constant around 1 mJ/m^2 when the MTJ diameter is above 22 nm, and shoots up quickly after the MTJ scales down to below 14 nm. The highest K_i values obtained in experiment is around 3.7mJ/m^2 which is also indicated by the yellow region in Figure 2-9.[118] At the end of this section, we will also briefly discuss the scaling of MeRAM beyond 20nm diameter for DRAM replacement.

For MeRAM that uses voltage to write the MTJ, another critical parameter is the voltage control magnetic anisotropy coefficient ξ, which can be calculated from Equation 2-17. This equation is defined when the applied critical voltage V_c can lower the energy barrier E_b to zero. When the MTJ diameter scales down, again E_b is kept constant, A decreases, the critical voltage V_c is limited by the maximum voltage the circuit can supply, and the MgO barrier thickness d is kept relatively constant for the VCMA effect to dominate over the STT effect. Hence, the VCMA coefficient is directly proportional to the inverse of the square of MTJ diameter, resulting in a very steep scaling trend as shown in Figure 2-9. The largest VCMA coefficient demonstrated in a MTJ device at present is by molecular beam epitaxy with a value of 370fJ/V-m, [119] while researchers at Toshiba Corporation has also demonstrated VCMA of around 750 to 1050 fJ/V-m using sputtering in a ferromagnet/insulator bilayer structure [120]. This highest value is also indicated by the yellow region in the figure.

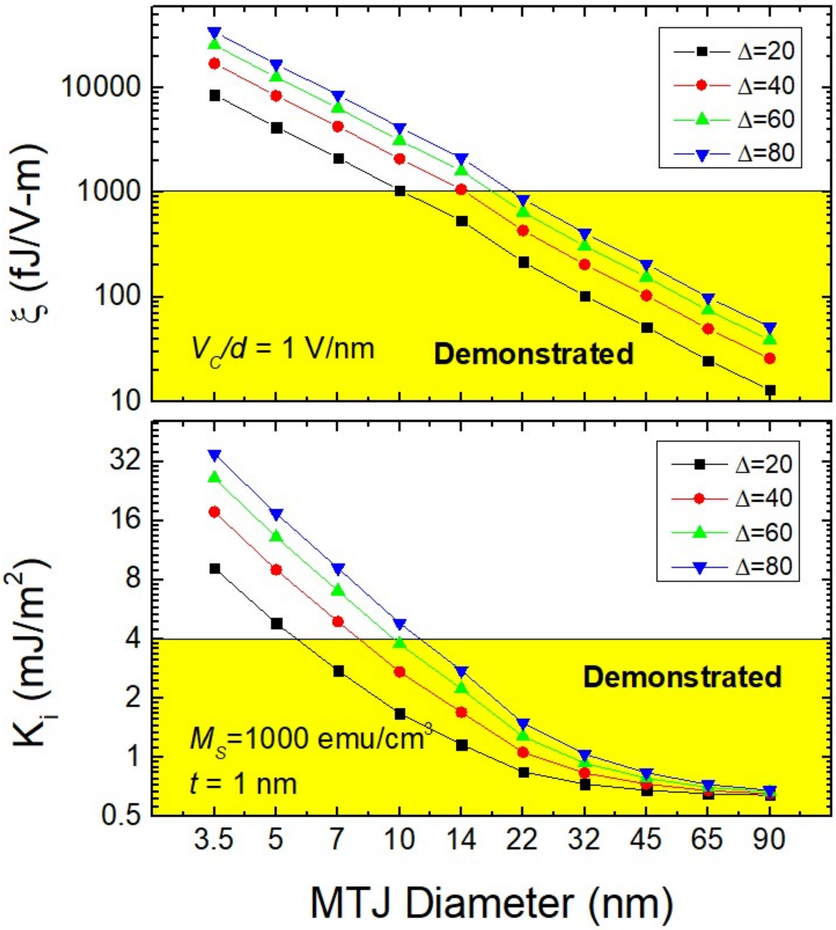

Figure 2-9 (Top) VCMA coefficient (ξ) scaling trend over different **MTJ diameter**, as a function of different thermal stability (Delta, or Δ), assuming the critical switching voltage V_C over MgO thickness d equals 1 V/nm. (Bottom) Interfacial perpendicular magnetic anisotropy (K_i) scaling trend over different MTJ diameter, as a function of different thermal stability (Delta, or Δ), assuming the saturation magnetization of CoFeB free layer is 1000 emu/cm^3, and the thickness of CoFeB free layer is 1nm. The yellow shaded regions refers to VCMA and interfacial PMA values demonstrated in experiments. [118, 120]

However, the above are all scaling analysis based on the MTJ diameter. In real applications, the density of MeRAM is limited by the transistor selector size, especially at advanced nodes beyond 28 nm where the CMOS transistor cell size keep increasing rapidly. Thus for a particular CMOS technology node, the MTJ diameter can be relaxed to be larger than the CMOS technology node size. In this case, the above scaling analysis as shown in Figure 2-9 is not as practical for benchmarking MeRAM against other technologies. With this in mind, next we will illustrate the VCMA coefficient ξ and interfacial PMA K_i scaling requirements for MeRAM to replace SRAM, eDRAM, eFlash, and DRAM, as a function of the CMOS technology node.

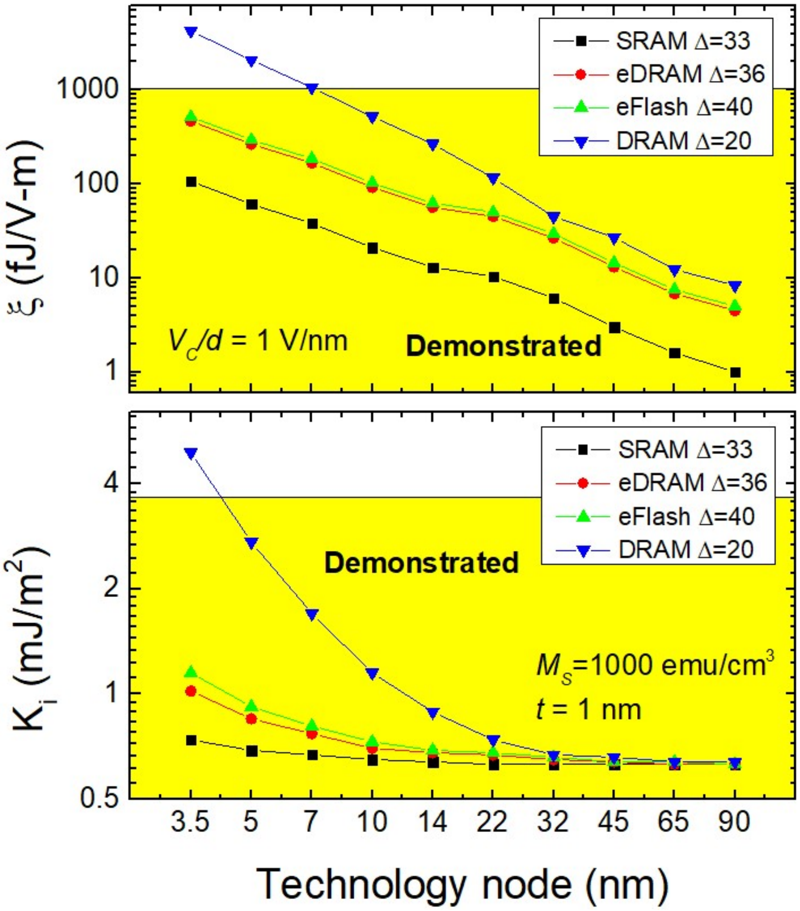

Figure 2-10 (Top) VCMA coefficient (ξ) scaling trend over different **CMOS technology node** for MeRAM to replace various technologies with different requirements of thermal stability (Δ), assuming the critical switching voltage V_C over MgO thickness d equals 1 V/nm. (Bottom) Interfacial perpendicular magnetic anisotropy (K_i) scaling trend over different CMOS technology node for MeRAM to replace various technologies, assuming the saturation magnetization of CoFeB free layer is 1000 emu/cm^3, and the thickness of CoFeB free layer is 1nm. For both figures, the size of MTJ cell to replace SRAM, eDRAM, and eFlash equals the 1/6 of a SRAM cell at the same node, while the size of MTJ cell to replace DRAM is the same size with a DRAM cell. The MTJ diameter equals to half of the MTJ cell length of side. The yellow shaded regions refers to VCMA and interfacial PMA values demonstrated in experiments. [118, 120]

For SRAM, eDRAM and eFlash replacement, MTJs will be built upon conventional transistor selectors. A good benchmark is the 1/6 size of a 6T-SRAM cell. Using this cell size (also indicated by the upper edge of the yellow region in Figure 1-6), the VCMA coefficient and interfacial PMA numbers required to replace SRAM, eDRAM, and eFlash at different technology nodes are calculated as shown in Figure 2-10. However, for DRAM replacement, as the cell size needs to be $8F^2$ size (also indicated by the bottom edge of the yellow region in Figure 1-6) to satisfy the high density requirement, the MTJ size is set to be the same as a DRAM cell. In the calculation, the MTJ diameter is assumed to be half of the cell length of side as demonstrated using a specialized process.[13] For MeRAM to replace different technologies, it is assumed that the characteristic retention time will stay unchanged, i.e. SRAM 1 day (Δ=33), eDRAM 1 month (Δ=36), eFlash 10 years (Δ=40), and DRAM 256ms (Δ=20). Note that for a larger array of MTJs, the thermal stability factor usually needs to be increased to account for process variations and temperature effects. While error correcting codes and scrubbing (ECC) will also be employed on the circuit level to reduce the errors introduced due to these variations.[121] In this dissertation, we assume that with sufficient ECC, the process variations induced thermal stability increase will be eliminated. It can be concluded that with the highest VCMA coefficient and interfacial PMA demonstrated, MeRAM can replace SRAM, eDRAM and eFlash up to 3.5nm and even smaller nodes (not calculated). While for both DRAM replacement, MeRAM can only scale to around 7nm. Note that a more general discussion of the MeRAM advantages and disadvantages against these existing memory technologies in terms of scaling is covered in Section 1.2.2.

2.5 Precessional Switching and Write Error Rate

Other than the above discussed requirement for high VCMA coefficient and interfacial PMA, the successful adoption of MeRAM using voltage-controlled MTJs require a sufficiently low write error rate on the bit-level and circuit-level. The precessional nature of the VCMA switching process is illustrated in Figure 2-11. With an external field applied along the in-plane orientation, the application of a voltage pulse across the MTJ will lower the energy barrier first. Then the magnetization will start precessing around the external field direction. Due to damping the magnetization will slowly point towards the in-plane direction. In this precession process, removing the applied voltage pulse will recover the energy barrier and the magnetization will choose to stay at the closest local minima. Hence, a precise timing of the voltage pulse to be half of the precession period is essential to enable high switching probability and low write error rate (WER). The switching time τ can be derived from Equation 2-8 as the following:

$$\tau = \frac{1}{2} \cdot \frac{2\pi}{\omega} = \frac{\pi(1+\alpha^2)}{\gamma_0 \mu_0 H_{eff}} \qquad \text{Equation 2-18}$$

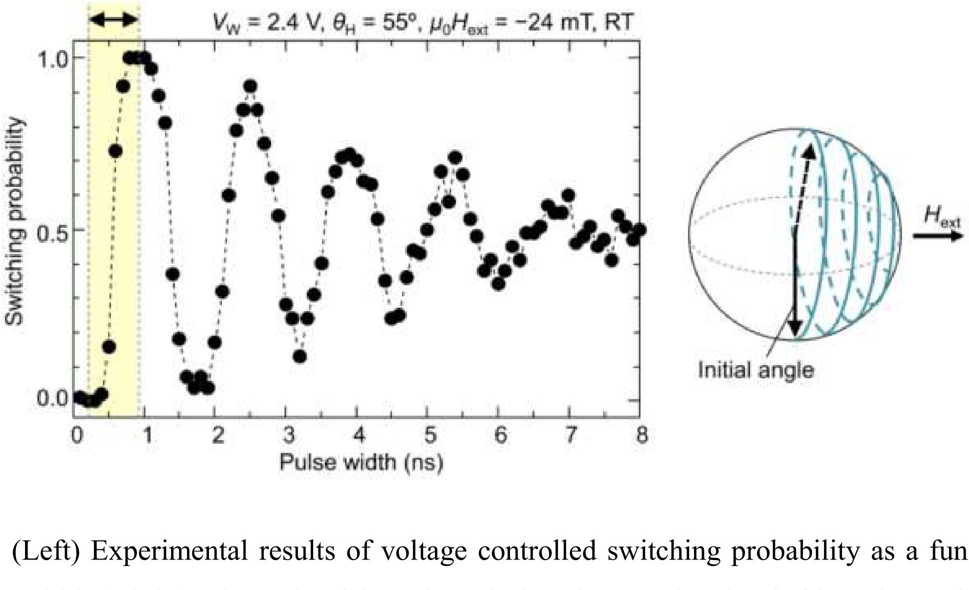

Figure 2-11 (Left) Experimental results of voltage controlled switching probability as a function of the voltage pulse width. (Right) Schematic of the voltage-induced precessional switching of MTJ free layer.[24]

where α is the Gilbert damping parameter, and H_{ext} is the in-plane external field. Note that in the above equation, we assume at the voltage pulse duration, the magnetic anisotropy field $H_k^{eff} \ll H_{ext}$, hence can be neglected.

In order to achieve a low WER, good timing and pulse shape are required by the writing circuitry. It is also possible to utilize multiple read/write cycles to lower the total WER.[122] However, there are couple of device-level parameters that are critical in decreasing the WER, including damping factor, thermal stability, and external in-plane field strength.

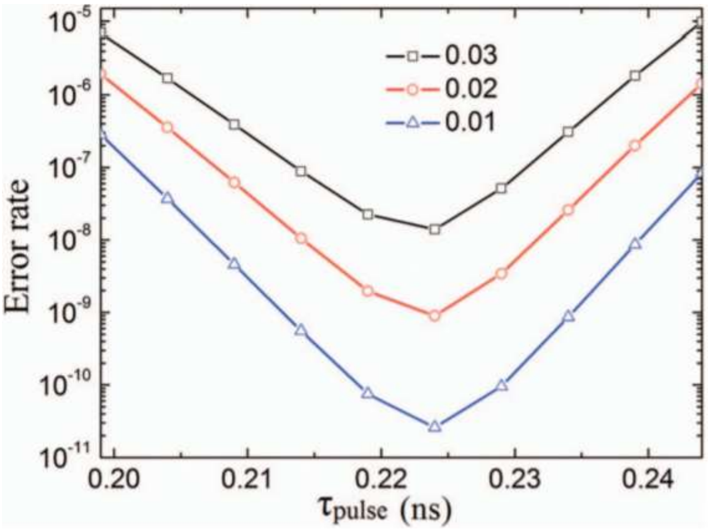

Figure 2-12 Calculated write error rate as a function of the write pulse duration τ_{pulse} for different values of damping factor α. The free layer diameter is 20nm, and the thermal stability Δ is 40, external in-plane field is 800 Oe.[123]

First, we will discuss the role of the damping factor. Using the Fokker-Planck equation, the WER has been numerically calculated under different damping factor scenarios as shown in Figure 2-12. It can be seen that the lower the damping is, the lower WER is. It can be understood considering that a higher damping will drive the magnetization into the in-plane state in a faster rate. Hence even under the precise switching time τ which is half the precession period, the faster deviation to the external field direction will decrease the switching probability.

In reality, the damping factor of the magnetic material is usually limited due to inherent material properties, non-uniformity of the material, such as pinning sites at the edges of the free layer, and incoherent switching via nucleation reversal.[124] Hence, it is important to consider other means to decrease WER. An experimental illustration of the impact of thermal stability and external in-plane field on WER is shown in Figure 2-13.

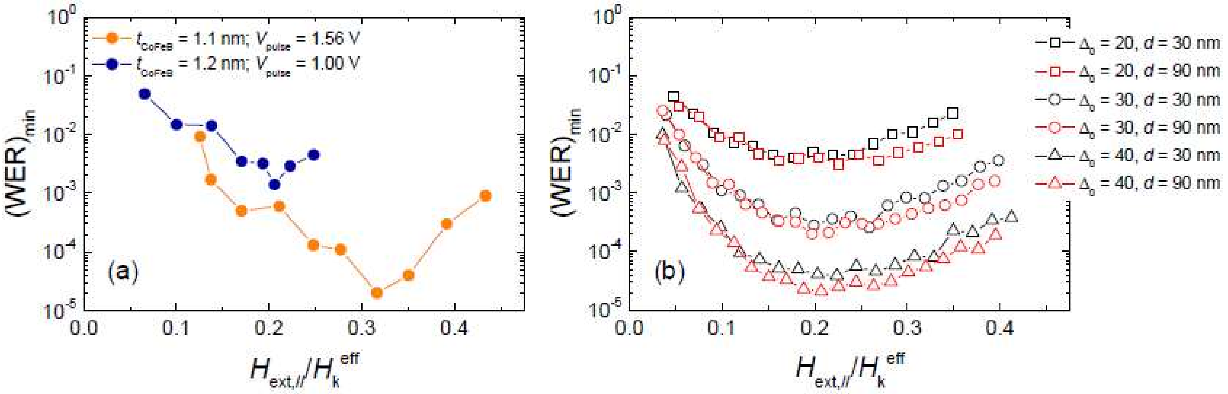

Figure 2-13 (Left) Experimentally obtained minimal write error rate as a function of the ratio of external magnetic field over effective anisotropy field of the free layer, under different CoFeB thicknesses. (Right) Calculated minimal WER as a function of the ratio of external magnetic field over effective anisotropy field of the free layer, for different thermal stability and junction diameters.[125]

The thinner CoFeB used here will result in a higher magnetic anisotropy thus higher thermal stability. The thermal stability factor effectively determines how much the thermal barrier is susceptible to thermal agitation. A low thermal stability factor will result in stronger thermal agitation of the free layer at the initial onset stage, the final relaxation stage, as well as the whole switching stage, inducing a larger variation of the free layer cone angle and decrease the switching probability. For different in-plane external fields applied during the switching process, the WER exhibits a minimum at a certain in-plane field, while the WER increases when the in-plane field strength is smaller or larger than the optimal in-plane field strength, as shown in Figure 2-13. This can be understood as follows: at a small in-plane field, the precessional switching period is longer during which the thermal agitation affects the magnetization, and the thermal agitation strength is effectively larger relative to the in-plane field, thus strongly randomizes the switching process. While at large in-plane field, the magnetization tilts towards the in-plane field direction and the thermal stability factor is lowered, also leading to a decreasing WER. [125]

2.6 Read Speed and Read Disturbance

In addition to the write operation, the read operation of a memory device is also critical. As mentioned in Section 1.2.3 briefly, MeRAM inherently has a thicker MgO tunnel barrier than the STT-MRAM, which will give rise to higher resistance-capacitance delay in the sensing circuit. However, there are some other factors that might remedy this high resistance-induced low read speed.

First, as the MgO barrier in a MeRAM device is usually around 1.4 nm [22] compared with that of around 0.9 nm [93] for a STT-MRAM device, the TMR values will increase giving rise to a larger read margin.[65] The cause of this is usually attributed to the better crystal quality of the barrier and/or the less shorting of the sidewall when the barrier is thicker. Secondly, as STT-MRAM uses positive and negative polarities to induce switching from anti-parallel to parallel and vice versa, if read current is large and close to the write current level, the read operation can induce switching of the memory bit, or the so-called read disturbance. Therefore, the read voltage needs to be relatively small to around 0.3-0.4V to avoid large read disturbance.

While for MeRAM, only the positive polarity is used when writing. Hence one can use the negative polarity V_{DD} value of around -1V for reading to achieve larger read margin as shown in Figure 2-14. In addition, due to the linear VCMA effect, the negative voltage applied to a MeRAM device can actually increase the thermal stability thus further reduce the read disturbance. [122]

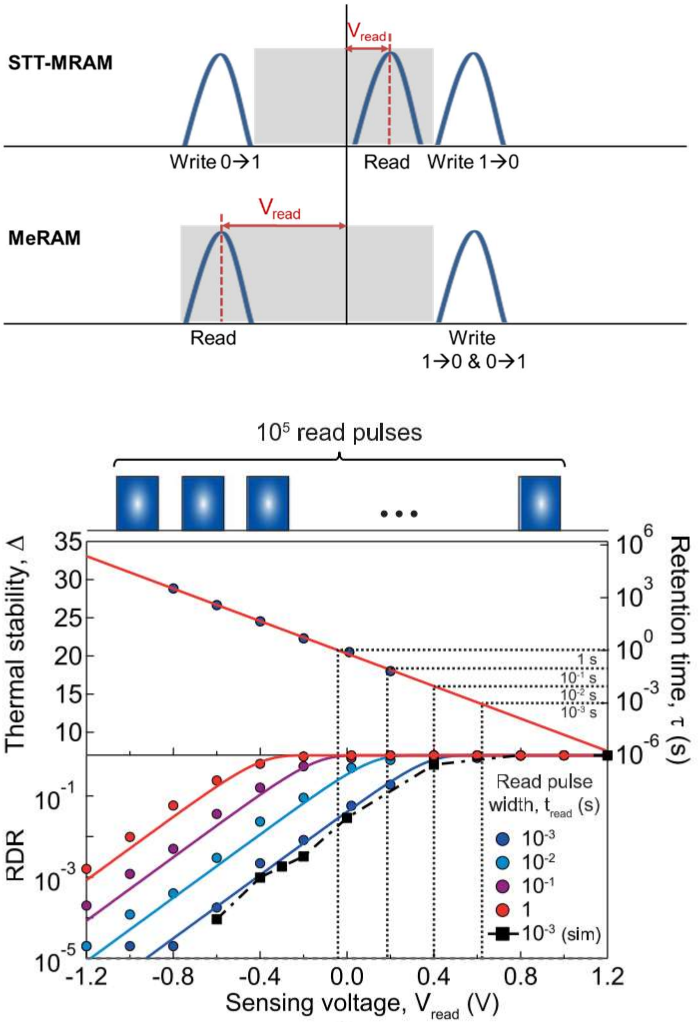

Figure 2-14 (Top) Schematic of STT-MRAM and MeRAM read voltage range with respect to the write voltage. (Bottom) Thermal stability, and measured (circles) and simulated (squares) read disturbance rate as a function of sensing voltage for read pulses of 1, 10, 100, and 1000 ms for a MeRAM device.

Chapter 3 Voltage-Controlled Magnetic Anisotropy: Fabrication and Characterization

3.1 Magnetic Tunnel Junctions Fabrication Process

Fabrication of MTJs involve multiple steps as shown in Figure 3-1. First, a multilayer of magnetic and nonmagnetic materials will be deposited by sputtering on a substrate, which is either a Si substrate with thermal oxide or a planarized CMOS wafer with some interconnect metal lines. Then the thin films need to be annealed at a high temperature and/or under the external magnetic field to improve the magnetic properties of the thin films. Next, a hard mask which has much slower etch rate compared with the MTJ materials will be defined and deposited for the subsequent etching of the MTJ pillar. Note that the etching depth of the pillar is critical in that the free CoFeB layer outside of the pillar region needs to be etched away but enough portion of the bottom electrode in the MTJ stack needs to be reserved. For the etching, multiple methods can be used separately or in combination including inductively coupled plasma (ICP) and ion-milling processes. Next, an oxide layer to protect the MTJ pillar will be deposited using plasma-enhanced chemical vapor deposition (PECVD), chemical vapor deposition (CVD), and atomic layer deposition (ALD) methods. To connect to MTJ's bottom and top electrodes, via will then be etched and contact metals are evaporated to form the top and bottom electrodes. In this whole process, the sputter deposition and pillar etching are the two most critical steps to ensure high fabrication yield and good MTJ device performance. Next, these two critical steps will be discussed at length.

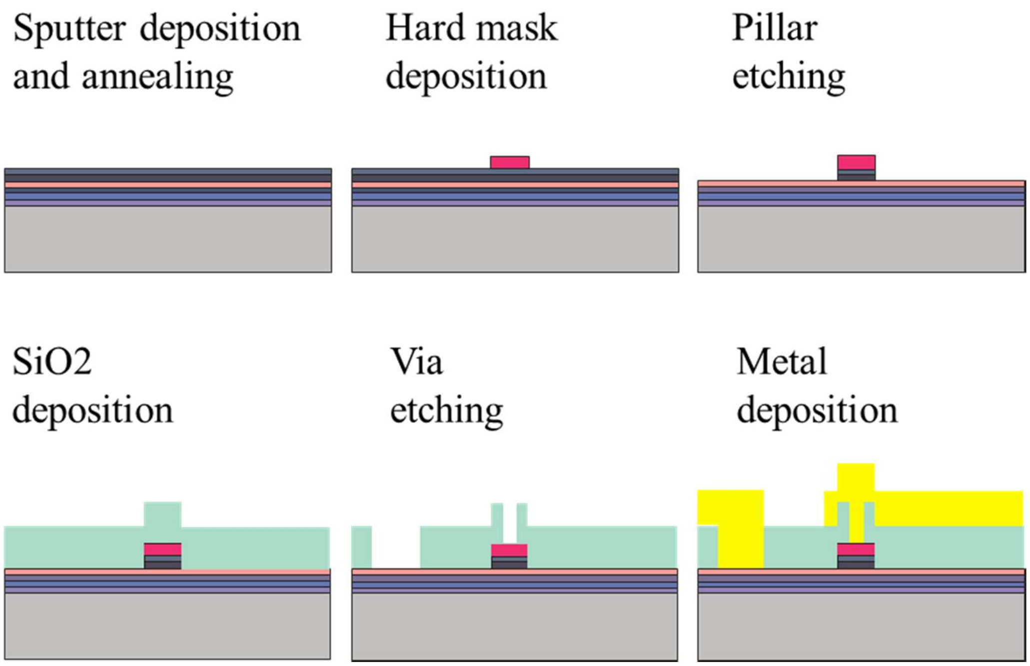

Figure 3-1 MTJs fabrication process flow schematics showing the cross-section of each step.

3.1.1 Magnetic Thin Film Epitaxial Growth via Molecular Beam Epitaxy (MBE)

One of the first attempts of MgO-based MTJ growth is done by MBE because of its superior control of film quality. The Ando group produced epitaxial Fe(001)/MgO(001)/Fe(001) MTJ and obtained up to 180% TMR at room temperature.[126] X-ray absorption spectroscopy (XAS) and x-ray magnetic circular dichroism (XMCD) have been carried out and none of the Fe atoms adjacent to the MgO(001) layer are oxidized.

However, the epitaxial growth of single-crystal MgO(001) barrier by MBE is not practical to industrial level production. For MBE growth, it starts with a single-crystal MgO(001) substrate, then a MgO(001) seed layer is deposited followed by epitaxial Fe bottom electrode. Sometimes, a Cr and/or Au seed layer[127] is also grown between the MgO seeding layer and Fe bottom electrode due to their small lattice mismatch to Fe(001). In the growth process, an ultra-high vacuum is required, while different annealing temperatures have to be optimized for each layer. To achieve the above mentioned epitaxial MTJ stacks, in-situ monitoring of the growth quality is essential, for instance, via reflection high-energy electron diffraction (RHEED).

3.1.2 Magnetic Thin Film Polycrystalline Growth via Magnetron Sputtering

Apart from the MBE growth, another pioneering work has been done using magnetron sputtering and ion beam deposition techniques. Parkin et al.,[80] sputtered MTJ stacks with highly oriented polycrystalline MgO(001) barrier on a SiO_2 substrate using TaN seed layer such that the CoFe electrodes along with the MgO barrier can be crystallized into (001) orientation. Significant and more practical as it is, the requirement of a particular seed layer for sizable TMR value is still too stringent for MRAM applications where a pinning layer might be necessary and need to be grown as the seed layer.

Another pioneering work is done by replacing the CoFe/Fe with CoFeB which will solve the abovementioned issue.[128] As grown the CoFeB is in an amorphous state. However, the MgO layer sputtered on the amorphous CoFeB is (001)-oriented and polycrystalline. And upon annealing, after all the layers are deposited, the amorphous CoFeB layer will crystalize according to the adjacent MgO orientation, i.e. into bcc(001) CoFe. The nature of the amorphous CoFeB indicates that the polycrystalline MTJ stacks can be grown on almost any materials, which make the CoFeB/MgO/CoFeB structure highly competitive for real production.

Although the polycrystalline MTJ stack is not fully epitaxial, research has shown that the grain-to-grain epitaxy of CoFe/MgO/CoFe more or less satisfies the coherent tunneling requirement for high TMR value.[129] Very interestingly, within each grain, a 45° epitaxial relationship is established to be (001)[110]CoFe//(001)[100]MgO//(001)[110]CoFe, as shown in Figure 3-2. The reason is that the MgO lattice constant (0.4202nm) is 32% larger than that of

CoFe (0.2866nm). Hence, a 45° rotational epitaxy can achieve only 2% lattice mismatch. And this has been verified by a real diffraction pattern from the experiment. In addition, it has also been observed that the grain boundaries offer very similar tunneling behavior compared with the grain itself, indicating that the CoFeB/MgO/CoFeB MTJs deviate little to the fully epitaxial MTJs in terms of TMR and RA products.[130]

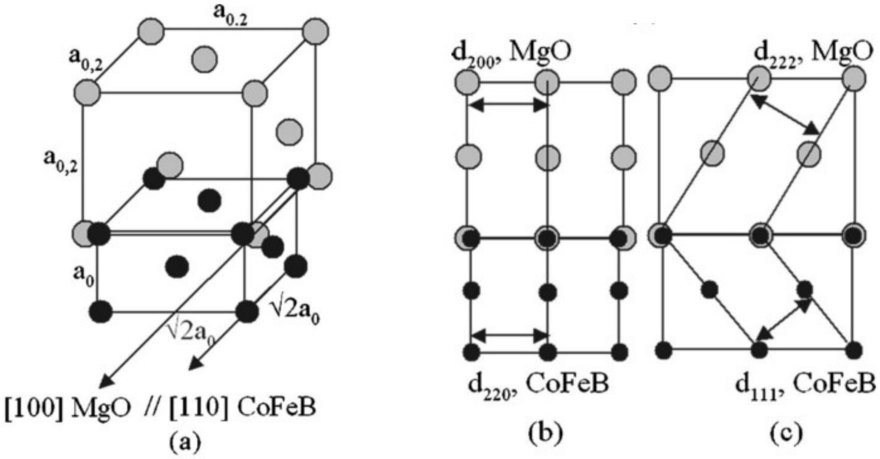

Figure 3-2 (a) Schematic of MgO and CoFeB unit cells when [100]MgO is parallel to [110]CoFeB. (b) and (c) are projected images of the schematic (a) when the electron beam is parallel to [100] MgO and [110] MgO, respectively.[129]

3.1.3 Magnetic Tunnel Junctions Etching via Ion Beam Etching (IBE)

The most widely used etching method for defining MTJ pillars is the ion beam etching (IBE) method or sometimes referred to as ion milling as shown in Figure 3-3. Ar plasma is first excited applying a high voltage between the extractor cathode and anode. The Ar gas molecules will then break down into Ar^+ ions and electrons. Under high electric field between the electrodes, Ar^+ ions will accelerate to gain high energy and bombard material clusters out of the materials under-etched. Because the size of the Ar plasma beam is limited and cannot cover the whole wafer area, in practice a wafer is usually tilted and rotating under etching. To ensure that the etching process stops right at the layer desired in the MTJ stack, in-situ monitoring equipment is included: a secondary ion mass spectroscopy (SIMS) system for etching end-point detection (EPD). The critical parameters of this etching process include the ion beam angles and desired cell-to-cell spacing widths of the MTJ pillars.

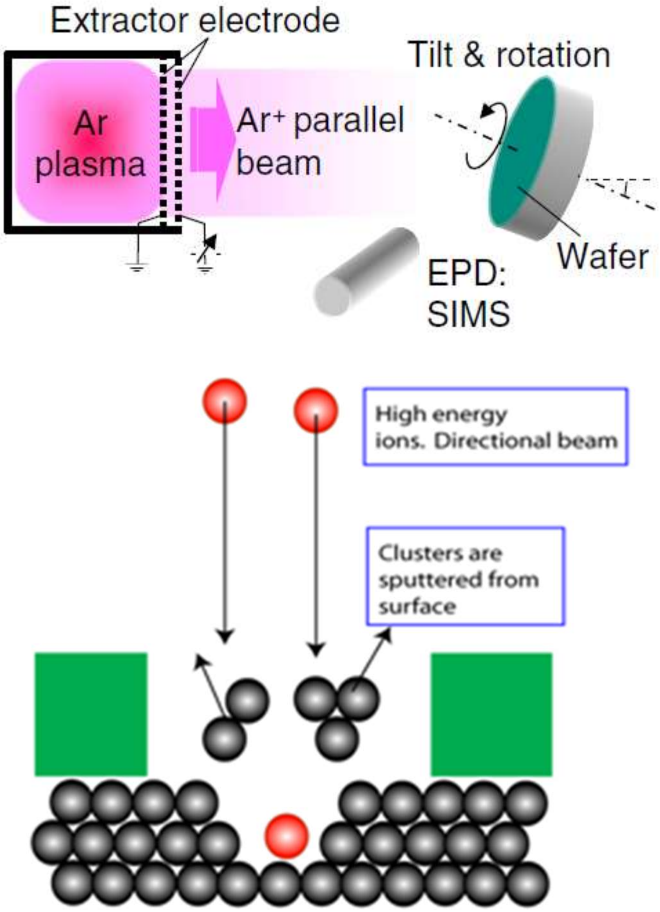

Figure 3-3 (Top) Experimental apparatus of an ion beam etching (IBE) system including a secondary ion mass spectroscopy (SIMS) system for etching end-point detection (EPD). (Bottom) Schematic of the ion beam etching process close to the material under-etched.[131][132]

The main advantage of ion milling is being free of chemical damage. The etching process only involves physical bombardment of inert gas ions. Thus it can achieve highly anisotropic etch with a low level of undercutting at the corner of the etched patterns. But it also results in a low selectivity of certain materials. Due to the fact that the ion beam is at a tilted angle with respect to the MTJ pillar, the flux of etched materials will be generated at different angles and some of them will be redeposited onto the sidewall of the MTJ pillars, as shown in Figure 3-4. In particular, this redeposition will depend on the cell-to-cell spacing and ion beam incidence angle. First, we know that etching happens at both the sidewall and the bottom electrodes due to the small spray of the ion beams. When the cell-to-cell spacing is large, a lower ion beam angle closer to grazing angle is used. The majority of ion beam will bombard the sidewall instead of the bottom electrodes, thus any redeposition of materials onto the pillar will be etched away efficiently. However, if the cell density is increased, the ion beam angle has to be increased closer to the normal direction. Otherwise, the neighboring pillars will also be etched. In this scenario, the etch rate of bottom electrodes will be increased relative to that of the sidewall. There will be redeposition of bottom electrode materials onto the sidewall. As the bottom electrodes are highly conductive metallic materials, the redeposition will short the MTJ and reduce TMR values. To resolve this, one method is to utilize various post-treatment process to remove the redeposition materials, such as oxygen showering, nitrogen, or hydrogen treatment.[133] If the MTJ cell spacing is large enough, the best way using IBE will be a two-step process: first, a perpendicular ion beam etching is used to define the pillar and etch to bottom electrodes, then a second grazing angle ion milling process can etch away the redeposition materials.

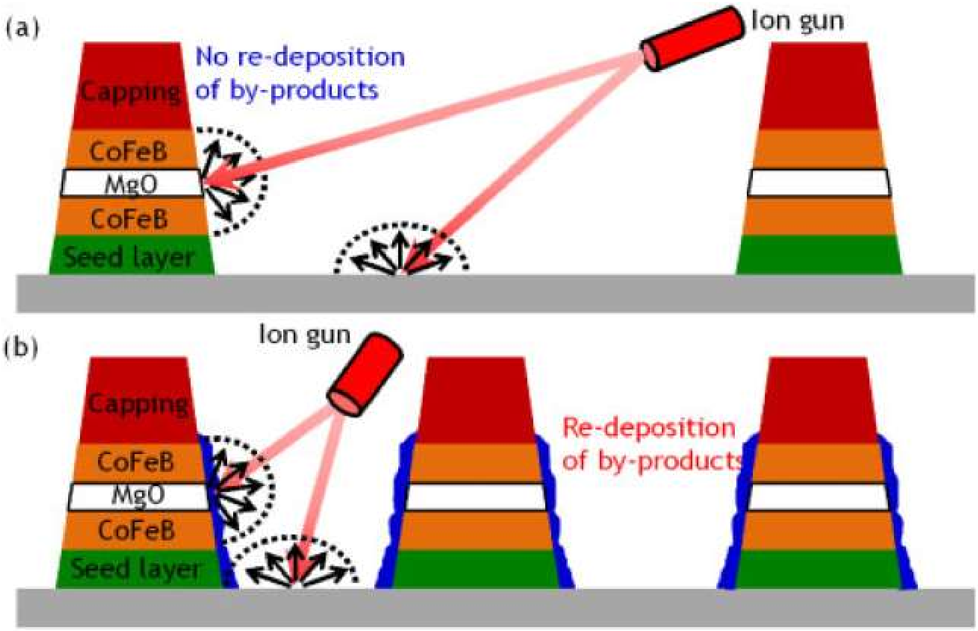

Figure 3-4 Re-deposition of metallic by-products during an ion beam etching process for (a) large cell-to-cell spacing and (b) small cell-to-cell spacing between the MTJ pillars.[133]

3.1.4 Magnetic Tunnel Junctions Etching via Inductively Coupled Plasma (ICP)

Compared with ion beam etching (IBE) processes which can become difficult for large-scale production due to the limited size of the ion beam source, reactive ion etching (RIE) using inductively coupled plasma (ICP) has been used for semiconductor mass production. Detailed studies on the performance of RIE ICP etching of MTJs thus are also of great importance for the MRAM industry.

As shown in Figure 3-5, reactive ion etching (RIE) uses an ICP source to generate plasma from reactive gases such as Chlorine and Fluorine. The gas molecules under high energy will break into electrons and Cl^-/F^- mobile ions, which will react with the materials to be etched. The volatile product will be formed through the reaction and pumped out. To ensure that the etching process stops right at the layer desired in the MTJ stack, in-situ monitoring equipment is included: an optical emission spectroscopy (OES) system for etching end-point detection (EPD). Other parameters of the etcher can be controlled too such as the gas composition, gas pressure, bias voltage/power of the plasma input, ion energy/voltage output of plasma, and hard mask taper angle.[131]

The main advantage of this method is that the plasma will cover a much wider area and the uniformity of this plasma etching will be significantly better than IBE. Also, the re-deposition rate of etched MTJ materials back onto the MTJ pillar sidewall will be lower compared to IBE considering that the byproducts of RIE etching is largely volatile but IBE etching will bombard metallic clusters out of the MTJ stacks. By selecting different reactive gases, one can etch different materials with high selectivity. However, the reactive chemical etching process is more isotropic than IBE. Also, the reactive gases cause chemical damage to the magnetic layers which will degrade the MTJ properties such as TMR values. To solve this process-induced damage (PID) problem, one can recover the MTJ properties by an additional plasma treatment using chemical gases that can eliminate the PID produced by the etching gas. For example, if methanol gas is used for etching, then He/H_2 treatment after etching has been shown to recover the TMR values.[134] Another way to reduce the PID is to use high-taper hard mask such that less area of the MTJ sidewall is exposed to the plasma and less ion radiation and PID happen. Apart from using RIE etching with a different gas, one can also use pure Argon gas in the ICP etcher such that PID due to the chemical reactions from the reactive gases can be minimized. But in this way which is effectively similar with an IBE etcher, more re-deposition of etched materials might happen.

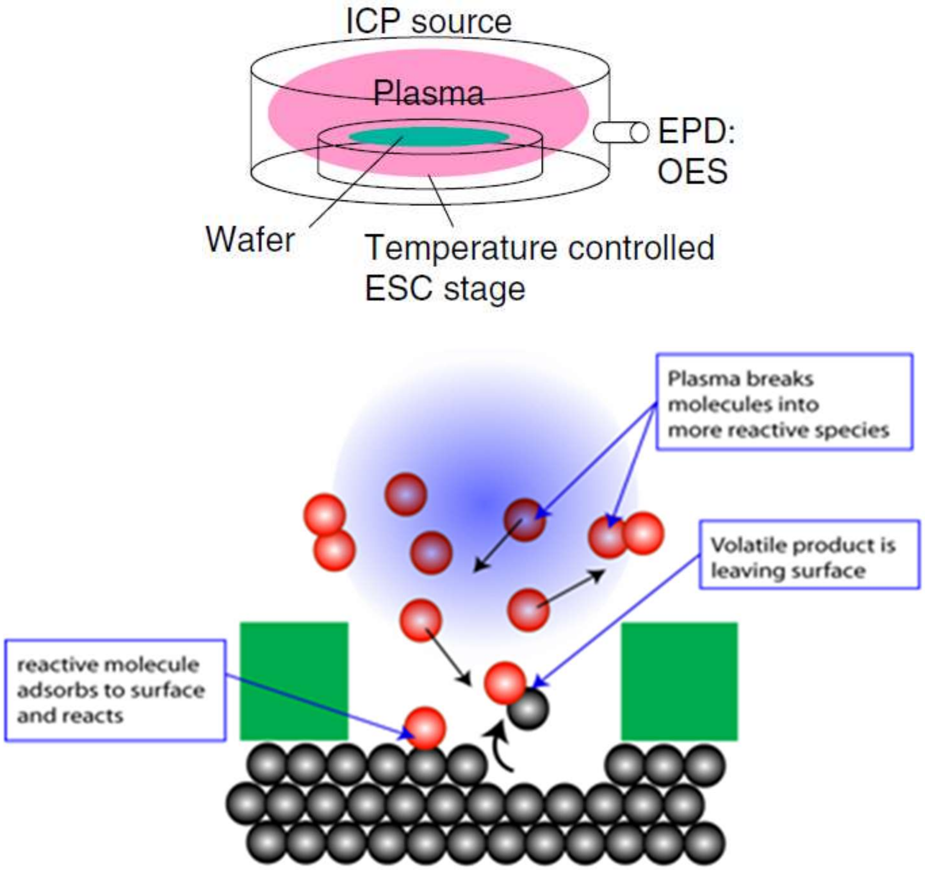

Figure 3-5 (Top) Experimental apparatus of an Inductively Coupled Plasma (ICP) etcher including an optical emission spectroscopy (OES) system for etching end-point detection (EPD). (Bottom) Schematic of the ICP reactive ion etching process close to the material under-etched.[131][135]

3.2 Device-Level Characterization of Voltage-Controlled Magnetic Anisotropy

The physics behind transport measurement is explained as the following. As the VCMA coefficient is defined as the change of interfacial magnetic anisotropy under unit electric field applied in the tunnel barrier, one need to first obtain the magnetic anisotropy energy of the free layer under different electric fields. By definition, the magnetic anisotropy K_{eff} equals the work done to bring a free layer from an easy axis orientation to a hard axis orientation. As shown in Figure 3-6, for a perpendicular free layer, by sweeping an in-plane field from 0 to above the saturation field H_k, a M-H curve can be obtained. Then the magnetic anisotropy K_{eff} is expressed as the following integral which is also illustrated in Figure 3-6. This equation is similar to Equation 2-1 in that any magnetic energy can be expressed as integration of the external magnetic field and the change of magnetic moment induced by that magnetic field.

$$K_{eff} = \mu_0 \int_0^{M_s} \vec{H} d\vec{M} = \mu_0 M_s \int_0^{M_s} H_x d\left(\frac{M_x}{M_s}\right) \qquad \text{Equation 3-1}$$

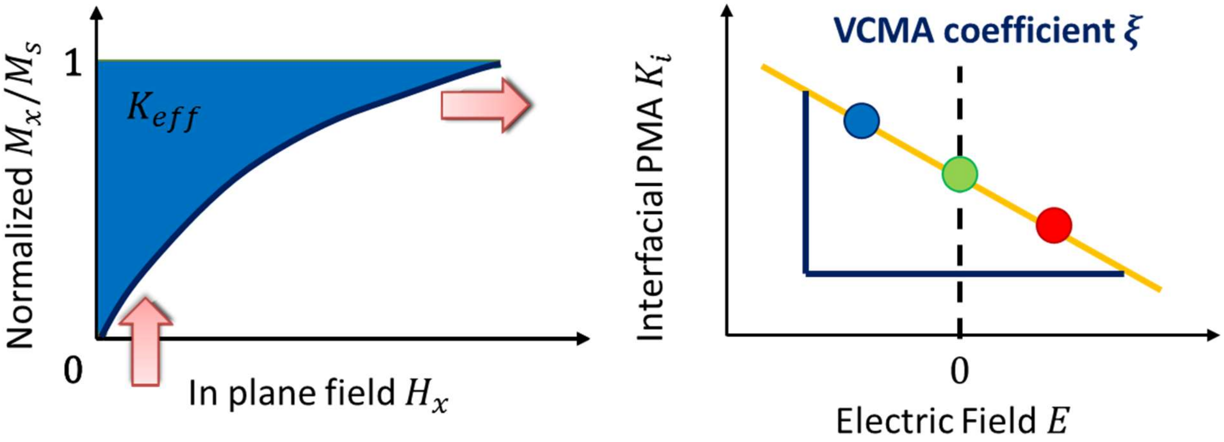

Figure 3-6 (Left) Normalized magnetization dependence on external magnetic field curves. The perpendicular magnetic anisotropy is plotted in the blue region. (Right) The dependence of interfacial PMA on electric field, with the slope as defined as the VCMA coefficient ξ.

After obtaining the magnetic anisotropy, the interfacial PMA K_i will be calculated using the following equation:

$$K_{eff} = \frac{K_i}{t_{CoFeB}} - \frac{1}{2}\mu_0\left(N_z - N_{x,y}\right)M_s^2 + K_b \qquad \text{Equation 3-2}$$

which is also embedded in Equation 2-16. As the CoFeB thin film is usually around 1-2 nm in polycrystalline state, the bulk anisotropy term is usually very small and can be neglected.[84] Note that the CoFeB thickness here should be after the subtraction of the dead layer. Then, the same procedure can be applied to different electric field cases, and by fitting the K_i dependence on electric field E, the VCMA coefficient ξ could be obtained.

For experimental characterization of the VCMA coefficient, one needs to measure the M-H loop via some means. The measurement of M-H loop using a superconducting quantum interference device (SQUID), vibrating sample magnetometer (VSM), Magneto-Optical Kerr Effect (MOKE) or angle-dependent ferromagnetic resonance (FMR) technique in a microwave cavity [136] is rather difficult as it requires a certain amount of un-patterned ferromagnetic thin films to generate enough signals, which cannot take into account of the edge effects in nanoscale MTJs. Also the application of voltage on these large-scale films are challenging. Hence, it is necessary to measure the M-H loop using patterned devices. There have been few studies to measure VCMA based on the effect of electric field on perpendicular CoFeB coercivities in MTJs.[100, 137] Though coercivity is correlated with saturation field, it is more accurate to quantify the VCMA effect in terms of interfacial PMA change per unit electric field.

Existing DC transport methods using patterned devices to achieve this goal mainly include two. One is anomalous Hall resistance measurement in CoFeB/MgO/oxide structures with an applied gate voltage, hereafter referred to as anomalous Hall measurement,[138]. The other is MTJ resistance measurement using a free layer and a fixed layer with specific magnetization configurations. The most accurate configuration to extract the VCMA coefficient is one where the fixed layer does not change its magnetization orientation when a hard-axis loop for the free layer is swept, hereafter referred to as strong fixed layer MTJ measurement.[139, 140] However, this scenario is rather difficult to achieve as a synthetic antiferromagnetic (SAF) structure is usually required for the strong pinning of the fixed layer. Henceforth, another special configuration that deviates from the abovementioned ideal scenario is often adopted which uses a weak in-plane layer that switches at a rather low in-plane magnetic field, [141, 142] hereafter referred to as weak reference layer MTJ measurement. In this scenario, the free layer has been assumed to be fully perpendicular at zero external magnetic field and fully in-plane at the maximum in-plane external field, while the saturation magnetization value does not change. Here we explore these different methods and evaluate the validity of the different assumptions used to quantify the VCMA strength, looking especially at the anomalous Hall and weak reference layer MTJ measurements methods.

3.2.1 Weak Reference Layer MTJ Measurement

We first used the MTJ structure with a weak in-plane fixed layer and a perpendicular free layer. The MTJ resistance was measured under a varying in-plane magnetic field while bias voltages were varied as shown in Figure 3-7(a). The positive bias voltage is defined as the top electrode is at a positive electric potential.

Using a similar method as used in Ref. [142], the perpendicular anisotropy energy K_{eff} can be obtained using Equation 3-1. In this structure with a weak in-plane fixed layer and a perpendicular free layer, the fixed layer will align to the in-plane field direction when the magnetic field is swept. Hence, the normalized in-plane magnetization component M_x of the free layer can be expressed as $M_x = M_s cos\theta$, where θ is the angle between the fixed layer and the free layer, as indicated in Equation 1-3 can be written as the following

$$G = G_0(1 + p_F^2 M_x/M_s) \qquad \text{Equation 3-3}$$

Namely, the conductance of the MTJ G is a linear function of the M_x/M_s value. As we know at zero external field, $\theta = 90°$, $G(0) = G_0$; at the maximum in-plane external magnetic field, $\theta = 0°$, $G(H_x^{max}) = G_0(1 + p_F^2)$. Hence we can express the M_x/M_s value at a given magnetic field as a function of the conductance value $G(H_x, E)$ for each applied electric field case E as follows

$$M_x/M_s = [G(H_x, E) - G(0, E)]/[G(H_x^{max}, E) - G(0, E)] \qquad \text{Equation 3-4}$$

Here, $G(H_x, E)$ is the MTJ conductance at an in-plane magnetic field H_x and electric field E, while $G(0, E)$ $[G(H_x^{max}, E)]$ is the conductance at zero [maximum] in-plane field and electric field E, which acts as the reference value in the normalization process.

Then the interfacial magnetic anisotropy K_i can be obtained by a simplified version of Equation 3-2$K_{eff} = \frac{K_i}{t_{CoFeB}} - \frac{1}{2}\mu_0\left(N_z - N_{x,y}\right)M_S^2 + K_b$ Equation 3-2 where the bulk magnetic anisotropy term K_b and the in-plane demagnetization factors N_x, N_y are neglected: [84]

$$K_i = \left(\frac{1}{2}\mu_0 M_S^2 + K_{eff}\right)t_{CoFeB} \qquad \text{Equation 3-5}$$

By applying different bias voltages, VCMA coefficient ξ can be calculated by linear fitting K_i as a function of E. The R-H loops for a MTJ with 0.91nm CoFeB free layer under different E are shown in Figure 3-7(a). The lower MTJ resistance at higher bias voltages is due to the inherent bias dependence of the TMR effect.

Note that this method is only valid if the magnetization of the free layer is fully perpendicular under zero external magnetic field and the saturation magnetization stays constant for all CoFeB thicknesses and all applied electric fields. As the normalization process that calculates M_x/M_s is carried out for conductance values at each individual measured electric field, we refer to the M_x/M_s value as the individual-normalized MTJ conductance $G_{MTJ}^{Individual-Norm}$, as shown in Figure 3-7(b).

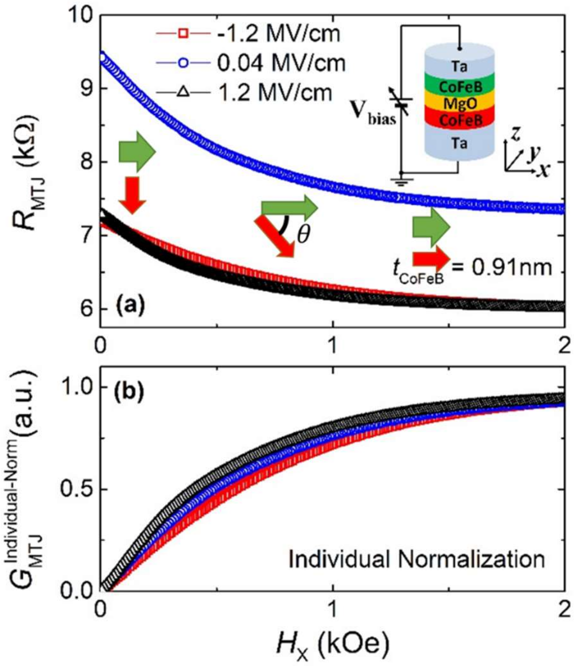

Figure 3-7 (a) Magnetic tunnel junction (MTJ) resistance R_{MTJ} versus external in-plane magnetic field H_X curves for different applied bias electric fields. The green and red arrows refer to the magnetization directions of the in-plane fixed layer and the free layer, respectively. The inset shows the schematic for the MTJ with varied bias voltage V_{bias} applied. (b) Individual-normalized MTJ conductance $G_{MTJ}^{Individual-N}$, which takes the maximum conductance range of each $G_{MTJ} - H_X$ loop as reference for normalization. The stack structure of MTJ is Ta(18)/$Co_{20}Fe_{60}B_{20}$(0.91)/MgO(2.5)/$Co_{20}Fe_{60}B_{20}$(2)/Ta(4)/Pt (2), (thickness in nm).

3.2.2 Anomalous Hall Measurement

The VCMA effect was also studied by measuring the Hall resistance R_{Hall} under a varying in-plane magnetic field H_X, with different applied gate voltages. The positive gate voltage is defined as the top gate electrode being at a positive electric potential similar as in the previous sections. The electric-field dependent *R*-*H* loops for a perpendicular Hall bar device with $t_{CoFeB} =$

0.8 nm is shown in Figure 3-8 (a). The switching behavior is due to the small misalignment of the device plane with respect to the in-plane magnetic field direction.

To quantitatively measure the VCMA coefficient ξ, we utilized a similar method as Ref.[138]. Note that here the CoFeB film is perpendicular easy axis, hence we have to apply an in-plane hard axis loop to characterize the perpendicular anisotropy. While in the previous chapter, an out-of-plane magnetic field is applied for the in-plane easy axis film. For anomalous Hall measurements, the Hall resistance can be expressed using the following equation [138]

$$R_{Hall} = \frac{R_0 \mu_0 H_Z}{t} + \frac{R_S M_Z}{t} \qquad \text{Equation 3-6}$$

where R_0 is the ordinary Hall coefficient, R_S is the anomalous Hall coefficient. Note that as the external in-plane field has a very small misalignment angle (determined to be less than 0.05 rad) with respect to the device plane, the ordinary Hall Effect contribution to the total Hall resistance is negligible. Hence, R_{Hall} can be safely assumed to be the same as the anomalous Hall resistance R_{AHE}, thus proportional to M_Z.

As shown in Figure 3-8(a), the perpendicular free layer will choose between pointing up and pointing down at zero external magnetic field. The switching is due to a very small perpendicular component of the external field due to misalignment. Hence, we know at zero external magnetic field, $M_z = \pm M_s$. Therefore, one can write down the M_z/M_s value at a given magnetic field as a function of the conductance value $R_{AHE}(H_x, E)$ for each applied electric field case E as follows

$$M_z/M_s = 2[R_{AHE}(E) - R_{min}^{AHE}(E)]/[R_{max}^{AHE}(E) - R_{min}^{AHE}(E)] - 1 \qquad \text{Equation 3-7}$$

Here, M_Z is the perpendicular component of the magnetization, and R_{max}^{AHE} (R_{min}^{AHE}) is the maximum (minimum) of R_{AHE} values.

Next, we can convert the M_z/M_s value into M_x/M_s value that is used in Equation 3-1$K_{eff} = \mu_0 \int_0^{M_s} \vec{H} d\vec{M} = \mu_0 M_s \int_0^{M_s} H_x d\left(\frac{M_x}{M_s}\right)$ Equation 3-1 to obtain the perpendicular magnetic anisotropy energy as follows

$$M_x/M_s = \sqrt{1 - (M_z/M_s)^2} \qquad \text{Equation 3-8}$$

Similar to the weak reference layer MTJ measurement described previously, the VCMA coefficient is then calculated by linearly fitting K_i as a function of E.

One caveat in the above-mentioned calculations is the choice of R_{max}^{AHE} and R_{min}^{AHE} values for each applied electric field case. Equation 3-7 uses R_{max}^{AHE} and R_{min}^{AHE} values for every individual electric field E. We will refer to the M_z/M_s value obtained in the way as the individual-normalized Hall resistance $R_{Hall}^{Individual-N}$, as shown in Figure 3-8(c). It is thus expected that the $R_{Hall}^{Individual-Nor}$ values will have a value of one at zero external field in all electric field cases. This means that the magnetization at $H_x = 0$ is constant under all electric fields, which is the same assumption used in the weak reference layer MTJ method.

However, as the Hall resistance is directly proportional to M_z, after careful inspection of Figure 3-8(a), the zero-field R or R_{max}^{AHE} changes with different electric fields. This clearly indicates that the free layer magnetization value changes when varied electric fields are applied. Because the PMA is very strong in this sample, we expect that the free layer magnetization is fully perpendicular under zero external field. Hence, another possible explanation is the interface magnetization modulation by electric field due to charge screening from the ferromagnetic Fe electrons, as described in Section 2.3.3.[110] As the change in magnetization value also goes into voltage-control of magnetic anisotropy, it is necessary to consider it in the calculation of the VCMA coefficient. If we take the maximum $\left(R_{max}^{AHE}-R_{min}^{AHE}\right)$ value across all electric field cases (E_0= -1.76 MV/cm in this experiment) in the normalization to obtain the M_Z/M_S value, which will be referred to as the overall normalization method hereafter, we can obtain the overall normalized Hall resistance $R_{Hall}^{Overall-Norm}$ as shown in Figure 3-8(b) using the following equation

$$M_Z/M_S = 2[R^{AHE}(E) - R_{min}^{AHE}(E_0)]/[R_{max}^{AHE}(E_0) - R_{mi}^{AHE}(E_0)] - 1 \quad \text{Equation 3-9}$$

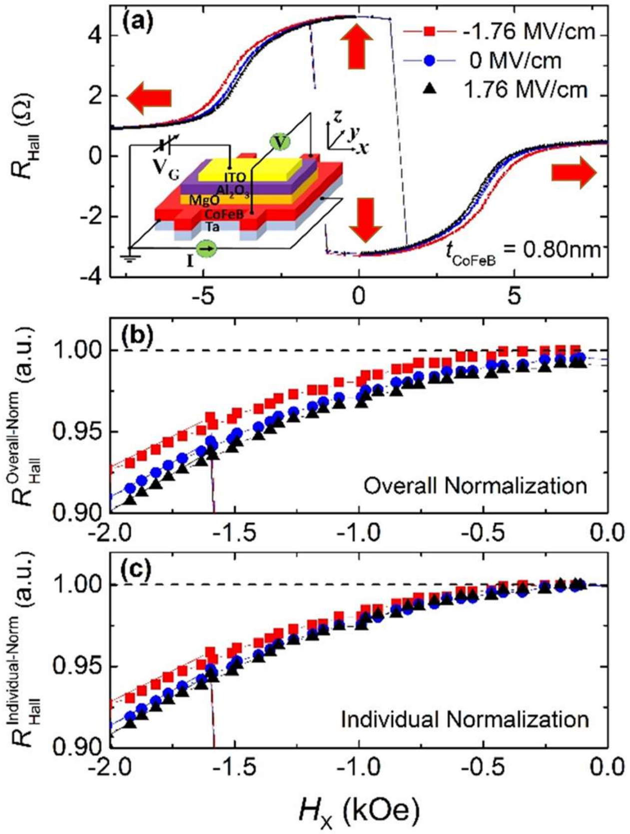

Figure 3-8 (a) Hall resistance R_{Hall} versus H_x curves for different applied electric fields. The inset shows the schematic for the Hall bar device with varied gate voltage V_G. The red arrows refer to the magnetization directions of the ferromagnetic layer. (b) Overall-normalized Hall resistance $R_{Hall}^{Overall-Norm}$, which takes the maximum conductance range of each $R_{MTJ}-H_x$ loop as reference for normalization. (c) Individual-normalized Hall resistance $R_{Hall}^{Individual-No}$, which takes the maximum resistance range of each $R_{Hall} - H_x$ loop at one specific electric field as reference for normalization. The stack structure is Ta(5)/$Co_{20}Fe_{60}B_{20}$(0.80)/MgO(2.5)/Al_2O_3 (38), (thickness in nm).

In this case, the M_Z/M_S value decreases under positive electric field, which is consistent with the decrease of calculated K_{eff} at positive electric field, both corresponding to a negative VCMA coefficient ξ.

3.2.3 VCMA Measurement Based on Different Normalization Methods

As discussed, we used the individual normalization method for the MTJ measurement, and both individual and overall normalization methods for the anomalous Hall measurement. The obtained magnitude of VCMA coefficient as a function of CoFeB thickness is shown in Figure 3-9 (a). Note that all measured VCMA coefficients are negative according to our definition that a higher electric potential at the top electrode (opposite to the substrate) corresponds to positive electric field.

It can be seen that the individual normalization method results in a similar strong VCMA dependence on the CoFeB thickness for both Hall and MTJ measurements, where the ξ values both peak at $t_{\text{CoFeB}} \sim$ 0.9nm. While the overall normalization method gives rise to a weak VCMA dependence on the CoFeB thickness when 0.8nm $< t_{\text{CoFeB}} <$ 0.95nm. The obtained weak VCMA dependence on the CoFeB thickness over the studied range is also consistent with previous work,[136] which indicates the interfacial origin of VCMA effect from the CoFeB/MgO interface.

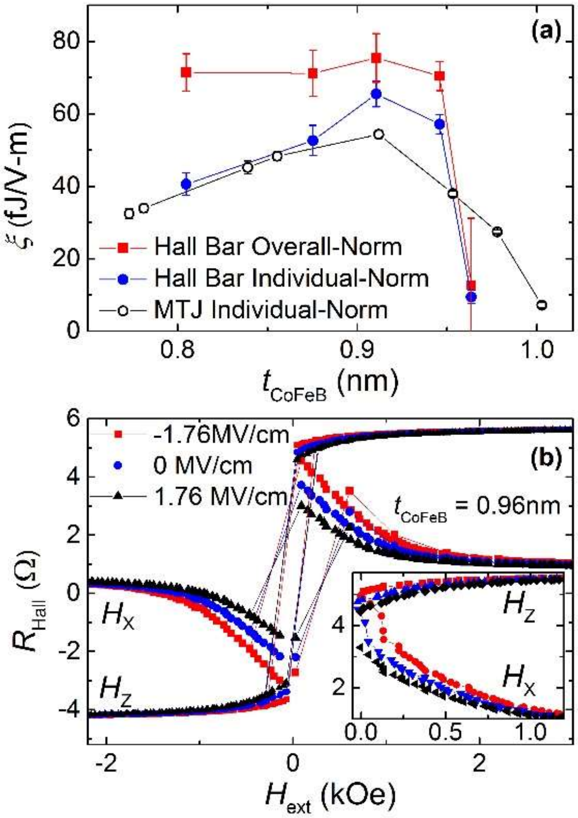

Figure 3-9 (a) VCMA coefficient ξ dependence on the CoFeB thickness t_{CoFeB}, obtained from the overall and individual normalized Hall bar R-H data, and individual normalized MTJ R-H data. (b) Hall resistance R_{Hall} versus external in-plane (out-of-plane) magnetic field $H_X(H_Z)$ curve for different applied electric fields. The inset shows the zoomed-in region with positive external magnetic field.

According to the decrease of $R_{\max}^{\text{AHE}}$ at positive electric fields, as indicated from Figure 3-8 (b), we can conclude that at zero external magnetic field ($H_x = 0$), the perpendicular component of magnetization (M_z) changes under different electric fields in the Hall bar device. Thus it is more accurate to use the overall normalization method to calculate the VCMA coefficient for the anomalous Hall measurement, which takes into account the change of magnetization under different electric field cases. On the other hand, the individual normalization method underestimates the VCMA coefficients and results in an artificially strong VCMA dependence on the CoFeB thickness due to an error in converting the anomalous Hall resistance into the magnetization values, or in other words assuming the zero-magnetic-field magnetization value does not change under electric fields.

If we compare both Hall and MTJ measurements using the individual normalization method, we can find a very similar trend of VCMA coefficients as a function of CoFeB thickness, with ξ peaking at $t_{\mathrm{CoFeB}}\sim$ 0.9nm. This suggests that similar to the Hall measurement where zero-magnetic-field magnetization changes under electric field, the same thing happens in the MTJ measurement too. Meanwhile, as both TMR and resistance of a MTJ at $H_x = 0$ depend on the bias voltage,[126, 143] it is very difficult to determine the actual M_z values at $H_x = 0$ under different electric fields using the MTJ measurement method alone. Hence, one might wonder if there is any way to remedy this and find a more accurate way to measure VCMA using the MTJ method. As mentioned before, the most accurate configuration to extract the VCMA coefficient from a MTJ is one where the fixed layer does not change its magnetization orientation when a hard-axis loop for the free layer is swept, or the strong fixed layer MTJ measurement.

Next, to explain the sharp decrease of VCMA with $t_{\mathrm{CoFeB}} >$ 0.95nm, we carried out both in-plane and out-of-plane *R*-*H* loops using the anomalous Hall measurement. As can be seen in the in-plane loops in Figure 3-9 (b), at $H_{\mathrm{X}} = 0$, the Hall resistance decreases significantly from negative to positive electric field (more than 30%). In contrast, the Hall resistance change under electric field at $t_{\mathrm{CoFeB}} < 0.95$ nm range is very small (less than 2%), as shown in Figure 3-8 (a) and (b). The out-of-plane loops further validates that the magnetization is not fully perpendicular at $H_{\mathrm{Z}} = 0$, and R^{AHE} decreases significantly at positive electric field (more than 10%). More importantly, the Hall resistance at zero external magnetic field for a single electric field, but with different external magnetic field directions (H_{X} or $H_{\mathrm{Z}} = 0$), do not coincide with each other. This means that the free layer breaks into multi-domain configurations, which will contribute to the reduction of the K_{eff} in addition to contribution from the external magnetic field. Thus, the VCMA coefficient calculated will be significantly smaller than the real VCMA value. This can also explain the decrease of VCMA obtained by the MTJ measurement at $t_{\mathrm{CoFeB}} > 0.95$ nm. Because the free layer CoFeB in these two structures should have similar transition thicknesses from perpendicular easy-axis to in-plane easy-axis.

In order to obtain accurate VCMA coefficients, the overall normalization method should be used in anomalous Hall measurements where the change of the perpendicular component of magnetization at zero external magnetic field under different electric fields is considered. On the contrary, the MTJ measurement using a weak in-plane fixed layer that switches at low in-plane field will result in artificially lowered VCMA coefficients. On top of this, for both experiments under zero external magnetic field, the magnetization needs to be fully perpendicular. Otherwise, the multi-domain behavior of the magnetization will result in a large error for VCMA calculation using a single-domain model.

In this dissertation, due to a lack of strong pinning layers in our sputtered film stacks, we used the weak in-plane fixed layer method for a preliminary measurement of the VCMA values. It should be always noted that the actual VCMA coefficients might be higher than what is measured using the weak in-plane fixed layer method.

Chapter 4 Tunnel Barrier Engineering with High Dielectric Constant

4.1 Introduction

As shown in Section 2.4, for MeRAM to replace eFlash, eDRAM, and DRAM applications at scaled CMOS below 10 nm, VCMA coefficients larger than 200 fJ/V-m may be needed.[23, 144] However, the traditional Ta/CoFeB/MgO system offers limited VCMA in the range of 10-60 fJ/V-m.[117, 136, 138-140, 142, 145]

To achieve a larger VCMA effect, multiple approaches have been explored, such as using different seed and cap layers adjacent to the ferromagnetic layer.[142, 146-149] *Ab initio* electronic structure calculations have revealed that epitaxial strain has a dramatic effect on increasing the VCMA.[116] Another promising method is by utilizing different dielectrics. As the VCMA effect originates from the charge accumulated at the CoFeB/oxide interface when voltage is applied,[127] it has been demonstrated theoretically that using a single oxide or multiple layers of oxides with higher dielectric constant(s) (ϵ) can induce a higher VCMA coefficient, thus a reduction of voltage for magnetization switching[110]. This is also discussed in Section 2.3.4. In past experimental works, enhanced VCMA effect was measured in CoFeB/oxide structures using MgO/Al_2O_3 and MgO/HfO_2/Al_2O_3 as the gate oxide,[117] but lacked an electrical readout because full MTJ was not fabricated. There has been intensive research on MTJs using barrier materials other than MgO. However, MTJs using $SrTiO_3$ with CoFe electrodes had a rather low TMR around 10%,[150] while multiferroic tunnel junctions with ferroelectric barriers such as $PbZr_{0.2}Ti_{0.8}O_3$ and $BaTiO_3$ with Co/Fe and $La_{0.7}Sr_{0.3}MnO_3$ electrodes only demonstrated a reasonable TMR below room temperature.[151, 152] Therefore, to achieve better writing efficiency with reliable readout for voltage-controlled MRAM, it is critical to have a sizeable room temperature TMR in addition to VCMA enhancement after integration of high-ϵ oxide(s) into the stack.

In this chapter, we demonstrated a novel method to integrate an ultra-thin layer of high-ϵ lead zirconate titanate (PZT or $Pb(Zr_xTi_{1-x})O_3$) thin film into the MgO tunnel barrier in order to enhance the VCMA effect while maintaining a sizeable TMR. A combination of sputtering and atomic layer deposition (ALD) techniques was used to grow MTJ stacks with an MgO/PZT/MgO tunnel barrier. Based on measurements on an ensemble of MTJ devices with the MgO/PZT/MgO barrier, the VCMA coefficients were improved by about 40% and room-temperature TMR values were only slightly lower than in those of MgO barrier MTJs.

PZT has been commonly used in Ferroelectric Random Access Memory (FeRAM) devices[153-155] and has been used in multiferroic tunnel junctions[151]. In this work, PZT thin film was integrated into the tunnel barrier because it has one of the largest dielectric constants (i.e. 300-1300 for 1-3 μm PZT thin films[156, 157]). Due to the fact that the PZT was interfaced with MgO on both sides, the interfacial dead layer that is intrinsic to electrode/dielectric boundary is expected to be negligible in our film.[158] PZT deposition was performed via ALD,[159, 160] which has previously been shown to provide conformal atomically smooth ultra-thin films with precise control over composition and thickness.[161]

4.2 Fabrication Methods and Materials Characterization

MTJs with a pure MgO tunnel barrier were used as the reference sample and compared to the MTJs with the MgO/PZT/MgO tunnel barrier (hereafter referred to as MgO MTJ and PZT MTJ, respectively). Sample structures are schematically illustrated in Figure 4-1, with the following structures: Ta(18nm)/ $Co_{20}Fe_{60}B_{20}$(0.9nm)/ MgO(2.5nm)/ $Co_{20}Fe_{60}B_{20}$(2.0nm)/ Ta(4nm)/ Pt(2nm) for the MgO MTJ, and Ta(18nm)/ $Co_{20}Fe_{60}B_{20}$(0.9nm)/ MgO(1.0nm)/ PZT(1.5nm)/ MgO(1.0nm)/ $Co_{20}Fe_{60}B_{20}$(2.0nm)/ Ta(4nm)/ Pt(2nm) for the PZT MTJ.

The stacks were deposited on thermally oxidized Si substrates using an AJA magnetron sputtering system and thermal ALD. All metallic layers were DC sputtered. The $Co_{20}Fe_{60}B_{20}$ bottom free layer has a thickness of 0.9 nm and the top fixed layer has a thickness of 2.0 nm; they were out-of-plane and in-plane magnetically anisotropic, respectively.[162] For the MgO MTJ, a 2.5 nm thick MgO tunnel barrier was grown by RF sputtering, while for the PZT MTJ, a 1.0 nm thick MgO layer was first sputtered, then a 1.5 nm thick PZT film was deposited via ALD at a substrate temperature of 250°C, and finally a 1.0 nm thick MgO was sputtered to form the MgO/PZT/MgO tunnel barrier. The synthesis of PZT thin film has been outlined in previous papers.[159, 160] The PZT MTJ film stack was annealed at 200°C under vacuum both before the PZT deposition and after depositing the whole film stack. The reason why an additional annealing step before the PZT deposition is needed is due to that this induces the crystallization of the bottom CoFeB/MgO bilayer into stable cubic crystal structure, and the ensuing PZT growth will not interfere much with the already crystallized CoFeB/MgO bilayer. As with the 200°C annealing temperature, this temperature is chosen because it yields the best MTJ perpendicular magnetic anisotropy among the four annealing temperatures tested, i.e. 200°C, 250°C, 300°C, and 350°C. Since the PZT MTJ film stack was also *in-situ* annealed during the ALD process under 250°C, we annealed the MgO MTJs at 250°C for a fair comparison. MTJ devices with elliptical diameters of 4×16 μm and 4×12 μm were subsequently fabricated using standard photolithography and dry etching techniques.

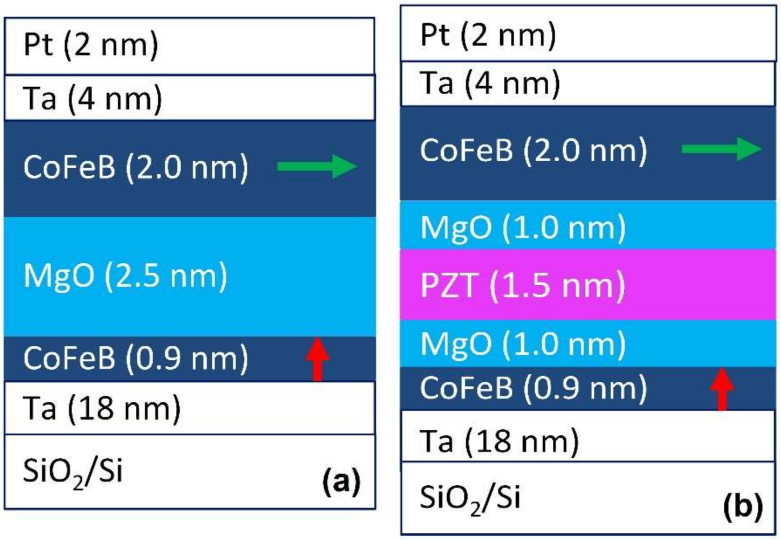

Figure 4-1 Schematics of (a) MgO MTJ, and (b) PZT MTJ with the MgO/PZT/MgO tunnel barrier measured in this work. Devices measured had elliptical dimensions of 4x16 µm and 4x12 µm. Arrows show the magnetic anisotropic directions of the CoFeB top fixed layer (in-plane) and the bottom free layer (perpendicular).

First, material properties of the MTJ stacks were characterized using Kratos AXIS X-ray photoelectron spectroscopy (XPS) and an FEI Titan scanning transmission electron microscope (STEM). XPS confirmed the composition ratio Zr:Ti = 52:48 of the PZT thin film deposited on the bottom layers of a film stack, as shown in Figure 2a. Note that it has been shown that PZT exhibits enhanced properties (e.g. dielectric constant) at the morphotropic phase boundary composition of Zr:Ti = 52:48.[163] The XPS survey scan also showed the Mg *KLL*, Co *2p*, Fe *2p*, and Ta *4d* elemental peaks. Note that the B *1s* peak was not observed because the estimated XPS penetration depth is limited to 10 nm and the boron diffused into the Ta layer due to the annealing process.[164, 165]

Cross-sectional TEM was performed on the fabricated MgO MTJ and PZT MTJ devices, as shown in Figure 4-2 (b) and (c), respectively, in which the arrows indicate the general location of layer interfaces, spaced per Figure 4-1. Nano-diffraction patterns were collected for both cross-sections, as shown in the insets of Figure 4-2 (b) and (c). A selected-area aperture was used for the MgO MTJ, but in order to maximize diffracted intensity from the ~3 nm thick MgO/PZT/MgO layers-of-interest in the PZT MTJ, we employed a highly condensed probe, elongated along the in-plane direction of the film, which provided informative results due to the FEI Titan's parallel beam nearly all the way to the crossover point. The inset diffraction patterns clearly showed that the MgO had crystallized; however, indexing of the remaining spots to either CoFeB or PZT was not possible due to resolution limitations.

Next, unpatterned MgO and PZT MTJ stacks were characterized for their magnetic properties using superconducting quantum interference device (SQUID) magnetometry. The saturation magnetizations (M_s) were measured to be 1017 ± 22 emu/cm^3 and 932 ± 41 emu/cm^3 for MgO and PZT MTJ stacks, respectively, indicating that the ALD PZT deposition had not significantly affected the magnetic properties of the CoFeB layers.

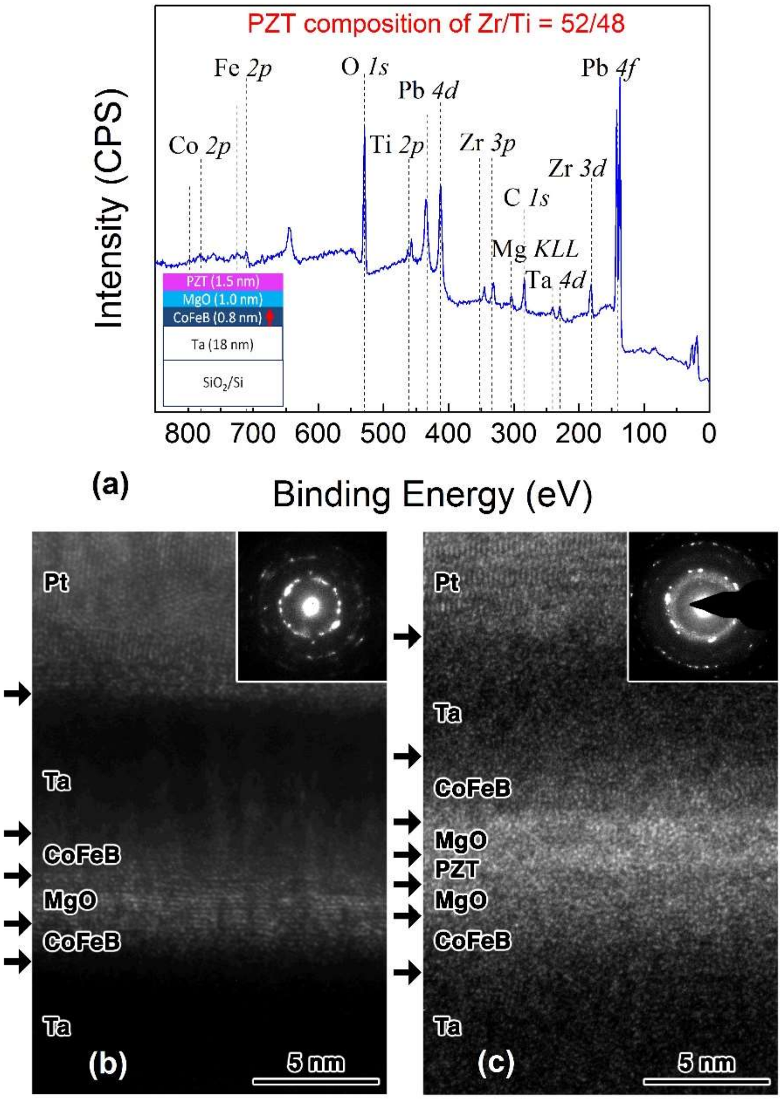

Figure 4-2 (a) XPS confirms PZT composition of Zr:Ti = 52:48 of a 1.5 nm thick PZT film deposited on Ta (18nm)/CoFeB (0.8nm)/MgO (1.0nm) followed by annealing at 200°C for 30 minutes. Schematic of stack is shown in the inset, with the red arrow denoting the bottom free CoFeB layer to have a perpendicular magnetically anisotropy. TEM of (b) MgO MTJ annealed at 250°C for 30 min and (c) PZT MTJ annealed at 200°C for 30 min. Both images are scaled identically, with the substrate-side in the bottom of each image. Nano-diffraction patterns are shown as inset in both (b) and (c), which have the same scale.

4.3 Electrical Characterization and Results

The MTJs were then measured electrically to investigate the VCMA effect via the TMR readout at room temperature.[142, 166] The resistance was measured as the in-plane magnetic field was swept while voltages were applied between -300 to +300 mV, as shown in Figure 4-3 (a). At zero magnetic field, the magnetic moment of the bottom CoFeB free layer was perpendicular and that of the top fixed CoFeB layer was in-plane, while at the maximum in-plane magnetic field, the two CoFeB layers were both in-plane magnetized. Hence, the resistance decreased as the magnetic field was increased. The resistance-area (RA) products of the PZT and MgO MTJ in Figure 4-3 (a) were 98 $k\Omega \cdot \mu\mathrm{m}^2$ and 14 $k\Omega \cdot \mu\mathrm{m}^2$, respectively, which are quite normal for voltage-controlled MRAM.[23, 100]

Following the weak fixed layer MTJ measurement discussed in Section 3.2.1, we can calculate the VCMA of these MTJs using Equation 1-3, the measured conductance G of the MTJ was related to the relative angle between the two CoFeB layers, where G_S was the mean surface conductance, θ was the angle between two CoFeB layers, and P_F was the effective spin polarization.[83] As the top 2.0 nm thick CoFeB layer was fixed at an in-plane direction, the in-plane magnetization component M_x of the bottom free layer CoFeB can be obtained by Equation 3-4, where $G(H_x)$, $G(H_x^{max})$, and $G(0)$, are respectively the MTJ conductances at in-plane magnetic field H, at the maximum in-plane magnetic field measured, and at zero external field. Note that here H_x^{max} was determined by saturation of the free layer magnetization to the in-plane orientation, and the PZT MTJ demonstrated a higher saturation field than the MgO MTJ. The perpendicular magnetic anisotropy energy K_{eff} can then be calculated by conducting the following integration for the free layer from the perpendicular easy axis (at zero external field), to the in-plane hard axis (at H_x^{max}) using Equation 3-1.

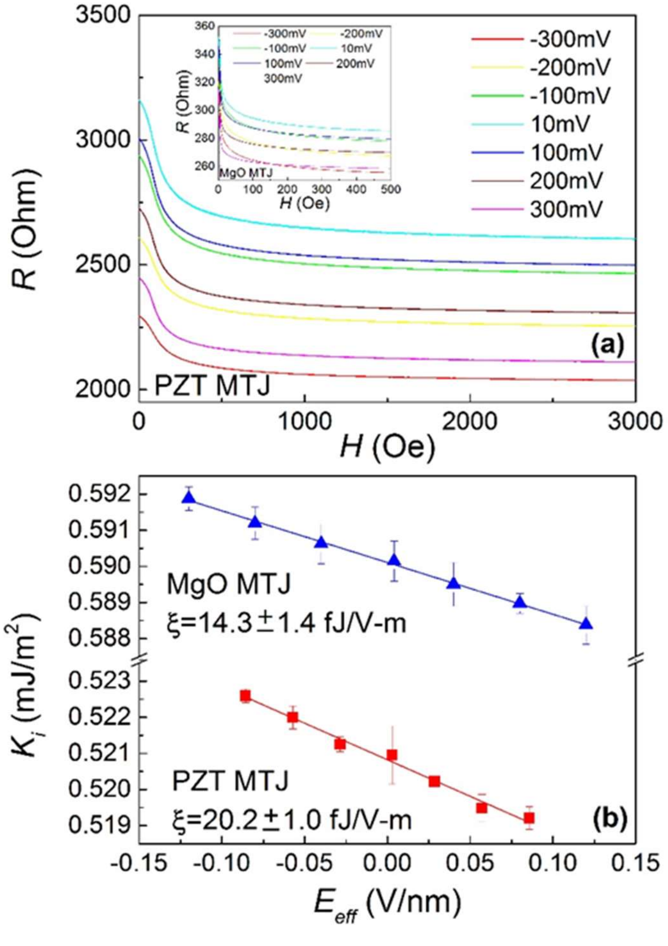

Figure 4-3 (a) Resistance vs. in-plane magnetic field of varying applied voltages from -300 to 300 mV for the PZT MTJ device, inset showing that of the reference MgO MTJ device and (b) interfacial perpendicular magnetic anisotropy (K_i) vs. applied electric field (E_{eff}) for an MgO and PZT MTJ device.

Using Equation 3-2 we can obtain the value of interfacial PMA (K_i),[84] where t_{CoFeB} is the thickness of the CoFeB free layer. Finally, the VCMA coefficient ξ was determined by $\xi = \Delta K_i/\Delta E_{eff}$, where the effective electric field E_{eff} was calculated by dividing the applied voltage V

with the total thickness *d* of the tunnel barrier. All measurements were performed at room temperature.

The VCMA coefficients ξ, (i.e. the slope of K_i versus E_{eff} plot) are shown in Figure 4-3(b) for two representative MgO and PZT MTJ devices. A total of six devices were measured for each MTJ stack. The average VCMA coefficients were $\xi_{\text{average}} = 14.3 \pm 2.7$ fJ/V-m for MgO MTJs, and $\xi_{\text{average}} = 19.8 \pm 1.3$ fJ/V-m for PZT MTJs, as shown in Figure 4-4(a). Therefore, by incorporating the PZT film into the MgO barrier, the VCMA effect was shown to be enhanced by about 40%.

4.4 Analysis of Dielectric Constants Enhancements

From the physics point of view, this enhanced VCMA effect could be understood as follows. As indicated from *ab initio* calculations, the K_i stemmed from the hybridization of Fe/Co *3d* orbitals and O *2p* orbitals at the CoFeB/MgO interface.[107, 108] The application of a positive electric field (i.e. top electrode of the MTJ at a higher electric potential) across the MgO barrier will induce accumulation of electrons at the bottom CoFeB/MgO interface, which in turn will affect the hybridization of Fe/Co and O orbitals, thus decreasing the value of K_i, which is consistent with the data shown in Figure 4-3(b). [110, 127] [110, 127] [106, 124] Hence, if the interface charge density σ_q increases for the same applied electric field E_{eff}, a larger VCMA coefficient ($\xi = \Delta K_i / \Delta E_{eff}$) can effectively be achieved. The interface charge density σ_q could be expressed as

$$\sigma_q = \epsilon_0 \epsilon_{eff} V/d = \epsilon_0 \epsilon_{eff} E_{eff} \qquad \text{Equation 4-1}$$

where ϵ_0 was the permittivity of free space, and ϵ_{eff} was the effective dielectric constant of the tunnel barrier.[110, 117] Thereby, for the same tunnel barrier thickness and applied voltage, the increase of the effective dielectric constant ϵ_{eff} by incorporating PZT in the tunnel barrier will give rise to a larger interface charge density change at the CoFeB/MgO interface, thus resulting in a larger overall VCMA. This is also explained in a more detailed manner in Section 2.3.4.

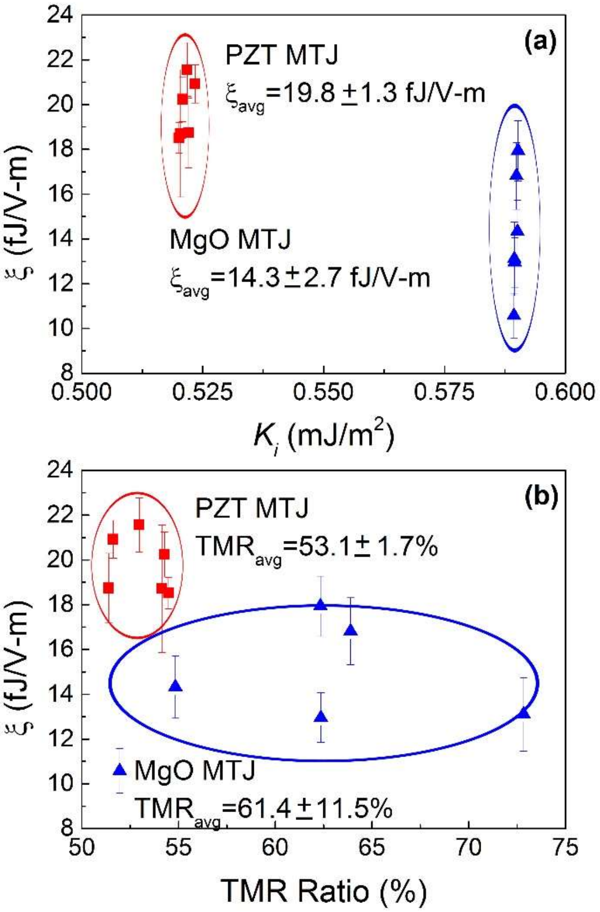

Figure 4-4 For all measured devices of MgO MTJ and PZT MTJ: VCMA coefficient ξ, vs. (a) K_i and (b) TMR ratio. The error bars are included for SQUID and electrical measurements, and subsequent VCMA calculations. The circles are drawn to illustrate the distribution of VCMA coefficients for the MgO and PZT MTJs.

From the obtained VCMA ratio between the PZT MTJ and the MgO MTJ, the dielectric constant for the PZT ultra-thin film could also be calculated using a serial capacitor assumption. First, the areal capacitance of the total PZT-MgO hybrid barrier is

$$C_{total} = C_{MgO} + C_{PZT} = \frac{\epsilon_{MgO}}{d_{MgO}} + \frac{\epsilon_{PZT}}{d_{PZT}} \qquad \text{Equation 4-2}$$

Hence for the PZT MTJ, the effective dielectric constant was

$$\epsilon_{PZT-MTJ} = C_{total}(d_{MgO} + d_{PZT}) = \frac{d_{MgO}+d_{PZT}}{\frac{d_{MgO}}{\epsilon_{MgO}}+\frac{d_{PZT}}{\epsilon_{PZT}}} \qquad \text{Equation 4-3}$$

While for the MgO MTJ, the dielectric constant was assumed to be $\epsilon_{MgO-MTJ} = \epsilon_{MgO} = 10$.[167] As the change of interfacial PMA is proportional to the change of interface charge density, i.e. $\Delta K_i \propto \Delta\sigma_q$, we can deduce $\xi \propto \epsilon_{eff}$.[117] Thus, based on the VCMA coefficients obtained for PZT and MgO MTJ, the dielectric constant of the PZT ultra-thin film was estimated to be 28.4, a plausible value taking into account the 1.5 nm PZT thickness, as well as existing literature values for an ultra-thin ALD PZT film.[158, 160]

Admittedly, there might be other factors driving the observed increase of VCMA coefficient besides the relatively higher dielectric constant of PZT, including the hybridization of PZT with CoFeB atoms, and ferroelectricity or piezoelectricity of PZT. However, as the PZT does not interface with the CoFeB layers, it is safe to exclude any orbitals contribution of PZT hybridizing with CoFeB. In addition, we have swept the K_i vs E_{eff} curve as shown in Figure 4-3(b) back-and-forth multiple times and do not see any hysteresis in the curves, which indicates that in the PZT MTJs, PZT does not produce any remnant ferroelectric polarizations contributing to the change of PMA of the CoFeB layers. Therefore, no piezoelectricity can emerge without any ferroelectric polarizations from the PZT.

The VCMA coefficients were also plotted against K_i (Figure 4-4a) and TMR ratio (Figure 4-4b) for all measured MgO and PZT MTJ devices. The PZT MTJs were observed to have a larger

VCMA effect and a slightly smaller TMR ratio compared to the MgO MTJs. The $\text{VCMA}_{\text{average}}$ was 14.3 ± 2.7 fJ/V-m for MgO MTJs, and 19.8 ± 1.3 fJ/V-m for PZT MTJs. The $\text{TMR}_{\text{average}}$ was $61.4 \pm 11.5\%$ for MgO MTJs, and $53.1 \pm 1.7\%$ for PZT MTJs. Note that the TMR ratio here was defined by $TMR = (R_{ap} - R_p)/R_p$, where the anti-parallel resistance R_{ap} was calculated according to equation [83], which can also be derived from Equation 1-3:

$$1/R_{ap} = 2/R_{ort} - 1/R_p \qquad \text{Equation 4-4}$$

where the parallel resistance R_p was the resistance at the maximum magnetic field or $1/G(H_{max})$, and the orthogonal CoFeB configuration resistance R_{ort} was the resistance at zero external magnetic field or $1/G(0)$.

Compared with other works on Ta/CoFeB/MgO in the literature with the VCMA coefficients ranging from 10-60 fJ/V-m,[117, 136, 138-140, 142, 145] the VCMA coefficient values in our PZT and MgO MTJs are at the lower bound, but the VCMA effect can be improved by optimizing a number of parameters including annealing conditions,[149] surface roughness,[168] and intrinsic strain[116] of the layers. Nevertheless, a 40% enhancement in the VCMA coefficient was achieved by using the MgO/PZT/MgO tunnel barrier while a relatively high TMR was still preserved.

In conclusion, by combining atomic layer deposition and magnetron sputtering techniques, an ultrathin PZT layer was successfully incorporated into the MgO tunnel barrier of a magnetic tunnel junction for the first time. The resulting magnetic tunnel junctions using a high-ϵ tunnel barrier were shown to have both large tunneling magnetoresistance (>50%) and an enhanced

VCMA effect (by 40%) at room temperature. This novel high-ϵ tunnel barrier MTJ is a potential candidate for future voltage-controlled, ultralow-power, high-density MRAM devices.

Chapter 5 Interfacial Engineering by Atomic Level Insertions

5.1 Motivation

In the past decade, CoFeB/MgO/CoFeB-based magnetic tunnel junctions (MTJs) have been at the core of spintronic memory research and development. For practical memory applications, large tunneling magnetoresistance (TMR), perpendicular magnetic anisotropy (PMA), and switching efficiency are desirable. The physics behind the TMR and PMA phenomena has been widely studied in the context of the CoFeB/MgO interface.[82, 169-171]

Recently, the electric-field-induced writing of perpendicular CoFeB/MgO/CoFeB MTJ structures has shown great promise for high density, high-speed, and energy efficient memory.[100, 101] Previous work has shown sub-nanosecond writing of perpendicular MTJs with voltages of approximately 2 V for VCMA coefficients near 30 fJ/V-m.[22, 172] In order to reduce the write voltage below 0.6 V to be compatible with advanced CMOS transistors, a higher VCMA coefficient of at least 100 fJ/V-m will be required.

The VCMA effect, i.e., the modification of the PMA by an external electric field, is also closely linked with the CoFeB/MgO interface. *Ab initio* calculations[108, 110] suggest that the application of an electric field, corresponding to charge accumulation/depletion at the CoFeB/MgO interface, modifies the occupation of the hybridized Fe/Co and O orbitals responsible for generating the PMA.[107, 108] More recent *ab initio* calculations revealed that epitaxial strain at the CoFe/MgO interface can lead to non-linear electric-field dependences of PMA.[115, 116] Experimentally, the VCMA effect is found to be independent of the CoFeB thickness,[136, 149, 173] which suggests that the VCMA effect indeed originates from the CoFeB/MgO interface. While previous works have explored various seed and capping layers,[146, 149] as well as insulating materials[117, 174] in the MTJ structure in order to enlarge the VCMA coefficient, direct modification of the ferromagnet/insulator interface may provide a deeper understanding of the underlying physics of the VCMA effect, as well as guidance to further enhance the VCMA coefficient.

Ab initio calculations in the past have investigated the impact of different oxidation levels at the Fe/MgO interface on the VCMA effect: over-oxidation, under-oxidation, and the ideal Fe/MgO interface.[113] The impact on the VCMA coefficient of various heavy metal insertion layers (Pd, Pt, and Au) at the Fe/MgO interface was also studied theoretically.[175, 176] Experimentally, there have been few VCMA studies using insertion layers at the ferromagnet/insulator interface. Hf insertion at the CoFeB/MgO interface[177] shows limited VCMA effect around 4 fJ/V-m. VCMA coefficient of around 86 fJ/V-m has been demonstrated using Pd insertion at the Co/MgO interface,[178] but it is not based on the typical CoFeB/MgO structure for magnetic memory. Previous works have demonstrated that a thin Mg interlayer can improve the MgO (001) texture and thus the TMR ratio, as well as the thermal stress stability of PMA.[179-181] However, the impact of Mg insertion on the VCMA effect is still missing. Hence, there is a need for experimental work studying the role of Mg and various heavy metal materials inserted at the standard CoFeB/MgO interface for increasing the VCMA effect.

In this chapter, the effect of Ta, Pt, and Mg insertion layers at the CoFeB/MgO interface is investigated. The VCMA coefficient, interfacial PMA, and saturation magnetization are analyzed for different insertion layer materials of various thicknesses. A maximum VCMA coefficient of 100 fJ/V-m is demonstrated for an Mg insertion layer thickness of 0.1-0.3 nm. In order to understand the observed trend and origin of the enhancement of the VCMA effect, synchrotron-based grazing-incidence wide-angle X-ray scattering (GIWAXS) was used to investigate the crystallinity and texture of the films as a function of the various insertion material thicknesses.

5.2 Fabrication Methods and Measurement Results

Three different materials were inserted into the CoFeB/MgO interface using magnetron sputtering. The stack structure consists of Ta(5)/CoFeB(1)/X(t)/MgO(2.5)/Al_2O_3(5) deposited on a thermally oxidized Si substrate, where the numbers in parentheses represent the layer thicknesses in nm. The insertion layer X (Ta, Pt, or Mg) has a continuously changing (wedged) thickness in the range of 0.1-0.3 nm for Ta and Pt and 0.1-2.4 nm for Mg. All metallic layers were grown using DC sputtering, while the insulating layers were grown using RF sputtering. The stacks were annealed at 325°C for 30 min *in situ* in the sputtering system with a base pressure lower than 10^{-7} Torr. Subsequently, the films were patterned into Hall bar devices by photolithography and dry etching. A 33 nm Al_2O_3 gate oxide was deposited using atomic layer deposition (ALD), and Cr/Au layers were fabricated as a top gate electrode. The dielectric constants of MgO and Al_2O_3 were assumed to be 10 and 7, respectively.[167, 182] The dimensions of the Hall bars were 20 μm x 130 μm. All electrical measurements were done at room temperature. The saturation magnetization values were obtained by measuring M-H loops via a superconducting quantum interference device (SQUID) magnetometer, and dividing the total magnetic moment by the total volume of the ferromagnetic layer in the sample of interest.

Figure 5-1 (a) shows the measured anomalous Hall resistance (R_{Hall}) as a function of the out-of-plane magnetic field (H_Z) for CoFeB/Ta/MgO-based films. For Ta insertion layers thinner than ~0.2 nm, the CoFeB layer has an out-of-plane easy axis; as the Ta insertion layer thickness increases beyond 0.2 nm, the magnetic easy axis of the CoFeB layer undergoes a gradual transition to in-plane. This trend also applies to the case of Pt and Mg insertion layers if the hard axis anisotropy fields (H_K) are plotted, as shown in Figure 5-1 (b). However, the insertion layer thickness at which this transition occurs is very thin in the cases of Ta and Pt (both around 0.2 nm) and much thicker in the case of Mg (1.5 nm). Possible reasons for this difference in transition thickness will be discussed later. Note that, since PMA is strongly desired in these devices, investigation into insertion layers thicker than the transition thicknesses is not the primary goal of this work. In addition, the resolution of Ta thickness down to 0.01nm does not mean the actual thickness of Ta as one monolayer of Ta is 0.33nm. Instead, the thickness numbers here represent the averaged thickness of a dusting layer of Ta with discontinuous and island-like morphology.

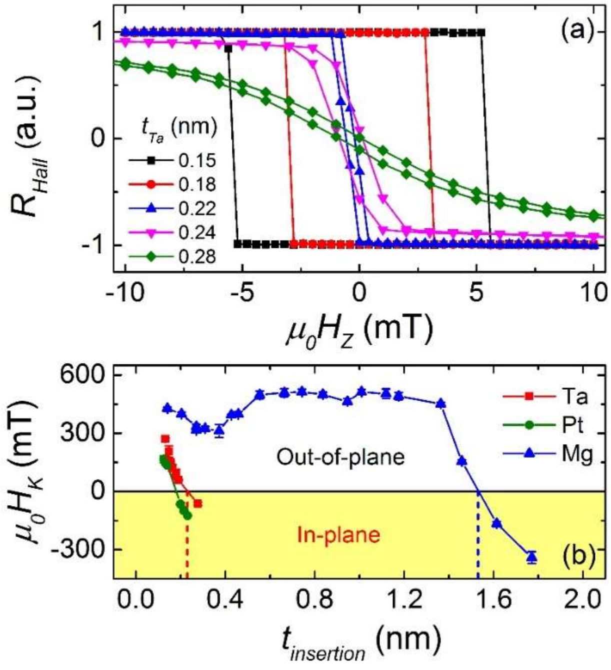

Figure 5-1 (a) Anomalous Hall resistance (R_{Hall}) as a function of applied perpendicular magnetic field ($\mu_0 H_Z$) for different Ta insertion thicknesses (t_{Ta}). (b) Hard axis anisotropy field ($\mu_0 H_K$) as a function of insertion layer thickness ($t_{insertion}$) for Ta, Pt, and Mg. The region where $\mu_0H_K > 0$ (< 0) refers to that the CoFeB is out-of-plane (in-plane) easy axis.

To extract the VCMA coefficient, anomalous Hall effect (AHE) is used to characterize the perpendicular anisotropy energy volume density (E_{perp}) under different gate voltages by sweeping the magnetic field along the hard axis of the CoFeB.[138, 149, 173] For perpendicular CoFeB, using the anomalous Hall measurement technique mentioned in Section 3.2.2, the perpendicular magnetic anisotropy energy can first be obtained using Equation 3-1, where the normalized in-plane magnetization, M_X/M_S, can be obtained through the normalized R_{Hall} values. The electric-field-dependent interfacial PMA values, K_i, can be obtained via Equation 3-5. The slope of K_i versus electric field equals the VCMA coefficient, ξ.

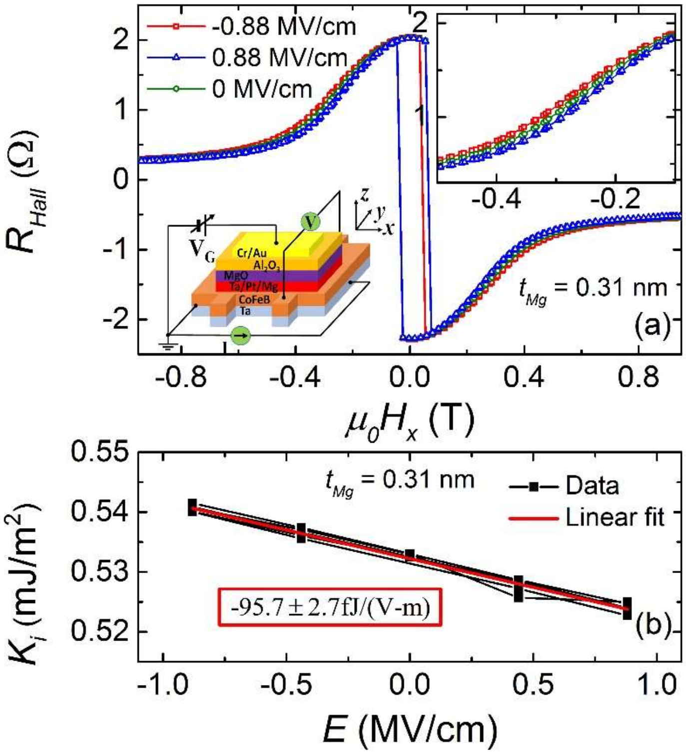

Figure 5-2 (a) Hall resistance (R_{Hall}) as a function of in-plane magnetic field (μ_0H_X) under different applied gate electric fields (E). Top right inset: Zoomed-in view of R_{Hall} - μ_0H_X data with -0.5 T < μ_0H_X <

-0.1 T. Bottom left inset: Schematic for the Hall bar device under different applied gate voltages (V_G). A positive gate voltage is defined as the top gate electrode being at a positive electric potential, as shown in the bottom left inset. (b) Interfacial perpendicular magnetic anisotropy (K_i) as a function E. The K_i values were obtained by applying multiple back-and-forth gate voltage sweeps: 5V to -5V and back to 5V, for three times. The linear fit of the K_i values versus E yields a VCMA coefficient $\xi = -95.7 \pm 2.7$ fJ/(V-m). Data from (a) and (b) are obtained from a device with a Mg insertion layer thickness of 0.31 nm.

One result of using this method for an Mg insertion layer sample ($t_{\mathrm{Mg}} = 0.31$ nm) is shown in Figure 5-2 (a). First, the anomalous Hall resistance dependence on the in-plane magnetic field is shown under various applied gate voltages. The inset in the upper right corner clearly shows the difference between the hard axis R_{Hall} - $\mu_0 H_X$ loops under three different gate voltages. The calculated values of K_i versus electric field are shown in Figure 5-2 (b). The linear fit gives a negative VCMA coefficient of -95.7 ± 2.7 fJ/V-m. Note that the K_i values were obtained by applying multiple back-and-forth gate voltage sweeps: 5V to -5V and back to 5V, swept three times. The small linear fitting error indicates that there is minimal mobile ionic charging in our material stacks.[127, 183]

Following the above method, the VCMA coefficient and interfacial PMA K_i were measured for various insertion materials with various thicknesses. The results are shown in Figure 5-3 (a) and (b). Note that all VCMA values are absolute values. For Ta and Pt insertions, the VCMA coefficients have maximum values in the range of 40-50 fJ/V-m. However, for the Mg insertion sample, the VCMA values show a large variation from almost zero to maximum values of around 100 fJ/V-m. Here, we will break down the range of Mg insertion thicknesses into four different regions: Region I, 0.1 nm < t_{Mg} < 0.3 nm; Region II, 0.5 nm < t_{Mg} < 1.1 nm; Region III, 1.1 nm < t_{Mg} < 1.3 nm; and Region IV, t_{Mg} > 1.3 nm. Compared with published VCMA coefficients of around 30 fJ/V-m based on Ta/CoFeB/MgO structures,[138, 139, 142] the

VCMA coefficients in Region I are improved by more than a factor of 3. The VCMA coefficients first decrease and then reach a plateau when from Region I to Region II and III. With further increase of the Mg thickness to Region IV, the VCMA coefficient drastically approaches zero. Interfacial PMA (K_i) values decrease for Ta and Pt at thicker insertion thicknesses. For Mg, the K_i dependence on Mg insertion layer thickness is non-monotonic. In Region III, where the VCMA plateaus around 70 fJ/V-m, the PMA reaches maximum. The PMA first sharply decreases and then increases slightly when t_{Mg} transitions from Region II to I. In Region IV, both VCMA and PMA decrease sharply.

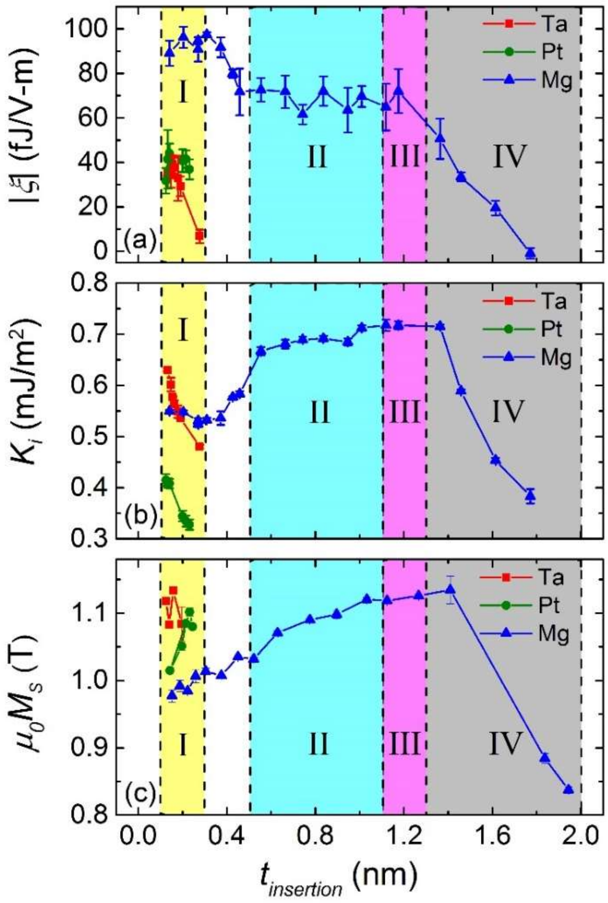

Figure 5-3 (a) VCMA coefficient (ξ), (b) interfacial perpendicular magnetic anisotropy (K_i), and (c) saturation magnetization ($\mu_0 M_S$) as a function of insertion layer thickness ($t_{insertion}$) for Ta, Pt, and Mg. The

VCMA coefficients here are all absolute values, while the measured values are all negative (according to the definition that positive voltage corresponds to higher electric potential at the top gate electrode). Region I to IV are designated with different colors.

The saturation magnetization (M_S) dependences on insertion material thickness for all three materials (Ta, Pt, Mg) are shown in Figure 5-3 (c). The saturation magnetization values of all three materials peak around 1.1 T. Interestingly, the peak of the M_S values for Mg is around 1.2 nm (Region III), where the PMA reaches maximum. For thicknesses less than 1.2 nm, M_S decreases gradually, while for Mg thickness larger than 1.2 nm, M_S decreases sharply. Note that all saturation magnetization values here were obtained without considering any CoFeB dead layer.

5.3 Analysis of Mg Insertions via X-Ray Diffraction

First, we will analyze the case of Mg insertion in detail before comparing it against Ta/Pt insertions. We hypothesize that the change of CoFe oxidation levels with varying Mg insertion thickness contributes to the above observed VCMA, PMA, and M_S dependence on the Mg insertion thickness. Here, the oxygen content responsible for oxidizing CoFe partly comes from the high energy O^- ions generated in the RF sputtering of MgO, which will bombard and oxidize the CoFeB/Mg layers underneath.[184-186] In addition, during the post annealing process, oxygen from the MgO and Al_2O_3 layers might diffuse into the CoFeB/Mg layers.[187] Thus, using a Mg insertion layer of an appropriate thickness can precisely control the oxidation level of the CoFeB layer. In particular, our hypothesis is that Region III corresponds to an ideal CoFe/MgO interface, Region I and II to an over-oxidized CoFe/MgO interface (Co/Fe-oxides at the interface), and Region IV to an under-oxidized CoFe/MgO interface (metallic Mg at the interface).

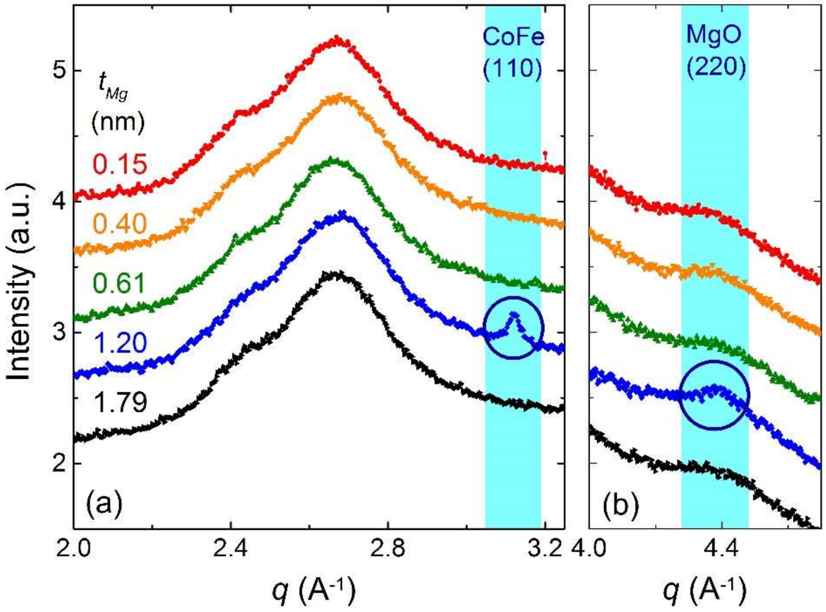

Figure 5-4 X-ray diffraction (XRD) intensity versus reciprocal lattice vector q for films with different Mg insertion layer thicknesses (t_{Mg}). (a) The data is integrated over azimuthal angle χ at $80^o < \chi < 100^o$. The q value region corresponding to the crystalline peak for CoFe (110) is highlighted. (b) The data is integrated over azimuthal angle χ at $40^o < \chi < 80^o$. The q value region corresponding to the crystalline peak for MgO (220) is highlighted.

To validate this hypothesis, XRD studies on the unpatterned film stacks were performed at the Stanford Synchrotron Radiation Lightsource (SSRL) using the 11-3 beamline, which is specially equipped for grazing incidence wide angle X-ray scattering (GIWAXS). Two-dimensional XRD patterns, which contain information on the phase, stress, texture, and grain size of the samples, were obtained for various Mg insertion layer thicknesses and integrated over a small range of azimuthal angle χ in the 2D scan. Two sets of data are obtained for different Mg insertion thicknesses as shown in Figure 5-4 (a) and (b) across different q and χ value ranges. As highlighted in Figure 5-4 (a) and (b), CoFe (110) and MgO (220) crystalline peaks only show up prominently for a Mg insertion layer thickness of 1.20 nm. This thickness range near 1.20 nm corresponds to Region III, where the PMA and M_S are also the highest as seen from Figure 5-3 (b)-(c). Figure 5-4 (a) shows a broad peak at q values from 2.4 to 2.8 A^{-1}, which we attribute to a convolution of amorphous and/or small crystallite signals from Ta, Al_2O_3, SiO_2, and possibly $CoFe_2O_4$. Unfortunately, the large number of overlapping peaks in this region prevented a quantitative analysis of each material as a function of the insertion layer thickness.

The above observation that the crystalline CoFe and MgO peaks only show up prominently in Region III corroborates our hypothesis that only Region III corresponds to an ideal CoFe/MgO interface. From the peak positions of CoFe and MgO, we can calculate that there is a 3-4% lattice mismatch between CoFe and MgO, which is consistent with published results.[129] This can be explained by considering the crystallization process of CoFeB in the CoFeB/MgO material system. It is widely accepted that the MgO becomes crystalline when deposited onto amorphous CoFeB and that the CoFeB crystalizes based on the crystallinity of the adjacent MgO layer.[129, 188] In other words, if the CoFe/MgO interface is under-oxidized, the excessive Mg interlayer between CoFe and MgO may prevent the formation of crystalline MgO during deposition, as well as the crystallization of CoFeB based on the MgO crystal orientation. On the other hand, if the CoFe/MgO interface is over-oxidized, the Co/Fe-oxides will also degrade the CoFeB crystallization quality. In the following discussion, we will explain the VCMA, PMA, and M_S dependence on the Mg insertion thickness using this corroborated hypothesis.

In order to understand why the maximum M_S value shows up in Region III, the effect of CoFeB oxidation on the magnetic properties of the layered system must be considered. Generally, it is known that CoFe oxidizes into either an antiferromagnetic (CoO, FeO, α-Fe_2O_3)[189] or ferrimagnetic (Fe_3O_4, γ-Fe_2O_3, $CoFe_2O_4$) phase, all of which have lower M_S

values than Co and Fe.[190] Thus, for Mg thickness smaller than Region III, the thinner the Mg is, the more CoFeB will be oxidized, resulting in a lower M_S value. As analyzed above, the CoFeB crystallization quality is degraded for regions other than Region III.[191] This degradation may be caused in part by the bombardment of high energy oxygen atoms during MgO sputtering, resulting in a lower M_S value with a thinner Mg layer as the sacrificial layer.[192]

The thickness of the Mg insertion layer also exhibits a complex effect on the PMA of CoFeB. *Ab initio* calculations have shown that an under-oxidized CoFe/MgO interface will lead to a decrease in PMA due to the disappearance of Fe/Co - O hybridized states compared to an ideal CoFe/MgO interface, while an over-oxidized CoFe/MgO interface similarly leads to a decrease in PMA as a result of the splitting of these same hybridized states.[107, 193] Experimental work also shows similar results.[194-196] Generally, the PMA decreases for Mg insertion layer thicknesses other than Region III. However, the PMA of the CoFeB shows a small increase when a very thin Mg insertion layer is inserted (Region I). This might be attributed to different strain conditions[109] at the over-oxidized CoFe/MgO interface as well as the formation of $CoFe_2O_4$.[197]

Lastly, the effect of Mg insertion layer thickness on the VCMA magnitude will be discussed. Our results suggest that a strongly over-oxidized CoFe/MgO interface will increase the VCMA effect. This observed trend is also consistent with *ab initio* calculations where an interfacial FeO layer enhanced the VCMA coefficient.[113, 175] A deeper understanding of the evolution of the VCMA effect from very thin Mg insertion thickness (Region I) to the Mg insertion thickness showing ideal CoFe/MgO interface (Region III) requires *ab initio* calculations which also take into account the different strain conditions when the CoFe/MgO interface are under different oxidation levels.[115, 116]

5.4 Analysis of Ta and Pt Insertions

After understanding the case of Mg insertion, Ta and Pt insertion layers will be discussed briefly as compared with Mg. First, as can be seen from both Figure 5-1 and Figure 5-3 (b), the PMA decreases with increasing Ta/Pt/Mg insertion thickness, consistent with previous reports.[181, 198] As shown in Figure 5-1 (b), an Mg insertion layer induces a much larger out-of-plane to in-plane transition thickness than either Ta or Pt. One cause for this difference in transition thickness might be that as the PMA originates from the hybridization of Co/Fe and O orbitals at the CoFeB/MgO interface,[107, 108] a sufficiently thick extrinsic insertion layer such as Ta or Pt, will weaken the Co/Fe and O orbitals hybridization by binding to the O atoms, thus leading to the decrease of PMA.[199] Secondly, as the VCMA effect relies on the modulation of PMA, the decreased extent of oxidation between the Co/Fe and O orbitals might also decrease the VCMA effect, as shown in Figure 5-3(a). Thirdly, at very small insertion thicknesses, the M_S values for Ta/Pt insertions are much larger than that of the Mg, as shown in Figure 5-3(c). This difference could be understood by considering that Ta/Pt has a smaller negative oxide formation enthalpy than Mg. Hence, during the MgO deposition and annealing processes, the lower degree of CoFeB oxidation for the Ta/Pt insertions scenario might result in a higher M_S. Another possible reason is that the MgO deposition process will also sputter the CoFeB and metallic insertion layers underneath.[192] With larger atomic numbers and higher sublimation temperatures than Mg, the Ta and Pt insertion layers are harder to be sputtered off. Therefore, less CoFeB is sputtered off and a larger M_S is obtained.

In conclusion, we systematically studied how inserting various materials (Ta, Pt, and Mg) at the CoFeB/MgO interface affects the VCMA effect. A maximum VCMA coefficient of around 100 fJ/V-m was realized for a very thin Mg insertion layer, which is more than 3 times larger compared to average VCMA values reported for traditional CoFeB/MgO stacks where no material is inserted. Using XRD results, the emergence of strong CoFe and MgO crystalline peaks is correlated to the maximum PMA and saturation magnetization. This indicates that precise control over the Mg insertion thickness and CoFe oxidation level at the CoFeB/MgO interface is critical to achieving the desired device performance, with a tradeoff between VCMA, PMA, and saturation magnetization. The high VCMA coefficient of around 100 fJ/V-m demonstrated in this work will pave the way for low-power high-density magnetoelectric memories utilizing electric-field-induced writing with very low write voltage.

Chapter 6 Seed and Spacer Layers Engineering for Thermal Stress Stability

6.1 Motivation

As mentioned in Chapter 1, the electric-field assisted writing of magnetic memory that exploits the voltage-controlled magnetic anisotropy (VCMA) effect offers great potential for high performance on-chip memory due to its low write energy and fast write speed.[100, 101] In particular, as the leakage power and cell size continue to increase at smaller nodes for traditional CMOS SRAM technology, it is of great promise to integrate Magnetoelectric Random Access Memory (MeRAM) into advanced CMOS back-end-of-line (BEOL) processes for high density SRAM replacement.[24, 99, 200, 201] To achieve the full potential of voltage-controlled Magnetoelectric random access memory (MeRAM), it is critical to design magnetic materials with a) high voltage-induced writing efficiency, i.e. VCMA coefficient, b) thermal stress stability under annealing process of 400°C, and c) high tunneling magnetoresistance for writing, i.e. TMR.

In the commonly used Ta/CoFeB/MgO system, the PMA and TMR cannot be sustained when an annealing temperature above 400°C is used,[202, 203] making it incompatible with advanced CMOS back-end-of-line processes, where metallic interconnects and low-k dielectrics used between the interconnects require a thermal budget over 400°C.[204, 205] Several works have recently explored MTJs with improved thermally stable TMR and PMA for STT-MRAM applications, primarily by blocking or eliminating Ta diffusion under high temperatures.[192, 204-206] Nevertheless, for VCMA-based embedded memory applications, it is critical to develop new material systems that can also provide thermally stable VCMA after annealing at 400°C.

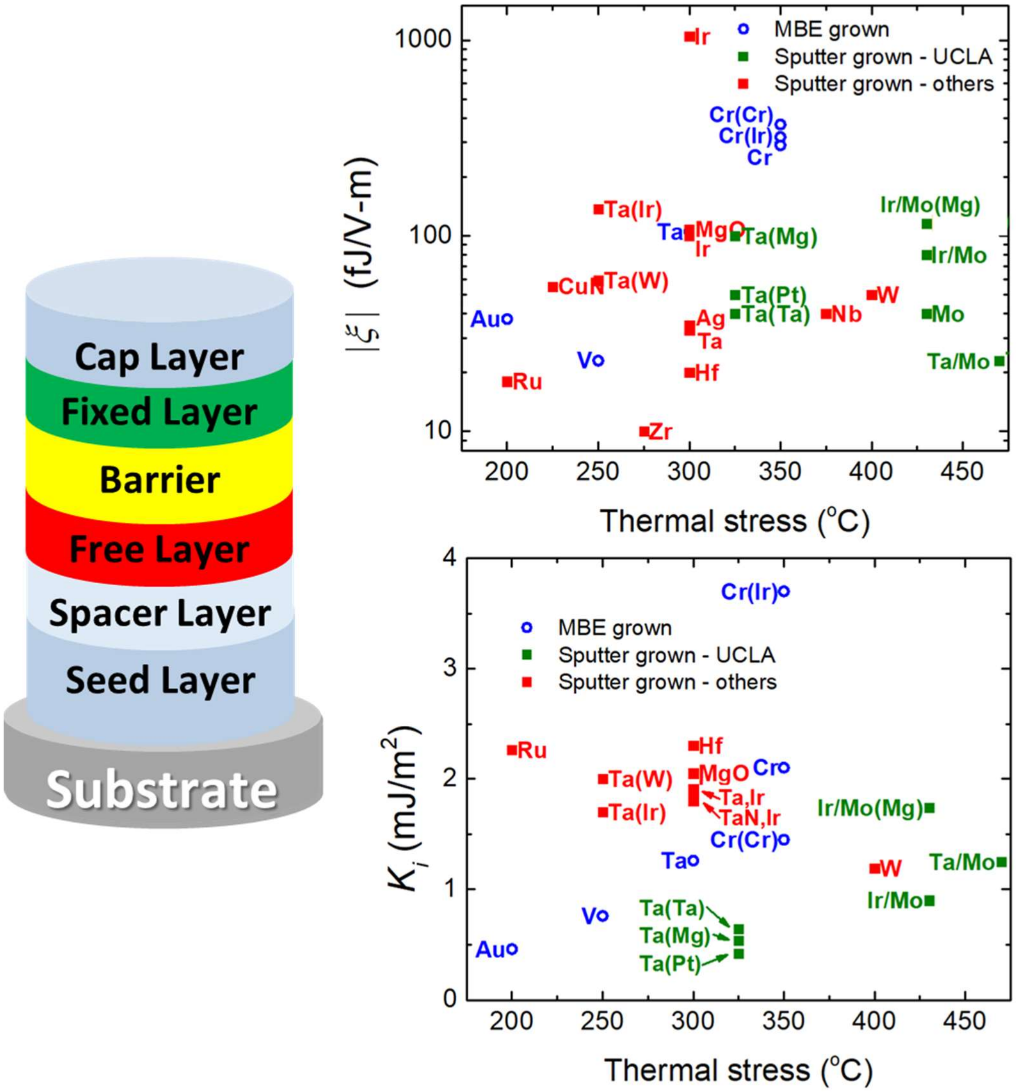

Figure 6-1 (Left) Schematic of MTJ stacks with different layers. (Right) Published VCMA and PMA experimental results for different seed/spacer/insertion layers as a function of thermal stress temperature: (Top) Absolute value of VCMA coefficient (ξ), (Bottom) interfacial PMA magnetization (K_i) values from published literature as a function of thermal stress temperature. The blue open circles refer to MTJ stacks grown by molecular beam epitaxy (MBE), the green (red) solid squares refer to those grown via sputtering by UCLA (other researchers). The labels besides each data point indicates the seed material used, while the bracket indicates the insertion material between the magnetic free layer and tunnel barrier.

A possible route to achieve this goal is to exploit the effect of the metal seed/spacer layer on the PMA and VCMA in MTJ structures as shown in Figure 6-1.[146, 149] First, the seed and spacer materials provide a template for the CoFeB/MgO/CoFeB trilayer growth, which is critical for both tunnel magnetoresistance (TMR) and VCMA. Next, in the annealing process, the inter-diffusion of seed and spacer layers and the CoFeB/MgO/CoFeB trilayer will also affect the TMR and VCMA. A survey of published works done by groups outside of UCLA are summarized in Figure 6-1. [141, 142, 146, 147, 149, 207-215] Note that the use of seed layer X and spacer layer Y is designated using X/Y labels, while the insertion material Z at the CoFeB/MgO interface is also included as indicated in the brackets in the labels as X/Y(Z).[118, 119, 216, 217]

As can be seen in the Figure 6-1, only recently, there have been reports on improving the thermal stability of PMA, TMR and VCMA in MTJs by changing the Ta-based material stacks to Mo/CoFeB/MgO [218] and W/CoFeB/MgO under annealing temperatures above 400°C. [146, 219] Hence, exploration of different seed/spacer materials to achieve thermal stability of PMA and VCMA after annealing above 400°C is highly desired for bringing MeRAM into embedded applications. Note that in relation to Chapter 4 and Chapter 5, the VCMA and PMA values obtained there are both annealed at temperatures below 400°C. In particular, the Ta(Pt), Ta(Ta), and Ta(Mg) data points refer to the insertion works in Chapter 5.

Here we will first present a detailed study on the effect of annealing on PMA, saturation magnetization (M_S), and VCMA in Mo/CoFeB/MgO film stacks. A VCMA coefficient (ξ) of 40 fJ/V-m is demonstrated after annealing at 430°C for 30 minutes.[220] We also observe a higher ξ of 50 fJ/V-m at lower annealing temperature (T_A) of 360°C. These VCMA coefficients are comparable to the best high-temperature VCMA (>400°C) values (40-50 fJ/V-m) reported to date for W-based samples in Ref. [146], as well as typical ξ values (30-60 fJ/V-m) measured in the Ta/CoFeB/MgO system.[136, 138-140, 142] The results also show that a higher annealing temperature improves the M_S, as well as the interfacial PMA K_i of the film stack within the studied temperature range. *Ab initio* electronic structure calculation results further show that the calculated K_i values increase as the epitaxial tensile strain on the FeCo layers relaxes. In addition, the CoFeB thickness dependences of the VCMA and K_i are studied in this work for annealing at different temperatures, showing no significant dependences over the measured thickness range.

Based on the above result using Mo seed, which can provide thermal stress stability for VCMA above 400°C, [149] we also explored various seed materials with Mo as a spacer layer between seed and free layer to enable thermal stress stability for TMR, PMA, and VCMA above 400°C. In particular, Ir, Ta seeds are investigated in two cases where Mo is used as a spacer and Mo is not used at all. By exploring these different seed/spacer combinations, high VCMA coefficient of 115 fJ/V-m, TMR of 160%, and PMA of 1.74 mJ/m^2 annealed above 400°C were demonstrated using industrially applicable sputtering process, which are among the highest values reported and represented in Figure 6-1.[118, 119, 216]

In addition, high resolution transmission electron microscopy (TEM) experiments were carried out to further study the material chemical and structural change when different seed materials are used and annealed under different temperatures. TEM results show that the crystallinity of CoFeB, MgO and seed layer, as well as the oxygen concentration in the Fe content of the top CoFeB layer both correlate well with device TMR. The CoFe alloy ratio correlates well with the saturation magnetization and interfacial PMA values. While the higher oxygen concentration in the bottom Fe correlates well with the VCMA coefficient. These well-established correlations indicate that by materials engineering using various stack structures and annealing conditions, it is most critical to control the Co, O, and Mg atomic concentration in the top and bottom CoFeB layers to achieve the optimal VCMA, PMA, saturation magnetization, and TMR values. These experimental results as well as physical understandings will shed light on how to further improve MeRAM materials for on-chip cache at advanced nodes as well as utilize Mo as spacer layer for embedded MRAM with high thermal stress stability.

6.2 Molybdenum Spacer Layer for High Thermal Stress Stability

6.2.1 Materials and Methods

The magnetic film stacks were deposited in a magnetron sputtering system on a thermally oxidized Si/SiO_2 substrate. We prepared samples with a uniform CoFeB thickness with the following structures: Mo(5)/$Co_{20}Fe_{60}B_{20}$(t=0.94,1.06,1.18)/MgO(2.5)/Al_2O_3(5), with the numbers in the parentheses designating nominal thickness in nm. We also deposited samples with gradually changing (wedged) CoFeB thickness with similar structures: Mo(5)/$Co_{20}Fe_{60}B_{20}$(t)/MgO(2.5)/Al_2O_3(5), where the CoFeB thickness t was continuously varied in the range of 0.65 to 1.45 nm across the wafer. All metallic layers were grown using DC sputtering, while the MgO and Al_2O_3 layers were RF sputtered from insulating MgO and Al_2O_3 targets. Stacks were annealed at 360°C, 400°C, and 430°C respectively for 30 minutes under vacuum (< 10^{-7} Torr). The rise time of the annealing system was less than 2 minutes, while the cool-down time from 430°C to 200°C was approximately 30 minutes. The samples were subsequently patterned into Hall bar devices by standard photolithography and dry etching techniques and further covered by a 33 nm Al_2O_3 gate oxide using atomic layer deposition (ALD). Last, a patterned ITO electrode was fabricated on top for gating. The dielectric constants of MgO and Al_2O_3 are assumed to be 10 and 7, respectively according to the literature, for the calculation of the electric field strength at the CoFeB/MgO interface.[167, 182] The dimensions of the Hall bars were 20 μm × 130 μm. For the wedged samples, the Hall bar length was perpendicular to the wedge direction.

Ab initio electronic structure calculations were carried out within the framework of the projector augmented-wave formalism, as implemented in the Vienna *ab initio* simulation package (VASP)[221] at the generalized gradient approximation level.[222] The slab supercell model of the magnetic layered structure consists of three monolayers (MLs) of bcc Mo, on top of 3 MLs of *B*2-type FeCo, on top of 7 MLs of MgO and a 15-Å-thick vacuum region, as shown in the inset of Figure 6-6(c). The O atoms at the interface are placed atop Fe atoms.

6.2.2 Dependence of Saturation Magnetization and Dead Layer on Annealing Temperature

The unpatterned films were first characterized by a vibrating sample magnetometer (VSM) to obtain M-H loops, in order to study the change of PMA and M_S with different annealing temperatures. Exemplary results from a sample with a uniform CoFeB thickness of 1.06 nm are shown in Figure 6-2 (a), where the magnetic field is swept in the out-of-plane direction. As the annealing temperature increases, the squareness of the M-H loop improves, and the out-of-plane saturation field decreases, both of which indicate that the PMA of the film increases at higher annealing temperatures. Similar results were also observed for samples with CoFeB thicknesses of 0.94 and 1.18 nm. By carrying out a linear fit of the magnetic moment per unit area as a function of the CoFeB thickness, we further obtained the saturation magnetization (M_S) and dead layer thickness (t_d) values at different annealing temperatures.[191] As shown in Figure 6-2 (b), both the M_S and t_d values increase at higher annealing temperatures. Note that all CoFeB thicknesses mentioned in the paper refer to the nominal thickness without dead layer subtraction.

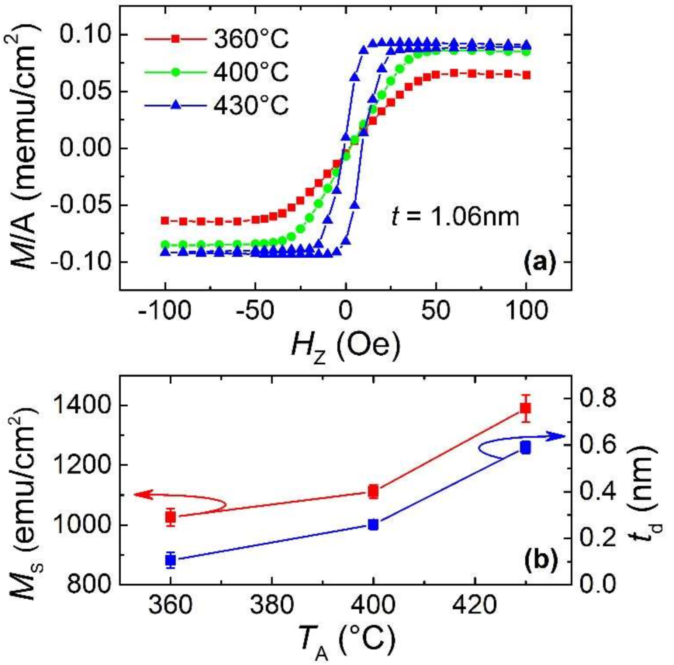

Figure 6-2 (a) M-H curves for different annealing temperatures ($\mathrm{T_A}$). $\mathrm{M/A}$ refers to magnetic moment per unit area. $\mathrm{H_Z}$ refers to out-of-plane magnetic field. The CoFeB thickness (t) is 1.06nm. (b) Dependence of saturation magnetization ($\mathrm{M_S}$) and dead layer thickness ($\mathrm{t_d}$) on $\mathrm{T_A}$.

This increase of PMA, M_S, and t_d in the Mo/CoFeB/MgO system with annealing temperature is consistent with the observations of Ref. [191], and can be associated with the competition between boron diffusion from the CoFeB layer into the molybdenum film,[223] and molybdenum diffusion into the CoFeB layer upon annealing. It is known that the diffusion of boron promotes better crystallization of CoFe from the amorphous state to a bcc(001) crystal structure,[164] resulting in a higher saturation magnetization. According to *ab initio* calculations, the PMA in the CoFeB/MgO system stems primarily from the hybridized Fe/Co *3d* orbitals and O *2p* orbitals at the interface,[107, 108] hence the decrease of boron atoms at the interface might be expected to induce stronger orbital hybridization and a higher PMA.

It is worth noting that the observed monotonic increase of both M_S and PMA from 360°C to 430°C in the Mo-based system is in sharp contrast to the Ta-based system, where both M_S and PMA drop when annealed at temperatures higher than 300°C.[203, 223] Similarly, the dead layer thickness of the Ta/CoFeB/MgO system increases above 0.5 nm at around 330°C[191] while the dead layer thickness increases above 0.5 nm at a higher temperature of around 430°C of the Mo/CoFeB/MgO system. This better thermal annealing stability of PMA and M_S in Mo/CoFeB/MgO structures can be explained by a number of causes. Namely, the smaller negative formation enthalpy of Mo oxides compared to Ta oxides, the crystalline structure of the sputtered Mo film,[191] and the smaller negative formation energy of Fe-Mo alloys compared to Fe-Ta,[224] all contribute to the prevention of molybdenum atoms from significantly diffusing into the free layer, leading to a more stable PMA and M_S after high-temperature annealing. On the contrast, the decrease of M_S in the Ta-based system at higher annealing temperatures has been attributed to intermixing of CoFeB and Ta,[215] while the decrease of PMA results mainly from the diffusion of Ta into the CoFeB/MgO interface.[170] Hence in our Mo/CoFeB/MgO system, as the magnetic properties keep improving from 360°C to 430°C, boron diffusion (out of the free layer) has a dominating effect over molybdenum diffusion (into the free layer) over the studied temperature range.

6.2.3 Dependence of VCMA and Interfacial PMA on Annealing Temperature

The VCMA was subsequently characterized as follows. The Hall resistance $\mathrm{R_{Hall}}$ was measured under a sweeping out-of-plane magnetic field while different gate voltages were applied. A positive gate voltage is defined as the top gate electrode being at a positive electric potential, as shown in Figure 6-3 top right inset. Figure 6-3 shows the measurement results of the wedged sample with a CoFeB thickness of 1.45nm, annealed at 430°C for 30 minutes, where three different gate voltages are applied. As the CoFeB in this case has an in-plane easy-axis, an out-of-plane (i.e. hard-axis) magnetic field is applied in order to obtain the perpendicular anisotropy energy (E_{perp}).[138] As can be seen from the bottom left inset of Figure 6-3, a noticeable difference of the R_{Hall}-H loop is observed for different applied electric fields.

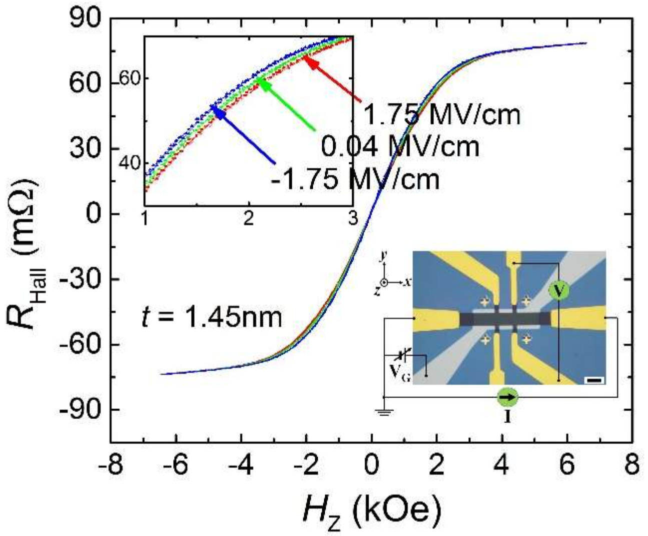

Figure 6-3 (Left) Hall resistance dependence on the out-of-plane magnetic field, under different gate voltages. The film stack was annealed at 430°C for 30 minutes. Top right inset: Top view of a Hall bar device with an ITO gate electrode. The scale bar is 20 μm. Bottom left inset: Zoomed-in view of the main figure with the same units for both axes.

To measure the VCMA coefficient ξ, we follow an approach similar to Ref.[138], also similar to the anomalous Hall measurement method mentioned in Section 3.2.2. The value of E_{perp} is obtained from the equation for an in-plane easy-axis film

$$E_{perp} = -\mu_0 \int_0^1 H_Z dM_Z \qquad \text{Equation 6-1}$$

where the normalized M_Z/M_S value can be expressed by Equation 3-7. The value of $-E_{perp}/M_S = \int_0^1 H_Z dM_Z/M_S$ is also shown in the right figure of Figure 6-3. Here, M_S is the saturation magnetization, M_Z is the perpendicular component of the magnetization, H_Z is the out-of-plane external magnetic field, R^{AHE} is the anomalous Hall resistance, and R^{AHE}_{max} (R^{AHE}_{min}) is the maximum (minimum) of R^{AHE} values measured. The value of R^{AHE} can be extracted from R_{Hall} by subtraction of the ordinary Hall contributions according to Equation 3-6, where the first term is the ordinary Hall resistance, and the second term represents R^{AHE}. Here, R_0 and R_S are the ordinary and anomalous Hall coefficients, respectively, and μ_0 is the permeability of free space. The ordinary Hall coefficients can be obtained from a fit to the $R_{Hall} - H_Z$ loop at the high field regions. From this, we can obtain the electric field dependence of the perpendicular anisotropy energy $E_{perp}(E)$, and hence the electric field dependent interfacial perpendicular anisotropy (K_i) can be calculated using Equation 3-5. Hence, one can obtain the electric field dependence of K_i and measure the VCMA coefficient ξ.

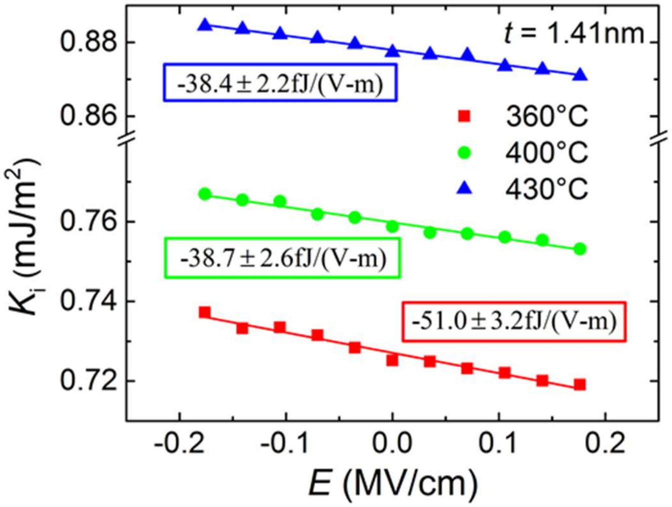

Figure 6-4 Interfacial perpendicular magnetic anisotropy (K_i) dependence on electric field (E) for different T_A. The inset numbers indicate the VCMA coefficient (ξ).

Next, we compare three exemplary dependencies of K_i as a function of electric field, for devices with the same CoFeB thickness annealed at different temperatures. As shown in Figure 6-4, a linear dependence with a negative slope is obtained, which means that depletion of electrons at the CoFeB/MgO interface increases the interfacial perpendicular anisotropy. From the fitted curves, a ξ of ~40 fJ/V-m is demonstrated after annealing at 430°C, along with a higher ξ of ~50 fJ/V-m at 360°C annealing temperature.

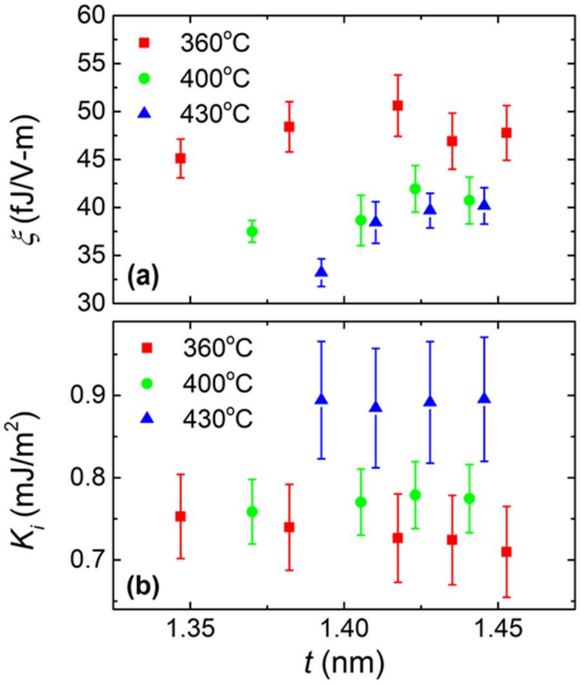

Figure 6-5 (a) VCMA coefficient ξ, and (b) Interfacial PMA K_i dependence on CoFeB thickness (t), under different T_A.

In addition, we carried out gate voltage-dependent hard-axis $R_{Hall} - H$ measurements for devices along the length of the wedge-shaped sample, to study the CoFeB thickness dependence of the VCMA coefficient (ξ) and interfacial perpendicular anisotropy (K_i) for different annealing temperatures, as shown in Figure 6-5 (a) and (b). No significant CoFeB thickness dependence of either ξ or K_i is observed over the measured thickness range, which is consistent with some previous reports,[136] that the interfacial anisotropy and its electric field control originate primarily from the CoFeB interfaces.

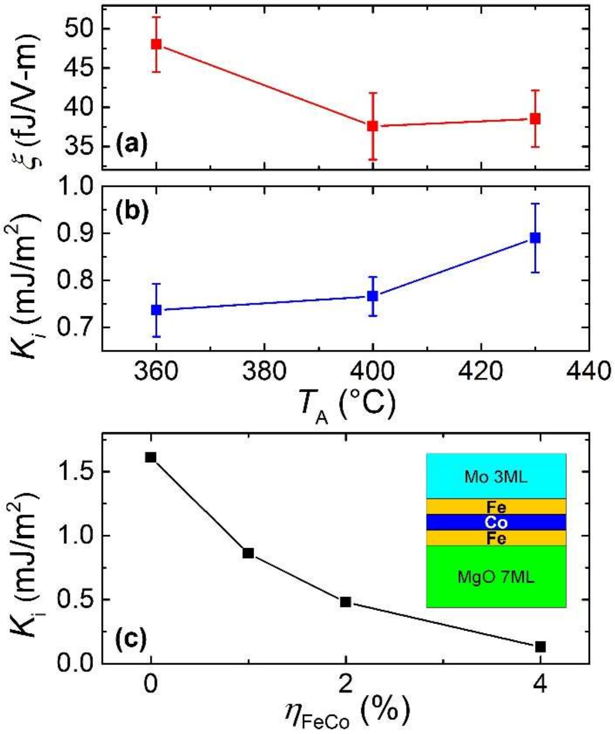

Figure 6-6 (a) ξ, and (b) K_i dependence on T_A. The VCMA coefficients here are all absolute values, while the measured values are all negative (according to the definition that a positive voltage corresponds to higher electric potential at the top gate electrode). Error bars are included to take into account the uncertainty in t_d and M_S values. (c) The *ab initio* electronic structure calculated K_i of Mo(3ML)/FeCo(3ML)/MgO(7ML) as a function of tensile strain on FeCo layer (η_{FeCo}).

The dependences of ξ and K_i (after averaging over the measured thickness values) on the annealing temperature are summarized in Figure 6-6 (a) and (b). Apart from the slight decrease of the VCMA coefficient, K_i increases by 20% from 0.74 mJ/m^2 to 0.89 mJ/m^2 after annealing. This slight drop of ξ along with a continued increase of K_i at higher annealing temperature is consistent with previous reports in Ir/CoFeB/MgO [209] and W/CoFeB/MgO systems [146] which indicates that the electric-field control of K_i is more sensitive to annealing effects than K_i itself. A possible reason for the increase of K_i and slight VCMA degradation at higher annealing temperature is that the annealing relaxes the compressive strain of the MgO layer, such that the lattice constant of the MgO approaches its bulk value.[82]

6.2.4 Analysis of Results via *Ab Initio* Calculations

To further investigate the effect of strain on K_i, we performed *ab initio* electronic structure calculations of interfacial PMA (K_i) in Mo(3ML)/FeCo(3ML)/MgO(7ML) structures, as a function of tensile strain on the FeCo layer (η_{FeCo}). As shown in Figure 6-6 (c), the relaxation of epitaxial FeCo strain, thus relaxation of epitaxial MgO strain, can give rise to an increase of K_i. Note that as discussed before, the diffusion of boron atoms away from the CoFeB/MgO interface might also contribute to the increase of interfacial PMA. According to our recent *ab initio* work on the dependence of VCMA on epitaxial strain of CoFeB/MgO structures, a relaxation of compressive strain of the MgO layer will lead to a lower dielectric constant of the MgO, which might reduce the VCMA effect.[116]

It is worthwhile to compare our results to those obtained in other material systems of interest for MeRAM. Thermal stability of VCMA above 400°C has been previously studied in the W/CoFeB/MgO system.[146] Our observed ξ values, along with a slight decrease of the ξ values above 400°C in the Mo-based system, are very similar to those in the W-based system. The comparable ξ values between the two material systems also agree well with a previous experiment on vacuum/Fe/Mo(110) and vacuum/Fe/W(110) systems using nanoscale ferromagnetic islands on metallic substrates at 45 K.[210] While for Ta/CoFeB/MgO structures, a VCMA coefficient of 30-60fJ/V-m has been obtained in several previous work with annealing temperatures below

300°C.[136, 138-140, 142] In other structures with seed layers such as Au,[101] Ru,[142] Ir,[209] Ag, CuN, Zr, Nb,[146] and MgO,[141] ξ values of 20-100fJ/V-m have been demonstrated with annealing temperatures generally not exceeding 350°C.

It is also worth noting that a number of reports have shown large ξ values of 100-1,200fJ/V-m,[127, 183, 225] which can be attributed to mobile ionic charges in the oxides besides the MgO layer. These charges may, however, be too slow to achieve high frequency memory writing using voltage pulses. To eliminate the possibility of such an ionic effect in our films, we carried out a hysteretic sweep of the gate voltage[127] from -10V to 10V and back to -10V. The K_i vs electric field plots for different sweeping directions coincide with each other and are within the error bars of the measurement, hence confirming that there is no contribution from mobile charges in our films.

In conclusion, it is demonstrated that the interfacial PMA in Mo/CoFeB/MgO structures increases and the VCMA is sustained with annealing temperatures up to 430°C. A VCMA coefficient of 40 fJ/V-m is demonstrated after annealing at 430°C, indicating a VCMA comparable to Ta-seeded systems, along with a marked improvement in its temperature stability. *Ab initio* electronic structure calculations further corroborate the enhancement of experimental K_i values at high temperatures. No significant CoFeB dependence of the VCMA effect and the interfacial PMA is observed over the thickness range studied. The demonstration of thermally stable VCMA and PMA provides a pathway for the integration of Mo/CoFeB/MgO into Magnetoelectric RAM devices compatible with advanced embedded CMOS technologies.

6.3 Seed Layer Engineering with Molybdenum Spacer Layer for Thermal Stress Stability

Based on the above results, Molybdenum seems to be a good material that has minimal diffusion compared with Ta. Hence, Mo can act as a spacer layer between seed layer such as Ta and the free layer CoFeB. When the Mo layer is thin enough, the seed layer such as Ta can still influence the free layer magnetic properties through diffusion of seed layer and the seed layer as a growth template for Mo/CoFeB layers. In this way, the seed layer/CoFeB bilayer properties can be partially maintained while possessing the thermal stress stability required for CMOS back-end-of-line (BEOL) processing.

Similar work has been done to investigate the effect of Mo insertion in Ta/Mo/CoFeB-based MTJs on PMA and TMR.[226] However, a detailed study of the effect of Mo spacer/insertion on the VCMA effect is missing. Also, a comparison between different seed materials combining with Mo spacer is desired to further understand the complex interplay between seed/spacer bilayer and the CoFeB/MgO/CoFeB junction. In terms of VCMA effect, Ir seed give rise to the highest VCMA coefficients (~ 100 fJ/V-m) reported by sputtering. However, Ir seeded MTJs will lose its PMA above 350ºC annealing.[209] Hence, the combination of Ir/Mo bilayers might produce both high VCMA values and PMA under high annealing temperatures. In this section, we will show the PMA, TMR, VCMA, and saturation magnetization values of MTJs using Ta and Ir seeds with/without the Mo spacer layers.

In addition, while there are already considerable amount of literature investigating the material properties of MTJ stacks, no clear material structural and chemical properties have been experimentally identified to explain the wide-spread magnetic properties values for different seeded materials annealed at different temperatures, especially the PMA and VCMA values. Hence, it is crucial to pinpoint experimentally what are the underlying material properties that govern the evolution of these magnetic properties. In this work, we carried out X-ray Diffraction (XRD) and transmission electron microscopy (TEM) studies to carefully investigate the materials structural and chemical properties. By carefully analyzing the Energy Dispersive X-ray Spectroscopy (EDS) data for each element distribution in the MTJ stack, we have established strong correlations between the PMA, TMR, VCMA, and saturation magnetization values and the element-specific Fe, Co, O, and Mg distribution profile. These correlations will provide critical guidance to the design and engineering of better materials for future STT-RAM and voltage-controlled magnetic memory.

6.3.1 Materials and methods

CoFeB with gradually changing (wedged) thickness were deposited as part of stacks grown on a thermally oxidized Si/SiO$_2$ substrate in a magnetron sputtering system to study the t_{CoFeB} dependence of the VCMA effect using the weak reference layer MTJ measurement method as in Section 3.2.1. The stack is seed/Co$_{20}$Fe$_{60}$B$_{20}$(t_{CoFeB})/MgO(2.5)/Co$_{20}$Fe$_{60}$B$_{20}$(2)/Ta(4)/Pt(2), (thickness in nm), consisting of a wedged CoFeB free layer and a 2 nm-thick weak CoFeB reference layer. In particular, there are 4 variations of the seed layer, i.e. Ta(18), Ta(18)/Mo(1), Ir(18), and Ir(18)/Mo(1). The wedged CoFeB layer thickness t_{CoFeB} is continuously varied in the range of 0.7 to 1.4 nm across the wafer. All metallic layers were deposited using DC sputtering, while the MgO layers were deposited using RF sputtering from insulating MgO targets. All stacks were annealed at various temperatures ranging from 290ºC to 470ºC for 30 minutes in a vacuum under 10^{-7} Torr, and then measured by a superconducting quantum interference device (SQUID) to obtain saturation magnetization values. The stack for MTJ measurement was fabricated into MTJs with the elliptical diameters of 4 $\mu m \times 8$ μm using standard photolithography and reactive ion etching (RIE) techniques. The dielectric constants of MgO are assumed to be 10 for the calculation of the electric field strength at the CoFeB/MgO interface.

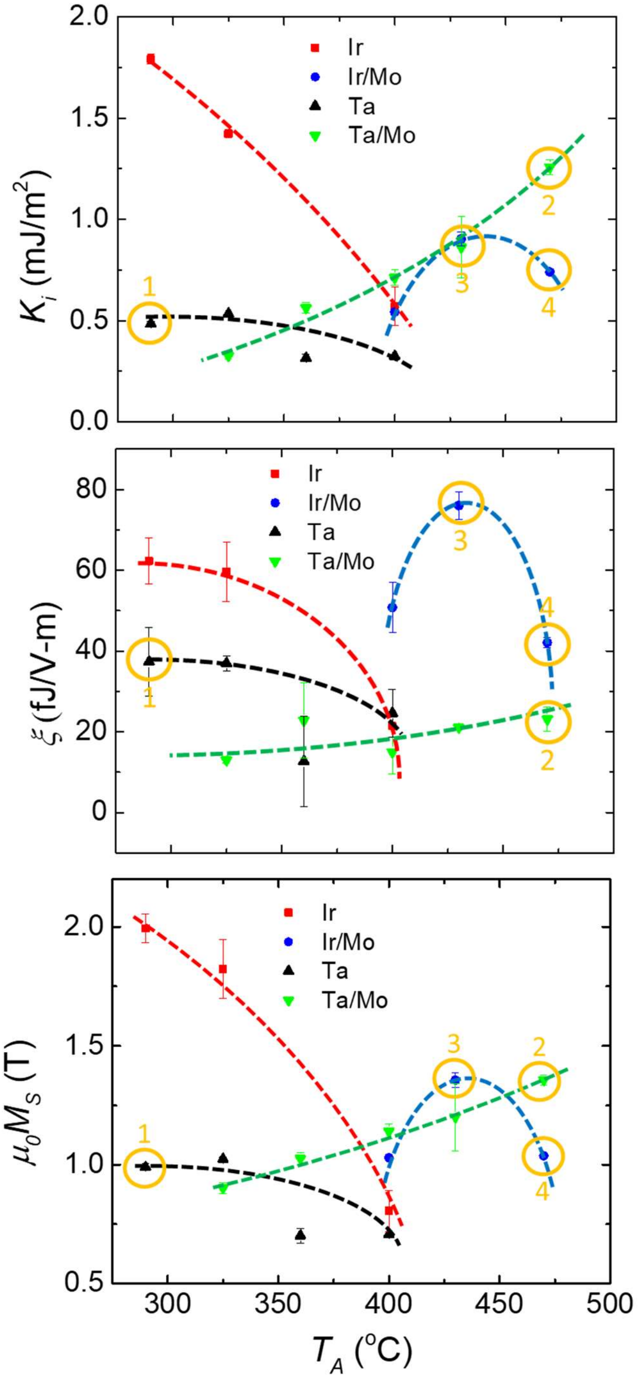

Figure 6-7 Interfacial PMA magnetization (K_i), VCMA coefficient (ξ), and saturation magnetization (M_S) values for MTJs with Ir, Ir/Mo, Ta, and Ta/Mo seed layers, annealed at different temperatures (T_A). The

circled data points refer to: 1, Ta seed annealed at 290°C; 2, Ta/Mo seed annealed at 470°C; 3, Ir/Mo seed annealed at 430°C; and 4, Ir/Mo seed annealed at 470°C. The detailed stack structure and annealing conditions of these 4 samples are also shown in Figure 6-9.

6.3.2 Saturation Magnetization and Device Level Electrical Results

First, using the weak reference layer measurement method as described in Section 3.2.1, interfacial PMA, VCMA coefficient and saturation magnetization values measured via SQUID are shown in Figure 6-7. It can be seen that the general trends of interfacial PMA, VCMA, and saturation magnetization values are similar. The Ta and Ir seeded samples show a monotonic decrease when annealed from 290°C to 400°C and loses both PMA and good saturation magnetization properties beyond 400°C annealing temperature. If Mo spacer is inserted however, the Ta/Mo samples show a monotonic increase of PMA and M_S from 325°C all the way to 470°C, while the Ir/Mo samples show an inverse V-shaped curve with optimal PMA, VCMA, and saturation magnetization values at 430°C.

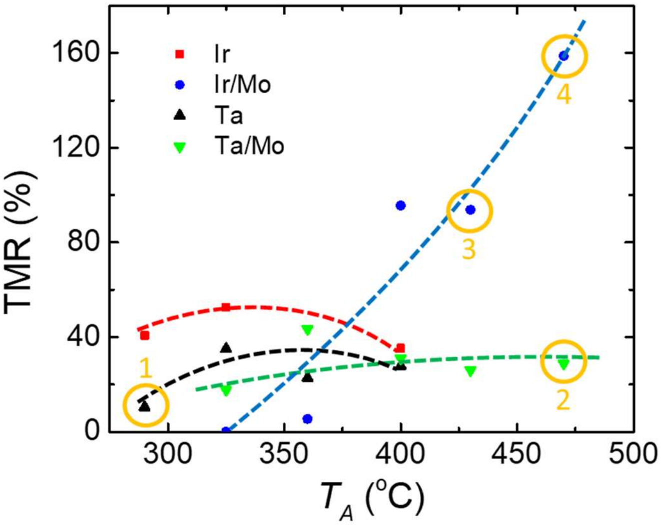

Figure 6-8 Full TMR values for MTJs with Ir, Ir/Mo, Ta, and Ta/Mo seed layers, annealed at different temperatures (T_A). The circled data points refer to: 1, Ta seed annealed at 290°C; 2, Ta/Mo seed annealed

at 470ºC; 3, Ir/Mo seed annealed at 430ºC; and 4, Ir/Mo seed annealed at 470ºC. The detailed stack structure and annealing conditions of these 4 samples are also shown in Figure 6-9.

Next, the full TMR value is measured and calculated based on the method described in Section 4.3, as shown in Figure 6-8. From the data, the trend of TMR for each seed material under different annealing temperatures is drastically different from that of PMA, VCMA, and saturation magnetization values. The Ir and Ta-seeded samples both show an inverse V-shaped curve with optimal TMR around 325ºC. The Ir/Mo seeded MTJs yield much higher TMR values (100-160%) with a monotonic increase at higher annealing temperature. While the Ta/Mo samples have plateaued TMR values around 30% at high annealing temperature.

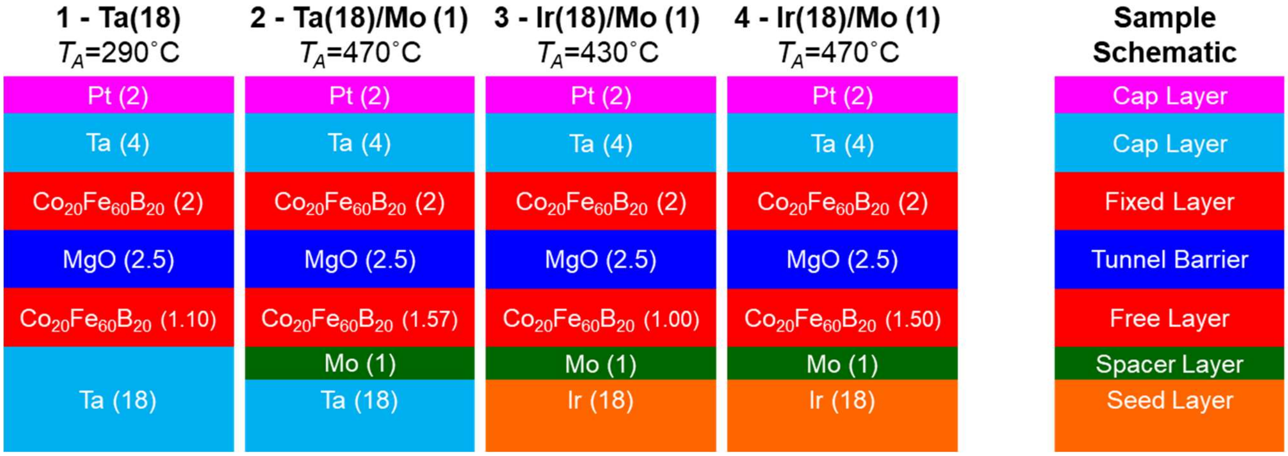

Figure 6-9 MTJ thin film stack for 4 samples selected for further TEM studies, i.e. 1, Ta seed annealed at 290ºC; 2, Ta/Mo seed annealed at 470ºC; 3, Ir/Mo seed annealed at 430ºC; and 4, Ir/Mo seed annealed at 470ºC. The schematic of the MTJ stack with each layer is also illustrated on the right hand side.

To further investigate the origin of these variation of TMR, PMA, VCMA, and saturation magnetization values, and especially the contrasting temperature dependent trends of TMR value versus PMA, VCMA and saturation magnetization values, we chose 4 samples as indicated by the circles in Figure 6-7 and Figure 6-8. The film structure of these 4 samples are also illustrated in

Figure 6-9. We first carried out X-ray diffraction (XRD) on these four set of samples to characterize the materials crystal structure in a rough manner. Then each of these 4 samples will be investigated using high resolution transmission electron microscopy (TEM) and Energy Dispersive X-ray Spectroscopy (EDS) to understand their detailed material and structural characteristics. The data will be shown in next Section.

6.3.3 Film Level Structural and Chemical Results

First, XRD is carried out to characterize the materials structural properties of the above selected 4 samples as well as an Ir-seeded sample annealed at 290°C, as shown in Figure 6-10. The crystalline peaks of relevant materials are identified by light colored regions. Note that we did not consider any CoFe, MgO, or Mo peaks even through some of their crystalline peaks might overlap with the identified Ir, α-Ta, and β-Ta peaks. The reason is that the thickness of CoFeB, MgO, and Mo are thinner than 3nm, thus cannot give rise to a large diffraction signal in the XRD setup we used where normal X-ray incidence angle is used, even when these ultrathin layers are well crystalized. As seen in the figure, the Ir and Ir/Mo-seeded samples all show a clear Ir (111) crystalline peak, lacking any clear Ir (200) peaks (data not shown). Hence, Ir seed are crystallized in (111) orientation mostly. While for Ta and Ta/Mo-seeded samples, they show a clear β-Ta (002) peak. As all samples have Ta as a capping layer on top of the CoFeB/MgO/CoFeB layers, but only Ta and Ta/Mo-seeded samples have Ta seed grown on top of the oxidized Si substrate, it can be concluded that the β-Ta (002) peak comes from the Ta seed. This is consistent with previous reports where Ta grown on top of oxidized Si substrate will be in β phase.[165] While for all samples, a weak and broad α-Ta (110) peak can be found, which can only be attributed to the Ta capping layer. This is consistent with previous reports where Ta grown on top of CoFeB will be partially crystalized into bcc (001) phase. [120]

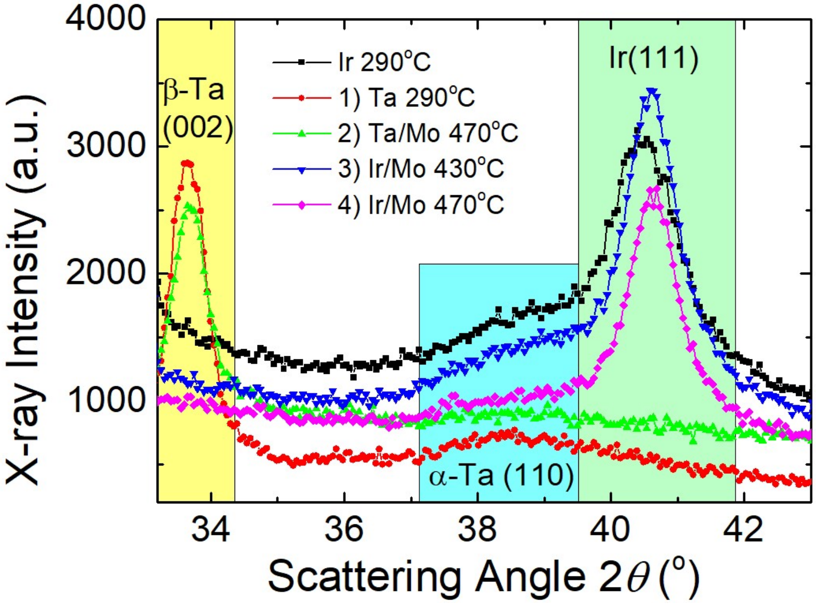

Figure 6-10 $\theta - 2\theta$ X-ray diffraction intensity scan for samples with Ir seed annealed at 290 ºC; 1, Ta seed annealed at 290ºC; 2, Ta/Mo seed annealed at 470ºC; 3, Ir/Mo seed annealed at 430ºC; and 4, Ir/Mo seed annealed at 470ºC. The detailed stack structure and annealing conditions of these 4 samples are also shown in Figure 6-9.

Then, transmission electron microscopy (TEM) are conducted to characterize the detailed structural difference between the four selected samples. As seen in Figure 6-11, the diffraction patterns evolve from blurry diffraction rings to more distinct and well-separated diffraction points as the sample moves from Ta seed annealed at 290ºC (sample 1), to Ta/Mo seed annealed at 470ºC (sample 2), Ir/Mo seed annealed at 430ºC (sample 3), and finally Ir/Mo seed annealed at 470ºC (sample 4). This is also consistent with the constant TMR value increase from sample 1 to sample 4 as shown in Figure 6-8. Hence, the improved crystallinity of CoFeB/MgO/CoFeB layers lead to the increase of TMR.

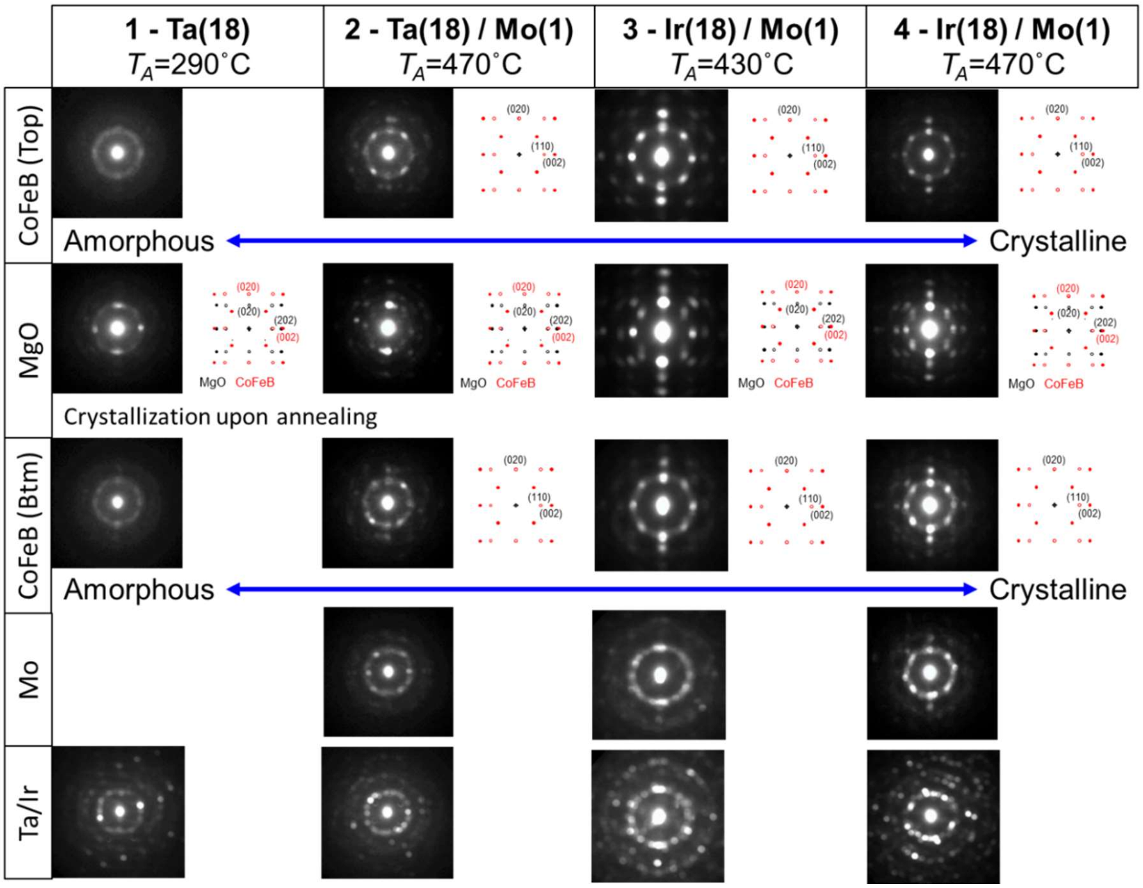

Figure 6-11 TEM diffraction patterns for different material layers (top CoFeB, MgO, bottom CoFeB, Mo spacer, and Ta/Ir seed) in the four selected samples: 1, Ta seed annealed at 290°C; 2, Ta/Mo seed annealed at 470°C; 3, Ir/Mo seed annealed at 430°C; and 4, Ir/Mo seed annealed at 470°C. The detailed stack structure and annealing conditions of these 4 samples are also shown in Figure 6-9. The key diagram of the diffraction patterns for CoFe and MgO are plotted against the diffraction pattern to illustrate the lattice orientation of CoFe and MgO layers. It is indicated using arrow that the multilayers evolve from amorphous to crystalline from sample 1 to sample 4, which is consistent with the increase of TMR from sample 1 to 4.

Before delving into the EELS and EDS data, it is worthy to compare the two Ir/Mo samples annealed at 430°C and 470°C respectively as shown in Figure 6-12. As shown in the Annular dark-field imaging of scanning transmission electron microscope ADF-STEM image on the top, the crystallinity of the CoFeB and MgO annealed at 470°C is enhanced compared with the case annealed at 430ºC. To check whether this is commonly observed feature, dark field imaging was done for large area. Excited diffraction spots are indicated by arrows in the diffraction patterns. As shown in the dark field images exciting MgO (020) and CoFe (020), the CoFeB and MgO layers in the sample annealed at 470ºC has more excited crystallites compared to those in the 430ºC annealed sample. This nature would explain the higher TMR in the sample annealed at 470ºC.

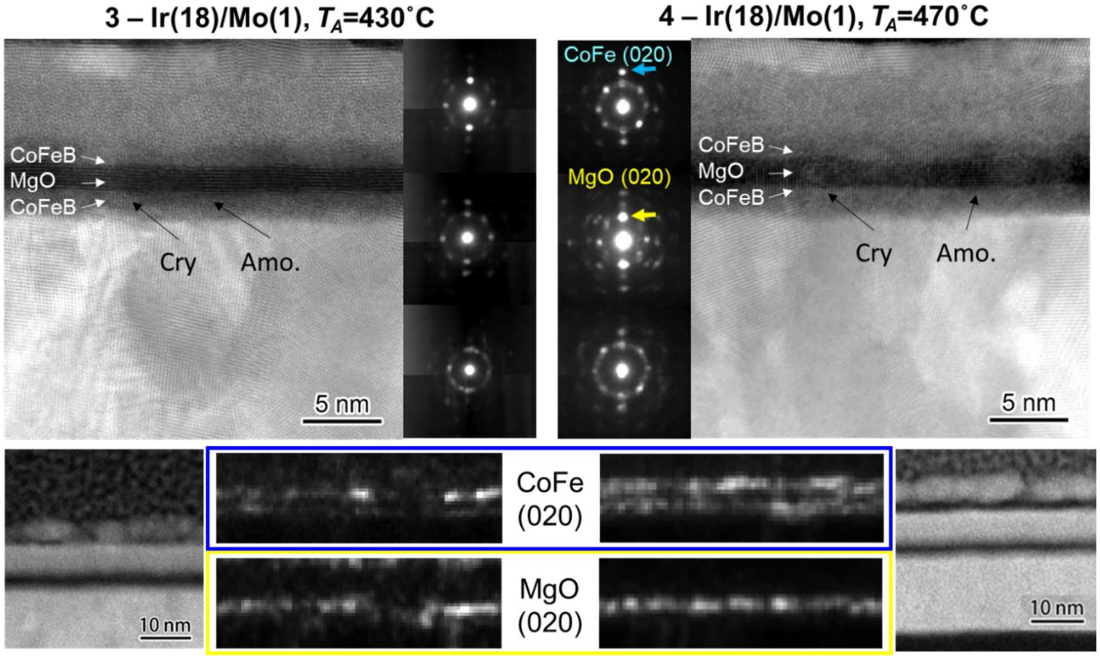

Figure 6-12 (Top) ADF-STEM imaging of sample 3 Ir/Mo seed annealed at 430ºC; and sample 4, Ir/Mo seed annealed at 470ºC. Diffraction patterns of CoFeB and MgO layers are shown in the middle with CoFe (020) and MgO (020) diffraction points indicted by arrows. (Bottom) Dark-field imaging of excited MgO (020) and CoFe (020) crystallites of sample 3 and 4. The larger number of both CoFe (020) and MgO (020) crystallites in sample 4 confirms the better crystallinity of sample 4 than sample 3, as shown in Figure 6-11.

Next, we will analyze the element-specific EDS data obtained on these 4 samples to further correlate the measured TMR, VCMA, PMA and saturation magnetization values with element-specific data. In particular, EDS is capable of capturing the inter-diffusion of different elements in a MTJ stack at different annealing temperatures. Thus we can obtain a lot of detailed material data including the degree of CoFe alloying, Fe/Co oxidation, inter-diffusion of Mg, seed and Mo spacer into CoFe, etc. As shown in Figure 6-13, the detailed distribution of all elements except Boron are mapped out along the vertical direction of the sputtered films.

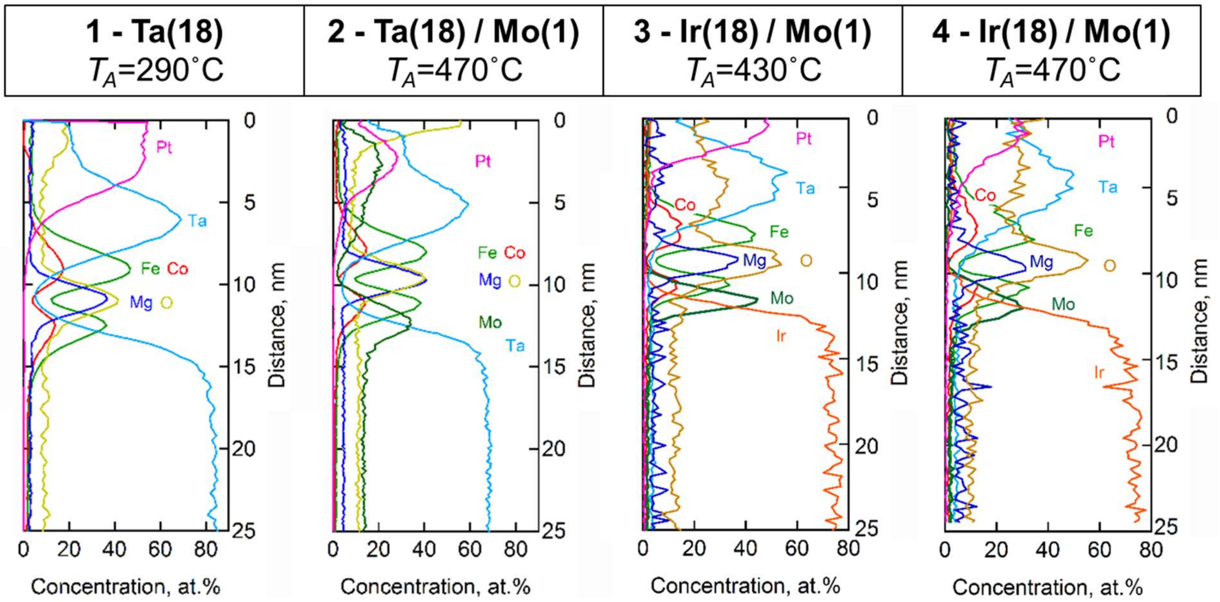

Figure 6-13 Energy Dispersive X-ray Spectroscopy (EDS) element distribution data of Ta, Co, Fe, Mg, O, Mo, Ir, Pt in the four selected samples, i.e. 1, Ta seed annealed at 290ºC; 2, Ta/Mo seed annealed at 470ºC; 3, Ir/Mo seed annealed at 430ºC; and 4, Ir/Mo seed annealed at 470ºC. The detailed stack structure and annealing conditions of these 4 samples are also shown in Figure 6-9.

6.3.4 Correlation between Element-Specific Data and Device-Level Data

First, the method we used to gather element-specific data is described as the following. As shown in Figure 6-14 Left figure, the EDS data illustrates the atomic concentration of each element along the depth profile of the whole MTJ stack. As illustrated in Figure 6-14 Left figure, the green region delineates the concentration of Fe in the CoFeB layer on top of the MgO barrier (hereafter referred to as the top Fe). Then the brown region delineates the concentration of O overlapping with the Fe content region in the top CoFeB layer. Hence, the O atomic concentration in the top Fe content can be calculated through dividing the O concentration (brown region) over the top Fe concentration (green region). If the O atomic concentration in top Fe is plotted for all the four selected samples, we find that the trend correlates rather well with the TMR ratio of these four samples, as shown in Figure 6-14 Right figure. This indicates that the TMR ratio increase driven by the crystallinity improvement of both CoFeB layers will also coexist with an increased oxygen content in the top Fe. Note that we also calculated the relative oxygen concentration in bottom Fe (see Figure 6-16) and in the MgO barrier region (data now shown), neither of these oxygen concentrations values correlate with the TMR values. The reason might be that the change of the top CoFeB polarization is more sensitive to different seeds and annealing temperatures than that of the bottom CoFeB.

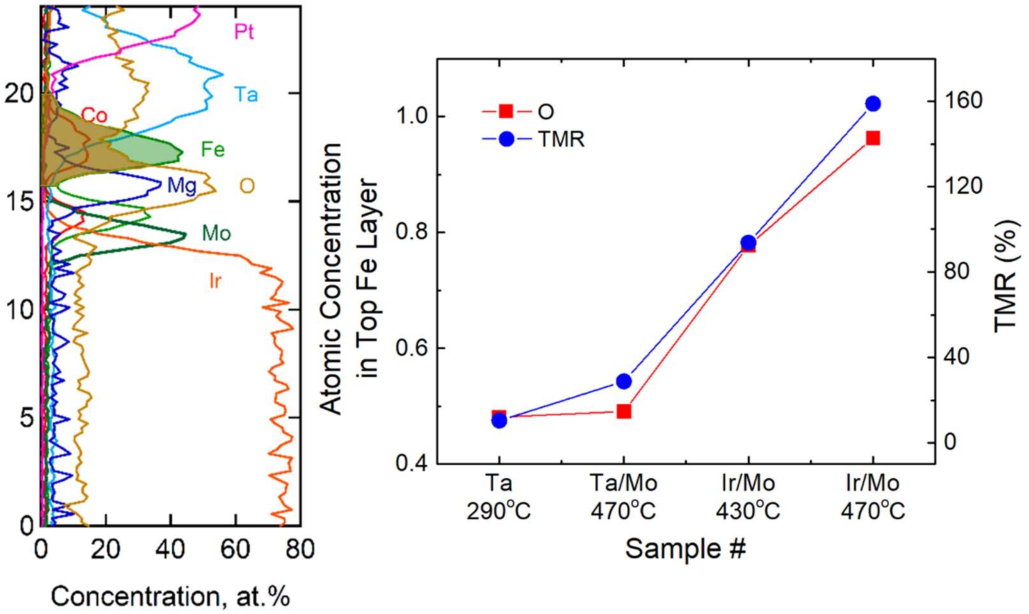

Figure 6-14 (Left) EDS element distribution data of sample 3, Ir/Mo seed annealed at 430°C. The Fe element concentration in the top CoFeB layer is highlighted with green color, and the O concentration overlapping with the top Fe content is highlighted with brown color. (Right) The atomic concentration of O in the top Fe, as calculated by the ratio of O highlighted area over Fe highlighted area in the Left figure, and the tunneling magnetoresistance (TMR) ratio as a function of the four selected samples, i.e. 1, Ta seed annealed at 290°C; 2, Ta/Mo seed annealed at 470°C; 3, Ir/Mo seed annealed at 430°C; and 4, Ir/Mo

seed annealed at 470ºC. The detailed stack structure and annealing conditions of these 4 samples are also shown in Figure 6-9. The correlation between the O concentration in top Fe and the TMR ratio confirms that TMR increase in our samples is driven by the O concentration in top Fe.

Below, we will analyze the effects of O concentration in the top Fe. Though some existing *ab initio* works [227, 228] indicate that the small oxygen concentration in the asymmetric Fe/FeO$_x$/MgO/Fe structure will result in a large decrease of TMR, there is inevitably diffusion of oxygen into the CoFeB layer adjacent to the MgO layer during annealing process[229]. Hence, *ab initio* calculation of the symmetric Fe/FeO/MgO/FeO/Fe structure is a better estimate of the experimental reality. One *ab initio* work [229] has found that the symmetric presence of FeO layer at both sides of the MgO barrier will result in coherent tunneling through interface resonance states in the FeO layer. While the asymmetric Fe/FeO/MgO/Fe structure does not have coherent tunneling thus exhibits a lower TMR than Fe/FeO/MgO/FeO/Fe. Therefore, the increase of O concentration at the Fe layers might also induce a higher TMR due to enhanced coherent tunneling.

Next, we will look at the correlation between the bottom CoFe alloy ratio, bottom CoFe saturation magnetization and interfacial PMA of the bottom CoFeB/MgO interface. Similar as Figure 6-14 Left figure, the relative concentration of Co and Fe in the bottom CoFeB layer can be obtained by integrating the area of the EDS Co and Fe curve for the bottom CoFeB layer. To compare the dependence of CoFe saturation magnetization and the Slater-Pauling curve, we plotted the average valence electrons number per atom (*Z*) for the CoFe alloy considering each Fe has 26 valence electrons and each Co 27. As shown in Figure 6-15 Top figure, the highest saturation magnetization values correspond to a *Z* number of around 26.26 to 26.30, while the saturation magnetization values will decrease when *Z* is outside of this range. This observed optimal *Z* number is consistent with the well-known Slater-Pauling curve of CoFe alloy.[230] Hence, it can be concluded that the CoFe alloy ratio is the most critical factor for determining the saturation magnetization in these ultrathin MTJ stacks. Another physical property that can be correlated with the CoFe alloy ratio is the interfacial PMA. As shown in Figure 6-15 Bottom figure, x as in $Co_{1-x}Fe_x$ and the interfacial PMA correlate very well with each other across the four selected samples. This clearly indicates that the interfacial PMA originates mainly from the Fe and O orbital hybridization, instead of the Co and O orbital hybridization. The above conclusion is also consistent with previous *ab initio* calculations[107] and experimental results[231] where Fe-rich CoFeB will give rise to larger interfacial PMA than Co-rich CoFeB.

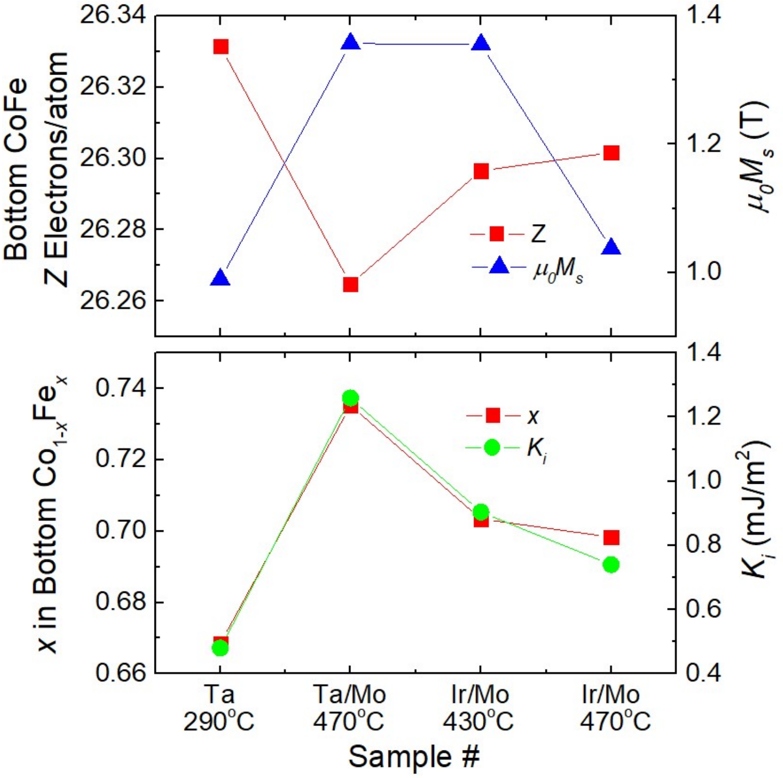

Figure 6-15 (Top) Number of valence electrons per atom *Z* for bottom CoFe alloy and saturation magnetization ($\mu_0 M_s$) of the bottom CoFeB layer; (Bottom) The alloy ratio x as in bottom $Co_{1-x}Fe_x$ and the interfacial PMA (K_i) as a function of the four selected samples, i.e. 1, Ta seed annealed at 290°C; 2, Ta/Mo seed annealed at 470°C; 3, Ir/Mo seed annealed at 430°C; and 4, Ir/Mo seed annealed at 470°C.

The detailed stack structure and annealing conditions of these 4 samples are also shown in Figure 6-9. The data shows clear correlation between the Fe concentration, PMA, and saturation magnetization of the bottom CoFe alloy.

Lastly, the VCMA coefficient can be correlated with the O and Mg concentration in the Fe content of the bottom CoFeB layer (hereafter referred to as bottom Fe). As shown in Figure 6-16 Top figure, the Mg and O concentration in the bottom Fe exhibit an opposite trend across the four selected samples. The higher the O content is, the lower the Mg content becomes. To better correlate the change of Mg and O with the evolution of the VCMA coefficient, it is useful to define the excessive O concentration which can be calculated through subtracting O concentration by Mg concentration. One justification for using this excessive O concentration is that as O has the highest formation enthalpy when reacting with Mg compared with Ta, Co, Fe, and Pt, and the Mg concentration profile follows that of the O closely, we can assume that all Mg will react with O and form MgO, thus the excessive O atomic concentration will be the dominating factor in reacting with the bottom Fe. As shown in Figure 6-16 bottom figure, the excessive O concentration correlates pretty well with the VCMA coefficient. This over-oxidation driven VCMA enhancement is consistent with Chapter 5 where the thin Mg insertion layer with over-oxidized CoFeB gives rise to the highest VCMA coefficient. Also, some *ab initio* works have shown similar results. [113, 175]

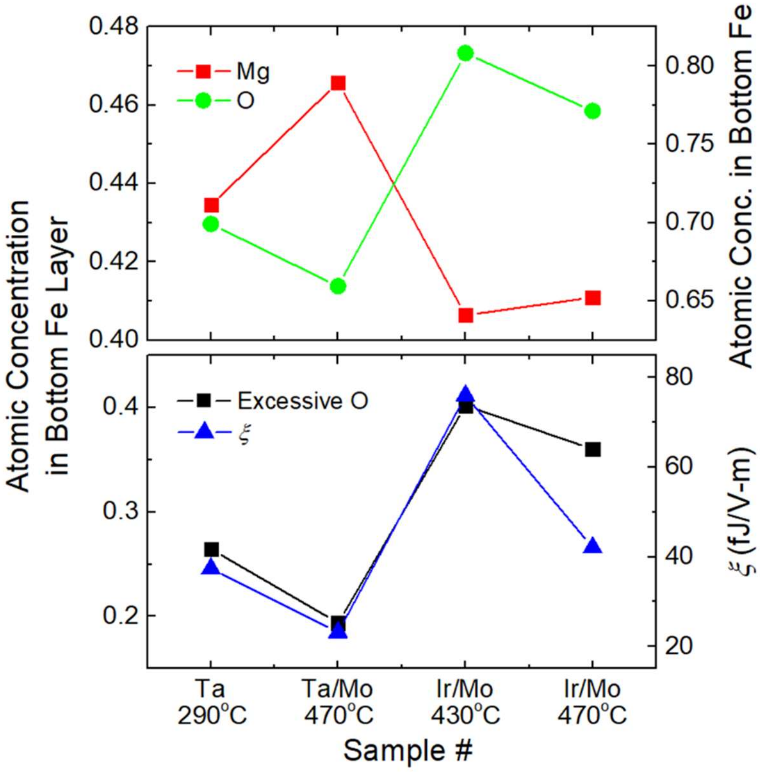

Figure 6-16 (Top) Mg and O atomic concentration in the bottom Fe; (Bottom) Excessive O atomic concentration in the bottom Fe and the VCMA coefficient (ξ) as a function of the four selected samples, i.e. 1, Ta seed annealed at 290ºC; 2, Ta/Mo seed annealed at 470ºC; 3, Ir/Mo seed annealed at 430ºC; and 4, Ir/Mo seed annealed at 470ºC. The detailed stack structure and annealing conditions of these 4 samples are also shown in Figure 6-9. The correlation between the excessive O concentration in bottom Fe and the VCMA confirms that VCMA increase in our samples is driven by the excessive O concentration in bottom Fe.

In addition, note that in Section 6.3.2, we found that the trend of TMR for a specific seed material annealed at different temperatures is in sharp contrast to the other values. Element-wise, we can explain the above observed trend by considering that only the TMR value is correlated to the top Fe, while VCMA, PMA, and saturation magnetization are all correlated to the bottom Fe. Because the top CoFeB layer is 2 nm and thicker than the bottom CoFeB layer ranging from 1 nm to 1.5 nm, the dependence of top and bottom Fe on annealing temperature is different. For the bottom Fe dependent properties (VCMA, PMA, and saturation magnetization), the Ir and Ta seeded samples show a monotonic decrease from 290ºC to 400ºC, the Ta/Mo seeded sample show a slow monotonic increase from 325ºC all the way to 470ºC, while the Ir/Mo samples show an inverse V-shaped curve with optimal value at 430ºC. If we look at the top Fe dependent property TMR, the Ir and Ta seeded samples show an optimal value at 325ºC, the Ta/Mo seeded sample still show a slow monotonic increase from 325ºC all the way to 470ºC, while the Ir/Mo samples show a large monotonic increase from 325ºC all the way to 470ºC. It can be concluded that the top Fe exhibit a higher thermal annealing stability than the bottom Fe. Effectively, the temperature-dependent curves of the TMR value is shifted to the high temperature end by around 40ºC. This indicates that the thicker CoFeB layer can sustain good magnetic properties at high annealing temperatures. The reason behind this might be that the other elements will have a smaller relative atomic concentration in Fe upon diffusion.[82]

Based on the insights gained from the above, we further designed an MTJ stack with even higher PMA and VCMA performance when annealed above 400ºC, which is also indicated by the green data point in Figure 6-1 as Ir/Mo(Mg). In particular, as shown in Figure 6-17(a), the new stack utilizes the Ir/Mo seed which possesses the best VCMA coefficient when annealed above 400ºC in the above analysis. It also takes advantage of the Mg insertion at the CoFeB/MgO interface which will induce over-oxidation of the CoFeB layers beneath the Mg insertion layer in the sputtering process.[217] In addition, an additional Mo insertion layer is used inside the CoFeB free layer, resulting in a much larger free layer thickness and interfacial PMA value. Similar works where Ta and W are inserted in the free layer also show drastic PMA increases.[232, 233] The cause of these higher PMA due to insertions could also be attributed to the higher Fe concentration in CoFe alloy. As Co has higher negative formation enthalpy to form alloy with Mo, Ta, W than Fe does,[234] Co tends to diffuse into the insertion layer and leave the CoFe layer more Fe-rich, thus resulting in a larger PMA.

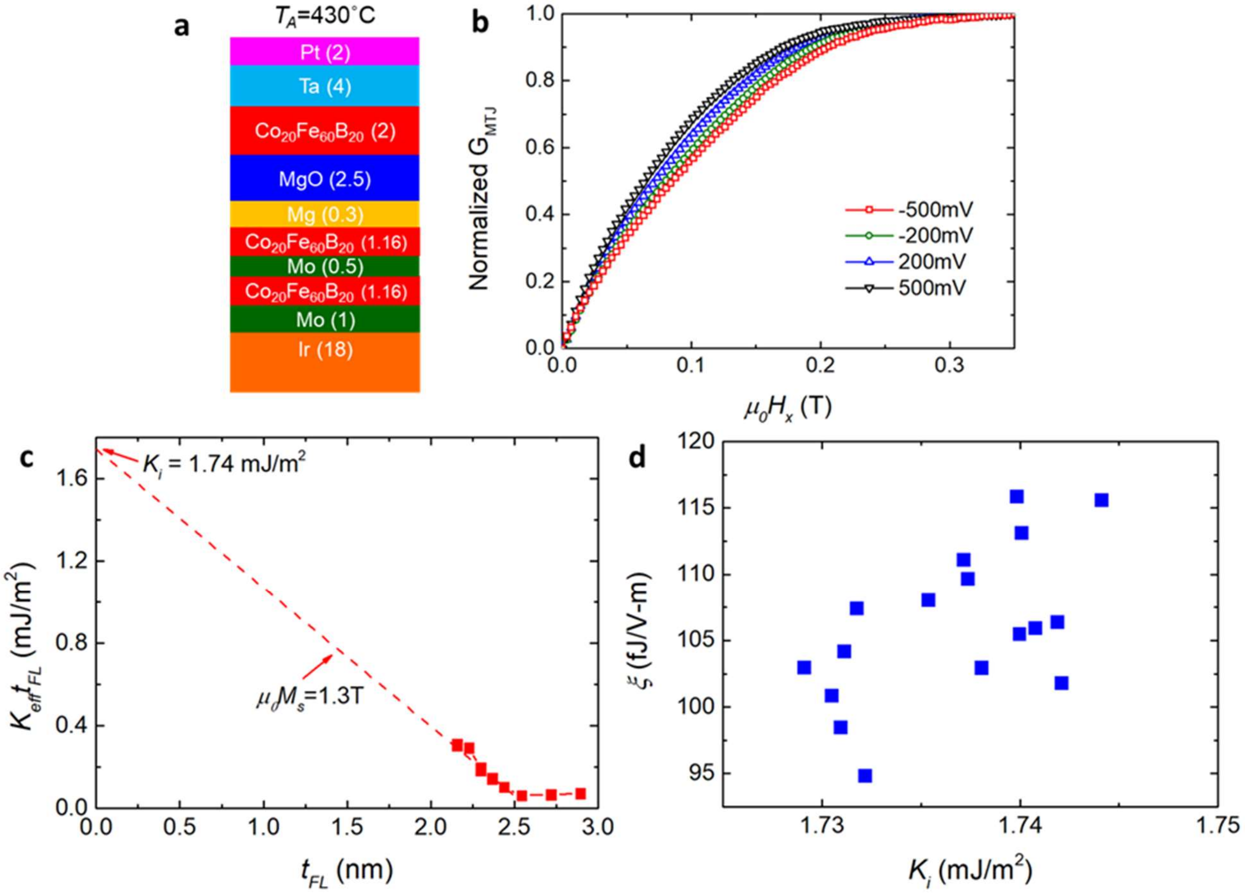

Figure 6-17 PMA and VCMA results for MTJ stack based on Ir/Mo seed and Mg insertion. a, MTJ stack structure and annealing condition. b, The normalized MTJ conductance dependences on in-plane external magnetic field for different MTJ bias voltages. c, Product of effective magnetic anisotropy (K_{eff}) and the total CoFeB thickness ($2t_{CoFeB}$) as a function of total CoFeB thickness. The interfacial PMA (K_i) and saturation magnetization ($\mu_0 M_s$) values obtained from linear fitting of the above curve are also indicated. d, The distribution of VCMA coefficients (ξ) and interfacial PMA values for 18 devices on the same chip.

As shown in Figure 6-17(c), the interfacial PMA and saturation magnetization values can be obtained from linear fitting of the $K_{eff}t_{FL}$ dependence of t_{FL} curve, resulting in an interfacial

PMA of 1.74mJ/m^2, where K_{eff} is the effective magnetic anisotropy and t_{FL} is the total free layer thickness adding the two CoFeB layers together. While in Figure 6-17(d), the VCMA and interfacial PMA distribution of 18 devices on the same chip is also illustrated, showing a rather tight distribution of VCMA ranging from 95 to 115 fJ/V-m, with K_i ranging from 1.73 to 1.75mJ/m^2.

This work has provided the key element-specific distribution parameters that directly correlates with these device-level parameters for device design. However, in practical materials design process, further guidance is required as with what materials stack and annealing conditions will result in the best CoFe alloy ratio and Fe oxidation concentration to achieve optimal device-level parameters such as high TMR for readout, enough PMA and saturation magnetization for thermal stability, and high VCMA for write efficiency. This requires a careful study on the diffusion coefficient of all used materials in the MTJ stack, the various formation enthalpy values for all possible chemical reaction in the MTJ stack upon annealing process, such as alloying, oxidation, and reduction. Based on these element chemical properties, the final element concentration distribution after annealing the whole MTJ stack might be simulated. Then the simulated data could be processed in the same manner as used in this work to predict the device-level parameters and provide feedback for iterative materials optimization towards the desired device parameters.

In conclusion, by exploring these different seed/spacer combinations, high VCMA coefficient of 115 fJ/V-m, TMR of 160%, and PMA of 1.74 mJ/m^2 annealed above 400°C were demonstrated using industrially applicable sputtering process, which are among the highest values reported.[118, 119, 216] In addition, we have carefully studied the correlation between element distribution and the magnetic properties of MTJ stacks with different seed annealed at different temperatures via high resolution transmission electron microscopy (TEM) experiments. The elemental distribution results show that the crystallinity of CoFeB, MgO and seed layer, as well as the oxygen concentration in the top Fe both correlate well with device TMR. The CoFe alloy ratio correlates well with the saturation magnetization and interfacial PMA values. While the higher oxygen concentration in the bottom Fe correlates well with the VCMA coefficient. These well-established correlations indicate that by materials engineering using various stack structures and annealing conditions, it is most critical to control the Co, O, and Mg atomic concentration in the top and bottom Fe to achieve the optimal VCMA, PMA, saturation magnetization, and TMR values. The insight obtained through the above analysis will provide critical guidance to future development of both spin-transfer torque and voltage-controlled magnetic memory.

Chapter 7 Summary and Outlook

7.1 Summary

Today, the world is on the cusp of transitioning from personal mobile electronic devices aiding almost all personal activities to intelligent low-power electronic devices controlling almost all human artifacts in the society. The need for faster, more energy-efficient and denser storage and access of information will continue to grow as data are being generated from more and more electronic devices. The continuous bandwidth advancement of logic transistors, Ethernet, and video outperforming the decades-old also calls for new memory solutions with higher bandwidth. More importantly, the emerging big data and machine learning applications that are data intensive have an even larger appetite for memory access with low latency and high bandwidth.

Various approaches have been explored to develop better memories, including further scaling down of existing technologies, various emerging non-volatile memory (NVM) technologies, and 3D stacking and packaging innovations over existing technologies to improve the memory bandwidth. In Chapter 1, we benchmark the newly emerging variation of Magnetoresistive Random Access Memory (MRAM), i.e. Magnetoelectric RAM (MeRAM) utilizing voltage-controlled magnetic anisotropy (VCMA) effect against other existing, prototypical, and emerging technologies with a focus on array-level memory performance, comparison in particular with spin-transfer-torque RAM (STT-RAM), potential system-level 3D integration, and scaling at advanced nodes. Then a historical overview of the evolution of different MRAM read and write mechanisms is presented to introduce the basic MRAM related technical concepts and parameters that are critical for understanding the remaining parts of this dissertation.

In Chapter 2, we introduce the fundamentals of magnetic memory analysis including statics and dynamics of the magnetization in any energy landscape. Then the physics origin of the perpendicular magnetic anisotropy (PMA) and the VCMA effect, i.e. spin-orbit coupling is discussed. The voltage-induced modulation of the orbitals occupancy and energy separations of these orbitals via spin-orbit coupling is the origin of the modulation of the PMA as well as the interfacial magnetization. In addition, we will discuss the drastic effect of strain in the magnetic multilayers on both PMA and VCMA, which is an important changing parameter under different deposition and annealing conditions. Based on the above basic understanding, the requirements for reliable MeRAM operation when scaled at advanced nodes is analyzed and other challenges facing MeRAM are briefly presented.

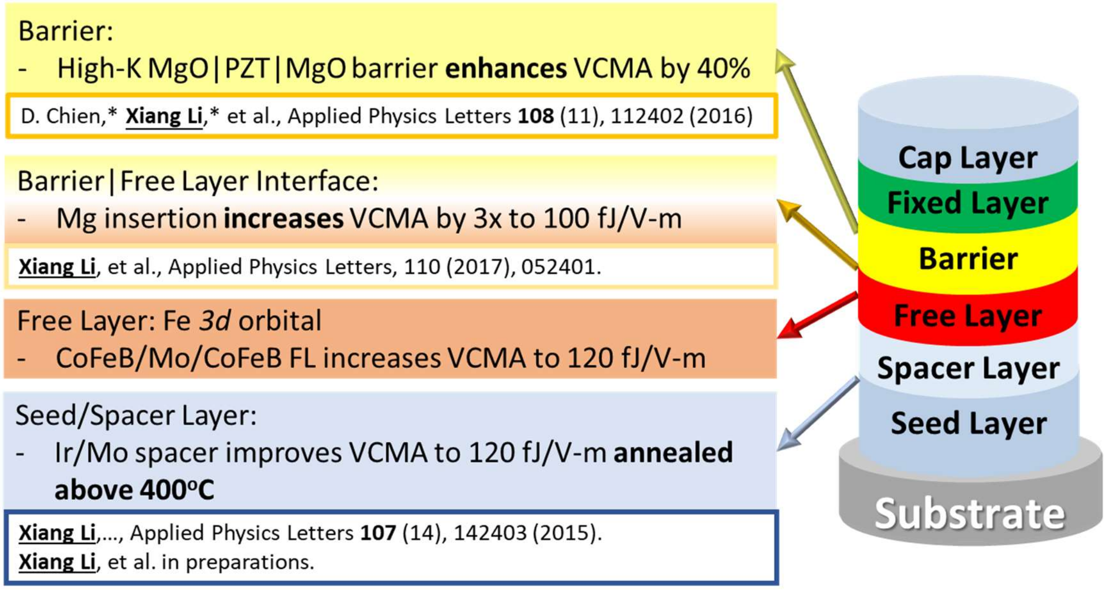

Figure 7-1 Summary of different approaches and potential future work to increase the VCMA coefficient by materials engineering of the MeRAM stack. Published paper references are also included.

Following the physics and device operation of the VCMA effect, in Chapter 3, we first briefly discuss the deposition and fabrication methods for MRAM devices. Among them, the magnetron sputtering and inductively coupled plasma (ICP) etching are used for MeRAM devices shown in this dissertation. Next, we discuss in detail the advantages and disadvantages of the two electrical measurement techniques we used to quantify the VCMA effect, i.e. the weak reference layer MTJ measurement, and the anomalous Hall measurement. We also emphasize the importance of using the most accurate assumptions in data processing.

Then, three approaches taken to enhance the VCMA coefficient with a value of around 30 fJ/V-m in standard Ta/CoFeB/MgO structures will be presented, a summary figure of these three approaches are also illustrated in Figure 7-1. As the VCMA effect takes place via charge accumulation and depletion at the insulator barrier interface, in Chapter 4, we demonstrated a novel method to integrate an ultra-thin layer of high-ϵ lead zirconate titanate (PZT or $Pb(Zr_xTi_{1-x})O_3$) thin film into the MgO tunnel barrier, which increases the VCMA coefficient by 40%, while maintaining sizable room-temperature tunneling magnetoresistance (TMR) values only slightly lower than in those of MgO barrier MTJs.

In Chapter 5, we systematically studied how inserting various materials (Ta, Pt, and Mg) at the CoFeB/MgO interface affects the VCMA effect. A maximum VCMA coefficient of around 100 fJ/V-m was realized for a very thin Mg insertion layer, which is more than 3 times larger compared to average VCMA values reported for traditional CoFeB/MgO stacks where no material is inserted. Using XRD results, the emergence of strong CoFe and MgO crystalline peaks is correlated to the maximum PMA and saturation magnetization. This indicates that precise control over the Mg insertion thickness and CoFe oxidation level at the CoFeB/MgO interface is critical to achieving the desired device performance, with a tradeoff between VCMA, PMA, and saturation magnetization.

Last in Chapter 6, different heavy metal based seed/Mo materials are explored to achieve stable VCMA coefficient of 115 fJ/V-m, TMR of 160%, and perpendicular magnetic anisotropy (PMA) of 1.74 mJ/m^2 when annealed at temperatures exceeding 400°C were demonstrated using industrially applicable sputtering process, which are among the highest values reported. This will enable MeRAM to be compatible with embedded applications. We have carefully studied the correlation between element distribution and the magnetic properties of MTJ stacks with different seed annealed at different temperatures via high resolution transmission electron microscopy (TEM) experiments. TEM results show that the crystallinity of CoFeB, MgO and seed layer, as well as the oxygen concentration in the top Fe both correlate well with device TMR. The CoFe alloy ratio correlates well with the saturation magnetization and interfacial PMA values. While the higher oxygen concentration in the bottom Fe correlates well with the VCMA coefficient. These well-established correlations indicate that by materials engineering using various stack structures and annealing conditions, it is most critical to control the Co, O, and Mg atomic concentration in the top and bottom Fe to achieve the optimal VCMA, PMA, saturation magnetization, and TMR values. These experimental results as well as physical understandings will shed light on how to further improve MeRAM materials for on-chip cache at advanced nodes as well as utilize Mo as spacer layer for embedded MRAM with high thermal stress stability.

7.2 Outlook

Looking to the future, the prospect of bringing MeRAM into commercial product faces several challenges.

First, the need for high VCMA and PMA materials that are compatible with BEOL processing temperatures is still a pre-requisite for commercial MeRAM cache solutions as discussed in detail in Section 2.4. In view of the recent breakthrough of sputtering deposited CoFe/MgO junction with VCMA around 750-1050 fJ/V-m with PMA of 1.91 mJ/m^2, [120] it is highly possible that by combining the highly epitaxial film stack with thermal diffusion barriers such as Mo and W as discussed in Chapter 6 of this dissertation, high VCMA and PMA that are stable under 400°C annealing temperatures can be achieved.

It is also critical to achieve high TMR ratio with BEOL-compatible processing temperature. The main driver behind this is actually that the majority of operation in a cache is read instead of write. [235] Though a lot of innovations have been discovered to increase the magnetic-based reading signal from around 1% in an AMR device to around 600% in an MgO-based in-plane magnetic tunnel junction as illustrated in Figure 1-10, the on/off ratio for readout is still significantly smaller than that of the CMOS technology which is usually above 10^4 [236, 237] or even other non-volatile memory technologies which ranges from 10 to 10^6 for ReRAM with different conducting mechanisms, i.e. oxide-RAM or conductive bridge RAM, and 10 to 1000 for PCRAM. [238] This small TMR ratio poses great challenges for designing circuits with fast sensing and low read disturbance. Though there are several circuit-level proposals to alleviate this issue via dual-data line sensing [239] and negative differential resistance[240], the quest for high TMR magnetic memory devices is still highly desired especially considering process variations.

Of course, materials-level innovations are not the guarantee of mass production. It is critical to improve the processing capabilities for high-yield devices manufactured in high volume. While commercialization also requires the product-market fit and strong competitive advantage over other alternative solutions.

Chapter 8 Appendices

Appendix 1: Julliere's Tunneling Magnetoresistance Theory

As introduced in Section 1.3.1, we will illustrate how Equation 1-1 is obtained in detail.

$$TMR = \frac{R_{AP}-R_P}{R_P} = \frac{2P_1P_2}{1-P_1P_2} \qquad \text{Equation 1-1}$$

First, for tunneling through an insulator with normal metals on two sides, we can write the quantum-mechanical transition current across the insulator from an occupied state $\boldsymbol{k_1}$ on the left side of the barrier to an unoccupied state $\boldsymbol{k_2}$ on the right side as the following [241]

$$i = 4\pi e/\hbar \sum_{k_t} \sum_{k_x} |M|^2 n_2 f_1 (1 - f_2) \qquad \text{Equation 8-1}$$

where k_t (k_x) is the component of wave number transverse (perpendicular) to the barrier, e is the electron charge, $|M|^2$ is the transition matrix element, n_1 (n_2) is the density of states on the left (right) of the barrier, f_1 (f_2) is the probability that state $\boldsymbol{k_1}$ $(\boldsymbol{k_2})$ is occupied.

Summing the above equation over k_x to an integral over the energy level with fixed k_t gives rise to

$$i = A \sum_{k_t} \int_{-\infty}^{\infty} |M|^2 n_1 n_2 f_1 (1 - f_2) dE \qquad \text{Equation 8-2}$$

where A is a constant and E is the energy measured from the Fermi energy. Then one can write similar current equation as above to describe the current flow from an occupied state on the right of the barrier to an unoccupied state on the left of the barrier. A simple subtraction of the two will result in the following

$$I = A \sum_{k_t} \int_{-\infty}^{\infty} |M|^2 n_1 n_2 (f_1 - f_2) dE$$ Equation 8-3

If we assume that $|M|^2$ is constant over the energy of interest, and the voltage potential difference between the barrier is V and minimally small, then the total current can be simplified as

$$I = A' n_1(E_F) n_2(E_F) eV$$ Equation 8-4

Then, if we consider there are two spin channels for a ferromagnetic/insulator/ferromagnet trilayer structure, and we assume there is no spin flip in the spin transport as a first approximation, then the total conductance is the sum of the two spin channel conductance as following

$$G = eA'(N_{\uparrow 1} N_{\uparrow 2} + N_{\downarrow 1} N_{\downarrow 2})$$ Equation 8-5

where $N_{\uparrow 1}(N_{\uparrow 2})$ is the spin up density of states on the left (right) of the barrier, while $N_{\downarrow 1}(N_{\downarrow 2})$ is the spin down density of states on the left (right) of the barrier. Then, we can write down the conductance of the MTJ when two ferromagnetic layers have parallel magnetization, and when they have anti-parallel magnetization.

$$G_P = eA'(N_{M1} N_{M2} + N_{m1} N_{m2});\ G_{AP} = eA'(N_{M1} N_{m2} + N_{m1} N_{M2})$$ Equation 8-6

where spin-split DOS at the Fermi level for majority and minority spin electrons are designated as N_M, N_m. Thus, we can write down the TMR value and find it to the same as Equation 1-1.

$$TMR = \frac{R_{AP} - R_P}{R_P} = \frac{G_P - G_{AP}}{G_{AP}} = \frac{2P_1 P_2}{1 - P_1 P_2}$$ Equation 8-7

where the spin polarization of the ferromagnet at the two sides of the barrier is defined as the following: $P_1 = \frac{N_{M1} - N_{m1}}{N_{M1} + N_{m1}}, P_2 = \frac{N_{M2} - N_{m2}}{N_{M2} + N_{m2}}$.

Appendix 2: Slonczewski's Tunneling Magnetoresistance Theory

As introduced in Section 1.3.1, we will illustrate how the following equation is obtained in detail.

$$G = G_0(1 + p_F^2 cos\theta) \qquad \text{Equation 1-3}$$

A more careful characterization of the tunneling magnetoresistance can be obtained by solving a full-fledged tunnel barrier problem in quantum mechanics. If one uses a free-electron approximation of the spin-polarized conduction electron inside the ferromagnetic electrodes, the Hamiltonian as a function of the longitudinal location across the MTJ stack will be the following:

$$\mathcal{K}_x = -\frac{1}{2}\left(\frac{d}{dx}\right)^2 + U(x) - \boldsymbol{h}(x) \cdot \boldsymbol{\sigma} \qquad \text{Equation 8-8}$$

which consists of the kinetic energy, potential energy, and the internal exchange energy where $-\boldsymbol{h}(x)$ is the molecular field and $\boldsymbol{\sigma}$ is the conventional Pauli spin operator. In this case, a rectangular barrier is used where $U = U_0$ and $\boldsymbol{h} = 0$ inside the barrier region with a depth of d, while outside we assume $U = 0$ and same ferromagnetic materials at both sides which possess the same $|\boldsymbol{h}| = h_0$ but different directions, the angle between the directions of $\boldsymbol{h_1}$ and $\boldsymbol{h_2}$ being defined as θ.

Then one can obtain the wave function solutions in all three regions for a spin-up incident wave in region 1 (left side of the barrier) by solving the Schrodinger equation with the above Hamiltonian and standard boundary conditions.

$$\psi_{\uparrow 1} = k_\uparrow^{-1/2} e^{ik_\uparrow x} + R_\uparrow e^{-ik_\uparrow x}, \psi_{\downarrow 1} = R_\downarrow e^{-ik_\downarrow x} \text{ for ferromagnet 1}$$

$$\psi_{\sigma 2} = A_\sigma e^{-\kappa x} + B_\sigma e^{\kappa x}, \sigma = \uparrow, \downarrow \text{ for barrier region}$$

$$\psi'_{\sigma 3} = C_\sigma e^{ik_\sigma (x-d)}, \sigma = \uparrow, \downarrow \text{ for ferromagnet 2} \qquad \text{Equation 8-9}$$

where k_σ is the electron momentum in the ferromagnet regions, and $i\kappa$ is the imaginary electron momentum, and the coefficients are expressed in more details in reference [83].

Next, based on the solved wave function, one can calculate the spin transmissivity as

$$T_p = \operatorname{Im} \sum_\sigma \sigma \psi_\sigma^* \left(\frac{d\psi_\sigma}{dx} \right) \qquad \text{Equation 8-10}$$

Then the conductance is expressed as a function of the spin transmissivity

$$G = \frac{e^2}{8\pi^2 \hbar} \frac{\kappa T_p}{d} = G_0 (1 + p_F^2 cos\theta) \qquad \text{Equation 8-11}$$

where the effective spin polarization of the ferromagnet-barrier couple is

$$p_F = \frac{(k_\uparrow - k_\downarrow)(\kappa^2 - k_\uparrow k_\downarrow)}{(k_\uparrow + k_\downarrow)(\kappa^2 + k_\uparrow k_\downarrow)} \qquad \text{Equation 8-12}$$

The mean surface conductance is

$$G_0 = \frac{\kappa}{\hbar d} \left(\frac{e\kappa(\kappa^2 + k_\uparrow k_\downarrow)(k_\uparrow + k_\downarrow)}{\pi(\kappa^2 + k_\uparrow^2)(\kappa^2 + k_\downarrow^2)} \right)^2 e^{-2\kappa d} \qquad \text{Equation 8-13}$$

Appendix 3: Spin-Transfer Torque Switching Critical Current

In order to derive the following two equations, one has to start with a Stoner-Wohlfarth macrospin model described using the Landau-Lifshitz-Gilbert equation.

$$\frac{I_{c0}}{\Delta} = \left(\frac{4e\alpha kT}{\hbar \eta} \right) \left(1 + \frac{H_d}{2H_k} \right) \qquad \text{Equation 1-4}$$

$$\frac{I_{c0}}{\Delta} = \frac{4e\alpha}{\hbar \eta} \qquad \text{Equation 1-5}$$

First, as defined in Figure 8-1, the magnetic layer has a length of l_m along the e_x direction, and a in both e_y, e_z directions.[242] The energy landscape can be fully described considering the following three items. An applied field H in the plane of $e_y - e_z$, making an angle of ψ with e_z; a uniaxial anisotropy energy U_K with easy axis along e_z direction; and an easy-plane anisotropy U_p in the plane of $e_y - e_z$, effectively describing the in-plane shape anisotropy when the ferromagnetic layer is a thin film with $l_m \ll a$. Then the magnetization M is described by the coordinates (θ, φ), and the spin current S possessing a direction at an angle of ϕ with e_z direction passing along the $-e_x$ direction, and the spin polarization factor is η.

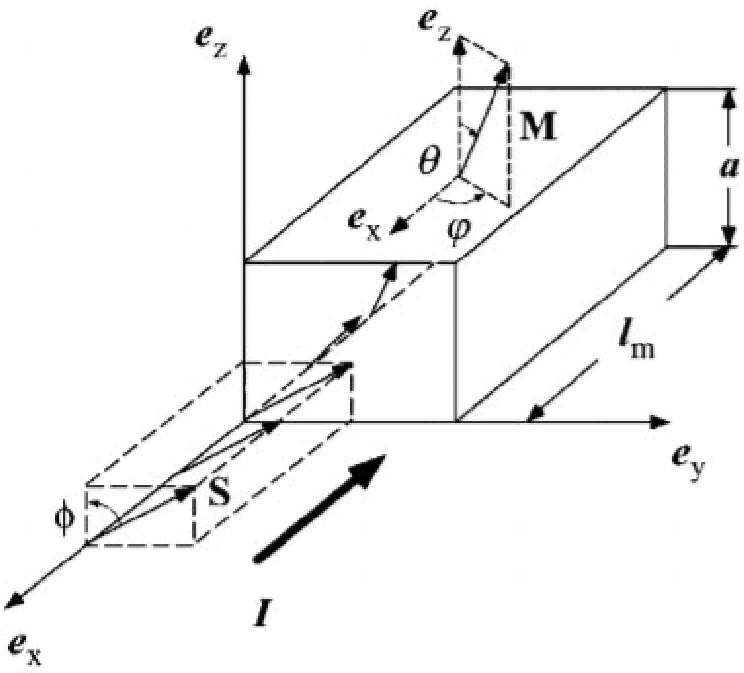

Figure 8-1 Model geometry definition and related mathematical symbols for a magnetic layer under spin current injection

Thus, one can write the total energy landscape to be

$$U = U_K + U_p + U_H = \frac{1}{2} M_s H_k \sin^2\theta + 2\pi M_s^2 (\sin^2\theta \cos^2\varphi - 1) -$$

$$MH(sin\theta sin\varphi sin\psi + cos\theta cos\psi) \qquad \text{Equation 8-14}$$

where H_k is the uniaxial magnetic anisotropy field, M_s is the saturation magnetization. Then the torques acting upon the magnetization can be obtained by taking the derivative of the total energy by the angles in a spherical unit system.

$$\frac{\Gamma_U}{l_m} = -n_m \times \nabla U(\theta, \varphi) \qquad \text{Equation 8-15}$$

Corresponding to the three terms in the energy landscape, there emerge three torques which are shown in [242]. In addition, the spin current will also generate a spin transfer torque. Assuming that the spin current only transfer angular-momentum to the magnetization in the direction perpendicular to M, then the spin torque can be expressed as

$$\Gamma_{ST} = \frac{\hbar\eta J}{2e} n_m \times (n_s \times n_m) \qquad \text{Equation 8-16}$$

where $s = \frac{\hbar\eta J}{2e}$ is the spin-angular momentum deposited per unit time, $\eta = (J_\uparrow - J_\downarrow)/(J_\uparrow + J_\downarrow)$ is the spin-polarization factor of the incident current J, and n_s is a unit vector of the initial spin direction of the current.

Substituting all of the above torques into the Landau-Lifshitz-Gilbert equation as

$$\frac{dn_m}{dt} = \frac{\gamma}{l_m M}(\Gamma_U + \Gamma_{ST}) - \alpha n_m \times \frac{dn_m}{dt} \qquad \text{Equation 8-17}$$

where α is the Gilbert damping coefficient and $\gamma = g\mu_B/\hbar$ is the gyromagnetic ratio. The above equation then can be simplified to be

$$\frac{1+\alpha^2}{\gamma H_k}\frac{d\theta}{dt} = -\theta\left[\alpha(1+h) + h_p(sin\varphi + \alpha cos\varphi)cos\varphi + h_s\right]$$

$$\frac{1+\alpha^2}{\gamma H_k}\frac{d\varphi}{dt} = -1 - h_p(cos\varphi - \alpha sin\varphi)cos\varphi - h + h_s\alpha \qquad \text{Equation 8-18}$$

where $h = H/H_k$, $h_p = 4\pi M_s/H_k$, $h_s = (\hbar/2e)\eta J/l_m M_s H_k$.

Then one can write the total energy change over time as the following while assuming $\varphi = \pi/2, \theta = \theta_0 \ll 1$ small initial angle

$$\frac{2}{M_s H_k}\frac{1+\alpha^2}{\gamma H_k}\frac{dU}{dt} = -2(1+h)\left[\left(1+h+\frac{1}{2}h_p\right)\alpha + h_s\right]\theta_0^2 \qquad \text{Equation 8-19}$$

For $|h| < 1$, the above equation presents the on-axis stability threshold for spin-current-driven motion at the small cone-angle limit. When the above equation is larger than zero, instability occurs as

$$h_s < h_{sc} = -\left(1+h+\frac{1}{2}h_p\right)\alpha \qquad \text{Equation 8-20}$$

Hence we have the critical current density as the following

$$I_c = a^2 J_c = \frac{2e}{\eta\hbar}\frac{\alpha}{|cos\phi|}a^2 l_m H_k M_s\left(1+\frac{2\pi M_s}{H_k}+\frac{H}{H_k}\right) \qquad \text{Equation 8-21}$$

Considering the thermal stability factor as the following

$$\Delta = \frac{a^2 l_m H_k M_s}{2kT} \qquad \text{Equation 8-22}$$

Therefore critical current over thermal stability factor under zero external magnetic field when the spin current direction is antiparallel to the magnetization direction ($\phi = \pi$) is

$$\frac{I_{c0}}{\Delta} = \left(\frac{4e\alpha kT}{\hbar\eta}\right)\left(1+\frac{2\pi M_s}{H_k}\right) = \left(\frac{4e\alpha kT}{\hbar\eta}\right)\left(1+\frac{H_d}{2H_k}\right) \qquad \text{Equation 8-23}$$

where $H_d = 4\pi M_s$ is the out-of-plane demagnetization field.

In the case of magnetic layer with an perpendicular easy-axis, the demagnetization field H_d effectively can be eliminated by the introduction of the perpendicular anisotropy field $H_{k\perp}$ ($> H_d$). In this case, the above equation will be modified to be

$$\frac{I_{c0}}{\Delta} = \frac{4e\alpha k}{\hbar\eta}$$ Equation 1-5

Next, we will consider the spin Hall effect induced switching of a ferromagnet/heavy metal bilayer structure. According to the definition of the spin Hall effect, the spin Hall angle θ_{SH} is defined as $J_S = \theta_{SH} J_C$ where J_S is the spin current density generated through a charge current with density J_C passing through the heavy metal strip adjacent to the ferromagnet layer. Considering that $I_{SH} = J_C A_{Ta}$, we can obtain the following equation

$$\frac{I_{SH}}{I_{STT}} = \frac{J_S^{SH} A_{Ta}/\theta_{SH}}{J_S^{STT} A_{MTJ}/\eta}$$ Equation 8-24

As the spin current needed to switch a ferromagnet is similar in both spin transfer torque and spin Hall cases, we can obtain Equation 1-6.

Appendix 4: Equivalence of Two forms of Landau-Lifshitz and Gilbert Equation

Here we refer to the first equation below as LL equation while the second one LLG equation.

$$\frac{dM}{dt} = -\gamma_0' M \times H_{eff} - \frac{\lambda}{M_s} M \times (M \times H_{eff})$$ (Landau-Lifshitz)

$$\frac{dM}{dt} = -\gamma_0 M \times H_{eff} + \frac{\alpha}{M_s} M \times \frac{dM}{dt}$$ (Gilbert)

Equation 2-7

Now we will prove the equivalence of the two equations above using a solution of LLG equation first, do the cross product of M with the LLG equation gives:

$$M \times \frac{dM}{dt} = -\gamma_0 M \times M \times H_{eff} + \frac{\alpha}{M_S}\left(M \times M \times \frac{dM}{dt}\right)$$ Equation 8-25

As $M \times M \times \frac{dM}{dt} = M\left(M \cdot \frac{dM}{dt}\right) - \frac{dM}{dt}M_S^2$, and $M \cdot \frac{dM}{dt} = 0$, thus

$$M \times \frac{dM}{dt} = -\gamma_0 M \times M \times H_{eff} - \alpha M_S \frac{dM}{dt} \qquad \text{Equation 8-26}$$

Further substitute LLG equation into the left-hand-side of the above derives

$$M \times \frac{dM}{dt} = -\gamma_0 M \times M \times H_{eff} - \alpha M_S \left(-\gamma_0 M \times H_{eff} + \frac{\alpha}{M_S} M \times \frac{dM}{dt}\right) \qquad \text{Equation 8-27}$$

Which can be written as

$$(1+\alpha^2) M \times \frac{dM}{dt} = \alpha\gamma_0 M_S M \times H_{eff} - \gamma_0 M \times M \times H_{eff} \qquad \text{Equation 8-28}$$

Cross product M with the above, similar as the first step will result in

$$-M_S^2(1+\alpha^2)\frac{dM}{dt} = \alpha\gamma_0 M_S\, M \times M \times H_{eff} - M_S^2 \gamma_0 M \times H_{eff} \qquad \text{Equation 8-29}$$

Thus

$$\frac{dM}{dt} = -\frac{\gamma_0}{1+\alpha^2}\, M \times H_{eff} + \frac{\gamma_0 \alpha}{(1+\alpha^2)M_S} M \times M \times H_{eff} \qquad \text{Equation 8-30}$$

If we assume in LL equation $\gamma_0' = \gamma_0/(1+\alpha^2)$ and $\lambda = \gamma_0\alpha/(1+\alpha^2)$, then the above equation has been proved to be the same with the LL equation.

Appendix 5: Spin-Orbit Interaction

For an electron orbiting the nucleus, in the reference frame of the electron, the nucleus appears to rotate around it and the moving nucleus charge will create a magnetic induction according to Maxwell's equation. Then one can write down the magnetic field experienced by the electron as [243]

$$B^* = -\frac{v \times E}{2c^2} \quad \text{Equation 8-31}$$

Note that by simple transformation between the electron frame and the nucleus frame the factor 2 is missing. This 2 factor can be explained via the Dirac equation that takes into account relativistic effects. Putting $E = -\nabla V$ we can get

$$B^* = \frac{1}{2m_e c^2}(p \times \nabla V) \quad \text{Equation 8-32}$$

Assume that $V(r) = Ze/(4\pi\epsilon_0 r)$ for the electrostatic potential of the nuclear charges $+Ze$ and define the orbital angular momentum operator as $(r \times p) = \hbar L$, we can write the spin orbit coupling Hamiltonian to be

$$H_{SOC} = \frac{e\hbar}{m_e}\sigma \cdot B^* = -\frac{e\hbar^2}{2m_e^2 c^2 r}\frac{dV(r)}{dr}\sigma \cdot L \quad \text{Equation 8-33}$$

$$\frac{dV(r)}{dr} = -\frac{Ze}{4\pi\epsilon_0 r^2} \quad \text{Equation 8-34}$$

To calculate the eigenvalue of the above spin orbit coupling Hamiltonian, in the first order of perturbation as the SOC matrix diagonal elements vanish due to time-reversal symmetry, effectively the energy shift is zero. Thus only the second order term will show up in the SOC induced energy change, which gives rise to Equation 2-11.

References

[1] H. Lee, A. Lee, F. Ebrahimi, P. K. Amiri, and K. L. Wang, "Array-Level Analysis of Magneto-Electric Random-Access Memory for High-Performance Embedded Applications," *IEEE Magnetics Letters,* vol. 8, pp. 1-5, 2017.

[2] Virtex UltraScale+ HBM FPGA: A Revolutionary Increase in Memory Performance, Xilinx, 2017/06/14, https://www.xilinx.com/support/documentation/white_papers/wp485-hbm.pdf

[3] J. L. Hennessy and D. A. Patterson, *Computer architecture: a quantitative approach*: Elsevier, 2011.

[4] How much SRAM proportion could be integrated in SoC at 20 nm and below? 2012/11/20, https://www.semiwiki.com/forum/content/1829-how-much-sram-proportion-could-integrated-soc-20-nm-below-q.html

[5] R. Dorrance, J. G. Alzate, S. S. Cherepov, P. Upadhyaya, I. N. Krivorotov, J. A. Katine*, et al.*, "Diode-MTJ Crossbar Memory Cell Using Voltage-Induced Unipolar Switching for High-Density MRAM," *Electron Device Letters, IEEE,* vol. 34, pp. 753-755, 2013.

[6] K. L. Wang, J. G. Alzate, and P. Khalili Amiri, "Low-power non-volatile spintronic memory: STT-RAM and beyond," *Journal of Physics D: Applied Physics,* vol. 46, p. 074003, 2013.

[7] The Non-Volatile Memory Technology Database (NVMDB), Kosuke Suzuki and Steven Swanson, CS2015-1011, May 15, 2015

[8] Matthew Marinella, Overview of ITRS Emerging Research Memory Devices, ITRS IEEE Rebooting Computing Symposium 4, Dec 11, 2015

[9] Y. Lee, H. Yoo, J. Jung, J. Jo, and I. C. Park, "A 2.74-pJ/bit, 17.7-Gb/s Iterative Concatenated-BCH Decoder in 65-nm CMOS for NAND Flash Memory," *Ieee Journal of Solid-State Circuits,* vol. 48, pp. 2531-2540, Oct 2013.

[10] B. C. Lee, E. Ipek, O. Mutlu, and D. Burger, "Architecting Phase Change Memory as a Scalable DRAM Alternative," *Isca 2009: 36th Annual International Symposium on Computer Architecture,* pp. 2-13, 2009.

[11] M. Mao, P. Y. Chen, S. Yu, and C. Chakrabarti, "A Multilayer Approach to Designing Energy-Efficient and Reliable ReRAM Cross-Point Array System," *IEEE Transactions on Very Large Scale Integration (VLSI) Systems,* vol. 25, pp. 1611-1621, 2017.

[12] S. A. Bota, G. Torrens, J. Verd, and J. Segura, "Detailed 8-transistor SRAM cell analysis for improved alpha particle radiation hardening in nanometer technologies," *Solid-State Electronics,* vol. 111, pp. 104-110, Sep 2015.

[13] The Non-Volatile Memory Technology Database (NVMDB), Kosuke Suzuki and Steven Swanson, CS2015-1011, May 15, 2015

[14] Matthew Marinella, Overview of ITRS Emerging Research Memory Devices, ITRS IEEE Rebooting Computing Symposium 4, Dec 11, 2015

[15] S. W. Chung, T. Kishi, J. W. Park, M. Yoshikawa, K. S. Park, T. Nagase*, et al.*, "4Gbit density STT-MRAM using perpendicular MTJ realized with compact cell structure," in *2016 IEEE International Electron Devices Meeting (IEDM)*, 2016, pp. 27.1.1-27.1.4.

[16] K. Rho, K. Tsuchida, D. Kim, Y. Shirai, J. Bae, T. Inaba*, et al.*, "23.5 A 4Gb LPDDR2 STT-MRAM with compact 9F2 1T1MTJ cell and hierarchical bitline architecture," in *2017 IEEE International Solid-State Circuits Conference (ISSCC)*, 2017, pp. 396-397.

[17] The Non-Volatile Memory Technology Database (NVMDB), Kosuke Suzuki and Steven Swanson, CS2015-1011, May 15, 2015

[18] Matthew Marinella, Overview of ITRS Emerging Research Memory Devices, ITRS IEEE Rebooting Computing Symposium 4, Dec 11, 2015

[19] C. H. Ho, T. Y. Shen, P. Y. Hsu, S. C. Chang, S. Y. Wen, M. H. Lin*, et al.*, "Random Soft Error Suppression by Stoichiometric Engineering: CMOS Compatible and Reliable 1Mb HfO2-ReRAM with 2 Extra Masks for Embedded IoT Systems," *2016 Ieee Symposium on Vlsi Technology,* 2016.

[20] The Non-Volatile Memory Technology Database (NVMDB), Kosuke Suzuki and Steven Swanson, CS2015-1011, May 15, 2015

[21] Matthew Marinella, Overview of ITRS Emerging Research Memory Devices, ITRS IEEE Rebooting Computing Symposium 4, Dec 11, 2015

[22] C. Grezes, F. Ebrahimi, J. G. Alzate, X. Cai, J. A. Katine, J. Langer*, et al.*, "Ultra-low switching energy and scaling in electric-field-controlled nanoscale magnetic tunnel junctions with high resistance-area product," *Applied Physics Letters,* vol. 108, p. 012403, 2016.

[23] P. Khalili Amiri, J. G. Alzate, X. Q. Cai, F. Ebrahimi, Q. Hu, K. Wong*, et al.*, "Electric-Field-Controlled Magnetoelectric RAM: Progress, Challenges, and Scaling," *Magnetics, IEEE Transactions on,* vol. 51, pp. 1-7, 2015.

[24] H. Noguchi, K. Ikegami, K. Abe, S. Fujita, Y. Shiota, T. Nozaki*, et al.*, "Novel voltage controlled MRAM (VCM) with fast read/write circuits for ultra large last level cache," in *2016 IEEE International Electron Devices Meeting (IEDM)*, 2016, pp. 27.5.1-27.5.4.

[25] S. H. Kang and C. Park, "MRAM: Enabling a Sustainable Device for Pervasive system architectures and applications," *2017 IEEE International Electron Devices Meeting (IEDM),* pp. 38.2.1-38.2.4, 2017.

[26] Julien Happich, "Time is ripe for emerging non-volatile memory, says Yole", eeNews Europe, June 23, 2017. http://www.eenewseurope.com/news/time-ripe-emerging-non-volatile-memory-says-yole

[27] Y. Wang, H. Ahn, U. Bhattacharya, T. Coan, F. Hamzaoglu, W. Hafez*, et al.*, "A 1.1GHz 12μA/Mb-Leakage SRAM Design in 65nm Ultra-Low-Power CMOS with Integrated Leakage Reduction for Mobile Applications," in *2007 IEEE International Solid-State Circuits Conference. Digest of Technical Papers*, 2007, pp. 324-606.

[28] F. Hamzaoglu, K. Zhang, Y. Wang, H. J. Ahn, U. Bhattacharya, Z. Chen*, et al.*, "A 153Mb-SRAM Design with Dynamic Stability Enhancement and Leakage Reduction in

45nm High-Κ Metal-Gate CMOS Technology," in *2008 IEEE International Solid-State Circuits Conference - Digest of Technical Papers*, 2008, pp. 376-621.

[29] S. Natarajan, M. Armstrong, M. Bost, R. Brain, M. Brazier, C. H. Chang*, et al.*, "A 32nm logic technology featuring 2nd-generation high-k + metal-gate transistors, enhanced channel strain and 0.171μm² SRAM cell size in a 291Mb array," in *2008 IEEE International Electron Devices Meeting*, 2008, pp. 1-3.

[30] M. E. Sinangil, H. Mair, and A. P. Chandrakasan, "A 28nm high-density 6T SRAM with optimized peripheral-assist circuits for operation down to 0.6V," in *2011 IEEE International Solid-State Circuits Conference*, 2011, pp. 260-262.

[31] E. Karl, Y. Wang, Y. G. Ng, Z. Guo, F. Hamzaoglu, U. Bhattacharya*, et al.*, "A 4.6GHz 162Mb SRAM design in 22nm tri-gate CMOS technology with integrated active V<inf>MIN</inf>-enhancing assist circuitry," in *2012 IEEE International Solid-State Circuits Conference*, 2012, pp. 230-232.

[32] E. Karl, Z. Guo, J. W. Conary, J. L. Miller, Y. G. Ng, S. Nalam*, et al.*, "17.1 A 0.6V 1.5GHz 84Mb SRAM design in 14nm FinFET CMOS technology," in *2015 IEEE International Solid-State Circuits Conference - (ISSCC) Digest of Technical Papers*, 2015, pp. 1-3.

[33] T. Song, W. Rim, S. Park, Y. Kim, J. Jung, G. Yang*, et al.*, "17.1 A 10nm FinFET 128Mb SRAM with assist adjustment system for power, performance, and area optimization," in *2016 IEEE International Solid-State Circuits Conference (ISSCC)*, 2016, pp. 306-307.

[34] J. Chang, Y. H. Chen, W. M. Chan, S. P. Singh, H. Cheng, H. Fujiwara*, et al.*, "12.1 A 7nm 256Mb SRAM in high-k metal-gate FinFET technology with write-assist circuitry for low-V<inf>MIN</inf> applications," in *2017 IEEE International Solid-State Circuits Conference (ISSCC)*, 2017, pp. 206-207.

[35] G. Wang, P. Parries, B. Khan, J. Liu, Y. Otani, J. Norum*, et al.*, "A 0.168 mu m(2)/0.11 mu m(2) highly scalable high performance embedded DRAM cell for 90/65-nm logic applications," *2005 IEEE VLSI-TSA International Symposium on VLSI Technology (VLSI-TSA-TECH), Proceedings of Technical Papers,* pp. 31-32, 2005.

[36] J. Barth, D. Plass, E. Nelson, C. Hwang, G. Fredeman, M. Sperling*, et al.*, "A 45 nm SOI Embedded DRAM Macro for the POWER (TM) Processor 32 MByte On-Chip L3 Cache," *Ieee Journal of Solid-State Circuits,* vol. 46, pp. 64-75, Jan 2011.

[37] J. Golz, J. Safran, B. He, D. Leu, M. Yin, T. Weaver*, et al.*, "3D stackable 32nm High-K/Metal Gate SOI embedded DRAM prototype," in *2011 Symposium on VLSI Circuits - Digest of Technical Papers*, 2011, pp. 228-229.

[38] K. C. Huang, Y. W. Ting, C. Y. Chang, K. C. Tu, K. C. Tzeng, H. C. Chu*, et al.*, "A high-performance, high-density 28nm eDRAM technology with high-K/metal-gate," in *2011 International Electron Devices Meeting*, 2011, pp. 24.7.1-24.7.4.

[39] M. Meterelliyoz, F. H. Al-amoody, U. Arslan, F. Hamzaoglu, L. Hood, M. Lal*, et al.*, "2nd generation embedded DRAM with 4X lower self refresh power in

22nm Tri-Gate CMOS technology," in *2014 Symposium on VLSI Circuits Digest of Technical Papers*, 2014, pp. 1-2.

[40] G. Fredeman, D. W. Plass, A. Mathews, J. Viraraghavan, K. Reyer, T. J. Knips*, et al.*, "A 14 nm 1.1 Mb Embedded DRAM Macro With 1 ns Access," *Ieee Journal of Solid-State Circuits,* vol. 51, pp. 230-239, Jan 2016.

[41] H. Mitani, K. Matsubara, H. Yoshida, T. Hashimoto, H. Yamakoshi, S. Abe*, et al.*, "A 90nm Embedded 1T-MONOS Flash Macro for Automotive Applications with 0.07mJ/8kB Rewrite Energy and Endurance Over 100M Cycles Under T-j of 175 degrees C," *2016 Ieee International Solid-State Circuits Conference (Isscc),* vol. 59, pp. 140-U187, 2016.

[42] C. Y. S. Cho, J. C. Wang, L. O. Huang, M. L. Weng, Y. F. Lin, C. F. Lee*, et al.*, "A 55-nm, 0.86-Volt operation, 75MHz high speed, 96uA/MHz low power, wide voltage supply range 2M-bit split-gate embedded Flash," *2013 International Symposium on Vlsi Design, Automation, and Test (Vlsi-Dat),* 2013.

[43] Y. K. Lee, H. Min, C. Jeon, B. Seo, G. Lee, E. Park*, et al.*, "Highly Scalable 2nd-Generation 45-nm Split-gate Embedded Flash with 10-ns Access Time and 1M-Cycling Endurance," *2016 Ieee 8th International Memory Workshop (Imw),* 2016.

[44] T. Kono, T. Ito, T. Tsuruda, T. Nishiyama, T. Nagasawa, T. Ogawa*, et al.*, "40nm Embedded SG-MONOS Flash Macros for Automotive with 160MHz Random Access for Code and Endurance Over 10M Cycles for Data," *2013 Ieee International Solid-State Circuits Conference Digest of Technical Papers (Isscc),* vol. 56, pp. 212-+, 2013.

[45] H. C. Yu, K. F. Lin, Y. D. Chih, and J. Chang, "A 40nm split gate embedded flash macro with flexible 2-in-1 architecture, code memory with 140MHz read speed and data memory with 1M cycles endurance," in *2017 Symposium on VLSI Circuits*, 2017, pp. C198-C199.

[46] Y. Taito, T. Kono, M. Nakano, T. Saito, T. Ito, K. Noguchi*, et al.*, "A 28 nm Embedded Split-Gate MONOS (SG-MONOS) Flash Macro for Automotive Achieving 6.4 GB/s Read Throughput by 200 MHz No-Wait Read Operation and 2.0 MB/s Write Throughput at Tj of 170 degrees C," *Ieee Journal of Solid-State Circuits,* vol. 51, pp. 213-221, Jan 2016.

[47] Y. K. Lee, C. Jeon, H. Min, B. Seo, K. Kim, D. Kim*, et al.*, "High-speed and logic-compatible split-gate embedded flash on 28-nm low-power HKMG logic process," in *2017 Symposium on VLSI Technology*, 2017, pp. T202-T203.

[48] S. Tsuda, Y. Kawashima, K. Sonoda, A. Yoshitomi, T. Mihara, S. Narumi*, et al.*, "First Demonstration of FinFET Split-Gate MONOS for High-Speed and Highly-Reliable Embedded Flash in 16/14nm-node and beyond," *2016 Ieee International Electron Devices Meeting (Iedm),* 2016.

[49] Arabinda Das, Hynix DRAM layout, process integration adapt to change, http://www.maltiel-consulting.com/Hynix-DRAM-31Vs44nm-layout.html

[50] M. F. Chang, C. W. Wu, C. C. Kuo, S. J. Shen, S. M. Yang, K. F. Lin*, et al.*, "A Low-Voltage Bulk-Drain-Driven Read Scheme for Sub-0.5 V 4 Mb 65 nm Logic-Process Compatible Embedded Resistive RAM (ReRAM) Macro," *Ieee Journal of Solid-State Circuits,* vol. 48, pp. 2250-2259, Sep 2013.

[51] C. P. Lo, W. Z. Lin, W. Y. Lin, H. T. Lin, T. H. Yang, Y. N. Chiang*, et al.*, "Embedded 2Mb ReRAM macro with 2.6ns read access time using dynamic-trip-point-mismatch sampling current-mode sense amplifier for IoE applications," in *2017 Symposium on VLSI Circuits*, 2017, pp. C164-C165.

[52] M. F. Chang, J. J. Wu, T. F. Chien, Y. C. Liu, T. C. Yang, W. C. Shen*, et al.*, "Embedded 1Mb ReRAM in 28nm CMOS with 0.27-to-1V Read Using Swing-Sample-and-Couple Sense Amplifier and Self-Boost-Write-Termination Scheme," *2014 Ieee International Solid-State Circuits Conference Digest of Technical Papers (Isscc),* vol. 57, pp. 332-+, 2014.

[53] Y. Hayakawa, A. Himeno, R. Yasuhara, W. Boullart, E. Vecchio, T. Vandeweyer*, et al.*, "Highly reliable TaOx ReRAM with centralized filament for 28-nm embedded application," *2015 Symposium on Vlsi Technology (Vlsi Technology),* 2015.

[54] R. Nebashi, N. Sakimura, H. Honjo, S. Saito, Y. Ito, S. Miura*, et al.*, "A 90nm 12ns 32Mb 2T1MTJ MRAM," in *2009 IEEE International Solid-State Circuits Conference - Digest of Technical Papers*, 2009, pp. 462-463,463a.

[55] T. Ohsawa, H. Koike, S. Miura, H. Honjo, K. Tokutome, S. Ikeda*, et al.*, "1Mb 4T-2MTJ nonvolatile STT-RAM for embedded memories using 32b fine-grained power gating technique with 1.0ns/200ps wake-up/power-off times," in *VLSI Circuits (VLSIC), 2012 Symposium on*, 2012, pp. 46-47.

[56] J. Guenole, L. Thomas, L. Son, L. Yuan-Jen, L. Huanlong, Z. Jian*, et al.*, "Demonstration of fully functional 8Mb perpendicular STT-MRAM chips with sub-5ns writing for non-volatile embedded memories," in *VLSI Technology (VLSI-Technology): Digest of Technical Papers, 2014 Symposium on*, 2014, pp. 1-2.

[57] H. Noguchi, K. Ikegami, K. Kushida, K. Abe, S. Itai, S. Takaya*, et al.*, "A 3.3ns-Access-Time 71.2 mu W/MHz 1Mb Embedded STT-MRAM Using Physically Eliminated Read-Disturb Scheme and Normally-Off Memory Architecture," *2015 Ieee International Solid-State Circuits Conference Digest of Technical Papers (Isscc),* vol. 58, pp. 136-U186, 2015.

[58] S. Chung, K. M. Rho, S. D. Kim, H. J. Suh, D. J. Kim, H. J. Kim*, et al.*, "Fully integrated 54nm STT-RAM with the smallest bit cell dimension for high density memory application," *2010 International Electron Devices Meeting - Technical Digest,* 2010.

[59] C. J. Lin, S. H. Kang, Y. J. Wang, K. Lee, X. Zhu, W. C. Chen*, et al.*, "45nm Low Power CMOS Logic Compatible Embedded STT MRAM Utilizing a Reverse-Connection 1T/1MTJ Cell," *2009 Ieee International Electron Devices Meeting,* pp. 256-259, 2009.

[60] Y. Lu, T. Zhong, W. Hsu, S. Kim, X. Lu, J. J. Kan*, et al.*, "Fully Functional Perpendicular STT-MRAM Macro Embedded in 40 nm Logic for Energy-efficient IOT Applications," *2015 Ieee International Electron Devices Meeting (Iedm),* 2015.

[61] Y. J. Song, J. H. Lee, H. C. Shin, K. H. Lee, K. Suh, J. R. Kang*, et al.*, "Highly functional and reliable 8Mb STT-MRAM embedded in 28nm logic," in *2016 IEEE International Electron Devices Meeting (IEDM)*, 2016, pp. 27.2.1-27.2.4.

[62] S. Fujita, H. Noguchi, K. Ikegami, S. Takeda, K. Nomura, and K. Abe, "Novel memory hierarchy with e-STT-MRAM for near-future applications," in *2017 International Symposium on VLSI Design, Automation and Test (VLSI-DAT)*, 2017, pp. 1-2.

[63] D. Saida, S. Kashiwada, M. Yakabe, T. Daibou, M. Fukumoto, S. Miwa*, et al.*, "1x-to 2x-nm perpendicular MTJ Switching at Sub-3-ns Pulses Below 100 mu A for High-Performance Embedded STT-MRAM for Sub-20-nm CMOS," *Ieee Transactions on Electron Devices,* vol. 64, pp. 427-431, Feb 2017.

[64] D. Shum, D. Houssameddine, S. T. Woo, Y. S. You, J. Wong, K. W. Wong*, et al.*, "CMOS-embedded STT-MRAM arrays in 2x nm nodes for GP-MCU applications," in *2017 Symposium on VLSI Technology*, 2017, pp. T208-T209.

[65] J. Hayakawa, S. Ikeda, F. Matsukura, H. Takahashi, and H. Ohno, "Dependence of Giant Tunnel Magnetoresistance of Sputtered CoFeB/MgO/CoFeB Magnetic Tunnel Junctions on MgO Barrier Thickness and Annealing Temperature," *Japanese Journal of Applied Physics,* vol. 44, pp. L587-L589, 2005.

[66] S. Yuasa and D. D. Djayaprawira, "Giant tunnel magnetoresistance in magnetic tunnel junctions with a crystalline MgO(0 0 1) barrier," *Journal of Physics D: Applied Physics,* vol. 40, pp. R337-R354, 2007.

[67] Introduction to TMR Magnetic Sensors, Doway Tech, March 12, 2015. http://www.shdingjun.com/dzzs/cgzs/71.html

[68] Coriolan Tiusan, Common magnetoresistance measurements: AMR, GMR, AHE/SHE, TMR. European School on Mangetism 2015, Aug 24 - Sep 4 2015, Cluj-Napoca, Romania. http://www.magnetism.eu/esm/2015/slides/tiusan-slides1.pdf

[69] W. Thomson, "XIX. On the electro-dynamic qualities of metals:—Effects of magnetization on the electric conductivity of nickel and of iron," *Proceedings of the Royal Society of London,* vol. 8, pp. 546-550, January 1, 1857 1857.

[70] I. A. Campbell, "Hall Effect and Resistivity Anisotropy in Ni Alloys," *Physical Review Letters,* vol. 24, pp. 269-&, 1970.

[71] Coriolan Tiusan, Common magnetoresistance measurements: AMR, GMR, AHE/SHE, TMR. European School on Mangetism 2015, Aug 24 - Sep 4 2015, Cluj-Napoca, Romania. http://www.magnetism.eu/esm/2015/slides/tiusan-slides1.pdf

[72] M. N. Baibich, J. M. Broto, A. Fert, F. N. Vandau, F. Petroff, P. Eitenne*, et al.*, "Giant Magnetoresistance of (001)Fe/(001) Cr Magnetic Superlattices," *Physical Review Letters,* vol. 61, pp. 2472-2475, Nov 21 1988.

[73] G. Binasch, P. Grunberg, F. Saurenbach, and W. Zinn, "Enhanced Magnetoresistance in Layered Magnetic-Structures with Antiferromagnetic Interlayer Exchange," *Physical Review B,* vol. 39, pp. 4828-4830, Mar 1 1989.

[74] B. Dieny, V. S. Speriosu, S. S. P. Parkin, B. A. Gurney, D. R. Wilhoit, and D. Mauri, "Giant Magnetoresistance in Soft Ferromagnetic Multilayers," *Physical Review B,* vol. 43, pp. 1297-1300, Jan 1 1991.

[75] Josef Weingand, IBM Tape Product Update and Future of Tape, TSM Symposium 2015, Sep 24, 2015. https://www.slideshare.net/JosefWeingand/tsm-symposium-2015-ibm-future-of-tape

[76] M. Julliere, "Tunneling between Ferromagnetic-Films," *Physics Letters A,* vol. 54, pp. 225-226, 1975.

[77] H. Lee, "Integration of Voltage-Controlled Spintronic Devices in CMOS Circuits," *PhD Thesis, University of California, Los Angeles,* vol. Electrical Engineering, 2017.

[78] T. Miyazaki and N. Tezuka, "Giant Magnetic Tunneling Effect in Fe/Al2o3/Fe Junction," *Journal of Magnetism and Magnetic Materials,* vol. 139, pp. L231-L234, Jan 1995.

[79] D. X. Wang, C. Nordman, J. M. Daughton, Z. H. Qian, and J. Fink, "70% TMR at room temperature for SDT sandwich junctions with CoFeB as free and reference layers," *Ieee Transactions on Magnetics,* vol. 40, pp. 2269-2271, Jul 2004.

[80] S. S. Parkin, C. Kaiser, A. Panchula, P. M. Rice, B. Hughes, M. Samant*, et al.*, "Giant tunnelling magnetoresistance at room temperature with MgO (100) tunnel barriers," *Nat Mater,* vol. 3, pp. 862-7, Dec 2004.

[81] W. Butler, X. G. Zhang, T. Schulthess, and J. MacLaren, "Spin-dependent tunneling conductance of Fe|MgO|Fe sandwiches," *Physical Review B,* vol. 63, 2001.

[82] S. Ikeda, J. Hayakawa, Y. Ashizawa, Y. M. Lee, K. Miura, H. Hasegawa*, et al.*, "Tunnel magnetoresistance of 604% at 300K by suppression of Ta diffusion in CoFeB∕MgO∕CoFeB pseudo-spin-valves annealed at high temperature," *Applied Physics Letters,* vol. 93, p. 082508, 2008.

[83] J. Slonczewski, "Conductance and exchange coupling of two ferromagnets separated by a tunneling barrier," *Physical Review B,* vol. 39, pp. 6995-7002, 1989.

[84] S. Ikeda, K. Miura, H. Yamamoto, K. Mizunuma, H. D. Gan, M. Endo*, et al.*, "A perpendicular-anisotropy CoFeB-MgO magnetic tunnel junction," *Nature Materials,* vol. 9, pp. 721-724, Sep 2010.

[85] J. C. Slonczewski, "Current-driven excitation of magnetic multilayers," *Journal of Magnetism and Magnetic Materials,* vol. 159, pp. L1-L7, Jun 1996.

[86] L. Berger, "Emission of spin waves by a magnetic multilayer traversed by a current," *Physical Review B,* vol. 54, pp. 9353-9358, Oct 1 1996.

[87] M. Tsoi, A. G. M. Jansen, J. Bass, W. C. Chiang, M. Seck, V. Tsoi*, et al.*, "Excitation of a magnetic multilayer by an electric current," *Physical Review Letters,* vol. 80, pp. 4281-4284, May 11 1998.

[88] J. Z. Sun, "Current-driven magnetic switching in manganite trilayer junctions," *Journal of Magnetism and Magnetic Materials,* vol. 202, pp. 157-162, Jul 1999.

[89] E. B. Myers, D. C. Ralph, J. A. Katine, R. N. Louie, and R. A. Buhrman, "Current-induced switching of domains in magnetic multilayer devices," *Science,* vol. 285, pp. 867-870, Aug 6 1999.

[90] J. A. Katine, F. J. Albert, R. A. Buhrman, E. B. Myers, and D. C. Ralph, "Current-driven magnetization reversal and spin-wave excitations in Co/Cu/Co pillars," *Physical Review Letters,* vol. 84, pp. 3149-3152, Apr 3 2000.

[91] MRAM History, MRAM-Info, https://www.mram-info.com/history

[92] H. Sato, E. C. I. Enobio, M. Yamanouchi, S. Ikeda, S. Fukami, S. Kanai*, et al.*, "Properties of magnetic tunnel junctions with a MgO/CoFeB/Ta/CoFeB/MgO recording structure down to junction diameter of 11 nm," *Applied Physics Letters,* vol. 105, p. 062403, 2014.

[93] K. Watanabe, B. Jinnai, S. Fukami, H. Sato, and H. Ohno, "Shape anisotropy revisited in single-digit nanometer magnetic tunnel junctions," *Nature Communications,* vol. 9, p. 663, 2018/02/14 2018.

[94] I. M. Miron, G. Gaudin, S. Auffret, B. Rodmacq, A. Schuhl, S. Pizzini*, et al.*, "Current-driven spin torque induced by the Rashba effect in a ferromagnetic metal layer," *Nat Mater,* vol. 9, pp. 230-4, Mar 2010.

[95] I. M. Miron, K. Garello, G. Gaudin, P. J. Zermatten, M. V. Costache, S. Auffret*, et al.*, "Perpendicular switching of a single ferromagnetic layer induced by in-plane current injection," *Nature,* vol. 476, pp. 189-93, Aug 11 2011.

[96] L. Liu, O. J. Lee, T. J. Gudmundsen, D. C. Ralph, and R. A. Buhrman, "Current-Induced Switching of Perpendicularly Magnetized Magnetic Layers Using Spin Torque from the Spin Hall Effect," *Physical Review Letters,* vol. 109, p. 096602, 08/29/ 2012.

[97] L. Liu, C. F. Pai, Y. Li, H. W. Tseng, D. C. Ralph, and R. A. Buhrman, "Spin-torque switching with the giant spin Hall effect of tantalum," *Science,* vol. 336, pp. 555-8, May 4 2012.

[98] K. Garello, C. O. Avci, I. M. Miron, M. Baumgartner, A. Ghosh, S. Auffret*, et al.*, "Ultrafast magnetization switching by spin-orbit torques," *Applied Physics Letters,* vol. 105, Nov 24 2014.

[99] P. Khalili and K. L. Wang, "The Computer Chip That Never Forgets," *Ieee Spectrum,* vol. 52, pp. 30-35, Jul 2015.

[100] W. G. Wang, M. Li, S. Hageman, and C. L. Chien, "Electric-field-assisted switching in magnetic tunnel junctions," *Nat Mater,* vol. 11, pp. 64-8, Jan 2012.

[101] Y. Shiota, T. Nozaki, F. Bonell, S. Murakami, T. Shinjo, and Y. Suzuki, "Induction of coherent magnetization switching in a few atomic layers of FeCo using voltage pulses," *Nat Mater,* vol. 11, pp. 39-43, Jan 2012.

[102] J. G. Alzate, P. K. Amiri, P. Upadhyaya, S. S. Cherepov, J. Zhu, M. Lewis*, et al.*, "Voltage-induced switching of nanoscale magnetic tunnel junctions," *Electron Devices Meeting (IEDM), 2012 IEEE International,* pp. 29.5.1-29.5.4, 10-13 Dec. 2012 2012.

[103] S. Kanai, M. Yamanouchi, S. Ikeda, Y. Nakatani, F. Matsukura, and H. Ohno, "Electric field-induced magnetization reversal in a perpendicular-anisotropy CoFeB-MgO magnetic tunnel junction," *Applied Physics Letters,* vol. 101, p. 122403, 2012.

[104] K. L. WANG and P. K. AMIRI, "VOLTAGE-CONTROLLED MAGNETIC ANISOTROPY IN SPINTRONIC DEVICES," *SPIN,* vol. 02, p. 1240002, 2012.

[105] S. Kanai, Y. Nakatani, M. Yamanouchi, S. Ikeda, H. Sato, F. Matsukura*, et al.*, "Magnetization switching in a CoFeB/MgO magnetic tunnel junction by combining spin-transfer torque and electric field-effect," *Applied Physics Letters,* vol. 104, p. 212406, 2014.

[106] M. Beleggia, M. D. Graef, Y. T. Millev, D. A. Goode, and G. Rowlands, "Demagnetization factors for elliptic cylinders," *Journal of Physics D: Applied Physics,* vol. 38, p. 3333, 2005.

[107] H. X. Yang, M. Chshiev, B. Dieny, J. H. Lee, A. Manchon, and K. H. Shin, "First-principles investigation of the very large perpendicular magnetic anisotropy at Fe$|$MgO and Co$|$MgO interfaces," *Physical Review B,* vol. 84, p. 054401, 08/01/ 2011.

[108] K. H. He, J. S. Chen, and Y. P. Feng, "First principles study of the electric field effect on magnetization and magnetic anisotropy of FeCo/MgO(001) thin film," *Applied Physics Letters,* vol. 99, p. 072503, 2011.

[109] P. V. Ong, N. Kioussis, P. K. Amiri, K. L. Wang, and G. P. Carman, "Strain control magnetocrystalline anisotropy of Ta/FeCo/MgO heterostructures," *Journal of Applied Physics,* vol. 117, p. 17B518, 2015.

[110] M. K. Niranjan, C.-G. Duan, S. S. Jaswal, and E. Y. Tsymbal, "Electric field effect on magnetization at the Fe/MgO(001) interface," *Applied Physics Letters,* vol. 96, p. 222504, 2010.

[111] C.-G. Duan, J. Velev, R. Sabirianov, Z. Zhu, J. Chu, S. Jaswal*, et al.*, "Surface Magnetoelectric Effect in Ferromagnetic Metal Films," *Physical Review Letters,* vol. 101, p. 137201, Sep 26 2008.

[112] M. Tsujikawa and T. Oda, "Finite Electric Field Effects in the Large Perpendicular Magnetic Anisotropy Surface Pt/Fe/Pt(001): A First-Principles Study," *Physical Review Letters,* vol. 102, 2009.

[113] K. Nakamura, T. Akiyama, T. Ito, M. Weinert, and A. J. Freeman, "Role of an interfacial FeO layer in the electric-field-driven switching of magnetocrystalline anisotropy at the Fe/MgO interface," *Physical Review B,* vol. 81, p. 220409(R), 2010.

[114] K. Nakamura, R. Shimabukuro, Y. Fujiwara, T. Akiyama, T. Ito, and A. J. Freeman, "Giant Modification of the Magnetocrystalline Anisotropy in Transition-Metal Monolayers by an External Electric Field," *Physical Review Letters,* vol. 102, 2009.

[115] P. V. Ong, N. Kioussis, P. K. Amiri, and K. L. Wang, "Electric-field-driven magnetization switching and nonlinear magnetoelasticity in Au/FeCo/MgO heterostructures," *Scientific Reports,* vol. 6, p. 29815, 07/18/online 2016.

[116] P. V. Ong, N. Kioussis, D. Odkhuu, P. Khalili Amiri, K. L. Wang, and G. P. Carman, "Giant voltage modulation of magnetic anisotropy in strained heavy metal/magnet/insulator heterostructures," *Physical Review B,* vol. 92, p. 020407, 07/20/ 2015.

[117] K. Kita, D. W. Abraham, M. J. Gajek, and D. C. Worledge, "Electric-field-control of magnetic anisotropy of Co0.6Fe0.2B0.2/oxide stacks using reduced voltage," *Journal of Applied Physics,* vol. 112, p. 033919, 2012.

[118] T. Nozaki, A. Koziol-Rachwal, M. Tsujikawa, Y. Shiota, X. D. Xu, T. Ohkubo*, et al.*, "Highly efficient voltage control of spin and enhanced interfacial perpendicular magnetic anisotropy in iridium-doped Fe/MgO magnetic tunnel junctions," *Npg Asia Materials,* vol. 9, Dec 5 2017.

[119] A. Kozioł-Rachwał, T. Nozaki, K. Freindl, J. Korecki, S. Yuasa, and Y. Suzuki, "Enhancement of perpendicular magnetic anisotropy and its electric field-induced change through interface engineering in Cr/Fe/MgO," *Scientific Reports,* vol. 7, p. 5993, 2017/07/20 2017.

[120] K. Yushi, Y. Hiroaki, S. Yoshiaki, O. Soichi, F. Keiko, Y. Masahiko*, et al.*, "Giant voltage-controlled magnetic anisotropy effect in a crystallographically strained CoFe system," *Applied Physics Express,* vol. 11, p. 053007, 2018.

[121] H. Naeimi, C. Augustine, A. Raychowdhury, S.-L. Lu, and J. Tschanz, "STTRAM SCALING AND RETENTION FAILURE," *Intel Technology Journal,* vol. 17, 2013.

[122] C. Grezes, H. Lee, A. Lee, S. Wang, F. Ebrahimi, X. Li*, et al.*, "Write Error Rate and Read Disturbance in Electric-Field-Controlled Magnetic Random-Access Memory," *IEEE Magnetics Letters,* vol. 8, pp. 1-5, 2017.

[123] H. G. Cheng and N. Deng, "Influence of thermal agitation on the electric field induced precessional magnetization reversal with perpendicular easy axis," *Aip Advances,* vol. 3, Dec 2013.

[124] S. Yoichi, N. Takayuki, T. Shingo, Y. Kay, K. Hitoshi, F. Akio*, et al.*, "Evaluation of write error rate for voltage-driven dynamic magnetization switching in magnetic tunnel junctions with perpendicular magnetization," *Applied Physics Express,* vol. 9, p. 013001, 2016.

[125] Y. Shiota, T. Nozaki, S. Tamaru, K. Yakushiji, H. Kubota, A. Fukushima*, et al.*, "Reduction in write error rate of voltage-driven dynamic magnetization switching by improving thermal stability factor," *Applied Physics Letters,* vol. 111, Jul 10 2017.

[126] S. Yuasa, T. Nagahama, A. Fukushima, Y. Suzuki, and K. Ando, "Giant room-temperature magnetoresistance in single-crystal Fe/MgO/Fe magnetic tunnel junctions," *Nat Mater,* vol. 3, pp. 868-71, Dec 2004.

[127] T. Maruyama, Y. Shiota, T. Nozaki, K. Ohta, N. Toda, M. Mizuguchi*, et al.*, "Large voltage-induced magnetic anisotropy change in a few atomic layers of iron," *Nat Nanotechnol,* vol. 4, pp. 158-61, Mar 2009.

[128] D. D. Djayaprawira, K. Tsunekawa, M. Nagai, H. Maehara, S. Yamagata, N. Watanabe*, et al.*, "230% room-temperature magnetoresistance in CoFeB∕MgO∕CoFeB magnetic tunnel junctions," *Applied Physics Letters,* vol. 86, p. 092502, 2005.

[129] Y. S. Choi, K. Tsunekawa, Y. Nagamine, and D. Djayaprawira, "Transmission electron microscopy study on the polycrystalline CoFeB∕MgO∕CoFeB based magnetic tunnel junction showing a high tunneling magnetoresistance, predicted in single crystal magnetic tunnel junction," *Journal of Applied Physics,* vol. 101, p. 013907, 2007.

[130] M. Mizuguchi, Y. Suzuki, T. Nagahama, and S. Yuasa, "In situ scanning tunneling microscopy observations of polycrystalline MgO(001) tunneling barriers grown on amorphous CoFeB electrode," *Applied Physics Letters,* vol. 91, p. 012507, 2007.

[131] K. Kinoshita, H. Utsumi, K. Suemitsu, H. Hada, and T. Sugibayashi, "Etching Magnetic Tunnel Junction with Metal Etchers," *Japanese Journal of Applied Physics,* vol. 49, Aug 2010.

[132] Alar Ainla, http://www.ims.ut.ee/~alar/microtech/Ch1_4/Ch_1_4_7.php#

[133] J. Jeong and T. Endoh, "Ion beam etching process for high-density spintronic devices and its damage recovery by the oxygen showering post-treatment process," *Japanese Journal of Applied Physics,* vol. 56, Apr 2017.

[134] K. Kinoshita, H. Honjo, S. Fukami, H. Sato, K. Mizunuma, K. Tokutome*, et al.*, "Process-induced damage and its recovery for a CoFeB–MgO magnetic tunnel junction with perpendicular magnetic easy axis," *Japanese Journal of Applied Physics,* vol. 53, p. 103001, 2014.

[135] Alar Ainla, http://www.ims.ut.ee/~alar/microtech/Ch1_4/Ch_1_4_7.php#

[136] A. Okada, S. Kanai, M. Yamanouchi, S. Ikeda, F. Matsukura, and H. Ohno, "Electric-field effects on magnetic anisotropy and damping constant in Ta/CoFeB/MgO investigated by ferromagnetic resonance," *Applied Physics Letters,* vol. 105, p. 052415, 2014.

[137] H. Meng, V. B. Naik, R. Liu, and G. Han, "Electric field control of spin re-orientation in perpendicular magnetic tunnel junctions—CoFeB and MgO thickness dependence," *Applied Physics Letters,* vol. 105, p. 042410, 2014.

[138] M. Endo, S. Kanai, S. Ikeda, F. Matsukura, and H. Ohno, "Electric-field effects on thickness dependent magnetic anisotropy of sputtered MgO/Co[sub 40]Fe[sub 40]B[sub 20]/Ta structures," *Applied Physics Letters,* vol. 96, p. 212503, 2010.

[139] J. Zhu, J. A. Katine, G. E. Rowlands, Y.-J. Chen, Z. Duan, J. G. Alzate*, et al.*, "Voltage-Induced Ferromagnetic Resonance in Magnetic Tunnel Junctions," *Physical Review Letters,* vol. 108, p. 197203, 05/09/ 2012.

[140] J. G. Alzate, P. Khalili Amiri, G. Yu, P. Upadhyaya, J. A. Katine, J. Langer*, et al.*, "Temperature dependence of the voltage-controlled perpendicular anisotropy in nanoscale MgO|CoFeB|Ta magnetic tunnel junctions," *Applied Physics Letters,* vol. 104, p. 112410, 2014.

[141] T. Nozaki, K. Yakushiji, S. Tamaru, M. Sekine, R. Matsumoto, M. Konoto*, et al.*, "Voltage-Induced Magnetic Anisotropy Changes in an Ultrathin FeB Layer Sandwiched between Two MgO Layers," *Applied Physics Express,* vol. 6, p. 073005, 2013.

[142] Y. Shiota, F. d. r. Bonell, S. Miwa, N. Mizuochi, T. Shinjo, and Y. Suzuki, "Opposite signs of voltage-induced perpendicular magnetic anisotropy change in CoFeB｜MgO junctions with different underlayers," *Applied Physics Letters,* vol. 103, p. 082410, 2013.

[143] K. Woojin, J. H. Jeong, Y. Kim, W. C. Lim, J. H. Kim, J. H. Park*, et al.*, "Extended scalability of perpendicular STT-MRAM towards sub-20nm MTJ node," *Electron Devices Meeting (IEDM), 2011 IEEE International,* pp. 24.1.1-24.1.4, 5-7 Dec. 2011 2011.

[144] J. G. Alzate, "Voltage-Controlled Magnetic Dynamics in Nanoscale Magnetic Tunnel Junctions," *PhD Thesis, University of California, Los Angeles,* vol. Electrical Engineering, 2014.

[145] L. Liu, C. F. Pai, D. C. Ralph, and R. A. Buhrman, "Magnetic oscillations driven by the spin Hall effect in 3-terminal magnetic tunnel junction devices," *Phys Rev Lett,* vol. 109, p. 186602, Nov 2 2012.

[146] W. Skowroński, T. Nozaki, D. D. Lam, Y. Shiota, K. Yakushiji, H. Kubota*, et al.*, "Underlayer material influence on electric-field controlled perpendicular magnetic anisotropy in CoFeB/MgO magnetic tunnel junctions," *Physical Review B,* vol. 91, p. 184410, 05/18/ 2015.

[147] A. Rajanikanth, T. Hauet, F. Montaigne, S. Mangin, and S. Andrieu, "Magnetic anisotropy modified by electric field in V/Fe/MgO(001)/Fe epitaxial magnetic tunnel junction," *Applied Physics Letters,* vol. 103, p. 062402, 2013.

[148] H. Kubota, S. Ishibashi, T. Saruya, T. Nozaki, A. Fukushima, K. Yakushiji*, et al.*, "Enhancement of perpendicular magnetic anisotropy in FeB free layers using a thin MgO cap layer," *Journal of Applied Physics,* vol. 111, p. 07C723, 2012.

[149] X. Li, G. Yu, H. Wu, P. V. Ong, K. Wong, Q. Hu*, et al.*, "Thermally stable voltage-controlled perpendicular magnetic anisotropy in Mo|CoFeB|MgO structures," *Applied Physics Letters,* vol. 107, p. 142403, 2015.

[150] E. M. J. Hassen, B. Viala, M. C. Cyrille, M. Cartier, O. Redon, P. Lima*, et al.*, "Room temperature magnetoresistance in CoFeB/SrTiO3/CoFeB magnetic tunnel junctions deposited by ion beam sputtering," *Journal of Applied Physics,* vol. 111, p. 07C727, 2012.

[151] D. Pantel, S. Goetze, D. Hesse, and M. Alexe, "Reversible electrical switching of spin polarization in multiferroic tunnel junctions," *Nat Mater,* vol. 11, pp. 289-93, Apr 2012.

[152] V. Garcia, M. Bibes, L. Bocher, S. Valencia, F. Kronast, A. Crassous*, et al.*, "Ferroelectric Control of Spin Polarization," *Science,* vol. 327, pp. 1106-1110, Feb 26 2010.

[153] K. Kim and Y. J. Song, "Integration technology for ferroelectric memory devices," *Microelectronics Reliability,* vol. 43, pp. 385-398, 3// 2003.

[154] H. Kohlstedt, Y. Mustafa, A. Gerber, A. Petraru, M. Fitsilis, R. Meyer*, et al.*, "Current status and challenges of ferroelectric memory devices," *Microelectronic Engineering,* vol. 80, pp. 296-304, 6/17/ 2005.

[155] S. T. Han, Y. Zhou, and V. A. Roy, "Towards the development of flexible non-volatile memories," *Adv Mater,* vol. 25, pp. 5425-49, Oct 11 2013.

[156] S. Trolier-McKinstry and P. Muralt, "Thin film piezoelectrics for MEMS," *Journal of Electroceramics,* vol. 12, pp. 7-17, Jan-Mar 2004.

[157] N. Ledermann, P. Muralt, J. Baborowski, S. Gentil, K. Mukati, M. Cantoni*, et al.*, "{100}-textured, piezoelectric Pb(Zr-x Ti1-x)O-3 thin films for MEMS: integration, deposition and properties," *Sensors and Actuators a-Physical,* vol. 105, pp. 162-170, Jul 15 2003.

[158] Y. Bastani, T. Schmitz-Kempen, A. Roelofs, and N. Bassiri-Gharb, "Critical thickness for extrinsic contributions to the dielectric and piezoelectric response in lead zirconate titanate ultrathin films," *Journal of Applied Physics,* vol. 109, p. 014115, 2011.

[159] J. H. Choi, F. Zhang, Y.-C. Perng, and J. P. Chang, "Tailoring the composition of lead zirconate titanate by atomic layer deposition," *Journal of Vacuum Science & Technology B,* vol. 31, p. 012207, 2013.

[160] F. Zhang, Y.-C. Perng, J. H. Choi, T. Wu, T.-K. Chung, G. P. Carman*, et al.*, "Atomic layer deposition of Pb(Zr,Ti)Ox on 4H-SiC for metal-ferroelectric-insulator-semiconductor diodes," *Journal of Applied Physics,* vol. 109, p. 124109, 2011.

[161] S. M. George, "Atomic Layer Deposition: An Overview," *Chemical Reviews,* vol. 110, pp. 111-131, Jan 2010.

[162] S. Ikeda, K. Miura, H. Yamamoto, K. Mizunuma, H. D. Gan, M. Endo*, et al.*, "A perpendicular-anisotropy CoFeB-MgO magnetic tunnel junction," *Nat Mater,* vol. 9, pp. 721-724, Sep 2010.

[163] B. Jaffe, W. R. Cook, and H. L. Jaffe, *Piezoelectric ceramics*. London, New York,: Academic Press, 1971.

[164] T. Miyajima, T. Ibusuki, S. Umehara, M. Sato, S. Eguchi, M. Tsukada*, et al.*, "Transmission electron microscopy study on the crystallization and boron distribution of CoFeB/MgO/CoFeB magnetic tunnel junctions with various capping layers," *Applied Physics Letters,* vol. 94, p. 122501, 2009.

[165] S. V. Karthik, Y. K. Takahashi, T. Ohkubo, K. Hono, H. D. Gan, S. Ikeda*, et al.*, "Transmission electron microscopy study on the effect of various capping layers on CoFeB/MgO/CoFeB pseudo spin valves annealed at different temperatures," *Journal of Applied Physics,* vol. 111, p. 083922, Apr 15 2012.

[166] Y. Shiota, S. Murakami, F. Bonell, T. Nozaki, T. Shinjo, and Y. Suzuki, "Quantitative Evaluation of Voltage-Induced Magnetic Anisotropy Change by Magnetoresistance Measurement," *Applied Physics Express,* vol. 4, p. 043005, 2011.

[167] J. Robertson, "High dielectric constant oxides," *The European Physical Journal Applied Physics,* vol. 28, pp. 265-291, 2004.

[168] R. Ahmed and R. H. Victora, "Possible Explanation for Observed Effectiveness of Voltage-Controlled Anisotropy in CoFeB/MgO MTJ," *IEEE Transactions on Magnetics,* vol. 51, pp. 1-4, 2015.

[169] J. Y. Bae, W. C. Lim, H. J. Kim, T. D. Lee, K. W. Kim, and T. W. Kim, "Compositional change of MgO barrier and interface in CoFeB⁄MgO⁄CoFeB tunnel junction after annealing," *Journal of Applied Physics,* vol. 99, p. 08T316, 2006.

[170] N. Miyakawa, D. C. Worledge, and K. Kita, "Impact of Ta Diffusion on the Perpendicular Magnetic Anisotropy of Ta/CoFeB/MgO," *Magnetics Letters, IEEE,* vol. 4, pp. 1000104-1000104, 2013.

[171] P. Khalili Amiri, Z. M. Zeng, J. Langer, H. Zhao, G. Rowlands, Y. J. Chen*, et al.*, "Switching current reduction using perpendicular anisotropy in CoFeB–MgO magnetic tunnel junctions," *Applied Physics Letters,* vol. 98, p. 112507, 2011.

[172] S. Kanai, F. Matsukura, and H. Ohno, "Electric-field-induced magnetization switching in CoFeB/MgO magnetic tunnel junctions with high junction resistance," *Applied Physics Letters,* vol. 108, p. 192406, 2016.

[173] X. Li, "Voltage-Controlled Magnetic Anisotropy in Heavy Metal|Ferromagnet|Insulator-Based Structures," *UCLA: Electrical Engineering 0303,* 2015.

[174] D. Chien, X. Li, K. Wong, M. A. Zurbuchen, S. Robbennolt, G. Yu*, et al.*, "Enhanced voltage-controlled magnetic anisotropy in magnetic tunnel junctions with an MgO/PZT/MgO tunnel barrier," *Applied Physics Letters,* vol. 108, p. 112402, 2016.

[175] F. Ibrahim, A. Hallal, B. Dieny, and M. Chshiev. (2016, October 1, 2016). Giant variation of the perpendicular magnetic anisotropy at Fe/MgO interfaces by oxygen migration: a first-principles study. *ArXiv e-prints 1610*. Available: http://adsabs.harvard.edu/abs/2016arXiv161008859I

[176] M. Tsujikawa, S. Haraguchi, and T. Oda, "Effect of atomic monolayer insertions on electric-field-induced rotation of magnetic easy axis," *Journal of Applied Physics,* vol. 111, p. 083910, 2012.

[177] T. Bonaedy, J. W. Choi, C. Jang, B.-C. Min, and J. Chang, "Enhancement of electric-field-induced change of magnetic anisotropy by interface engineering of MgO magnetic tunnel junctions," *Journal of Physics D: Applied Physics,* vol. 48, p. 225002, 2015.

[178] H. Yuki, K. Tomohiro, O. Aya, M. Kazumoto, O. Shimpei, and C. Daichi, "Electric field modulation of magnetic anisotropy in perpendicularly magnetized Pt/Co structure with a Pd top layer," *Applied Physics Express,* vol. 8, p. 113002, 2015.

[179] G.-X. Miao, K. B. Chetry, A. Gupta, W. H. Butler, K. Tsunekawa, D. Djayaprawira*, et al.*, "Inelastic tunneling spectroscopy of magnetic tunnel junctions based on CoFeB⁄MgO⁄CoFeB with Mg insertion layer," *Journal of Applied Physics,* vol. 99, p. 08T305, 2006.

[180] Y. Lu, C. Deranlot, A. Vaurès, F. Petroff, J. M. George, Y. Zheng*, et al.*, "Effects of a thin Mg layer on the structural and magnetoresistance properties of CoFeB⁄MgO⁄CoFeB magnetic tunnel junctions," *Applied Physics Letters,* vol. 91, p. 222504, 2007.

[181] Q. L. Ma, S. Iihama, T. Kubota, X. M. Zhang, S. Mizukami, Y. Ando*, et al.*, "Effect of Mg interlayer on perpendicular magnetic anisotropy of CoFeB films in MgO/Mg/CoFeB/Ta structure," *Applied Physics Letters,* vol. 101, p. 122414, 2012.

[182] M. D. Groner, J. W. Elam, F. H. Fabreguette, and S. M. George, "Electrical characterization of thin Al2O3 films grown by atomic layer deposition on silicon and various metal substrates," *Thin Solid Films,* vol. 413, pp. 186-197, Jun 24 2002.

[183] U. Bauer, M. Przybylski, J. Kirschner, and G. S. Beach, "Magnetoelectric charge trap memory," *Nano Lett,* vol. 12, pp. 1437-42, Mar 14 2012.

[184] K. Ono, N. Ohshima, K. Goto, H. Yamamoto, T. Morita, K. Kinoshita*, et al.*, "Effect of O-Ion Beam Irradiation during RF-Magnetron Sputtering on Characteristics of CoFeB–MgO Magnetic Tunnel Junctions," *Japanese Journal of Applied Physics,* vol. 50, p. 023001, 2011.

[185] H. Toyoda, K. Goto, T. Ishijima, T. Morita, N. Ohshima, and K. Kinoshita, "Fine Structure of O-Kinetic Energy Distribution in RF Plasma and Its Formation Mechanism," *Applied Physics Express,* vol. 2, p. 126001, Dec 2009.

[186] T. Ishijima, K. Goto, N. Ohshima, K. Kinoshita, and H. Toyoda, "Spatial Variation of Negative Oxygen Ion Energy Distribution in RF Magnetron Plasma with Oxide Target," *Japanese Journal of Applied Physics,* vol. 48, p. 116004, Nov 2009.

[187] X. Qiu, K. Narayanapillai, Y. Wu, P. Deorani, D.-H. Yang, W.-S. Noh*, et al.*, "Spin–orbit-torque engineering via oxygen manipulation," *Nat Nano,* vol. 10, pp. 333-338, 05//print 2015.

[188] S. Yuasa, Y. Suzuki, T. Katayama, and K. Ando, "Characterization of growth and crystallization processes in CoFeB⁄MgO⁄CoFeB magnetic tunnel junction structure by reflective high-energy electron diffraction," *Applied Physics Letters,* vol. 87, p. 242503, 2005.

[189] B. D. Cullity and C. D. Graham, "Ferromagnetism," in *Introduction to Magnetic Materials*, ed: John Wiley & Sons, Inc., 2008, pp. 115-149.

[190] H. M. Lu, W. T. Zheng, and Q. Jiang, "Saturation magnetization of ferromagnetic and ferrimagnetic nanocrystals at room temperature," *Journal of Physics D: Applied Physics,* vol. 40, p. 320, 2007.

[191] T. Liu, Y. Zhang, J. W. Cai, and H. Y. Pan, "Thermally robust Mo/CoFeB/MgO trilayers with strong perpendicular magnetic anisotropy," *Sci Rep,* vol. 4, p. 5895, Jul 31 2014.

[192] J. Swerts, S. Mertens, T. Lin, S. Couet, Y. Tomczak, K. Sankaran*, et al.*, "BEOL compatible high tunnel magneto resistance perpendicular magnetic tunnel junctions using a sacrificial Mg layer as CoFeB free layer cap," *Applied Physics Letters,* vol. 106, p. 262407, 2015.

[193] W. Kim, J. H. Jeong, Y. Kim, W. C. Lim, J. H. Kim, J. H. Park*, et al.*, "Extended scalability of perpendicular STT-MRAM towards sub-20nm MTJ node," *2011 Ieee International Electron Devices Meeting (Iedm),* 2011.

[194] L. E. Nistor, B. Rodmacq, C. Ducruet, C. Portemont, I. L. Prejbeanu, and B. Dieny, "Correlation Between Perpendicular Anisotropy and Magnetoresistance in Magnetic Tunnel Junctions," *Ieee Transactions on Magnetics,* vol. 46, pp. 1412-1415, Jun 2010.

[195] W. C. Tsai, S. C. Liao, H. C. Hou, C. T. Yen, Y. H. Wang, H. M. Tsai*, et al.*, "Investigation of perpendicular magnetic anisotropy of CoFeB by x-ray magnetic circular dichroism," *Applied Physics Letters,* vol. 100, p. 172414, 2012.

[196] N. Sato, A. El-Ghazaly, R. M. White, and S. X. Wang, "Effect of Mg Oxidation Degree on Rashba-Effect-Induced Torques in Ta/CoFeB/Mg(MgO) Multilayer," *IEEE Transactions on Magnetics,* vol. 52, pp. 1-4, 2016.

[197] A. Lisfi, C. M. Williams, L. T. Nguyen, J. C. Lodder, A. Coleman, H. Corcoran*, et al.*, "Reorientation of magnetic anisotropy in epitaxial cobalt ferrite thin films," *Physical Review B,* vol. 76, p. 054405, 08/03/ 2007.

[198] G. Yu, P. Upadhyaya, X. Li, W. Li, S. K. Kim, Y. Fan*, et al.*, "Room-Temperature Creation and Spin–Orbit Torque Manipulation of Skyrmions in Thin Films with Engineered Asymmetry," *Nano Letters,* vol. 16, pp. 1981-1988, 2016/03/09 2016.

[199] G. Yu, L.-T. Chang, M. Akyol, P. Upadhyaya, C. He, X. Li*, et al.*, "Current-driven perpendicular magnetization switching in Ta/CoFeB/[TaOx or MgO/TaOx] films with lateral structural asymmetry," *Applied Physics Letters,* vol. 105, p. 102411, 2014.

[200] K. L. Wang and P. K. Amiri, "Nonvolatile Spintronics: Perspectives on Instant-on Nonvolatile Nanoelectronic Systems," *Spin,* vol. 02, p. 1250009, 2012.

[201] W. Kang, L. Chang, Y. G. Zhang, and W. S. Zhao, "Voltage-Controlled MRAM for Working Memory: Perspectives and Challenges," *Proceedings of the 2017 Design, Automation & Test in Europe Conference & Exhibition (Date),* pp. 542-547, 2017.

[202] W.-G. Wang, S. Hageman, M. Li, S. Huang, X. Kou, X. Fan*, et al.*, "Rapid thermal annealing study of magnetoresistance and perpendicular anisotropy in magnetic tunnel junctions based on MgO and CoFeB," *Applied Physics Letters,* vol. 99, p. 102502, 2011.

[203] M. Yamanouchi, R. Koizumi, S. Ikeda, H. Sato, K. Mizunuma, K. Miura*, et al.*, "Dependence of magnetic anisotropy on MgO thickness and buffer layer in Co20Fe60B20-MgO structure," *Journal of Applied Physics,* vol. 109, p. 07C712, 2011.

[204] K. Yamane, Y. Higo, H. Uchida, Y. Nanba, S. Sasaki, H. Ohmori*, et al.*, "Spin Torque Switching of Perpendicularly Magnetized CoFeB-Based Tunnel Junctions With High Thermal Tolerance," *Ieee Transactions on Magnetics,* vol. 49, pp. 4335-4338, Jul 2013.

[205] L. Thomas, G. Jan, J. Zhu, H. Liu, Y.-J. Lee, S. Le*, et al.*, "Perpendicular spin transfer torque magnetic random access memories with high spin torque efficiency and thermal stability for embedded applications (invited)," *Journal of Applied Physics,* vol. 115, p. 172615, 2014.

[206] M. Gottwald, J. J. Kan, K. Lee, X. Zhu, C. Park, and S. H. Kang, "Scalable and thermally robust perpendicular magnetic tunnel junctions for STT-MRAM," *Applied Physics Letters,* vol. 106, p. 032413, 2015.

[207] T. Liu, J. W. Cai, and L. Sun, "Large enhanced perpendicular magnetic anisotropy in CoFeB⁄MgO system with the typical Ta buffer replaced by an Hf layer," *AIP Advances,* vol. 2, p. 032151, 2012.

[208] D. C. Worledge, G. Hu, D. W. Abraham, P. L. Trouilloud, and S. Brown, "Development of perpendicularly magnetized Ta|CoFeB|MgO-based tunnel junctions at IBM (invited)," *Journal of Applied Physics,* vol. 115, p. 172601, 2014.

[209] W. Skowroński, T. Nozaki, Y. Shiota, S. Tamaru, K. Yakushiji, H. Kubota*, et al.*, "Perpendicular magnetic anisotropy of Ir/CoFeB/MgO trilayer system tuned by electric fields," *Applied Physics Express,* vol. 8, p. 053003, 2015.

[210] A. Sonntag, J. Hermenau, A. Schlenhoff, J. Friedlein, S. Krause, and R. Wiesendanger, "Electric-Field-Induced Magnetic Anisotropy in a Nanomagnet Investigated on the Atomic Scale," *Physical Review Letters,* vol. 112, 2014.

[211] T. Kazuhito, M. Shinji, S. Yoichi, M. Norikazu, S. Teruya, and S. Yoshishige, "Large voltage-induced magnetic anisotropy field change in ferrimagnetic FeGd," *Applied Physics Express,* vol. 8, p. 073007, 2015.

[212] T. Nozaki, A. Kozioł-Rachwał, W. Skowroński, V. Zayets, Y. Shiota, S. Tamaru*, et al.*, "Large Voltage-Induced Changes in the Perpendicular Magnetic Anisotropy of an MgO-Based Tunnel Junction with an Ultrathin Fe Layer," *Physical Review Applied,* vol. 5, p. 044006, 04/15/ 2016.

[213] T. Nozaki, H. Arai, K. Yakushiji, S. Tamaru, H. Kubota, H. Imamura*, et al.*, "Magnetization switching assisted by high-frequency-voltage-induced ferromagnetic resonance," *Applied Physics Express,* vol. 7, p. 073002, 2014.

[214] T. Nozaki, Y. Shiota, M. Shiraishi, T. Shinjo, and Y. Suzuki, "Voltage-induced perpendicular magnetic anisotropy change in magnetic tunnel junctions," *Applied Physics Letters,* vol. 96, p. 022506, 2010.

[215] J. Sinha, M. Hayashi, A. J. Kellock, S. Fukami, M. Yamanouchi, H. Sato*, et al.*, "Enhanced interface perpendicular magnetic anisotropy in Ta|CoFeB|MgO using nitrogen doped Ta underlayers," *Applied Physics Letters,* vol. 102, p. 242405, 2013.

[216] T. Nozaki, T. Yamamoto, S. Tamaru, H. Kubota, A. Fukushima, Y. Suzuki*, et al.*, "Enhancement in the interfacial perpendicular magnetic anisotropy and the voltage-controlled magnetic anisotropy by heavy metal doping at the Fe/MgO interface," *APL Materials,* vol. 6, p. 026101, 2018.

[217] X. Li, K. Fitzell, D. Wu, C. T. Karaba, A. Buditama, G. Yu*, et al.*, "Enhancement of voltage-controlled magnetic anisotropy through precise control of Mg insertion thickness at CoFeB|MgO interface," *Applied Physics Letters,* vol. 110, p. 052401, 2017.

[218] H. Almasi, D. R. Hickey, T. Newhouse-Illige, M. Xu, M. R. Rosales, S. Nahar, J. T. Held, K. A. Mkhoyan, and W. G. Wang, "Enhanced tunneling magnetoresistance and perpendicular magnetic anisotropy in Mo/CoFeB/MgO magnetic tunnel junctions," *Applied Physics Letters*, vol. 106, p. 182406, 2015.

[219] G.-G. An, J.-B. Lee, S.-M. Yang, J.-H. Kim, W.-S. Chung, and J.-P. Hong, "Highly stable perpendicular magnetic anisotropies of CoFeB/MgO frames employing W buffer and capping layers," *Acta Materialia,* vol. 87, pp. 259-265, 4/1/ 2015.

[220] Note that due to finite temperature rise and fall time of the annealing process, the actual annealing time is in fact longer.

[221] G. Kresse and J. Furthmuller, "Efficiency of ab-initio total energy calculations for metals and semiconductors using a plane-wave basis set," *Computational Materials Science,* vol. 6, pp. 15-50, Jul 1996.

[222] J. P. Perdew, K. Burke, and M. Ernzerhof, "Generalized gradient approximation made simple," *Physical Review Letters,* vol. 77, pp. 3865-3868, Oct 28 1996.

[223] J. Sinha, M. Gruber, M. Kodzuka, T. Ohkubo, S. Mitani, K. Hono*, et al.*, "Influence of boron diffusion on the perpendicular magnetic anisotropy in Ta|CoFeB|MgO ultrathin films," *Journal of Applied Physics,* vol. 117, p. 043913, 2015.

[224] H. Almasi, D. R. Hickey, T. Newhouse-Illige, M. Xu, M. R. Rosales, S. Nahar*, et al.*, "Enhanced tunneling magnetoresistance and perpendicular magnetic anisotropy in Mo/CoFeB/MgO magnetic tunnel junctions," *Applied Physics Letters,* vol. 106, p. 182406, 2015.

[225] F. Bonell, S. Murakami, Y. Shiota, T. Nozaki, T. Shinjo, and Y. Suzuki, "Large change in perpendicular magnetic anisotropy induced by an electric field in FePd ultrathin films," *Applied Physics Letters,* vol. 98, p. 232510, 2011.

[226] H. Almasi, M. Xu, Y. Xu, T. Newhouse-Illige, and W. G. Wang, "Effect of Mo insertion layers on the magnetoresistance and perpendicular magnetic anisotropy in Ta/CoFeB/MgO junctions," *Applied Physics Letters,* vol. 109, p. 032401, 2016.

[227] X. G. Zhang, W. H. Butler, and A. Bandyopadhyay, "Effects of the iron-oxide layer in Fe-FeO-MgO-Fe tunneling junctions," *Physical Review B,* vol. 68, p. 092402, 09/04/ 2003.

[228] P. Bose, A. Ernst, I. Mertig, and J. Henk, "Large reduction of the magnetoresistance in Fe/MgO/Fe tunnel junctions due to small oxygen concentrations at a single FeO interface layer: A first-principles study," *Physical Review B,* vol. 78, Sep 2008.

[229] C. Tusche, H. L. Meyerheim, N. Jedrecy, G. Renaud, A. Ernst, J. Henk*, et al.*, "Oxygen-induced symmetrization and structural coherency in Fe/MgO/Fe(001) magnetic tunnel junctions," *Phys Rev Lett,* vol. 95, p. 176101, Oct 21 2005.

[230] R. C. O'Handley, *Modern Magnetic Materials: Principles and Applications*: Wiley, 1999.

[231] S. Yakata, H. Kubota, Y. Suzuki, K. Yakushiji, A. Fukushima, S. Yuasa*, et al.*, "Influence of perpendicular magnetic anisotropy on spin-transfer switching current in CoFeB∕MgO∕CoFeB magnetic tunnel junctions," *Journal of Applied Physics,* vol. 105, p. 07D131, 2009.

[232] V. B. Naik, H. Meng, and R. Sbiaa, "Thick CoFeB with perpendicular magnetic anisotropy in CoFeB-MgO based magnetic tunnel junction," *Aip Advances,* vol. 2, Dec 2012.

[233] K. Yakushiji, H. Kubota, A. Fukushima, and S. Yuasa, "Perpendicular magnetic tunnel junction with enhanced anisotropy obtained by utilizing an Ir/Co interface," *Applied Physics Express,* vol. 9, Jan 2016.

[234] F. De Boer, R. Boom, W. Mattens, A. Miedema, and A. Niessen, "Cohesion in Metals: Transition Metal Alloys. Vol. 1," *Elsevier Science Publishers B. V., 1988,* p. 758, 1988.

[235] Y. Zhang, Y. Li, Z. Sun, H. Li, Y. Chen, and A. K. Jones, "Read Performance: The Newest Barrier in Scaled STT-RAM," *IEEE Transactions on Very Large Scale Integration (VLSI) Systems,* vol. 23, pp. 1170-1174, 2015.

[236] Y. Morita, T. Mori, K. Fukuda, W. Mizubayashi, S. Migita, T. Matsukawa*, et al.*, "Experimental Realization of Complementary p- and n- Tunnel FinFETs with Subthreshold Slopes of less than 60 mV/decade and Very Low (pA/mu m) Off-Current on a Si CMOS Platform," *2014 Ieee International Electron Devices Meeting (Iedm),* 2014.

[237] M. H. Han, C. Y. Chang, H. B. Chen, J. J. Wu, Y. C. Cheng, and Y. C. Wu, "Performance Comparison Between Bulk and SOI Junctionless Transistors," *Ieee Electron Device Letters,* vol. 34, pp. 169-171, Feb 2013.

[238] S. Yu and P. Y. Chen, "Emerging Memory Technologies: Recent Trends and Prospects," *IEEE Solid-State Circuits Magazine,* vol. 8, pp. 43-56, 2016.

[239] A. Lee, H. Lee, F. Ebrahimi, B. Lam, W. H. Chen, M. F. Chang*, et al.*, "A Dual-Data Line Read Scheme for High-Speed Low-Energy Resistive Nonvolatile Memories," *IEEE Transactions on Very Large Scale Integration (VLSI) Systems,* vol. PP, pp. 1-8, 2017.

[240] S. Wang, A. Pan, C. O. Chui, and P. Gupta, "Tunneling Negative Differential Resistance-Assisted STT-RAM for Efficient Read and Write Operations," *Ieee Transactions on Electron Devices,* vol. 64, pp. 121-129, Jan 2017.

[241] I. Giaever and K. Megerle, "Study of Superconductors by Electron Tunneling," *Physical Review,* vol. 122, pp. 1101-1111, 05/15/ 1961.

[242] J. Z. Sun, "Spin-current interaction with a monodomain magnetic body: A model study," *Physical Review B,* vol. 62, pp. 570-578, Jul 1 2000.

[243] J. Stöhr and H. C. Siegmann. (2006). *Magnetism from fundamentals to nanoscale dynamics*. Available: http://dx.doi.org/10.1007/978-3-540-30283-4